Doctoral theses at NTNU, 2023:230

Irina-Mihaela Ciortan

Spectral and Multi-light Imaging for Cultural Heritage

Material Analysis and Appearance Reconstruction

Doctoral thesis

NTNU
Norwegian University of Science and Technology
Thesis for the Degree of
Philosophiae Doctor
Faculty of Information Technology and Electrical Engineering
Department of Computer Science

NTNU
Norwegian University of
Science and Technology

Irina-Mihaela Ciortan

Spectral and Multi-light Imaging for Cultural Heritage

Material Analysis and Appearance Reconstruction

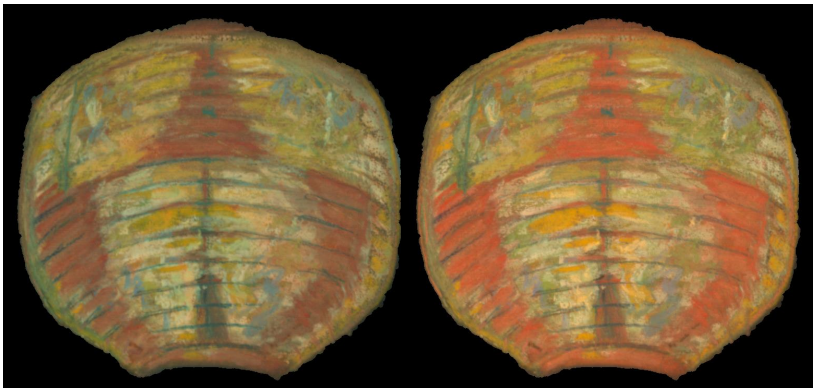

Thesis for the Degree of Philosophiae Doctor

Gjøvik, July 2023

Norwegian University of Science and Technology
Faculty of Information Technology and Electrical Engineering
Department of Computer Science

NTNU
Norwegian University of
Science and Technology

NTNU
Norwegian University of Science and Technology

Thesis for the Degree of Philosophiae Doctor

Faculty of Information Technology and Electrical Engineering
Department of Computer Science

Illustration: Simulations of the future degradation (left) and past appearance (right) of the central lantern in Oda Krohg's painting "A Japanese Lantern", presented in full detail in Part II, Paper 7.

ISBN 978-82-326-7160-1 (printed ver.)
ISBN 978-82-326-7159-5 (electronic ver.)
ISSN 1503-8181 (printed ver.)
ISSN 2703-8084 (online ver.)

Doctoral theses at NTNU, 2023:230

Printed by NTNU Grafisk senter

Abstract

The visual characteristics of an object are defined by complex light-matter interaction phenomena. The field of visual computing studies these phenomena in order to better understand optical properties of real world scenes so that ultimately, the reality can be approximated and reconstructed by life-like models. These models can be rooted in theoretical frameworks, or they can be constructed through the analysis of data, collected to enclose different aspects of the reality. Nowadays, there is a plethora of sensing techniques, able to capture various dimensions of an object, such as its spatial distribution, depth, color and reflectance, and even its aging behaviour.

This thesis pivots around the capture and analysis of spectral and multi-light images towards the recovery of material properties and appearance attributes, with a focus on cultural heritage applications. As part of the spectral module, the following techniques are used to measure the electromagnetic fingerprint of materials: reflectance image spectroscopy and microfading. Multi-light imaging records the interplay between the light and an object, when the former moves at different angles in the hemisphere above the latter. The spectral signals and multi-light image stacks are processed to create prototype representations of a given object, whereby its color, material and shape are reconstructed.

For cultural heritage, the term reconstruction carries a double meaning. On the one hand, it refers to the estimation of appearance properties from the analysis of data and images. On the other hand, it alludes to the restoration of damaged objects. Artworks have different ages that can date far back in history, as well as an inherent sensitivity to environmental factors. For this reason, many have incurred losses or degradation that altered their original appearance when they were first created.

This thesis proposes novel solutions to both meanings of appearance reconstruc-

tion for a diverse range of cultural heritage objects: bas-reliefs, paintings, drawings, murals. A share of the research outcomes is concerned with the assessment of shape reconstruction for fluorescent and non-fluorescent objects, relying on polynomial models to explain the multi-light image collections. In addition, characterization of material properties is performed using spectral signatures. Then, another area of research is dedicated to the restoration of artworks. In particular, a color-consistent method for loss infilling is proposed for the retouching of wall paintings. Furthermore, this thesis considers the temporal dimension related to light-induced aging, and integrates it to digitally simulate the past and future appearance of an artwork, with a method anchored in multivariate algebra. This innovative spatio-temporal simulation approach bridges the data collected with two spectral capture techniques, namely microfading and hypespectral imaging.

Finally, this thesis reviews the ethical implications of imaging workflows for cultural heritage applications, from acquisition to storage in digital repositories, processing, manipulation and reproduction.

To my ancestors

THE MUSHROOM HUNTERS *by Neil Gaiman*

Science, as you know, my little one, is the study
of the nature and behaviour of the universe.
It's based on observation, on experiment, and measurement,
and the formulation of laws to describe the facts revealed.

In the old times, they say, the men came already fitted with brains
designed to follow flesh-beasts at a run,
to hurdle blindly into the unknown,
and then to find their way back home when lost
with a slain antelope to carry between them.
Or, on bad hunting days, nothing.

The women, who did not need to run down prey,
had brains that spotted landmarks and made paths between them
left at the thorn bush and across the scree
and look down in the bole of the half-fallen tree,
because sometimes there are mushrooms.

Before the flint club, or flint butcher's tools,
The first tool of all was a sling for the baby
to keep our hands free
and something to put the berries and the mushrooms in,
the roots and the good leaves, the seeds and the crawlers.
Then a flint pestle to smash, to crush, to grind or break.

And sometimes men chased the beasts
into the deep woods,
and never came back.

Some mushrooms will kill you,
while some will show you gods
and some will feed the hunger in our bellies. **Identify.**
Others will kill us if we eat them raw,
and kill us again if we cook them once,
but if we boil them up in spring water, and pour the water away,
and then boil them once more, and pour the water away,
only then can we eat them safely. **Observe.**

Observe childbirth, measure the swell of bellies and the shape of breasts,
and through experience discover how to bring babies safely into the world.

Observe everything.

And the mushroom hunters walk the ways they walk
and watch the world, and see what they observe.
And some of them would thrive and lick their lips,
While others clutched their stomachs and expired.
So laws are made and handed down on what is safe. **Formulate.**

The tools we make to build our lives:
our clothes, our food, our path home…
all these things we base on observation,
on experiment, on measurement, on truth.

And science, you remember, is the study
of the nature and behaviour of the universe,
based on observation, experiment, and measurement,
and the formulation of laws to describe these facts.

The race continues. An early scientist
drew beasts upon the walls of caves

to show her children, now all fat on mushrooms
and on berries, what would be safe to hunt.

The men go running on after beasts.

The scientists walk more slowly, over to the brow of the hill
and down to the water's edge and past the place where the red clay runs.
They are carrying their babies in the slings they made,
freeing their hands to pick the mushrooms.

Acknowledgements

Every road in nature has its share of straight, flat, open lanes where you always clearly see the vanishing point as well as winding, steep curves, where you don't know what awaits you after the next turn. Sometimes, the scenery is breathtaking and inspiring, other times it's repetitive and not engaging.

In my case as well, the road to becoming a researcher, even though consistent, hasn't always been linear and full of visibility. Sometimes, I felt alone in the middle of the desert, other times I felt drawn by a whirlpool of forces and ideas that helped me drive through rewarding cliffs. What I often found comforting was to know that every time I needed, I could pull over and rest for a while on the shoulder of giants. Therefore, in this place I want to thank all the giants of research who served as inspiration. Those I haven't met in person, I tried to thank them through my citations. A few of those I had the pleasure to meet and talk to, I tried to include in the following lines.

I would like to thank my advisors, Sony George and Jon Yngve Hardeberg for choosing me as their co-worker all these years and for offering me the opportunity to fulfill my PhD at the NTNU. Sony, thanks for the reality checks and Jon, thank you for sharing your visionary mindset! I would like to add special thanks to Jon for having believed in my potential as a researcher ever since I was a CIMET master student, and for having offered me plenty of opportunities along the road. It is he who opened my eyes towards research as a great career choice - Jon, I will always be grateful for this!

A well-deserved appreciation goes to Prof. Marius Pedersen, the head of Colourlab, who, with his coordination, made sure that we, PhDs, are working in a friendly and thriving learning environment. On this note, I would like to thank all the colleagues in my office, in the Colourlab and the Computer Science department, who

were my net for social interactions and with whom I created a couple of great memories throughout the past years.

I would also like to express my gratitude to Tina Grette Poulsson for a great collaboration and teamwork spirit, I fully enjoyed our passionate detective work in studying the pastels of Oda Krohg. Likewise, I am thankful to Holly Rushmeier, for having hosted me at Yale University during my research visit - she is a role model for me as to what a researcher should become, and it was an honor to get to work with her, even if only for a brief period.

Before my PhD I had the pleasure to be part of a Horizon2020 research project, Scan4Reco, which was a truly formative experience for me. I would like to acknowledge all the consortium for I definitely grew as a researcher as a result of our partnership. In particular, I would like to send special thanks to my close collaborators and supervisors, Andrea Giachetti and Ruggero Pintus, from whom I learned a great deal about scientific methodology and conducting high quality research.

Other networking projects I feel privileged to have participated to, and that shaped my professional path in a beautiful and memorable way are: Color and Space in Cultural Heritage (COSCH), Archaeological Practices and Knowledge Work in the Digital Environment (ARKWORK), and Material Appearance Network for Education and Research (MANER).

During my PhD I held teaching activities, which strengthened the foundation of my academic curriculum. I would like to give credit to Prof. Deepti Mishra with whom I shared my first course as a lecturer, "Information Database Structure", for imparting with me valuable didactic practices. Similarly, I thank Sony George for supporting me in running and crafting the labs for the Computer Vision course, where I had the chance to revisit with higher depth some pioneering algorithms in the field.

I want to wholeheartedly acknowledge Prof. Alexander Wilkie, and his team for their great contribution to the field of computer graphics through ART - the Advanced Rendering Toolkit, and for kindly answering my emails with a great level of detail. I am grateful as well for having had the privilege to interact with Prof. Shoji Tominaga, and have thought-provoking discussions with him on the topic of fluorescence.

Many thanks to FUGE Gjøvik Kunstforening who, by organizing all the art exhibitions in the historic house of Kauffeldtgården, administered the dose of fiction I very much needed in the past years. I particularly want to express my gratitude to Ingrunn Myrland, Hilde Brovold and Elise Schonhowd for actively trying to integrate me in the art scene of Gjøvik. Also, I would like to thank Oda Krohg,

a pioneer woman artist, who broke the time barrier and managed to communicate with me through her painting, “A Japanese Lantern”, that I grew very fond of while studying it. Just like the lady in the painting, I found solace many times sitting by the window and admiring the Norwegian fjords (and lake Mjøsa in my case).

I also want to thank Giacomo Marchioro for the times he was there for me, for having cheered me up and encouraged me in my endeavours, even when I didn’t believe in myself, for being my Python cheat-sheet and my go-to conservation scientist for all sorts of questions. Also, to the rest of G.M.s, for the times they made me feel at home.

Most importantly, I would like to thank my family. Not only because they are the people who love me most in this whole world, but because they are all role-models for me, and they contributed to my learning process in various inspiring ways. To my mother Gina, who is my favourite woman, chemist, researcher and chef in the whole world. To my father Marin for all the math lessons, for having gifted us the first computer, Pentium 2, and for being an admirer of my first ASCII robot coded in Turbo Pascal, back when I was in the fifth grade. To my sister Cristina, who is a great data analyst, and inspired me with her passion for statistics and her fine sense of aesthetics. To my brother Mari, a holistic engineer, for his warmth and care, his overall dedication to family and for having awakened in me the passion for good literature at an early age. To my sister-in-law Ioana for her business spirit and organizational piece of advice. To my niece Nati and nephews Matei, Victor & Marc for keeping my playfulness and creativity up-to-date. To my kind uncle Tatanelu, who was a dreamer and a great mind for inventions, and to my strong grandmother, Mamaica, who was the best storyteller I’ve ever known and a truly good person, despite witnessing so many historic hardships of the current and the previous century: I miss you.

Thank you all, giants!

Contents

List of Acronyms

AI	Artificial Intelligence
ACF	Autocorrelation Function
ARIMA	Auto-regressive Moving Average Models
BRDF	Bidirectional Reflectance Distribution Function
BBRDF	Bispectral Bidirectional Reflectance Distribution Function
CIE	Commission Internationale de l'Éclairage
CCD	Charge-Coupled Device
CMOS	Complementary Metal-Oxide Semiconductor
CNN	Convolutional Neural Network
CH	Cultural Heritage
DSLR	Digital Single-Lens Reflex
FTI	Fluorescence Transformation Imaging
GAN	Generative Adversarial Network
HSH	Hemispherical Harmonics
IR	Infrared
LED	Light Emitting Diode
MLIC	Multi-light Image Collection

MFT	Microfadeometer
NIR	Near Infrared
PACF	Partial Autocorrelation Function
PARAFAC	Parallel Factor Analysis
PCA	Principal Component Analysis
PLD	Portable Light Dome
PS	Photometric Stereo
PSNR	Peak Signal to Noise Ratio
PTM	Polynomial Texture Map
PTMD	Polynomial Texture Map by Drew
RIS	Reflectance Image Spectroscopy
RBF	Radial Basis Function
RTI	Reflectance Transformation Imaging
SSIM	Structural Similarity Index Measure
UV	Ultraviolet
UVF	Ultraviolet-induced Fluorescence
UNESCO	United Nations Educational, Scientific and Cultural Organization
VIS	Visible range of the electromagnetic spectrum
SNR	Signal-to-noise Ratio

List of Publications

Paper 1 Ciortan, I. M., Dulecha T. G., Giachetti, A., Pintus, R., Jaspe-Villanueva A., Gobbetti, E. (2018). Artworks in the spotlight: Characterization with a multispectral LED dome. IOP Conference Series: Materials Science and Engineering, 364. https://doi.org/10.1088/1757-899X/364/1/012025

Paper 2 Ciortan, I. M., Giachetti, A., George, S., & Hardeberg, J. Y. (2021). Fluorescence Transformation Imaging. Optics for Arts, Architecture, and Archaeology VIII, 11784, 156–172. https://doi.org/10.1117/12.2593651

Paper 3 Ciortan, I. M., George, S., & Hardeberg, J. Y. The Influence of Interreflections on Shape from Fluorescence. (Submitted)

Paper 4 Ciortan, I. M., Poulsson, T. G., George, S., & Hardeberg, J. Y. (2022). Spectral Classification of Paper Fixatives: A Case Study on Thomas Fearnley's Drawings, IS&T Archiving Conference, 19: 89–94. https://doi.org/10.2352/issn.2168-3204.2022.19.1.18

Paper 5 Ciortan, I. M., Poulsson, T. G., George, S., & Hardeberg, J. Y. (2022). Predicting Pigment Color Degradation with Time Series Models. Color and Imaging Conference, 30, 250–257. https://doi.org/10.2352/CIC.2022.30.1.44

Paper 6 Ciortan, I. M., Poulsson, T. G., George, S., & Hardeberg, J. Y. (2023). Tensor Decomposition for Painting Analysis. Part 1: Pigment Characterization. Heritage Science, 11(1), 76. https://doi.org/10.1186/s40494-023-00910-x

Paper 7 Ciortan, I. M., Poulsson, T. G., George, S., & Hardeberg, J. Y. (2023). Tensor Decomposition for Painting Analysis. Part 2: Spatio-temporal Simulation. Heritage Science, 11(1), 84. https://doi.org/10.1186/s40494-023-00913-8

Paper 8 Ciortan, I. M., Grillini F., George, S., & Hardeberg, J. Y. Estimating

Optical Properties of Pigments from Color Charts with Multi-contrast Background. (Submitted)

Paper 9 Ciortan, I. M., George, S., & Hardeberg, J. Y. (2021). Colour-Balanced Edge-Guided Digital Inpainting: Applications on Artworks. Sensors, 21(6), Article 6. https://doi.org/10.3390/s21062091

Paper 10 Ciortan, I. M., George, S., & Hardeberg, J. (2022). Better Sensors, Better Forgers: An Adversarial Loop. Authenticity Studies. International Journal of Archaeology and Art, 1(Volume 1, Issue 1), 168-193. https://doi.org/10.14658/PUPJ-AS-2022-1-12

Part I

Introduction

Chapter 1

Introduction

Eu nu strivesc corola de minuni a
lumii
şi nu ucid
cu mintea tainele, ce le-ntâlnesc
în calea mea.

Lucian Blaga

I do not crush the sense of wonder
in the world and I do not murder
in my inquiry
the mystery
that meets me.

English translation by Irina Ciortan

1.1 Motivation and Area of Research

Cultural heritage (CH) is a legacy of the past and a witness of history, which helps humanity understand its present through the study of previous artistic expressions. As with all matter, tangible CH undergoes continuous transformation that alters its original form, which in turn may affect the understanding and interpretation of the meaning it was intended to convey at the incipient moment of its creation. Moreover, cultural heritage is at risk of destruction, due to natural and human-provoked disasters, such as floods [1], earthquakes [2], fires [3, 4] and wars [5].

For this reason, it is crucial to gather as much knowledge as possible and as fast as possible by documenting and analyzing existing CH. However, this urge ought to adhere to a certain priority-based selectivity, as excessive digitization has a high cost to it, and subsequently translates to further depletion of financial [6] and environmental resources required for the preservation of digital data [7]. Once digitization is accomplished, further actions can be taken towards CH preservation and conservation. The past decades brought a surge in accessible digitization techniques, concomitant to an increased awareness to CH needs, which has leveraged the possibilities to capture, study and analyze CH objects. Because visual appearance entails complex physical phenomena, sensing techniques, although in a continuous progress, still present numerous challenges especially if they are not designed with the CH applications in mind.

This PhD thesis falls at the intersection of two scientific fields: visual computing and heritage science. Visual computing [8] is a collective term that encompasses all the computational methods that deal with the capture, processing, analysis, understanding and rendering of visual data. Accordingly, visual computing is a somewhat multidisciplinary field, an umbrella for the fields of image acquisition, image processing, computer vision and computer graphics. Similarly, heritage science is a generic term, that refers collectively to all the scientific and humanities investigation methods employed to understand, manage and conserve cultural heritage artifacts [9]. Although the term "heritage science" was officially coined by the House of Lords in 2006 [10], the first scientific study on heritage dates back to the 19^{th} century, when Sir Humphry Davy analyzed the chemical composition of the pigments and papyri in the archaeological sites of Pompeii [11] and Herculaneum [12], respectively. Davy's work on heritage was followed up by his pupil, Michael Faraday, who researched the effects of indoor air pollution on the chemical degradation of books made of leather. While primarily, heritage science was associated with the conservation and archaeological sciences, the former has evolved to a larger sphere of influence, which now includes computer vision approaches [13] that empower the interpretation of CH. Thus, visual computing can offer a set of toolboxes to improve and solve current CH needs in a tangential way to the heritage science approaches [14]. The following CH needs are identified as topical and pertinent to be addressed with visual computing techniques:

- *Documentation* - the need to record the present status of conservation of a tangible cultural heritage object, which includes its visual appearance, towards establishing preservation and conservation policies [15].

- *Material analysis and identification* - the need to track down the chemical composition of a work of art, which becomes a fingerprint helpful for un-

derstanding the artist's technique, for geographical or historical dating, and for detection of forgeries. In addition, material analysis plays a role, as a diagnostic tool, and serves the decision-making process in preventive conservation.

- *Classification of artistic style* - because there are artworks with anonymous creator or wrongly, if not falsely attributed, it is important to develop tools that can distinguish between artists and their style [16, 17]. Zooming out, in the broad perspective of the history of art, it is of interest to differentiate between art periods as well [18].

- *Visualization* - the need to render a cultural heritage object and interact with as many of its dimensions as possible, in a photorealistic [19] or non-photorealistic instance, and under different lighting and viewing conditions. With the advent of virtual reality technologies and immersive environments, the need for visualization has gained increasing attention [20].

- *Restoration of damaged and lost art* - from a physical restoration point of view, this translates to the need to retouch a work of art so that the original artistic intention, together with the aesthetic unity, are reclaimed. Under a virtual restoration perspective, this need adheres to multiple scenarios. For instance, it can refer to the possibility to reverse the aging effects of an artwork, and simulate a digital rejuvenation of its original appearance. In a conservation-restoration theory, it can create a digital workshop for a restorer to practice before an actual physical restoration, by trying out various materials and retouching methods computationally.

- *Ethical digitization, diagnostic, conservation and restoration* - beyond artistic and historical value, CH has an appreciable monetary value as well, and the numbers of trades and stocks on the art market, especially in the Western side of the world, speak for themselves. This financial glow may attract stakeholders who are more interested in profit rather than the wellness and conservation of the CH artifact. For this reason, it is necessary to establish ethical guidelines to ensure that the digitized data is collected, reported and analyzed in an unbiased and truthful manner, and leave no room for unjustified digital manipulations of the raw data that might tamper with the subsequent steps in the diagnostic, conservation and restoration of a CH object.

1.2 Research Objectives and Questions

Drawing from the pool of identified CH conservation-restoration needs in the previous section, this PhD thesis targets three research objectives: **1)** digitize CH objects in a non-invasive way, so as to capture optical properties that characterize the multilateral appearance of the objects; **2)** analyze the visual data to characterize the material and appearance of the CH object; **3)** model the captured and analyzed data to reconstruct the appearance. Thus, the objectives correspond to three subareas of research: data capture, analysis, and appearance reconstruction. The core methods for data acquisition and analysis in this thesis revolve around spectral and multi-light imaging techniques. In particular, the following four research questions were defined:

- **RQ1**: How to capture the appearance of artworks in a non-invasive way and beyond what is visible to the naked eye?
- **RQ2**: How to extract appearance and material properties based on descriptors in the color, spectral and multi-light domains?
- **RQ3**: How to digitally reconstruct, restore and predict the appearance of artworks using data-driven and physical models?
- **RQ4**: What are the ethical and legal implications of cultural heritage digitization and virtual restoration given the increasing accessibility of imaging sensors and the recent take-off of AI techniques?

1.3 Thesis Structure

This dissertation is a compilation of 10 research articles and is organized in two parts. **Part I** is an introductory narrative that is meant as a guide for the reader to understand at a high-level the theoretical concepts and methodologies elaborated in the articles, and to show how the articles inter-connect and how they contribute to the formation of an entity (the thesis) that is bigger than the sum of its parts (articles). **Part I** is divided into 5 chapters. **Chapter 1** introduces the field of research and highlights the research needs and gaps that this thesis aims to address. **Chapter 2** is a brief overview of the background of the performed research, and brings together theoretical concepts and a review of state-of-the-art related works. In **Chapter 3**, the experimental designs throughout the articles are synthesized, grouping the articles based on methodology and employed datasets. After a general summary, each article is succinctly described, one by one. Subsequently, **Chapter 4** presents a general discussion of the research outcomes of

this thesis, in the context of the main contributions and novelties proposed. Finally, **Chapter 5** concludes with the main take-aways and reflects upon future directions of research, that can build on the findings of this thesis while following the state-of-the-art trends in appearance reconstruction.

Part II is an anthology of the 10 articles (8 published and 2 under peer review) in their original and full versions. Out of the 8 publications, 4 are published in journals and 4 in conference proceedings. The remaining 2 were submitted for a journal and a conference, respectively. The articles are enumerated below, and Fig. 1.1 illustrates with a Venn diagram, the contributions of the articles for the research tasks addressed in this thesis, and how they relate to the research questions.

List of Publications

P1 Ciortan, I. M., Dulecha T. G., Giachetti, A., Pintus, R., Jaspe-Villanueva A., Gobbetti, E. (2018). Artworks in the spotlight: Characterization with a multispectral LED dome. IOP Conference Series: Materials Science and Engineering, 364. https://doi.org/10.1088/1757-899X/364/1/012025

P2 Ciortan, I. M., Giachetti, A., George, S., & Hardeberg, J. Y. (2021). Fluorescence Transformation Imaging. Optics for Arts, Architecture, and Archaeology VIII, 11784, 156–172. https://doi.org/10.1117/12.2593651

P3 Ciortan, I. M., George, S., & Hardeberg, J. Y. The Influence of Interreflections on Shape from Fluorescence. (Submitted)

P4 Ciortan, I. M., Poulsson, T. G., George, S., & Hardeberg, J. Y. (2022). Spectral Classification of Paper Fixatives: A Case Study on Thomas Fearnley's Drawings, IS&T Archiving Conference, 19: 89–94. https://doi.org/10.2352/issn.2168-3204.2022.19.1.18

P5 Ciortan, I. M., Poulsson, T. G., George, S., & Hardeberg, J. Y. (2022). Predicting Pigment Color Degradation with Time Series Models. Color and Imaging Conference, 30, 250–257. https://doi.org/10.2352/CIC.2022.30.1.44

P6 Ciortan, I. M., Poulsson, T. G., George, S., & Hardeberg, J. Y. (2023). Tensor Decomposition for Painting Analysis. Part 1: Pigment Characterization. Heritage Science, 11(1), 76. https://doi.org/10.1186/s40494-023-00910-x

P7 Ciortan, I. M., Poulsson, T. G., George, S., & Hardeberg, J. Y. (2023). Tensor Decomposition for Painting Analysis. Part 2: Spatio-temporal Simulation. Heritage Science, 11(1), 84. https://doi.org/10.1186/s40494-023-00913-8

P8 Ciortan, I. M., Grillini F., George, S., & Hardeberg, J. Y. Estimating Optical Properties of Pigments from Color Charts with Multi-contrast Background. (Sub-

mitted)

P9 Ciortan, I. M., George, S., & Hardeberg, J. Y. (2021). Colour-Balanced Edge-Guided Digital Inpainting: Applications on Artworks. Sensors, 21(6), Article 6. https://doi.org/10.3390/s21062091

P10 Ciortan, I. M., George, S., & Hardeberg, J. (2022). Better Sensors, Better Forgers: An Adversarial Loop. Authenticity Studies. International Journal of Archaeology and Art, 1(Volume 1, Issue 1), 168-193. https://doi.org/10.14658/PUPJ-AS-2022-1-12

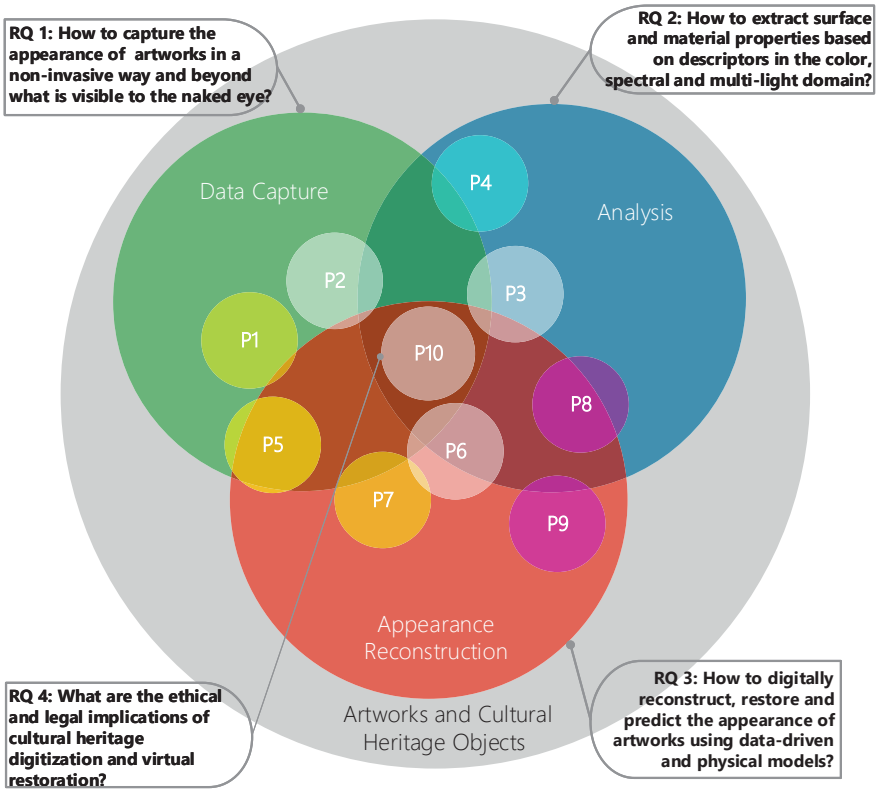

Figure 1.1: A Venn diagram illustrating the relationship between the three sub-areas of research in this thesis and the corresponding publications, which propose solutions to the four identified research questions. The color coding of the publications follows the RGB mixing model.

1.4 Research Design

Broadly, the reasoning that shapes research design can be of two types: inductive and deductive. In the inductive paradigm, the trajectory to confirming a scientific theory is built in a bottom-up direction, starting from particular instances to reach a general formulation [21]. In the deductive logic, hypotheses regarding the general theory are considered known, so the reasoning searches for the proofs to confirm the theory in a top-down manner [21]. It is common to link inductive logic with qualitative research and deductive reasoning with quantitative research [22]. Nonetheless, it can be argued that the difference between inductive and deductive reasoning overcomes the strict dichotomy of qualitative/quantitative and is positioned in the territory defined by the nature of the experimental variables [23]. On the one hand, deductive logic better addresses problems in exact sciences with clear and easy to control variables. On the other hand, inductive reasoning better copes with complex, multidisciplinary dilemmas in exact sciences, where the involved variables are intractable and not entirely known in advance [24, 25]. In this thesis, a combination of inductive and deductive reasoning is employed, i.e. the so-called mixed methods approach to research [22]. The motivation for juxtaposing both paradigms lies in the assumption that this design leads to a holistic understanding and interpretation of the research problem.

The foundation to research design is rooted in the following four philosophical worldviews [22]: postpositive, constructive, transformative, pragmatic. Postpositivism is a deterministic philosophy, where laws and theories that govern the world are the cause of all effects, phenomena and manifestations of the real world. Here, the goal of research is to find evidence that prove the ruling theories. Thus, postpositivism is based on deductive reasoning, and it supports quantitative or scientific research method. Opposite to positivism, constructivism relies on the subjective interpretation of humankind in their interaction with the world to seek meaning and understanding. This philosophy follows an inductive logic, and is associated with qualitative or social inquiries. The transformative worldview has a political stand, and advocates for an open, fair and unbiased research, where marginalized social groups and categories are included in the research process. Lastly, pragmatism is a problem-centric philosophy, where the research question guides the methods employed, which can be a mix of quantitative and qualitative approaches. The intention is to exhaust pluralistic methods to derive knowledge in finding the solution to the research problem. The pragmatic stance holds accountability of the political context and social justice [22]. Therefore, it can be claimed that the pragmatic philosophy, in its openness to the use of multiple methods, circumscribes the other three systems of beliefs, namely postpositivism, constructivism and transformative. Because of its multidisciplinarity, this dissertation is dominated by pragmat-

ism. Nevertheless, being a primarily scientific thesis, it focuses on quantitative methods, with a postpositivistic lens. At the same time, the opinion and judgement of CH experts are kept in the loop, while the ethical impact of all actions involved is reflected upon in a transformative spirit. In section 4.5, the research paradigms are further discussed in relationship with every article attached to this thesis.

I would like to conclude this chapter with a personal reflection and a joke, gathered from [21] that exemplifies the inductive reasoning. Even though I'm an advocate of both deductive and inductive research, I consider that because reality is complex and multi-faceted, only by continuing to observe and explore the world with an inductive attitude, and from a kaleidoscopic multidisciplinary point of view, we can formalize and understand phenomena which are yet hidden, or simply a mystery. It might be that sometimes, deductive research has the pitfall of tuning a method in biased ways until the desired and known results are reached, whereas in inductive research, it's mostly the data that speaks for itself. The following joke, with detective Sherlock Holmes and Dr Watson as protagonists, shows how we can solve a detective case, following multiple leads: *"Sherlock Holmes and Dr Watson went on a camping trip. In the middle of the night, Holmes wakes up and give Dr. Watson a nudge. "Watson," he says, "look up in the sky and tell me what you see." Watson replied, "I see millions of stars." "And what do you conclude from that, Watson?" Watson thinks for a moment. "Well,", he says, "astronomically, it tells me that there are millions of galaxies and potentially billions of planets. Astrologically, I observe that Saturn is in Leo. Horologically, I deduce that the time is approximately a quarter past three. Theologically, I can see that God is all-powerful and that we are small and insignificant. Meteorologically, I suspect that we will have a beautiful day tomorrow. Uh, what does it tell you, Holmes?" "Watson, you fool. Someone has stolen our tent."*

Chapter 2

Fundamentals

La steaua care-a răsărit
E-o cale-atât de lungă,
Că mii de ani i-au trebuit
Luminii să ne-ajungă.

Mihai Eminescu

'Tis such a long way to the star
Rising above our shore
It took its light to come so far
Thousands of years and more.

English translation by Adrian George Sahlean

This chapter brings together a short compendium of theoretical notions approached in this thesis. Thus, it elaborates on the appearance and material properties of cultural heritage objects, state-of-the-art optical techniques for capturing these properties, and finally, analysis methods towards appearance reconstruction. Then, every article attached as a research outcome to this thesis, further includes an in-depth background review for each addressed topic in particular.

2.1 Appearance Representation

The appearance of an object is influenced by the intrinsic characteristics of the object, and their interaction with the light conditions under which the object is

observed [26]. The intrinsic characteristics refer to the shape and chemical composition of an object. The former defines the visibility and interaction of certain elements on the surface of the object and explains the formation of shadows and interreflections, whereas the latter determines the spectral signature of a material, which in turn affects the color. Generally speaking, appearance properties are concentrated only on what is visible, i.e. to the range of electromagnetic spectrum of radiation confined to 400 - 700 nm. Meanwhile, material properties emerge as well from the light-matter interaction beyond the visible range.

2.1.1 Optical Properties of Materials

Cultural Heritage objects are often made of coloring materials, namely dyes or pigments [27]. When light collides with a colored material, it can get absorbed, scattered or transmitted [27]. The higher the absorption of a colorant, the darker it looks, as there remains less energy for the light to bounce off the surface. When scattering occurs, the incoming light is redirected from the surface back into the observation hemisphere. If the light passes through the material without being absorbed nor scattered, then, the layer behind that of the colorant becomes visible, which enacts translucency and transparency effects. The optical properties manifest in a wavelength-dependent way, which means that a colored material selectively absorbs, scatters and transmits spectral bands of a given light. By knowing the selective absorption and scattering of a material, it is possible to compute its spectral reflectance, a measure of how much light is reflected off the surface of the material. The mathematical expression of reflectance as a function of absorption and scattering is given by the Kubelka-Munk model [28], detailed in an upcoming subsection. Fig. 2.1 depicts the absorption, scattering and reflectance of a vermilion pigment, as wavelength-dependent functions.

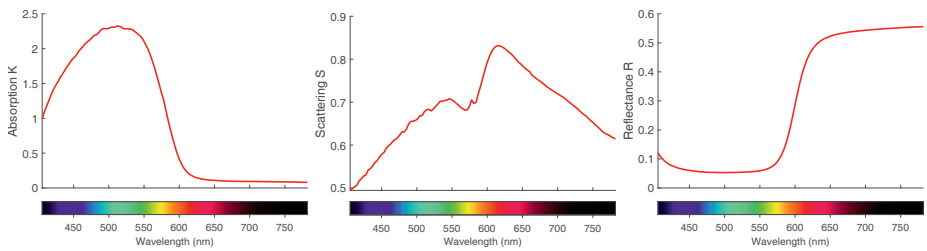

Figure 2.1: Absorption, scattering and reflectance factors of a vermilion pigment. Data from **P8**, where scattering and absorption were computed from the known measured spectral reflectance, using Kubelka-Munk equations.

2.1.2 Fluorescence

In addition to reflectance, when excited by short-wavelength light, fluorescent materials re-emit the light at a higher spectral range [29]. The difference in energy between the excitation and emission is denominated the Stokes shift [30], after the Irish physicist, George Stokes who first coined the term fluorescence and observed its manifestation in various materials. The existence of the two spectra, absorption of the stimulating radiation source and the luminescence, respectively, dictates the bispectral nature of fluorescent materials.

Fluorescence is a time-resolved photo-luminescence phenomenon, where an excited electron returns to its lower-energy ground state by releasing its excess energy as a photon. This electronic transition process occurs without a change in the electron spin, thus keeping the electrons in an excited state for a short period of time, of microseconds order. Fluorescence is similar to the phosphorescence phenomenon, that is also based on energy transfer, but the latter triggers a change of the electron spin and so has a longer lifetime and a latency in light re-emission [31]. In other words, fluorescence happens as long as the activation light source is turned on, and the re-emission happens almost instantly, at an order of nanoseconds up to microseconds [27]. Conversely, phosphorescence is delayed more than microsecond levels, and lingers even after the stimulating light source is turned off.

The bispectral nature of fluorescent materials can be represented graphically in three ways. The first is to plot the spectral distributions of reflectance, excitation and emission as a function of wavelength. The second method is to translate each optical property as a dimension in a 3D plot, the so-called Donaldson matrix [32], where the luminescence is perceived as a bump. This representation is the one that best depicts the fact that fluorescence is a low-intensity signal, when compared with the reflectance. The third method, entitled reradiation matrix, is the one commonly used in the field of computer graphics. In the reradiation matrix, the x-axis represents the wavelengths of incident lights, and the y-axis the wavelengths of the response recorded from the material. Thus, the values on the diagonal, where the incident wavelength equals the detecting wavelength, denote the reflectance. The off-diagonal values in the bottom left corner of the matrix delineate the emission. Then, the off-diagonal values in the top right corner are zero, because there can be no emission for incident light's wavelength longer than the sensing wavelength. For this reason, the reradiation matrix is a sparse array. Fig. 2.2 illustrates the three graphical representation methods for a green daylight fluorescent material.

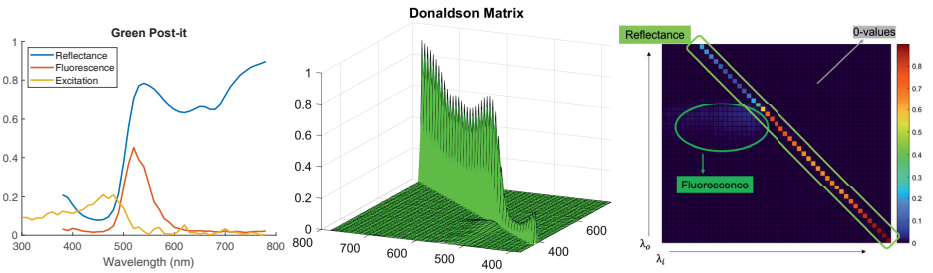

Figure 2.2: Three representations of a green daylight fluorescent material: spectral plot, Donaldson matrix, reradiation matrix.

Fluorescent materials for Cultural Heritage

In CH, fluorescent materials are very important from two perspectives: conservation and visual effects. Firstly, several colorants, binding media and varnish types consist of chemical compounds that have a UV-induced fluorescence. This can be helpful for the detection of fading red lakes [33], the formation of metallic soaps [34] or for the segmentation of old varnish from new varnish that typically indicates interventions or retouchings [35]. Secondly, ever since the 1960s, when daylight fluorescent pigments were made commercially available, they became widespread in the art scene, and new tools for artists such as Andy Warhol, Frank Stella, Herb Aach, Richard Bowman, James Rosenquist [36], Felix DeBoeck [37], and so on and so forth. Daylight fluorescent pigments are particularly successful in the art world because of the increased brightness and vividness, which can lead to special visual effects. For example, in the "Irregular Polygons" paintings' series by Frank Stella [38], it has been discovered in a psycho-physical experiment, that alternating stripes of fluorescent colors with stripes of conventional colors, resulted in an increased perception of depth. In comparison, when only conventional colors were displayed, the pictures were interpreted as overall flatter.

2.1.3 Kubelka-Munk Model

The Kubelka-Munk model [28] stipulates a mathematical expression (see Eq. 2.1 and 2.2) where the reflectance $R(\lambda)$ of a colored specimen is a non-linear function of four variables: absorption $K(\lambda)$, scattering spectrum $S(\lambda)$, thickness of the colored layer X and the reflectance factor of the background $R_{bg}(\lambda)$, where λ refers to the spectral dependencies of these parameters. This is the general expression, valid for translucent, as well as opaque colored colorants [31]. For the latter, the equation can be further simplified by removing the variables that characterize translucent coatings (thickness and background reflectance) and by assuming that scattering is so strong that it approaches unity. In this case, the reflectance

$R_{opaque}(\lambda)$ of the colorant is orchestrated only by the ratio of absorption over scattering, as in Eq. 2.3.

$$R(\lambda) = \frac{1 - R_{bg}(\lambda)[a(\lambda) - b(\lambda)\coth(b(\lambda)S(\lambda)X)]}{a - R_{bg}(\lambda) + b(\lambda)\coth(b(\lambda)S(\lambda)X)} \tag{2.1}$$

$$a(\lambda) = \frac{K(\lambda)}{S(\lambda)} + 1, b(\lambda) = \sqrt{a(\lambda)^2 - 1} \tag{2.2}$$

$$\frac{K}{S}(\lambda) = \frac{(1 - R_{opaque}(\lambda))^2}{2R_{opaque}(\lambda)} \tag{2.3}$$

Based on the Kubelka-Munk model, Duncan [39] proposed a linear model to simulate the mixtures of pigments from the scattering and absorption coefficients. As formulated in Eq. 2.4, the absorption of the mixture, K_{mix}, is a sum of the absorptions of each constituent, weighted by their concentrations c_i, akin to the overall scattering coefficient of the mixture S_{mix}.

$$K_{mix} = \sum c_i k_i, S_{mix} = \sum c_i s_i \tag{2.4}$$

Thus, the Kubelka-Munk model can be employed to solve forward tasks, such as simulating the reflectance of colorant mixtures given their optical coefficients and concentration values, as well as for inverse tasks, such as estimating the optical properties of colorants and their concentrations from reflectance measurements [40]. As a preview, in this thesis, **P8** uses the Kubelka-Munk model first for the inverse task, to recover absorption and scattering coefficients of a set of pigments. Then, it uses the recovered coefficients and combines them with previously known concentration maps to simulate the reflectance of a painting.

The Kubelka-Munk model works well for describing most of the colored materials, but under the assumption that the material is isotropic, and so it diffuses light equally in all directions. In addition, the Kubelka-Munk has not yet been fully defined for fluorescent materials [31]. Nevertheless, it was used for the correction of the apparent emission spectrum in UV-induced fluorescent images (UVF) under the opaque assumption [41, 42], which was later extended to translucent luminescent pigments [43] and also for creating an optical model to characterize fluorescent dental resins [44].

In particular, Verri et al. [41] point out the importance of correcting for the apparent fluorescence, also known as pseudo-fluorescence [33] that happens when

non-fluorescent components located in the proximity of fluorescent components absorb the fluorescence of the latter. For artworks, such an interaction is often triggered by the degraded varnishes that emit fluorescence and is absorbed by non-luminescent pigments. Verri et al. exemplify their workflow for UVF images of the wall paintings from the Mogao caves [45] at the UNESCO Dunhuang site. The post-capture correction is carried out with a model based on the Kubelka-Munk theory and adapted for fluorescent spectra, originally proposed by Ramos [46] for the correction of chlorophyll's fluorescence in plant leaves. As such, the paint layer is assumed to be opaque and homogeneous and characterized by two parameters: the absorption and scattering coefficients. Under the opaque assumption, the ratio of these two coefficients, called remission function, can be measured from the spectral reflectance. Based on the remission component, a correction factor that eliminates the absorption of fluorescence by surrounding non-fluorescent elements is computed. Further on, the initially captured UVF image is divided pixel-wise by the correction factor resulting in the corrected UVF image, unaffected by the presence of fluorescence absorbing and scattering media. By visualizing the corrected fluorescent images of the Dunhuang wall paintings, the interpretability of the materials changed with respect to the uncorrected UVF images: some areas that appeared luminescent initially lost the fluorescent effect after correction, meaning that they were apparent emissions caused by the fluorescing binder. Therefore, this type of correction for UVF images adds precision in material analysis. It is worth mentioning that even if the authors focused on UVF images, the method can be extrapolated to fluorescent images in general, excited by lights other than UV. This correction methodology was used in a study on the emissiveness of carmine lake paints in the presence of lead white [42] that acts as a scattering agent, increasing the fluorescing effect of the former.

Even though Verri et al. [41] and Clementi et al. [42] found the Kubelka-Munk model suitable and leading to sufficiently accurate interpretations, both for a mockup test target and for a painting by Vasari, the authors concluded that the self-absorption model can not fully describe all the chemical and physical interactions between fluorophores and other materials in a painting. Moreover, they stress the importance of validating the corrected fluorescence information with measurements provided by other analytical techniques.

2.1.4 (Bispectral) Bidirectional Reflectance Distribution Function

The optical properties presented so far are presented under the isotropic assumption, meaning that they are not affected when the illumination angle shifts with respect to the viewing angle. However, most real-world materials are not isotropic and their appearance change with the illumination-viewing configuration. This gonio-dependent behaviour is described by the Bidirectional Reflectance Distribu-

tion Function (BRDF) [26], first formalized by [47], where the spectral reflectance of a surface is described as a function of the illumination and viewing directions with respect to the normal (the angle perpendicular to the tangent of a surface):

$$f_r(w_o, w_i, \lambda) = \frac{dL_o(w_o, \lambda)}{dE(\lambda)} = \frac{dL_o(w_o, \lambda)}{L_i(w_i, \lambda)\cos\theta_i dw_i}[sr^{-1}] \tag{2.5}$$

In Eq. 2.5, w_o and w_i represent the outgoing and incident light vectors with respect to the surface normal, $dL_o(w_o, \lambda)$ is the differential of light radiance exiting in the viewing direction, and $dE(\lambda)$ is the irradiance received by the surface from the incoming light. The latter term can be replaced by the product of the incident light radiance, $L_i(w_i, \lambda)$ with the cosine of the angle θ_i between the incident light and the surface normal, and the differential of the incident light direction vector.

The simplest instance of a BRDF is given by the Lambertian model [48], which characterizes isotropic materials, that reflect light equally in all directions, and have constant appearance regardless of the angle of observation. Even though Lambertian materials are ideal, they are a good approximation for flat and matte real-world material. The Spectralon target typically used for white balancing is an example of what is considered to be a perfect diffuser. In the Lambertian case, by cancelling out the angular terms, Eq. 2.5 becomes:

$$f_r(\lambda) = \frac{\rho(\lambda)}{\pi}[sr^{-1}] \tag{2.6}$$

where $\rho(\lambda)$ is the albedo, i.e. the ratio of diffusely reflected to incident electromagnetic radiation.

The definition in Eq. 2.5 is valid for opaque and reflective surfaces, and does not account for transmissive and fluorescent materials. For fluorescent materials, the bispectral factor needs to be incorporated. Hullin et al. [49] introduced the mathematical expression for the bispectral BRDF (BBRDF), by considering the incident and outgoing wavelengths, λ_i, and λ_o:

$$f_r(w_o, w_i, \lambda_o, \lambda_i) = \frac{dL_o^2(w_o, \lambda_o)}{L_i(w_i, \lambda_i)\cos\theta_i dw_i d\lambda_i}[sr^{-1}\cdot nm^{-1}] \tag{2.7}$$

Although fluorescent materials are considered to be isotropic [50], Hulin et al. [49] discovered a weak directionality. Hence, the expression in Eq. 2.7 is a generalization that makes no assumption on the directionality of a given fluorescent object. This is suitable for the characterization of multi-layered objects, where for instance, the fluorescent layer is covered by a specular coating.

In **P3** of this dissertation, synthetic images of fluorescent objects are created with a spectral renderer given a bispectral Lambertian definition of the fluorescent material.

2.2 Data Capture

A basic setup for an appearance capture system includes an acquisition scene, a light source, a sensing device that can detect the signal given by the interaction of the scene with the light, and a geometric arrangement that positions the light relative to the scene.

2.2.1 Spectroscopy, Colorimetry, Fluorimetry

Spectroscopy is a metrological technique, where the purpose is to measure the interaction between electromagnetic radiation and the atoms and molecules in a material, on a per-wavelength basis. This thesis focuses mainly on the spectroscopic techniques that measure the transfer of energy between a sample and photons released by ultraviolet, visible and near-infrared light, with emission in the 380 - 1000 nm range of the electromagnetic spectrum. In its basic configuration, a spectroscopic technique collects point measurements, without considering the spatial dimension. To measure the spectral curve, a dispersive element is needed, that splits either the light or the detected response into narrow-band signals. There are two types of dispersive elements [31, 29]: the prism and the diffraction grating. Typically, in a spectroscopic measurement, a broad-band polychromatic illumination is needed. Then, the sensor typically consists of a single photodiode or an array of photodiodes, that converts light photons to electrons. Optical instruments that measure single point spectral reflectance carry the following names: spectrophotometers, spectroreflectometers or reflectometers [31].

Based on the spectral reflectance of a material, it is possible to reach its colorimetric property, by mathematically integrating with the spectral power distribution of the light source and the color matching function of a standard observer, as indicated by CIE. This way, the tristimulus values *X, Y, Z* are obtained computationally. There are instruments that can substitute the mathematical integration with an optical integration, the so-called colorimeters [29]. By design, a traditional colorimeter contains an R, G, B color filter array, attached to the photodetector. The transformation to *X, Y, Z* implies simple linear equations, with weighting constants for the R, G, B responses.

Fluorimeters are the instruments that measure the fluorescence. The most accurate design of a fluorimeter is the one with a double monochromator configuration, initially proposed by [32], because it captures the bispectral matrix that fully describes the excitation, emission and reflectance spectra. In a double monochro-

mator setup, there are two dispersive components: one at the light end to record excitation, the other at the detector's end to record emission. An abridged method to measure fluorescence includes one monochromator, that must be placed between the detector and the sample [31, 29]. In this setting, the output of the measurement is the total radiance factor, which represents the sum of the fluorescent and reflectance radiance factors, intertwined. The recovery of each factor individually can be performed mathematically under given assumptions and prior knowledge about the material [51]. Tristimulus values of fluorescence can be computed with the same mathematical integration as for conventional colors, where the total radiance factor (that encompasses the fluorescent radiance factor) substitutes the plain reflectance factor [31].

CIE recommends three standard light-sample geometries for measuring spectral reflectance [29]: 1) bidirectional geometry suitable for the capture of diffuse reflectance, noted as 0°/45° or 45°/0°, where light and viewing can interchange the positions based on Helmholtz reciprocity principle; 2) integrating sphere geometry with diffuse illumination and perpendicular or near-normal viewing angle, d/0° or d/8°; 3) variable angle geometry, where the incidence-viewing angles have a more dense distribution, which is especially useful for BRDF measurement. These geometries cover all types of materials. However, in the case of fluorescence, the integrating sphere design is not recommended, because the color of the fluorescent sample might be influenced by the color of the perfect white diffuser of the integrating sphere [29].

2.2.2 Microfading

Microfading is a spectrophotometric technique that measures the light-induced degradation of colored materials, and is commonly used for non-destructive pigment aging analysis in CH applications [52]. Microfading is a variant of accelerated aging techniques, that casts a light with a strong flux over a tiny area (< 1 mm^2) of a sample and measures the spectral curve of the area after a defined unit of time over a limited exposure in order to assess the lightfastness of the sample. Because of the small area of measurement, microfading is considered to be a non-destructive technique and thus suitable for the evaluation of real artworks. Nonetheless, the technique is arguably regarded as micro-destructive by others [53].

In a microfading experiment, the optical instrument is called a microfadeometer. The first proposed microfadeometer [52] consists of a spectrophotometer with a photodiode array, a xenon lamp as light source, arranged in a bidirectional setup (0°/45°). Following the work of [52] and a similar configuration, with variation in light sources, the next microfadeometers were proposed towards the improvement of the system's portability [54, 55] or that of measurements' accuracy and quality

[56]. As a result of the increased portability, microfading spectrometry has recently appeared in numerous CH lightfastness case studies for rock art [57], paintings [58, 59], natural history collections [60], feathers in ornithological and ethnographic artifacts [61] and tapestries [62].

In most applications, microfading was used to to establish the light sensitivity of museum materials in order to define and improve display policies. Microfading also proved to be insightful for a secondary, less common use-case, that of pigment identification based on its un-aged and aged spectral reflectance curves, as was the case with realgar in the study of Kogou et al. [63]. When justifying suitable illumination conditions for museum display with the results of accelerated aging experiments it is often taken for granted that the reciprocity principle of light exposure is obeyed by all museum materials. The reciprocity principle implies that the light-induced aging of a material is proportional to the total amount of energy that the material receives, where the contributing parameters, i.e. time or light intensity can switch magnitude [54, 64]. In other words, long exposure of a sample at low intensity illumination is equivalent to short exposure at high intensity light. Hence, if the reciprocity principle holds, then the microfading procedure, usually performed at higher light intensity, can be used to estimate the degradation of an object for the dimmer light levels of the museum exhibition conditions. However, Liang et al. [54] found that the reciprocity principle breaks down for orpiment and Prussian blue pigments, when measured with a microfadeometer that operates at levels of light 4 times higher than museum exhibition levels. Similarly, del Hoyo-Melendez and Mecklenburg [64] pointed out that in general, unstable colorants are more likely to deviate from the reciprocity principle at high intensity illumination. Notwithstanding these limitations, microfading is still able to provide an approximation of the evolution of a material's degradation helpful for conservation policies [54].

Microfading data collection is incorporated in **P5, P6** and **P7** of this thesis.

2.2.3 Color, Multispectral and Hyperspectral Imaging

So far, 1D point capture techniques were discussed that ignore the 2D spatial dimension beyond the instrument's aperture size. In this subsection, the focus is shifted to imaging methods, where color and reflectance are measured for the entire X-Y spatial extent of a sample. If we consider a pixel to be the spatial subdivision of an image [65], then imaging systems record a signal on a pixel basis. The output of an imaging system is defined by its sensor and any other optical component coupled with the sensor. There are mainly two digital sensors most commonly used for imaging: charge-coupled device (CCD) and complementary metal-oxide semiconductor (CMOS) [66]. Both of them are built as arrays of pho-

todiodes. The main difference in the two technologies lies in the way photons are stored and then, read out to be converted to electrons. For a CCD, the reading is grouped for a register, i.e. a horizontal line of photons at a time, while CMOS reads every pixel individually. Thus, if the sensor is monochromatic, and no filter is attached, the output is a single-channel image, where only gray levels are recorded. To capture color images, typically a Bayer filter array [67] is attached in front of a monochromatic sensor to capture the trichromatic R, G, B values. Then, for multi-channel images beyond R, G, B, the Bayer filter array can be substituted by a spectral filter array in the so-called snapshot multispectral cameras [68] or by a filter apparatus, with motorized wheel configuration [69] and Liquid Crystal Tunable Filters (LCTF) [70]. The spectral filters are selective for narrow bands, centered around a wavelength of interest. The above-mentioned techniques refer to passive setups where the number of channels is modulated at the detector end. The alternative is to assemble an active system of lights with various spectral distributions, that multiplex the signal received by the monochromatic sensor [71, 72].

As far as hyperspectral imaging is concerned, for every pixel, a full spectral curve is collected. For this reason, hyperspectral imaging is also known as reflectance imaging spectroscopy (RIS) [73]. Typically, a hyperspectral camera includes a dispersive element, like a prism or grating. Nonetheless, there are hyperspectral cameras that, similar to the multispectral systems obtain the spectral information by filtering either the light or the reflected signal before reaching the sensor. According to the classification in [65], the available hyperspectral imaging systems fall in the following categories: point-based scan (whisker-broom configuration), line scan (push-broom configuration), spatio-spectral scan, plane scan (also known as staring), and snapshot camera. A whisker-broom scanner collects one point at a time, while the sample is moved in an X-Y grid to map the spatial dimension. The pushbroom scanner senses an array (line) of pixels of the surface at a time and then either the system or the sample is moved, to gather these lines sequentially over the surface of the sample [65]. An example of pushbroom hyperspectral imaging system is HySpex VNIR-1800 camera [74], used in **P4, P7, P8** of this thesis. The spatio-spectral scanner captures wavelength-coded images at different times, and then superimposes them to build a full spectral representation for each pixel in the spatial grid (i.e. a spectral cube) [75, 76]. In the plane scan or staring devices, a 2D image is collected for a single wavelength individually. This is similar to multispectral imaging setups. Likewise, the snapshot hyperspectral systems are similar to the snapshot multispectral cameras in that they use a spectral filter array. However, if the system is called hyperspectral, this presumes a higher resolution in the spectral dimension than the multispectral case, although the precise number of recorded spectral bands that makes the distinction between the two systems is yet an unsettled question [77, 78].

Multispectral and hyperspectral imaging are more informative to the material properties than color imaging. For this reason, there have been numerous applications of multispectral [70, 79, 80, 72] and hyperspectral imaging for CH analysis, in particular for pigment mapping [81, 82] and identification [83], in paintings and manuscripts [84], for ink segmentation in historical documents [85], and for the digitization of film and stained glass [86, 87]. Sometimes, in the conservation community, multispectral is used interchangeably with multimodal imaging, where the photographs of different imaging techniques with probably different spatial resolutions (e.g. color image, X-Ray, infrared) are fused to characterize a CH object at widely separated parts of the electromagnetic spectrum [77]. However, in this thesis, multispectral refers to a limited number of images, captured with the same sensor, along the visible range and its adjacent parts in the ultraviolet and near-infrared.

Fluorescence Imaging

In fluorescence imaging applications, a filter system to be mounted in front of the camera's objective is typically necessary to separate the wavelengths of incidence from those of detection [51]. The quality of the filters directly affects the quality of the images in the fluorescence state. In [88], Pereira et al. compare classical dyed UV blocking filters, that absorb unwanted wavelengths, with interference (also known as dichroic) filters, made of multiple thin layers of materials with different refractive indices, and that reflect rather than absorb unwanted wavelengths of the incident radiation. The former group of filters are prone to exhibit internal fluorescence, casting an unwanted secondary source of light to the scene that tampers with the accuracy of the measurements, while the latter group removes UV radiation more efficiently at the cost of a high angular dependency that needs to be optimized for. Albeit the need to be placed perpendicularly to the optical axis and the sub-optimal performance when coupled with a wide angle lens, the interference filters produce UV fluorescent images of a higher quality than dyed filters, when subjectively assessed by art UV photographers [88]. The main quality criteria considered by the experts was the lack of UV radiation present in the fluorescence images. Apart from the comparison between the filters, the authors in [88] also include a short list of additional recommendations to ensure high quality fluorescence images. In a nutshell, they suggest that using interference filters alone is not enough. Other filters might be attached as well to cut off undesired light leakage in the red part (cyan filter) and the blue part (yellow filter) of the electromagnetic spectrum. Moreover, the need of white balance is emphasized, where daylight color temperature is recommended, in order to align the appearance of the images with what a human observer perceives when seeing the fluorescent scene.

2.2.4 Multi-light Image Collection

A multi-light image collection (MLIC) is captured for lights with different angular distribution, while the object and the imaging device remain static. To acquire as much as possible of the light-object interplay, the light distribution should be dense, and sample the hemisphere. This way, a MLIC can be considered to capture a 2D slice of the BRDF [89, 90], for a single viewing angle. A MLIC which follows a hemisphere-like distribution of light is often called Reflectance Transformation Imaging (RTI), especially in CH.

Because the angular distribution of the light is an essential component, most RTI systems proposed in the literature compete based on the novelty of the design and the engineering intelligence of light arrangements. Substantially, there are three main RTI setups: free-form, where the light is moved freely so as to recreate a virtual hemisphere [91]; dome, where the lights are fixed and embedded inside a dome-like construction [19, 92]; robotic where the light source is controlled mechanically by a robotic arm [93, 94]. The free-form setup is flexible and practical for on-site and offline measurements, but lacks perfect reproducibility and repeatability. For this reason, it is not suitable for CH monitoring applications. On the contrary, the dome setup is robust thanks to the stationarity of the fixed lights. Nevertheless, dome setups are tailor-made for a certain object size, and so the limitation here is the extent of the object that can be captured. Lastly, the robotic arm setups are superior to the other two because they are very customizable, allowing the acquisition of objects of various dimensions (still within a range defined by the reach of the robotic arm), while maintaining the rest of the settings (light position, distance light-object) repeatable. However, in the CH context, the robotic RTI systems are seen as posing a bigger risk on the object, because if a hardware error were to happen, collisions might occur.

Several of the recently proposed RTI devices are multispectral in an active configuration (i.e. the lights are filtered or narrow-band LEDs [92, 95], similar to the design proposed in **P1** of this thesis), while other use polychromatic illumination in addition to a snapshot spectral filter array camera [93]. However, there is a scarcity of hyperspectral RTI setups. To the best of the author's knowledge, there is only one work in the literature that proposed a fully hyperspectral RTI setup, within a project dedicated to the study of palimpsests and manuscripts [96]. In the white paper report of this project [97], a hyperspectral MLIC acquisition system is compared to a computational method to merge monochromatic MLIC with a single hyperspectral capture. The computational method assumes that spectral material properties are isotropic, so they do not change with light direction. Hence, the variation in luminance from the monochromatic MLIC is merged with the chromatic channel derived from the single hyperspectral capture, to generate a color image

at every light position captured in the former, by operating in the CIE L*a*b* or YCbCr color spaces. For the examined manuscripts, the results showed that the computational approach performed better than the full hyperspectral MLIC acquisition, where at each distinct light position, a hyperspectral image was shot.

Even with limited spectral resolution, color and multispectral MLIC proved useful in numerous investigations of CH surfaces. To name a few applications: surface inspection of archaeological findings [98], interactive visualization of numismatics [99], enhancement of engravings in rock art [100, 101] and inscriptions in cuneiform tablets [102], material study in historical documents and manuscripts, identification of retouchings in a gilded icon [103], [104], crack detection in frescoes [19] and paintings [105].

MLIC for fluorescent materials

Fluorescent materials, due to the Stokes shift and bispectral nature, require additional filtering and in a MLIC framework, the level of complexity is thus increased. There are few attempts that exploit the angularity of the light to visualize the relief of the fluorescent signal [106]. More precisely, Kotoula et al. [106] show the benefits of capturing reflectance transformation imaging in the UV-reflected (UVR) and UV-fluorescent (UVF) ranges for visualizing traces of conservation on two real ceramic vases from a museum. The filters proposed in the setup of [106] are off-the-shelf solutions for UV imaging: for the UVR, the UV-transmitter (Hoya 330 [107]) and, because the DSLR camera has the IR-filer cut off, IR barrier (Schott [108] BG 38); for the UVF, an UV and IR barrier filters were used. In the UVF RTI mode, traces of conservation, like previous repair of the ceramics become visible, because common adhesives become luminescent when lit by the UV light, revealing details otherwise obscure in the visible light. Actually, the authors in [106] argue that UVF RTI is basically an efficient way of recording a good practice of conservators when they visually inspect an artifact with UV light: they position the light around the artifact, at different raking lights and statically inspect the change in the appearance of the object at each distinct position of the light. In this way, UVF RTI becomes a way of documenting this process of dynamic inspection by stacking together all the static frames at each light direction into a single relightable file. In contrast with UVF, the UVR mode highlights the subtle variations in the surface, such as scratches and smudges, as well as remains of glaze and salt encrustations. Even though such variations might be revealed as well in the visibile RTI, the contrast is enhanced under UV reflected light and the variations gain clarity. This work [106] exposes effectively how the combined forces of RTI and UV imaging can export useful visualizations for the analysis of CH objects.

Under this topic, **P1** in this thesis proposes a dome configuration with multispectral

lights for the MLIC capture of opaque reflective CH objects, and this setup is extended for fluorescent objects in **P2.**

2.3 Multivariate Analysis

A tensor is a multidimensional or multi-way array, with more than two dimensions. Many of the capture techniques reviewed in the previous section and used in this thesis have a tensor output: a collection of color or multispectral images with a discrete sampling in the color and electromagnetic spectrum, respectively; a hyperspectral image that characterizes every pixel with a spectral signature; a MLIC where every pixel is described by photometric variations triggered by a change in the incident light direction; a time-series of spectral observations gathered with a microfadeometer. The multidimensionality of these techniques is sketched in Fig. 2.3. The main advantage of a tensor as opposed to its 1D or 2D flattened variants is the preservation of the multidimensional structure, that hides latent representations and high-order correlations [109]. For this reason, the tensor is a key data structure in deep learning techniques and it stands at the core of convolutional neural networks (CNN) (see last illustration in Fig. 2.3). Mathematical operations with tensors are carried out in the so-called multivariate or multi-linear algebra.

Hereinafter, this section elaborates on a tensor processing method, which is the essence of **P6** and **P7**, and then briefly describes the rationale of CNN as a multivariate method for image formation that relates to **P9**.

2.3.1 Tensor Decomposition

Tensor decomposition can be perceived as an exploratory analysis method, where the purpose is to find hidden representations and higher-order correlations in multidimensional data [109]. This method was engaged successfully in visual data interpretation [110], signal processing [111], and machine learning algorithms [112]. To name a few examples, Zhao et al. [113] used tensor decomposition to denoise hyperspectral images and then, detect targets of interest for remote sensing applications, such as pines in a forest or vehicles in a naval airport. Then, Cichocki et al. [111] illustrated how tensor decomposition is useful for predicting arm movements from brain electrocortigram signals. As presented in the survey of Panagakis et al. [109], tensor decomposition brings multiple improvements to deep learning approaches. One such idea of improvement is the use of tensor decomposition to project the activation maps in a CNN to a lower dimensional space through, the so-called tensor contraction layer. The same dimensionality reduction operation can be inserted at the very end of a CNN, before the prediction output. In this case, the fully connected layer becomes a tensor regression layer [109]. All these improvements alleviate the known problem of overparametrization in neural net-

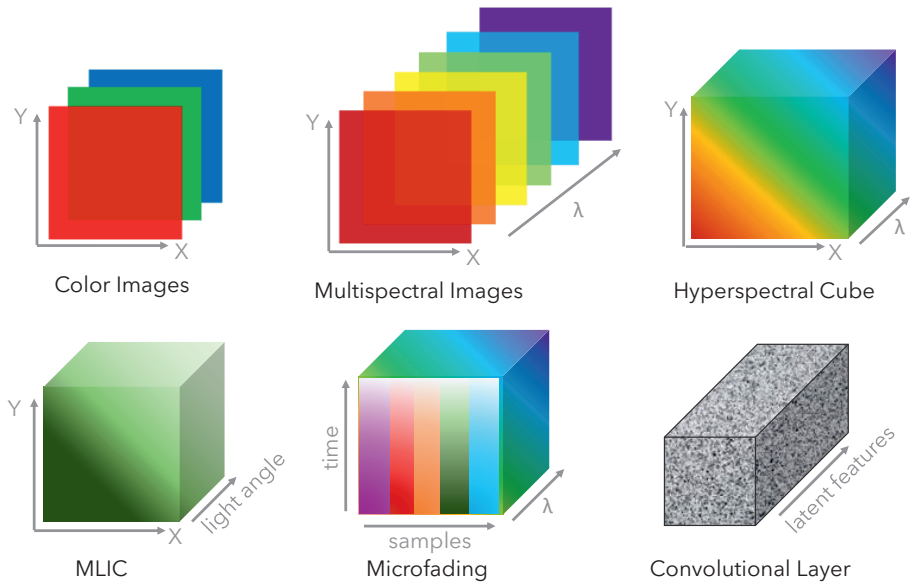

Figure 2.3: Tensor representations: color images, multispectral image, hyperspectral cube, MLIC, microfading measurements, feature vectors in a CNN. Here, X and Y refer to the spatial dimensions of an image, while λ indicates the spectral dimension.

works. Furthermore, directly related to material analysis, in chemometrics, tensor decomposition was employed to extract in an unsupervised way, the excitation and emission spectra of fluorophores from a set of spectroscopic measurements of yoghurt samples [114].

In the remainder of this subsection, mathematical details of a tensor decomposition algorithm, which underpins **P6** and **P7**, will be elaborated. In parallel, properties of this multivariate method will be contrasted to those of matrix decomposition, in the two-dimensional space.

Harshman [115] proposed parallel factor analysis (PARAFAC) as a method to explain multivariate data collected from user studies in psychometrics. Mathematically, PARAFAC is a tensor rank decomposition method and can be considered a generalized expression of the bilinear principal component analysis (PCA) [116] method [117]. In tensor decomposition methods, the input data can be explained as a linear combination of basis factors. These factors are also called scores and loading vectors. As opposed to PCA, the scores and loadings don't have rotational freedom in PARAFAC, making the fitted solutions unique. There is room for variation as far as the order and scale of the factors are concerned. However, similar to PCA, the scale of the loading vectors is unidentifiable, i.e. not immediately relat-

able to real units of measure [118]. Such a relation can be established as a scaling factor with respect to a ground-truth quantitative measurement.

Let us consider a 3D tensor, $X^{M \cdot K \cdot N}$, where M, K and N represent the cardinality of the three dimensions. Then, using three-way decomposition, we can model this tensor as the outer product of 3 factor matrices, A, B, C:

$$\hat{X}^{M \cdot K \cdot N} = A^{M \cdot F} \otimes B^{K \cdot F} \otimes C^{N \cdot F}, \tag{2.8}$$

where F is the user-defined number of components to split the tensor into. Using the Kathri-Rao product $\odot$, Eq. 2.8 can be rewritten in the following flattened form:

$$\hat{X}^{M \cdot KN} = A^{M \cdot F} \times (C^{N \cdot F} \odot B^{K \cdot F})^T, \tag{2.9}$$

where $\times$ denotes the conventional matrix multiplication. The flattened array can then be reshaped to match the original size of the tensor.

A, B, C factors are identified with the alternating least squares algorithm [119] where the squared residuals between the actual data and the model are minimized in an iterative fashion. If E is the tensor corresponding to the residuals, defined by $E^{M \cdot K \cdot N} = X - \hat{X}$, then the loss function is $\min_{A,B,C} E^2$. Alternating least squares algorithm implies that the factors A, B, C will be conditionally estimated on each other. While numerically there is no difference between scores and loadings, it is common practice to consider that the first factor, A refers to the scores of the model and B and C to the loadings.

Finding the right number of components F in multi-way decomposition is not straightforward. Unlike the bilinear case, where the fit for more components includes the results of a fit with lower component, in the multi-way case, the solutions will be different for a different number of components. Typically, if no previous knowledge is known about the chemical content of the data, then the number of components is tested on an empirical basis. Thus, models are fitted for 1 component, then 2, and so on and so forth, until the resulting signals become very noisy and start to lose chemical significance. Moreover, statistical analysis of the residuals is used to choose between the different models.

This method is employed for the analysis of the microfading data towards pigment unmixing and spatio-temporal simulation in **P6** and **P7** of this thesis. In this context, the input tensor is given by the following three dimensions: *samples* x *spectra* x *temporal change*.

2.3.2 Convolutional Neural Networks

A CNN is a neural network, i.e. a biologically-inspired computational model that follows principles of the neural activity in the brain, that uses convolutions or

spatial filtering to extract features from the input data [66]. A convolutional layer is a fundamental element in the architecture of a CNN, and it is basically a tensor.

A CNN is a data-driven model that learns patterns in the data [66]. Typically, a CNN is designed as a feedforward neural network, where the mappings follow a one-way direction from the multidimensional input to the one-dimensional output, without recurrent connections from output to input in a cyclic pattern. Generally, CNN architecture consists of sequential layers, where a convolutional layer is followed by downsampling, non-linear transformation, and fully connected layers. The convolutional layer is where the learning of the latent feature space occurs, by pixel-wise multiplication of the input image with a kernel or sliding window. There are hyperparameters that are essential in the design of the filtering process: the kernel size, the stride (steps of iteration over the pixels), the padding (addition of empty values to reduce the border artifacts) and the depth (number of features to be computed). The weights of the model that maps the input-output correspondence are updated via backpropagation after each forward pass, based on a cost/loss function that is supposed to minimize the estimated output from the ground-truth input. The optimization is typically done with a gradient descent method.

The specific design of a CNN architecture depends on the tasks. For example, for the image classification task, only an encoder module is inserted before the fully connected one-dimensional representation, while the image generation task has as well a decoder module, which is made of deconvolutional layers that are undoing the convolution process.

There are two main CNN architectures with the scope of image formation: generative adversarial network (GAN) [120] and variational autoencoder (VAE) [121]. In a GAN, two neural networks, a generator and a discriminator, are trained in an adversarial setting inspired from game theory, where the purpose is for the generator to improve based on the feedback of the discriminator, and create fake images that look realistic. VAE is a probabilistic generative model, with an encoder-decoder architecture.

2.4 Appearance Reconstruction

This section focuses on the background of specific appearance reconstruction tasks addressed in this dissertation: appearance properties and relighting, aging simulation, and image inpainting.

2.4.1 Albedo, Shape Estimation and Relighting from MLIC

As mentioned in the previous section, a MLIC can be regarded as a tensor. From this tensor, appearance attributes, such as normal and albedo, can be extracted in

an unsupervised way, with decomposition methods [122]. The alternative, and more common method, is to define a model and apply regression on the MLIC to find the appearance properties defined by the model. In this sense, a MLIC can be formalized as a linear system of equations, where on one side we have the intensity values and on the other side we have the polynomial based on the light direction vector. The terms and order of the polynomial depend on the assumptions made with respect to the surface appearance. Woodham [123] proposed the first such polynomial model, namely the photometric stereo (PS) model, where the material is assumed to be Lambertian and the polynomial has a first-order and is modelled as follows:

$$\rho n l = I_k \tag{2.10}$$

where ρ represents the albedo, n the normal, l the light direction vector, I the intensity and k the number of images taken at different illumination angles. If we split the light direction vectors into its x, y, z components, and knowing that the albedo is a constant that can be computed as the norm of the normal vector, Eq. 2.10 becomes:

$$n_{1k} l_x + n_{2k} l_y + n_{3k} l_z = I_k \tag{2.11}$$

In this system of equations, the unknowns are the components of the normal vectors. Thus, there are three unknowns, and in order for the equation system to be overdetermined and reach a unique solution, there need to be at least three instances of the Eq. 2.11, so at least three images.

However, most of the real objects are not perfectly Lambertian. For these objects, a second-order polynomial considers more complex appearance effects such as specularities, shadows or interreflections. In the context of multi-light image collections, the biquadratic polynomial was first framed in the PTM work by Malzbender et al. [124], with the following terms:

$$c_{1k} l_x^2 + c_{2k} l_y^2 + c_{3k} l_x l_y + c_{4k} l_x + c_{5k} l_y + c_{6k} = I_k \tag{2.12}$$

One limitation of the PTM polynomial is that, in case the analyzed object has a subset of its surface that is perfectly Lambertian, then the regression of the biquadratic polynomial in 2.12 does not directly output the normal vectors. This limitation is accounted for by the PTM proposed by Drew et al. (PTMD) in [125]:

$$c_{1k} l_x + c_{2k} l_y + c_{3k} l_z + c_{4k} l_z^2 + c_{5k} l_x l y + c_{6k} = I_k \tag{2.13}$$

where $l_z = \sqrt{1 - l_x^2 - l_y^2}$ and the normal vectors are given by the first three coefficients, c_{1k}, c_{2k}, and c_{3k}. Simultaneously with the straightforward recovery of the

normal vectors for the Lambertian parts, PTMD models as well high-frequency non-Lambertian components (c_{4k}) and low-frequency non-Lambertian components (c_{5k}). However, the distinction between the nature of these components (highlights, interreflections, shadows) is not trivial. Several solvers for the polynomial models were proposed in the literature, that rely mostly on multivariate regression techniques, and differ based on their invariance to outliers (i,e. deviations from the Lambertian assumption): least-squares regression [123], least-median squares [125, 126], convex optimization in a low dimensional space [127], sparse Bayesian regression [128].

These models can be fitted at the image or pixel level, depending on whether the light positions are available globally or locally, respectively. In this thesis, **P2** presents a comparison of the performance of per-pixel and per-image fitting PS and PTMD models for the normal recovery of reflective and fluorescent objects.

Other models were proposed for the analysis of MLIC, towards shape estimation and relighting from unmeasured light directions: the cubic polynomial in polar coordinates called hemispherical harmonics [129], discrete modal decomposition [130], interpolation methods such as the radial basis function [131] and ultimately CNNs [132, 133, 105, 134].

For a more detailed review of surface analysis techniques based on MLIC processing, the reader can refer to the following surveys and monographs: [135, 19, 134].

2.4.2 Aging Simulation

Appearance of an object is prone to change with the passing of time, as aging occurs. The pace of this alteration depends on the sensitivity of the object's material to aging factors, and usually has a direct impact on the visual properties of the object. Therefore, aging simulation, the task of modelling the degradation of objects and their constituent materials is of high importance in the field of appearance. It can be performed in a forward (predict the future degradation) [136] or inverse way (undo degradation and restore the past appearance) [137, 138]. The inverse way is particularly relevant for CH objects, where aging and patina might have already occurred, and it is of interest to restore the past appearance.

Because aging is a complex phenomenon, the majority of proposed models include a data-driven component. Given a set of data that captures the behaviour of a material to specific triggering factors as a function of time (i.e. a time-series), we can apply multivariate techniques to model the degradation pattern. For example, in the context of colorant analysis, such data can be collected with the microfading technique, previously described. A straightforward way to obtain a model for

the aging pattern is to apply line fitting, where the aging function is defined by two coefficients, namely the slope and intercept of the line. With this parametric representation, unmeasured values of the degradation curve can be retrieved. This method was used in **P6** to simulate the spectral fading rates of pigments beyond the measured data domain.

A more elaborate processing method is to use time-series analysis that, based on a set of values that characterize a variable temporally, can forecast the future evolution of the variable by inferring from past observations. Auto-Regressive Moving Average Models (ARIMA) [139] are a generalized polynomial expression of time-series models [140], suitable for stationary data, i.e. which neither has a trend, nor seasonality. Fig. 2.4 outlines a mathematical synopsis of the ARIMA model. The polynomial expression can be split into three components: the auto-regressive part that refers to the past values of the time-series, the moving average part that describes the error of the model as dependent of the previous errors, and a constant term. To define the number of polynomial terms for each component, three parameters or orders need to be defined: p, d, q. The priority is given to d, which is the order of the derivative transformation enforced on the original data in case it is non-stationary. The stationarity is typically determined through graphical examination of the data and its rolling statistcs, or with a statistical test, such as Augmented Dickey-Fuller [141] and Kwiatkowski-Phillips-Schmidt-Shin [142]. Afterwards, the data undergoes the first derivative transformation d times until stationarity is verified.

The following step is to identify the p and q orders. Systematically, this is achieved through the analysis of the auto-correlation (ACF) and partial-autocorrelation (PACF) graphical plots, also known as correlograms [140]. The former measures the correlation between the last observation in the time-series and all the previous values, whereas the latter measures the direct correlation between the last observation and a specific past value, omitting intermediate correlations. Generally, p is obtained by counting the significant lags (i.e. time steps) in PACF, and q by counting the significant lags in the ACF. Exceptions to this thumb rule consist of specific patterns described in the synopsis in Fig. 2.4. Once the three orders of the ARIMA are established, the polynomial can be fitted with the maximum likelihood estimation method [143]. The model in Fig. 2.4 is presented for a univariate signal, but ARIMA can be employed for multivariate data as well [144, 145]. In **P5**, univariate ARIMA is used to predict the change of pigment samples for each color coordinate individually, based on a set of microfading measurements.

The methods above are primarily designed for the aging simulation of one measurement point at a time. Nevertheless, the overarching goal of aging simulation is to be modelled for the entire spatial extent of an object. Thus, mapping strategies

need to be developed to propagate the degradation rate in the 2D. In this sense, **P7** proposes a novel mapping model that combines the temporal information from microfading with the spatial distribution from a hyperspectral image.

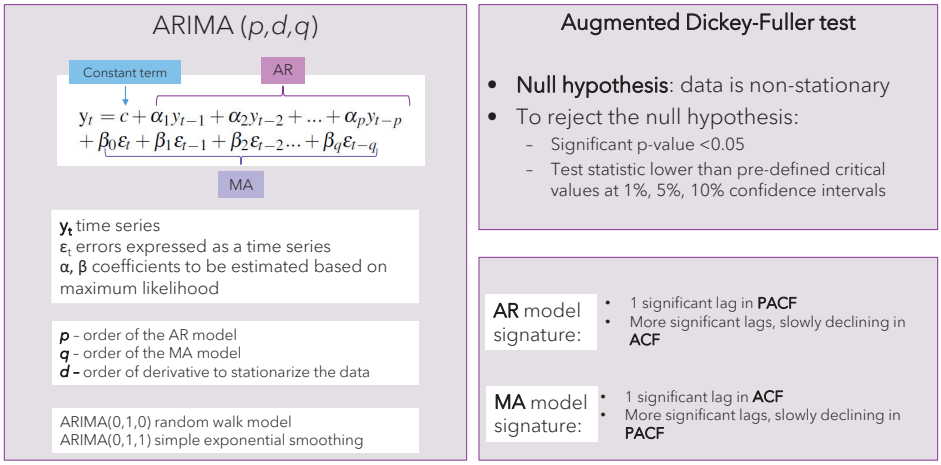

Figure 2.4: A synopsis of the ARIMA time-series model.

2.4.3 Image Inpainting

In the previous subsection, the examples of aging simulation approaches relied on a dataset that showed a temporal evolution of a material. However, aging can reach dramatic levels to the point that the information of the original appearance is completely lost. In cases of complete loss, appearance restoration becomes more challenging, because there is typically no unique solution to infill the missing information, so the problem can be poorly constrained.

In computer vision, image inpainting is the task of recovering missing information in an image by infilling the gap with the original content, preferably without any noticeable change in appearance [146]. Image inpainting is a particular case of image restoration, together with denoising, super-resolution and colorization. Although image inpainting was successfully applied for the virtual restoration of works of art, the problem of retouching in CH is older than in computer vision, and is surrounded by a body of theories and practices, mainly because it dealt primarily with the need for physical restoration and conservation. Only recently, in the last 20-30 years, with the increasing digitizations and the progress of digital image restoration techniques, virtual inpainting gained attention in the eyes of art conservators and restorers.

In the remainder of this subsection, concepts related to the theory of art restoration created exclusively for CH will be described. Afterwards, two paradigms of im-

age inpainting will be presented as approaches to physical and digital restoration. Then, case studies of digital image inpainting techniques applied on CH are briefly reviewed.

Theory of Art Restoration

Cesare Brandi, the author of the Theory of Restoration [147], claims that *"restoration should aim to re-establish the potential oneness of the work of art, as long as this is possible without committing artistic or historical forgery, and without erasing every trace of the passage through time of the work of art"* (quote taken from the English translation [148]). The concept of oneness is inspired from the Gestalt philosophy of perception [66], where the aesthetic unity overshadows the sum of the parts. In Brandi's opinion, a lacuna, i.e. an area of loss in an artwork, is a disruption in the aesthetic interpretation of an artwork because it protrudes as a silhouette that detaches itself from the rest of the artwork that gets pulled from the focal plane to the background. Essentially, a lacuna interferes with the aesthetic appreciation of an artwork. Therefore, the process of restoration becomes a process of reintegration of the loss within the artwork, in order to preserve the *"oneness"*. Nonetheless, Brandi raises the attention to the fact that such reintegration *"should never be based on sheer imagination"*. In addition, he recommends that any integration should remain discernible, when examining the work of art from a close distance and that the original materials should be replaced by volatile substitutes (for example, watercolors in paintings [149]).

Although Brandi's principles are contextualized to the physical restoration of an artwork, where there is less freedom of intervention, some if not all of these principles can be transferred to the digital restorations. In this sense, digital restorations can also simulate discernible reintegration techniques and take into account the remarks regarding the retouching material and the Gestalt notions towards aesthetic unity. At the same time, digital methods for inpainting should be allowed to be based on *"sheer imagination"* or "analogy"[148], as long as it clearly and openly remains a mere hypothesis, not a certainty, and is backed by a strong scientific rationale (such as deep learning methods).

Discernible Inpainting

Inspired from Brandi's theory of restoration, four main techniques for discernible reintegration were proposed [150]: 1) neutral retouching where the missing area is infilled with a uniform, contiguous color; 2) *tratteggio* or *rigatini*, where tiny dots or parallel vertical lines of (not necessarily primary) colors similar in hue and chromaticity to the surrounding are drawn in a hatching pattern; 3) *selezione cromatica* or chromatic selection, a regional variant of *tratteggio* proposed by Baldini

[151], where brushstrokes of primary colors are superimposed, in a direction that follows the surrounding structure in the integral part of the artwork (as opposed to parallel and vertical in *trattegio*) [152]; 4) *astrazione cromatica* or chromatic abstraction is similar to chromatic selection, albeit the targeted result color is neutral in tone, approaching an average of the color surrounding the lacuna.

Neutral retouching is not highly recommended [153] as it is considered to contaminate the overall chromatic appearance of the painting, as justified by the simultaneous contrast effect. This results in a retouching that is more intrusive than recessive [148]. Chromatic abstraction is preferred to *tratteggio* and chromatic selection when the area of loss is too large [150] and it is difficult to assign the wide palette of encircling colors. Apart from the neutral reintegration, all the discernible retouching techniques rely on the spatial mixing of the individual brushtrokes when viewed from a distance, as showcased in Fig. 2.5. This is similar to the Pointilist color theories behind the Impressionistic art style.

Cappellini et al. [154] engineered a computational tool, ArtShop, that implements the hatching discernible retouching techniques with the help of digital image processing techniques. The coveted functionality of this software was to guide restorers in the process of physical restoration of a painting or fresco by allowing them to first practice in a digital environment. In the same spirit, Grementieri et al. [155] addressed the neutral tone reintegration of lacunae in frescoes with a digital image approach. More precisely, the color to be infilled is computed mathematically by minimizing the perceived local contrast between the lacuna and the surrounding regions. These two works stand as proof that there is interest in adopting the traditional theory of restoration principles in digital image inpainting.

Fig. 2.6 illustrates a chronological series of sequential restorations applied on the wall painting "The Legend of the True Cross" created by the artist Piero della Francesca, throughout the 19^{th} and 20^{th} centuries. At the same time, this series of restorations allows a comparative assessment of the result obtained with three reintegration techniques: *rigatini*, neutral and chromatic abstraction.

Mimetic Inpainting

In physical mimetic restoration of CH, the goal is to imitate the original content of the loss, in a seamless reintegration with the rest of the painting. Although visually the practice of imitation seems to break the principles of Brandi's theory of restoration, this is compensated from a material perspective, where water-based, modern pigments are used, such as watercolors or gouache, that can be easily reversed, and are different from the historical, original pigments.

When imitative restoration is desired, one of the encountered challenges is given by

Figure 2.5: Discernible retouching (impressionistic hatching) examples at Kretzulescu church, Bucharest (external wall, front entrance), visualized from different distances. The inpainted areas are meant to make the lacunae look less disruptive from far away, as spatial mixing occurs. At the same time, from up-close, every line in the hatching is supposed to be distinguishable.

metamerism, i.e. when a pair of two spectrally distinct materials match colorimetrically under a given illuminant or for a given observer, but lose their resemblance when one of these two conditions change. In the digital image inpainting literature, the are several approaches dedicated solely to the problem of metamerism [156, 157, 158]. Their purpose is to help art conservators and restorers to digitally simulate paint mixtures for replacing a loss and to pick pigments that minimize metamerism. Staniforth [156] compares reflectance curves for a set of blue pigments and, by considering the overlap between their spectrally selective feature and the spectral power distribution of common light sources, recommends the best substitutes for a given condition. Berns et al. [157] introduce an instrumental-based color-matching software for selecting optimal mixtures of paints, by running multiple linear regression in a database of pigments characterized by the absorption over scattering ratio. The pigment mixing is performed using Kubelka-Munk theory. The method in [157] is improved in terms of computational efficiency and speed by a subsequent work [158], where the possible substitution palette is constrained to a subset of only ten paints.

Figure 2.6: Examples of three different discernible restoration techniques, applied on Piero della Francesca's wall painting cycle "The Legend of the True Cross", in the church St. Francis, Arrezzo. *Left: rigatini* or impressionistic hatching with small brushstrokes. *Middle:* neutral retouching. *Right:* chromatic abstraction. Image courtesy: [152].

Usually, metamerism is disregarded in those general digital image inpainting applications, where the purpose is not specifically to guide physical restoration. Nonetheless, there is an impressive corpus of works on image inpainting in the computer vision field, and most of them can be applied, with small adjustments, for the digital retouching of works of art. Roughly, the image inpainting algorithms can be divided into three categories [159]: geometry-based, patch-based, and learning-based. Geometry-based inpainting [160] uses partial differential equations and total variation to extrapolate the information from the undamaged part to the missing area. Patch-based techniques exploit texture repetition and similarity [161, 162] to hallucinate the lost content based on a defined optimization function. Learning-based methods refer to the recent generative approaches to image synthesis, such as GAN and VAE [163]. Typically, in CH, because of data scarcity, these methods are currently pre-trained on large datasets of natural images, and then finetuned to smaller datasets of works of art [164].

In this dissertation, **P9** proposes a novel learning-based method with a GAN architecture for the digital retouching of wall paintings. The proposed method attempts to imitate the artistic process, "lines first, color palette after, color tones at last" by ensuring the edge continuity and color consistency in the infilled region.

Chapter 3

Summary of Articles

Veni din întuneric spre mine el,
poetul,
Poetul de spaimă ratat.
Era foarte frumos. Ca la razele
röntgen
I se vedea în trup poezia.
Poezia nescrisă de frică.

Ana Blandiana

He approached me from the
darkness. Him, the poet.
The lost, frightened poet.
He was very beautiful. Just like
X-rays,
You could see the poetry inside his
body.
The poetry unwritten for fear.

English translation by Irina Ciortan

In this chapter, first a general overview of the articles that support this thesis is presented. The intersection between the topics addressed in the articles is introduced, and organized according to data capture methods and models used for analyses. Then, the CH objects that serve as datasets and case studies for the articles

are briefly presented. Finally, each article included in this thesis is summarized, one by one.

3.1 Overview

There are several ways in which the papers in this thesis connect. One of them is represented by the data capture methods. As can be seen in Fig. 3.1, there are three groups: color imaging, multispectral and multi-light imaging, and spectrometry. While **P9** uses a dataset of RGB images of the Dunhuang wall paintings [165], the analysis in **P5** is carried out in the color domain as well. However, the CIE L*a*b* values in the latter are computed based on the spectrophotometric data that was collected with the microfadeometer. For this reason, **P5** fits better under the spectrometry group. The spectrometry category can be further split into two sub-types, namely reflectance image spectroscopy, where spectra is collected along the spatial dimension, and microfading spectroscopy, where spectra is collected along the temporal dimension. **P4, P8, P7** analyze hyperspectral images, using the HySpex VNIR-1800 system [74], that for every scanned pixel, gives a full spectral description between 400 and 1000 nm. **P6** is an extension of **P5** by modelling the pigment degradation in the spectral domain. **P7** combines the point measurements given by the microfading technique with the hyperspectral image of the same artwork. **P1** and **P2** process multi-light image collections of cultural heritage objects, that were gathered with a dome of multispectral lights and a modified DSLR trichromatic camera with filters mounted on the lens to select difference spectral ranges. **P2** and **P3** focus on the analysis of fluorescent objects. Whereas the input to the former is real captured data, the latter introduces physically-based rendered multi-light images of fluorescent surfaces.

Fig. 3.2 shows how the papers are grouped based on the type of model designed to solve various appearance reconstruction tasks. **P3** and **P9** employ physically based representation of materials. **P3** uses a bispectral BRDF characterization for the synthesis of fluorescent surfaces. **P8** uses the Kubelka-Munk optical model to estimate scattering and absorption properties of pigments and simulate in a non-linear way mixtures of various paints. The rest of the papers use mainly fitting strategies to extract knowledge from data. **P1** and **P2** target photometric stereo, which is essentially regression applied on a set of images taken from a static viewpoint, but from dynamic light positions. From this photometric variation, the albedo and shape can be recovered. Nonetheless, in the traditional photometric stereo method, this is performed assuming a Lambertian model for appearance. So from this point of view, one might argue that this is a hybrid model. However, in these papers we also include other polynomial functions besides the Lambertian model, so for simplicity we keep them under data-driven category. Furthermore,

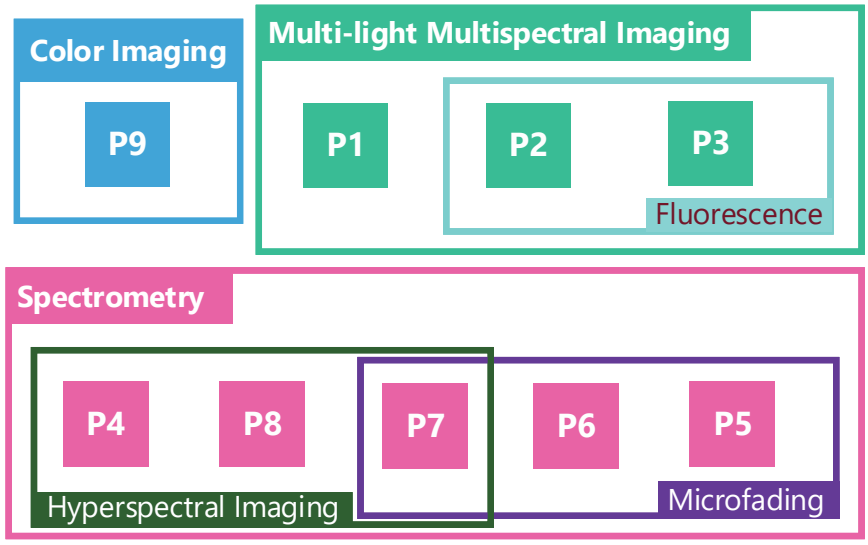

Figure 3.1: Publications grouped by data capture methods.

P5 uses time-series analysis to predict pigment degradation. Then, **P6** and **P7** use tensor decomposition to characterize the changing behaviour of pigments towards the digital rejuvenation and aging simulation of a detail in a painting. In addition, **P9** proposes a learning approach based on generative adversarial networks to synthesize missing information in damaged wall paintings.

Last but not least, this thesis introduces a reflective essay on the ethical and legal implications of cultural heritage digitization and artificial intelligence art. This is not a technical paper and for this reason, it is not included in the diagrams in Fig. 3.1 and Fig. 3.2. Nonetheless, it overarches the other papers that all deal to a certain extent with cultural heritage digitization and restoration.

3.2 Datasets and Objects of Study

This thesis analyzes several types of cultural heritage surfaces. Fig. 3.3 presents an overview of the datasets. Most articles in this thesis explore case studies related to real CH objects, taking as input on-site digitizations of artworks from cultural venues and museums. **P1** deals with a multi-light image acquisition of a golden lamina (i.e. a thin plate meant to be attached to another surface) which is an artifact found in an archaeological site in Sardinia, Italy, dated to the 8^{th}-7^{th} century BC and stored at the National Archaeological Museum of Cagliari. **P4** studies two

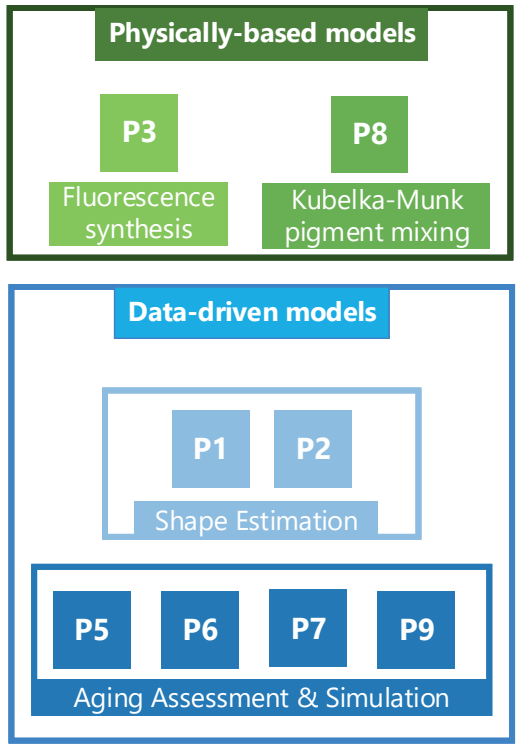

Figure 3.2: Publications grouped by the type of model employed to reconstruct appearance properties.

drawings on paper, made by the 19^{th} century Norwegian artist, Thomas Fearnley and part of the collection of the National Museum of Norway. **P5**, **P6**, **P7** revolve around the pastel painting "A Japanese Lantern" by Norwegian painter Oda Krohg, present as well in the National Museum of Norway. **P9** features the wall paintings of Cave 7 of the Mogao Grottoes from the Dunhuang UNESCO site [45]. The wall paintings date back to the Mid-Tang Dynasty (AD 766-835), and are rich in semantics, depict various motifs, such as Buddha statues, bodhisattvas, buildings, dancing scenes, musical instruments, figurative patterns, etc. Other articles in this thesis study mockups created in-house to contain specific materials. For instance, **P2** introduces two gesso moulds that contain a UV-induced fluorescent pigment, **P4** adds two targets with common fixatives applied on two different paper substrates, and **P8** analyzes mixtures of historical pigments in linseed oil and gum Arabic paint-outs.

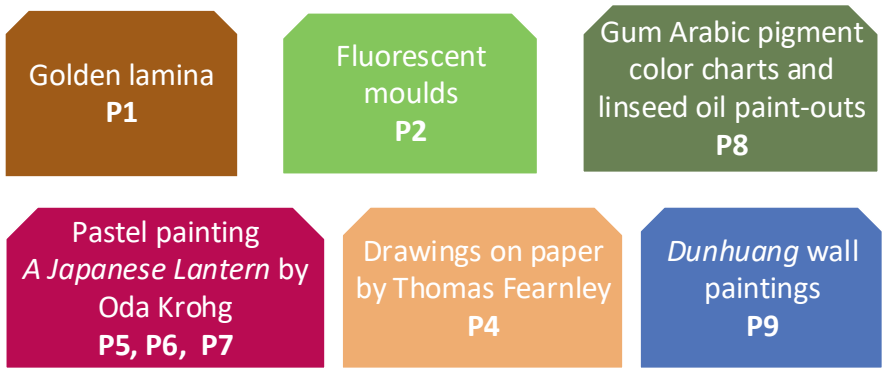

Figure 3.3: The objects studied in this thesis include real artworks, as well as mockups.

3.3 P1 - Artworks in the Spotlight: Characterization with a Multispectral Dome

This paper proposes an acquisition and processing pipeline for multispectral and multi-light image collections. The acquisition setup consists of a dome with fixed light positions and a DSLR camera placed on the top center of the dome. The IR cut-off filter that comes with the commercial version of the camera was removed to increase the sensitivity for the NIR range. The dome has 52 light boards, and at each position, there are three types of LEDs: white that emits in the visible spectral range, monochromatic UV light with the peak at 395 nm, and a NIR light with the peak at 850 nm. For each type of light, images are shot sequentially at each light position, with a short intermediate break to ensure that no signal leaks from the previous capture. The structure of the dome is made of wood, and was sprayed with a thick layer of minimally reflective black coating to remove the possibility of the light being bounced off the dome construction and back on to the object. In addition, before starting the acquisition process, the dome was covered on the outside with a black curtain to reduce the amount of stray light. The processing of the multi-light image collection comprises per-pixel light calibration and flat-fielding to compensate for the spatial non-uniformity of the light distribution [166].

The system is portable and suitable for on-site acquisitions. In fact, the paper presents a case study on a cultural heritage artifact from the National Archaeology Museum in Cagliari, Italy. A golden lamina broken in two fragments was digitally acquired. Based on the exploration of the MLIC, it was possible to enhance the visibility of several inscriptions by relighting the surface of the object from un-

measured light positions, as exemplified in Fig. 3.4. This was supplemented by the different contrast of the multispectral bands. The shape of the two fragments were reconstructed by integrating over the normal map in the two spatial dimension to obtain the gradient field. This enabled the manual reassembly of the two fragments by importing the shapes in a 3D software, as shown in Fig. 3.4. Visualizing the shape information facilitates the detection of good matching points to virtually reattach the two parts into one single object.

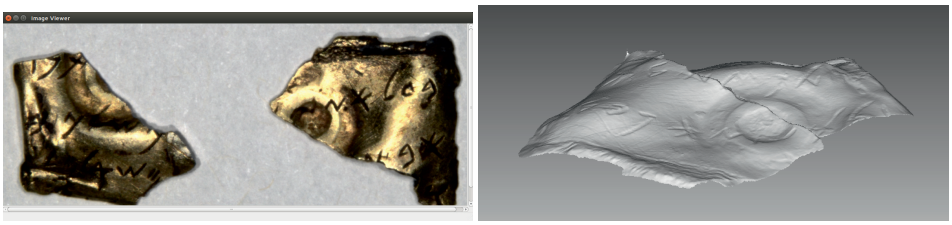

Figure 3.4: *Left:* The two fragments of the lamina relighted from a perpendicular light position, which is originally uncaptured, as it coincides with the camera position in the acquisition setup. *Right:* The virtual reassembly of the two fragments by visually matching shape clues.

3.4 P2 - Fluorescence Transformation Imaging

Objects with a special property are investigated and analyzed in **P2**, namely fluorescence. More precisely, gesso was mixed with a commercial lime pigment, that presents UV-induced fluorescence. Out of this material, two mockups with various geometrical inscriptions and impressions were crafted in a handmade way. The pigment is green in reflective mode and in fluorescence mode, meaning that there is an overlap between the spectral distributions of its reflectance and emission. Such material is susceptible to self interreflections. The purpose of this paper was to analyze whether the shape reconstruction of the mockups when fluorescence is activated is different and better than in normal visible reflectance. As a consequence, MLICs were captured with the setup presented in paper **P1**. To ensure that there is no leak of UV reflectance signal in the images of fluorescence, a Hoya K2 [107] filter that removes any signal below 500 nm was mounted on the lens. This filter was coupled with a UV cut-off filter, Hoya Pro1Digital UV filter, to avoid internal fluorescence of the Hoya K2 filter.

The acquired MLICs were grouped to consider four different light distributions. Then, each group was fitted to four polynomial models: first-order polynomial with a global light direction, first-order polynomial with local light direction, second-order polynomial with local light direction, and first-order polynomial with robust fitting strategy. The recovered normal maps in each case were compared to the

ground-truth given by 3D scans of the two mockups, based on visual assessment and quantitatively, by computing the angular errors between the normal vectors. Fig. 3.5 shows the ground-truth normal mas of one of the mockups, together with the reconstructed normal maps for the MLICs in reflective and fluorescent modes. The results showed that for both mockups, the angular error maps were higher for the fluorescence mode than for the reflective mode.

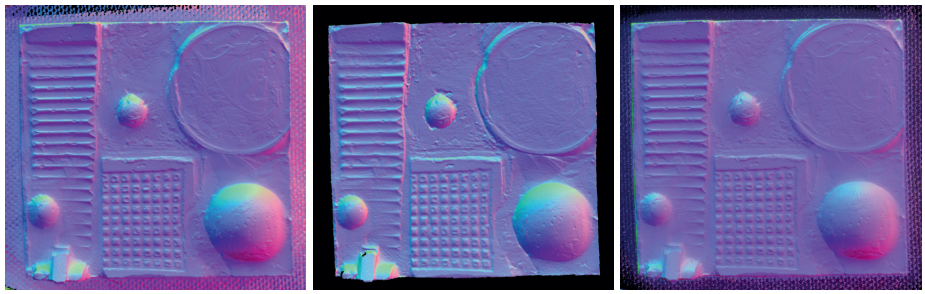

Figure 3.5: Normal maps of a green fluorescent mockup: as recovered with a second-order polynomial from the MLIC in the visible reflective mode (*left*); as captured with a structured light scanner (*middle*); and as recovered with a second-order polynomial from the MLIC in the UVF mode (*right*). A normal map encodes the three spatial dimensions (x, y, z) of the normal vector with an R, G, B encoding. In such representation, the parts that directly face the viewing point look light blue.

3.5 P3 - The Influence of Interreflections on Shape from Fluorescence

The research in **P3** was motivated by the results of paper **P2**. Thus, the aim of **P3** was to check whether the interreflections are indeed the reason for the difference between fluorescent and visible reflectance mode. For this reason, this time, experiments were performed on synthetic data, where the global illuminations effects (interreflections) can be separated from direct light. Thus, in this paper, a virtual setup for MLIC capture was simulated in a spectral renderer that supports fluorescence. Afterwards, MLICs were rendered for two geometries: one of the mockups analyzed in **P2** and a simpler v-shaped object. These two shapes were covered with the bispectral BRDF of dayglo materials, measured from commercial post-its, and they were all rendered as Lambertian surfaces. Afterwards, the normal maps from each rendered MLIC was estimated with the photometric stereo model. The same quantitative comparison as in **P2** was performed, where the angular errors between the estimated and reference normal maps were computed.

It was discovered that while the interreflections affect the normal estimation, there is no major difference between the fluorescent and visible reflectance modes. In

addition, variations in albedo were more noticeable for the v-shaped object than for the mockup. Therefore, it would seem that the discrepancies between the reflective and fluorescent modes in **P2** are not due to interreflections. Nonetheless, we have to keep in mind that there are still differences between the rendered data and the real capture. First, the fluorescent material in the rendering is not the same as the one in the mockups, as the latter's bispectral information was unknown. Secondly, the variations in the albedo of the real objects is more grainy than for the synthetic data. Moreover, the real capture might include other physical effects that were not included in the rendering, such as scattering and self-scattering.

3.6 P4 - Spectral Classification of Paper Fixatives: A Case Study on Thomas Fearnley's Drawings

The work in **P4** is targeted at material analysis, and it sparked from a real case study regarding two drawings made by the 19^{th} century Norwegian artist, Thomas Fearnley. Notwithstanding the different color appearance, as can be perceived in Fig. 3.6, the two drawings were covered with the same fixative. The role of the fixative was to protect friable media from smudging and smearing. The origin of the fixative was previously verified through analytical techniques and documentary sources regarding the practices of other artists, contemporary to Thomas Fearnley.

Figure 3.6: The two drawings studied in **P4** have different color appearance in the area where the same fixative was applied.

The research question in this paper was to check whether the spectral signal in the visible and near-infrared can identify the type of fixative used, and detect the similarity of the fixative between the two drawings. To this purpose, fragments of the two drawings were scanned with a hyperspectral imaging system, HySpex VNIR-1800 [74], with two broad-spectrum tungsten lights, located at 45° with respect to the captured scene. In addition, two mockups, on different substrates, were designed to include various types of fixatives, of animal and vegetal origin, in different concentrations. The mockups were scanned with the same setup as the drawings. Representative regions, corresponding to each material, were averaged spatially. Then, the mean reflectance of each material, and its first derivative were compared with all the others to look for similarity, based on spectral correlation and spectral angle metrics.

The similarity was visualized in the form of confusion matrices, illustrated in Fig. 3.7. For the mockups, the inflection points in the first derivative pointed out to two groups of fixatives, one defined by rice starch and egg white and another one defined by milk, sturgeon glue and gelatine. This qualitative grouping was further confirmed by the spectral metrics. As far as the drawings are concerned, resemblance was found between the areas with fixatives between the two drawings. In addition, out of the two groups in the mockups, the fixative areas in the two drawings were found to be spectrally closest to the group that included the milk samples. Therefore, the results obtained in **P4** show that the spectral analysis in the visible (400 - 750 nm) and near infrared (750 - 1000 nm) can reveal useful characteristics in the study of paper fixatives. The accuracy and insight of the results could be further improved by enlarging the range of analysis to short-wave infrared (960 - 2500 nm).

3.7 P5 - Predicting Pigment Color Degradation with Time Series Models

The input for the analysis in **P5** is given by a series of colorimetric measurements of pigment samples while undergoing accelerated light-induced aging. As shown in Fig. 3.8, the measurements were collected with a microfadeometer [55], at a 0°/45° geometry. The pigment samples were taken from a fragment in the painting “A Japanese lantern” by the Norwegian painter, Oda Krohg. The data was split into training and test set. For each pigment, the time series corresponding to every color coordinate in the CIE L*a*b* color space was fitted to an auto-regressive integrated moving average model (ARIMA) [139]. The predictions of the model were validated against the test set. The research proved that the ARIMA models were robust to instrumental noise and irregular change patterns in the data. The bests fits were found for those coordinates of the pigments that were most lightfast.

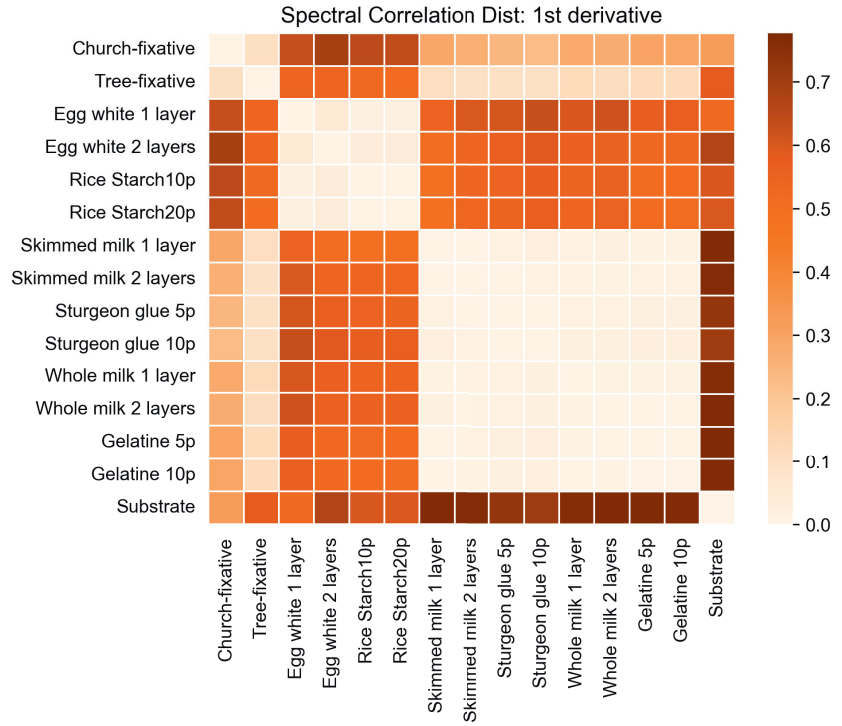

Figure 3.7: Confusion matrix, as a visualization method for spectral similarity metrics. Figure adapted from **P4**.

This is in agreement with the data stationarity requirement of ARIMA. While stationarity was enforced in pre-processing for all the measurements, there is room for fine-tuning the parameters of the models towards finding better fits of those pigments that are more fugitive.

3.8 P6 - Tensor Decomposition for Painting Analysis. Part 1: Pigment Characterization

P6 builds on **P5**, by taking the same set of measurements, only this time, the analysis is performed in the spectral space. Moreover, **P6** is the first part of a series of two articles, and is continued by **P7**. Fig. 3.9 illustrates the complete workflow shared between the two papers in the series. Essentially, the microfadeometer used for measuring pigments in **P5** is a spectrophotometer, so the data collected is reflectance. Thus, in **P6**, the spectrophotometric information is used in combination with the temporal change to characterize the pigments. The methodology consists in the multivariate analysis technique entitled tensor decomposition. In

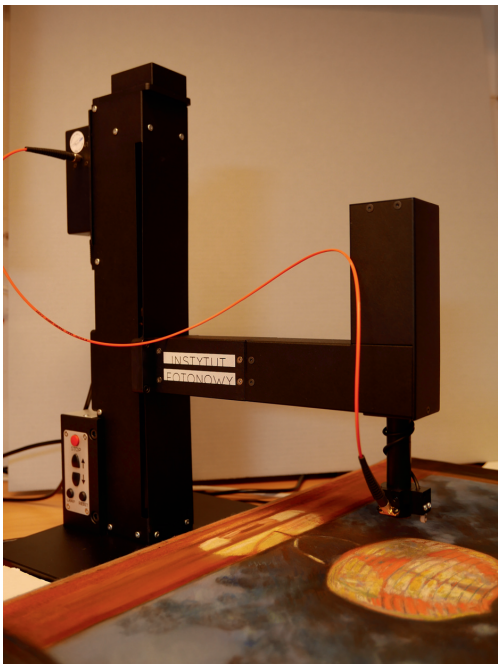

Figure 3.8: Microfading measurement of the painting "A Japanese Lantern". Image courtesy: Tina Grette Poulsson.

particular, it uses the PARAFAC [115] implementation of the tensor decomposition technique. In other words, the time series of spectral measurements for each pigment were arranged into a 3D tensor representation, where the dimensions are defined by samples, spectra, and fading rate. This tensor was then reduced to a set of basis factors using parallel factor analysis. According to the chemical meaningfulness of the resulting loadings and statistical analysis of the model's residuals, the cardinality of the factors was chosen to be 6. Thus, PARAFAC gives the pure spectra underlying the sample (3^{rd} mode), the concentration of all pure components for each sample (1^{st} mode), and the temporal change of every endmember (2^{nd} mode).

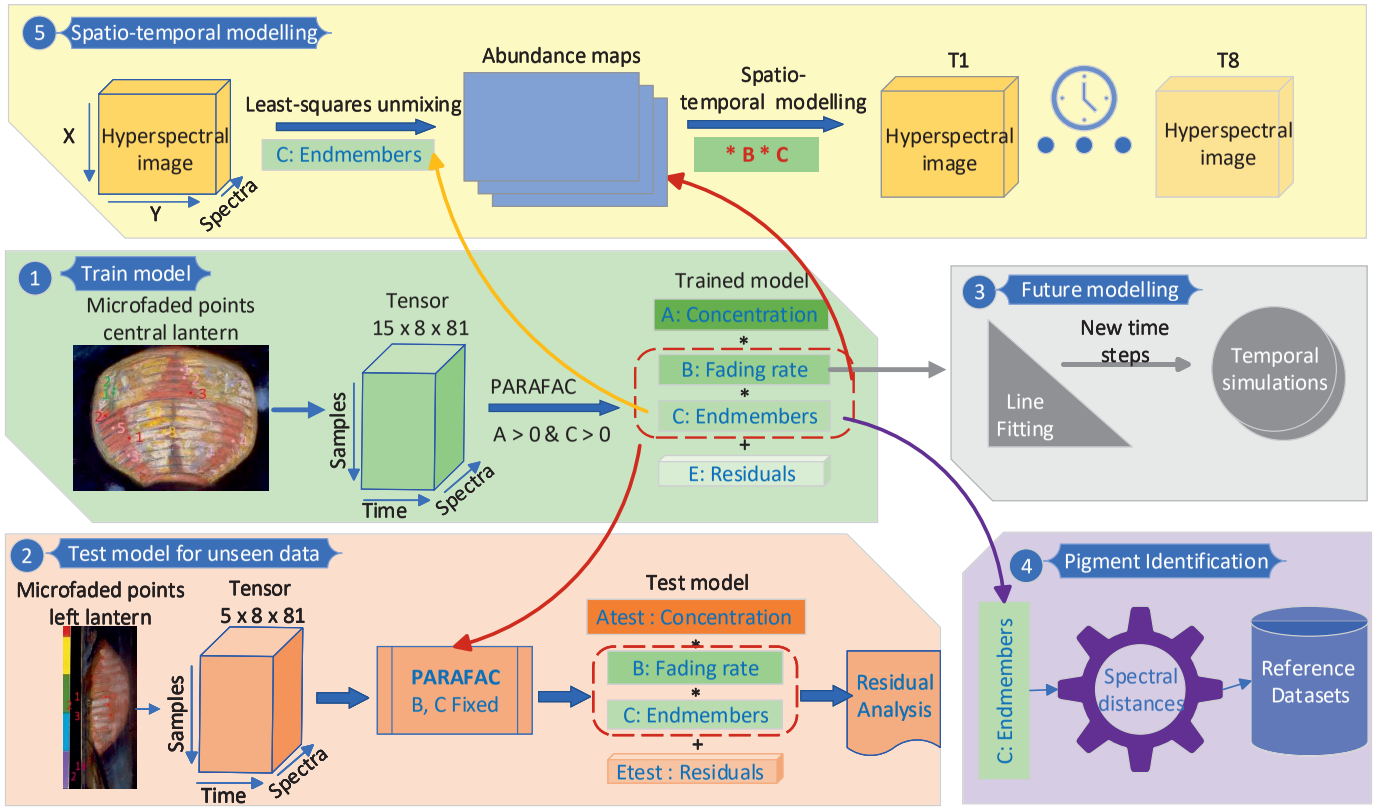

Figure 3.9: The diagram of the method presented in **P6** and **P7**. The module (1) is the core model, where endmembers and their fading rates are extracted with three-way tensor decomposition from a collection of microfading observations. Then, the trained model is tested on new microfaded data (2). Moreover, by applying regression on the fading rates, future and past changes can be extrapolated (3). Afterwards, the endmembers are compared with databases of reference pigments in an attempt to identify the materials used in the painting (4). Finally, spatio-temporal fading simulation is performed by capturing a hyperspectral image of the same microfaded scene (5). The hyperspectral image is unmixed to retrieve the abundance map for each endmember, and then recomposed as a tensor product that includes the temporal behaviour of fading.

Once the model was trained, it was tested for new samples believed to be made of the same materials, and unseen at the calibration stage, by keeping modes 1 and 2 fixed. In addition, the fading rate was approximated with a function that changes linearly with the time step of the fading process. Consequently, the samples and their future alteration, beyond the time steps included in the training step, were predicted by the model. This forecast was checked against several temporal measurements left out in the training procedure.

Moreover, **P6** attempts pigment identification by comparing the endmembers obtained with the trilinear decomposition, to spectral libraries. The comparison was done with the same metrics as in **P4**, namely spectral angle and spectral correlation. In this case, a new visualization method in the form of a bubble chart was designed to represent the numerical output of the spectral metrics. The bubble chart (see Fig. 3.10) allows the visualization of three spectral metrics simultaneously. Apart from the two metrics plotted along the x-y axes, another metric can be incorporated in the size of the bubbles. In this work, x-axis represents the spectral angle between reflectance curves, y-axis the spectral angle between the first-derivative curves, and the bubble size is modulated by the spectral correlation of the reflectances. Although the ground-truth with regards to the pigment chemical composition is unknown, the bubbles show a clear separation between the various endmembers, as portrayed in Fig. 3.10.

3.9 P7 - Tensor Decomposition for Painting Analysis. Part 2: Spatio-temporal Simulation

As a continuation of **P6**, **P7** translates the trilinear representation of the microfading measurements to a hyperspectral image of the same scene (see Fig. 3.11), i.e. the central lantern in the painting "A Japanese Lantern". More precisely, abundance maps for the endmembers previously identified are obtained by running least-squares unmixing in the hyperspectral image (see Fig. 3.9). Using the tensor model created in **P6**, the abundances maps are then recomposed with the fading rate and endmembers to have a complete spatio-temporal description of the scene. The recomposition is performed in a trilinear way, by multiplying with a tensor product the abundance maps with the endmembers and their fading rate. Subsequently, this was used in conjunction with the linear approximation of the fading rate to digitally rejuvenate and age the central lantern for a range of ± 1.19 Mlux hr.

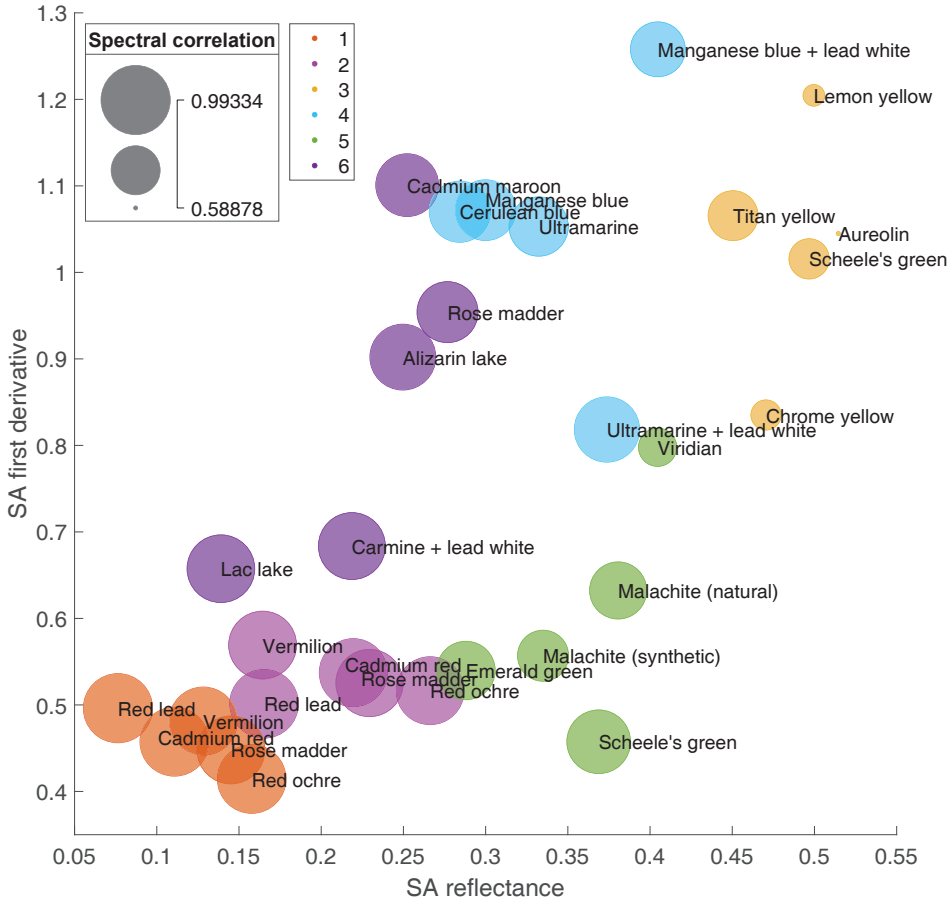

Figure 3.10: Bubble chart, as a visualization method that allows the simultaneous inspection of three spectral similarity metrics. Figure adapted from **P6**.

3.10 P8 - Estimating Optical Properties of Pigments from Color Charts with Multi-contrast Background

This paper addresses the recovery of pigment scattering and absorption coefficients from the spectral signal of pigment color charts, drawn on a 4-step grayscale gradient. The method used is based on the black and white formulation of Kubelka-Munk with the distinction that instead of only two substrates, the variation of the 4-step background in the color charts is used to select the optimal pair of substrates. The proposed method is compared with two other methods. The first one is non-linear optimization, which considers a system of equations based on 4 reflectance values contained by the color charts and their description with the gen-

Figure 3.11: Setup for the in-situ hyperspectral image acquisition of the painting "A Japanese Lantern".

eral two-constant expression of Kubelka-Munk. The second method is based on the single-constant simplification of Kubelka-Munk, where the ratio of absorption over scattering is estimated from a set of opaque patches of the pigments mixed with linseed oil.

The performance of the three methods was assessed by their accuracy in reconstructing two reference targets made of mixtures of the estimated pigments. For these two case studies, the results show that single-constant simplification gives the best reconstruction, followed by non-linear optimization and the modified black and white method. A reason for this order might be the difference in binding media and preparation technique between the color charts (gum Arabic) and the mockup

(linseed oil). The latter was used for the single-constant simplification. Nevertheless, the modified black and white method showed that there is an improvement when considering more than two substrate intensities.

3.11 P9 - Colour-Balanced Edge-Guided Digital Inpainting: Applications on Artworks

P9 proposes a novel a edge and color aware method to infill lacunae in color images of artworks. In particular, this work highlights a case study on a set of images of the wall paintings from the Dunhuang site [165]. The approach consists in a learning based technique, where two generative adversarial networks (GANs) are trained to extract and synthesize structural features and color content, respectively. To better control the accuracy of the colors, the CIE L*a*b* space rather than RGB is employed, and priors in the chromatic dimensions are computed by quantizing the a* and b* values. This color palette is then used in a loss function designed for the color generator, in order to constrain the network to generate colors that are close to the priors. This way, a more balanced distribution of generated colors is ensured. At the same time, the bias intrinsic to the L1 loss to optimize for mean values is counteracted [167].

The missing regions in the wall paintings are modelled with a random walk, to reflect the stochasticity of the aging phenomenon in reality. For the learning process in GAN [120], the size and pattern of the masks are important because they defined the resolution of the details to be inpainted. To cover for a wider range of resolution of the missing details, three morphological operations (dilation, skeletonization, medial axis transform) were applied to the original random walk masks, and they were all input to the reconstruction method. The analysis of the results and comparison with other state-of-the-art inpainting methods showed the choice of image quality metric is critical. For instance, using novel CNN-trained reference quality metrics, our method performs better than others, as opposed to the output of the traditional metrics such as PSNR or SSIM [168]. Fig. 3.12 showcases two examples where it is easy to observe by visual assessment that our approach outperforms the baseline method [169].

3.12 P10 - Better Sensors, Better Forgers: An Adversarial Loop

The last paper in this dissertation, **P10** tackles the ethical and legal implications of cultural heritage digitization in a reflective essay. In particular, connections are made with the problem of art authenticity examination. **P10** poses the following question: to what extent are current digitization techniques able to detect forgeries? Then, to what extent the knowledge obtained with the advancement of the sensing

Figure 3.12: The columns represent in order, from left to right: original image, simulated deteriorated image with random walk mask, inpainted image with our approach, inpainted image with the approach of [169]. In the highlighted regions of interest, our approach outputs more color coherent and sharper results. Figure adapted from **P9**.

techniques becomes a tool in the hands of the forgers?

The essay is structured in two main parts. In the first part, an overview of art forensics methods is presented, together with a set of case studies showing how forgers learned to deceive some of the authenticity examination procedures. The second part of the essay focuses on the specific issues that digitization brings in the context of authenticity studies. Thus, it discusses the mechanisms and the existence of guidelines for digitization, that make the difference between digitization as a reproduction technique or a creative process that changes the acquired reality. Then, it continues to stress the importance of digital repositories, by ensuring their integrity and the accuracy of metadata. Digital data can be manipulated and edited, which can contaminate diagnostic results, as well as the input to examination procedures. In this regard, the essay integrates the aspect of the born digital art and the generative paradigm for creating fake, but realistic images with AI-enabled algorithms, such as GAN [120]. The essay concludes that digital data in the age of AI-enabled art needs to be treated and examined with extra care. In the end, it is not surprising that the algorithm behind GAN is based on adversarial learning, where the generator (the forger) improves by striving to fabricate convincing realistic imagery for the discriminator (the art detective).

Chapter 4

Discussion

eu cu lumina mea sporesc a lumii
taină -
şi-ntocmai cum cu razele ei albe
luna
nu micşorează, ci tremurătoare
măreşte şi mai tare taina nopţii,
aşa îmbogăţesc şi eu întunecata
zare
cu largi fiori de sfânt mister
şi tot ce-i neînţeles
se schimbă-n neînţelesuri şi mai
mari
sub ochii mei.

Lucian Blaga

I with my glow enhance world's mystery -
exactly how the moon, with her white rays,
doesn't diminish, but with a tremor intensifies night's magic,
I also enrich the gray horizon with shivers of dear mystery,
and all that's poorly understood changes in bigger mysteries under my eyes.

English translation by Laura [170]

This chapter discusses the research contributions of this thesis. In the introduction chapter of this dissertation, several research aims were defined, and here I will reflect upon the outcomes of each article in this thesis in connection with the original research questions. Fig. 4.1 organizes the various research tasks where this thesis brought a contribution, in the shape of a tree. Similar to the life cycle of leaves, the level of knowledge regarding the appearance of cultural heritage objects matures as it transits from image and data capture, to analysis and finally, to synthesis. The left side of the tree leans more towards the analysis based on color and spectral imaging, while the right side concentrates on the knowledge derivation from MLIC.

In order to better follow the upcoming discussion, let's revisit Fig. 1.1 by drawing the connection between the articles in this thesis and the established research questions, as shown in Fig. 4.2.

4.1 RQ1: How to capture the appearance of artworks in a non-invasive way and beyond what is visible to the naked eye?

In this thesis, several non-invasive capture methods were proposed depending either on the appearance reconstruction tasks, or on the particularities of the materials and objects to be digitized. As such, **P1** introduces a portable setup for the acquisition of multi-spectral multi-light images, that was proved suitable for the capture of on-site specular and diffuse, opaque cultural heritage objects with low-relief. The setup consists in a dome of LEDs that emit in the UV, VIS and NIR, a modified DSLR camera and a set of calibration targets that allow per-pixel light correction. The main limitation of this setup is given by the maximum size of the objects that can be captured (20x20 cm), which is constrained by the diameter of the dome of lights. Building on the setup proposed in **P1**, **P2** introduces a setup to capture fluorescent materials, through the mounting of a filter system that separates

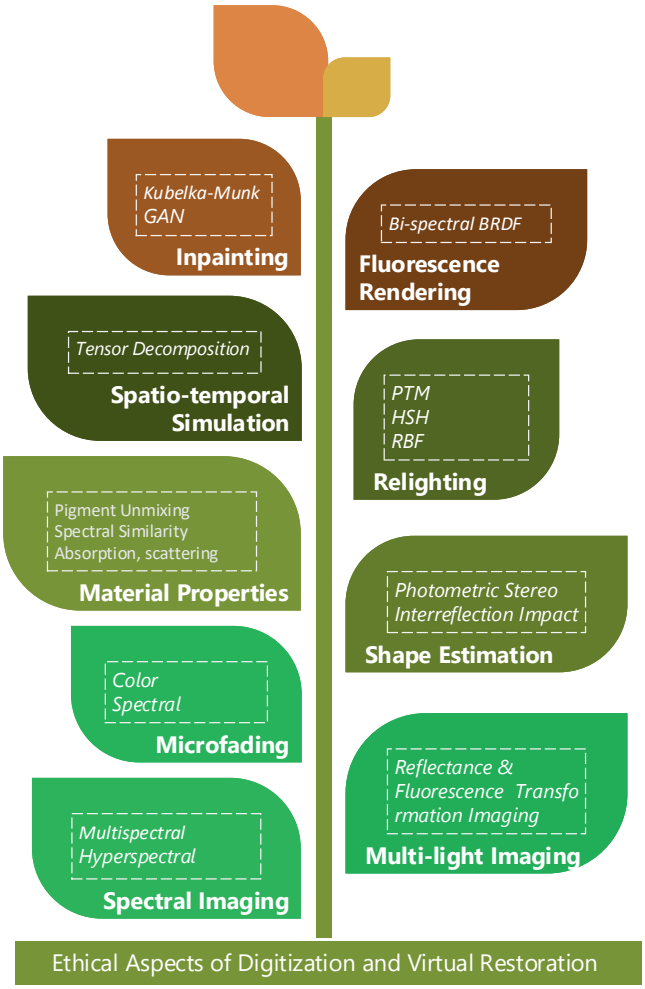

Figure 4.1: The efforts of my PhD, as a tree metaphor. The level of understanding of appearance grows with the tree branches, starting from capture, moving on to analysis and reconstruction of various appearance attributes and finalising with synthesis based on physical and data-driven models. The tree is rooted in ethical considerations regarding cultural heritage digitization and virtual restoration.

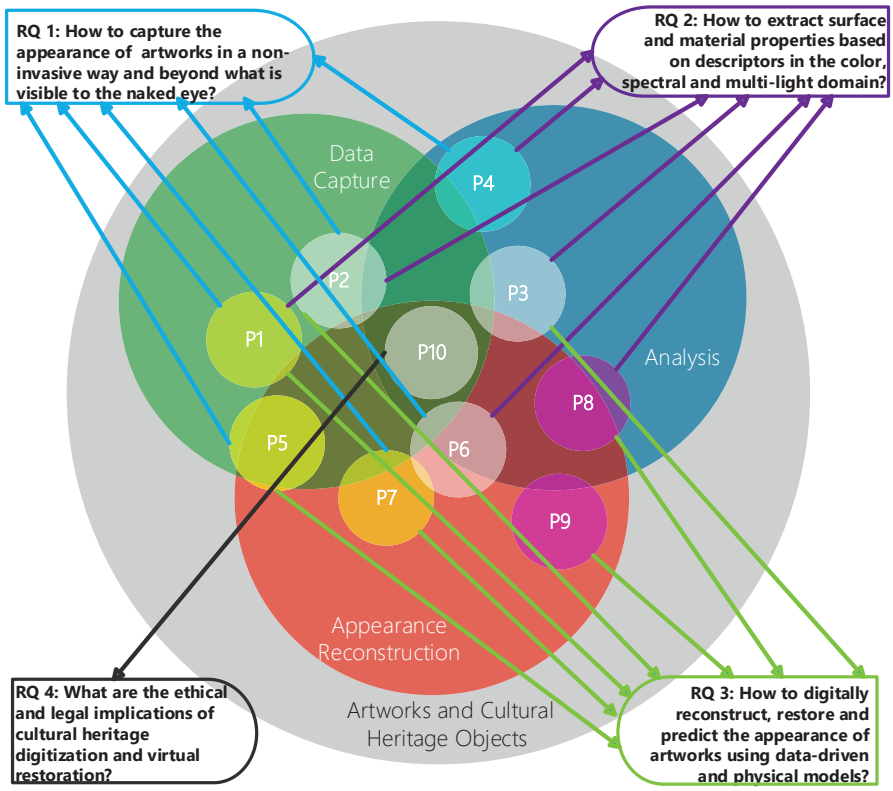

Figure 4.2: Revisiting the research questions and the contributions of this thesis. Several papers contribute to more than one research question.

the fluorescent signal from the reflective signal. While the case study presented in **P2** shows only the capture of UV-induced visible fluorescence, the setup can be applied as well to fluorescence excited by the visible spectrum and noticeable in the NIR, as the camera has sensitivity in that range.

P4 and **P7** show practical examples of hyperspectral imaging of museum objects. **P4** uses the horizontal setup, where a translational stage is electronically controlled to move the objects to be scanned, while **P7** uses a vertical arrangement, where a rotational stage moves the camera as it faces the object. **P8** uses the same setup as **P4**, with the difference that the scanning is carried out in laboratory, not in-situ conditions. For this reason, in Fig. 4.2, **P8** is assigned to the analysis and reconstruction bubbles (corresponding to **RQ2** and **RQ3**, respectively) because it

has a larger contribution there than as a capture method.

In **P5** and **P6**, the temporal dimension of visible light-induced aging in an artwork is captured with a point-based measurement instrument, namely the microfadeometer. Adequate for on-site experiments, the microfadeometer exposes only a very small area of the object, 0.5 mm. In addition, the experiment is stopped when the exposed area reaches a change equivalent to $\Delta E_{00} = 2$. As a result, it is considered to be a non-invasive or at most, under a stricter definition, a minimally invasive technique. Furthermore, the change triggered by the exposure to light is recorded not only in the color dimension, but spectrally as well.

Limitations

In the proposed works, only a subset of appearance attributes were captured for non-fluorescent and fluorescent objects. Ideally, a dense spectral BRDF acquisition and bispectral BRDF would fully capture the effects of light-object interaction. In addition, given a non-uniform surface, such measurements should be done on a spatial-varying basis. The approaches in **P1** and **P2** measure only a slice of the full BRDF, for only one viewpoint. Throughout the articles, the measured spectral range is limited mainly to the visible range, and only short portions of the ultraviolet and the near infrared regions, i.e. the invisible range of the electromagnetic spectrum. For some objects and materials, these ranges are not sufficient to capture unique, descriptive features, beyond the surface. For instance, in the study of paper fixatives in **P4**, data in the short-wave infrared would have been more discriminative in classifying the different types of fixatives, because short-wave infrared reaches the molecular properties of a material. In addition, this thesis did not include capture with other diagnostic analytical methods common in conservation science. Although a short survey of sensing techniques other than spectral imaging, MLIC and microfading is included in **P10**, no data was captured with other methods. In this sense, the X-ray fluorescence technique, that detects chemical elements, would have been useful to provide a ground-truth to the results regarding pigment unmixing and identification in **P6**. In addition, fluorescence spectroscopy would have been helpful to confirm the presence of the red lake pigment, which is more troublesome to detect with X-ray fluorescence [33].

4.2 RQ2: How to extract appearance and material properties based on descriptors in the color, spectral and multi-light domains?

RQ2 is concerned with the recovery of material and appearance properties as a result of the analysis of multi-light and multi-spectral images. **P1**, **P2** and **P3**

analyze MLIC to recover the albedo and normal maps of the digitized objects and to achieve relighting from unmeasured light positions (**P1**). The analysis is performed with polynomial models fitted on either a local (per-pixel) appearance profile or global (image level) appearance profile. The appearance profile is a descriptor that stacks the photometric variation captured in a MLIC. The main contribution of **P2** and **P3** is that of being the first to analyze MLIC of fluorescent objects with non-uniform albedo. In addition, **P2** and **P3** together, form a dataset of MLIC of real and synthetic fluorescent objects, the first of its kind. A collateral research outcome of **P3** is the analysis of the effect of interreflections on the shape reconstruction for concave fluorescent surfaces made of materials that reflect in the same spectral range they fluoresce, specifically dayglo pigments.

P4, **P6** and **P8** extract material properties by relying on spectral data. **P4** uses two spectral descriptors to differentiate between fixatives applied to protect friable media in paper drawings: spectral angle and spectral correlation. The two descriptors are computed for the reflectance signal and for the first-derivative of the reflectance. In an analogue way, **P6** uses the same spectral descriptors to address the pigment identification task, by comparing endmembers with spectral libraries. A challenge with spectral metrics is the visualization beyond the numerical representation. In this sense, **P4** and **P6** offer two innovative visualization methods to assess the similarity between material based on spectral descriptors: confusion matrix and bubble chart. The confusion matrix facilitates the detection of any grouping trend of the analyzed materials based on a single spectral descriptor. The bubble chart is three-dimensional, and it permits the simultaneous assessment of three spectral metrics, where clusters of materials can easily be identified.

P6 introduces the tensor decomposition method, that based on a stack of spectral microfading measurements of paint samples, it recovers the endmembers, their abundance and their alteration rate. This is the first attempt in the literature to extract this knowledge from a set of spectral microfading measurements.

P8 proposes a optimized black and white method of the Kubelka-Munk model to recover the scattering and absorption coefficients of pigments from color charts. The novelty of this approach is anchored in the extraction of optical coefficients based on pigment charts created with a certain binding media, and then the reconstruction of reflectance for paint mixtures executed with a different binding media. Because it proposes a method for appearance reconstruction, in addition to the contribution for **RQ2**, **P8** fits in the reign of **RQ3** as well.

Limitations

There are numerous descriptors that could be computed from visual data, such as edges, corners, image statistics, texture features, neural features. In this thesis, the main descriptors used for analysis are the spectral signature and related similarity metrics in the spectral domain (based on spectral imaging), and the appearance profile that encodes photometric variation dependent on the incident light position (from MLIC). Because of the simplicity of the spectral descriptors, **P4** can be considered to offer a rather superficial solution to the problem of material classification. In addition, CNN features are used in **P9**, but because the purpose was image formation, not material analysis, this article is not considered as a contribution to **RQ2**. Furthermore, another main limitation of the pigment analysis method in **P6** is given by the lack of ground truth with respect to the chemical composition of the microfaded paints, and supplementary validation on control samples and other objects.

4.3 RQ3: How to digitally reconstruct, restore and predict the appearance of artworks using data-driven and physical models?

P1, P2, and **P3** bring a contribution to the reconstruction of geometric information for low-relief objects. In particular, **P1** proposes the virtual reassembly of two fragments of a golden lamina by exploiting the visualization of depth, extracted from the normal map. In addition, **P1** relights the appearance of the golden lamina from virtual light positions, excluded from the stack of original measurements. **P2** reconstructs the appearance attributes of real fluorescent objects with non-uniform albedo for different illumination configurations, and compares the recovered normal maps with the ground-truth shape scanned with a structured light scanner. The results indicate the best polynomial model and the best illumination configuration, and highlight as well, that based on the real measurements, the errors are higher when fluorescence is activated. To complement the real acquisition setup in **P2**, **P3** recreates the MLIC setup in a virtual environment, constructed in a spectral renderer, where the fluorescent materials are spectrally rendered as Lambertian, but considering their bispectral properties. After rendering fluorescent objects in a fully spectral way, scene interactions and global illuminations effects were analyzed in relation to the normal map recovery.

Time-series analysis is employed in **P5** towards the prediction of future aging of pigment samples from microfading color data. This is reportedly the first attempt to apply auto-regressive moving average models to color coordinates. The results obtained show that ARIMA are robust to modelling non-linear change trends and

surpass instrumental noise. A limitation of this method is that it treats the change of each color coordinate as a univariate series, neglecting the inter-correlation.

P7 extends the knowledge derived in **P6** regarding pigment properties, from isolated single locations to the spatial level. This is accomplished by connecting the microfading measurements with a hyperspectral image of the same scene. The link is achieved through the endmembers, where the abundance maps of the endmembers in the hyperspectral image are obtained with least-squares unmixing. The abundance maps can then be recomposed into a tensor, where the temporal dimension that mirrors the spectral degradation is included. As a result, the proposed method allows for the virtual simulation of the restored and aged versions of the painting, for a given illuminant at specific amounts of light exposure.

Both models in **P5** and **P7** revolve around measurements that reflect the current status of conservation of a painting. This implies that while mathematically, it is feasible to apply rejuvenation (reverse the fading process), this requires additional validation from a physical perspective. Moreover, the ARIMA are designed to be forecast methods. For this reason, no rejuvenation attempt was showed in **P5**. However, using the coefficients of the model, together with cross-validation methods, mathematically it is possible to explore the rejuvenation using ARIMA. This is suggested as future work as a follow up of this thesis. In addition, the predictions in both **P5** and **P7** are based on microfaded data that was collected for a short period of time, but at very high illumination levels (12.5 Mlux). This most probably breaks down the reciprocity principle of light exposure according to the findings in [54, 64]. Hence, it is challenging to make an equivalence between the proposed simulations in **P5, P7** and the museum display conditions where light levels have considerably lower magnitude and possibly different emission characteristics than in the microfading experiment. This becomes even more problematic for the digital rejuvenation, as it is not trivial to trace back the precise record of all the light conditions the artwork was exposed to between its creation and before its inclusion as an exhibit in the museum collection.

Finally, **P8** uses the Kubelka-Munk model to approximate the appearance of uniform patches of mixed paints and a painting with complex semantics. The accuracy of the method is limited by the differences in binding media between the objects used for the estimation of the optical coefficients and the reconstruction. In addition, for the painting reconstruction, another impediment is represented by the ground-truth abundance maps that were obtained with a computational method and thus, carry with themselves a baseline error.

P9 answers to **RQ3** by proposing a generative adversarial approach to imitative loss restoration in wall paintings. The method is color and structure aware, and it

uses priors that summarize the color distribution of the dataset to control the bias towards mean colors. Although the approach is meant to offer seamless reconstruction, depending on the complexity of the image and the loss area, the retouchings are not perfectly imitative. Thus, images with more complex semantics (such as faces) are not reconstructed as fine as those with simpler content. In these cases, it is mainly the structural elements that do not get recovered rather than the color information. In addition, the quality of the inpainted images is inversely related to the extent of the loss.

Limitations

Appearance reconstruction, being an inverse imaging problem comes with many challenges, and thus limitations of the proposed solutions. Some of these limitations reside in the modelling stage, while others in the quality of the input data. Thus, a limitation of **P2** is given by the lack of a proper image correction workflow for the MLIC in the fluorescent mode. While the MLIC in conventional reflective mode contains several calibration targets, including a white diffuse target for flat-fielding and correcting the light fall-off factor, no such target was used for the fluorescence mode. The reason for this is the scarcity of calibration targets and correction workflows for fluorescence in general. Nonetheless, in future work, targets such as [171] can be used for the calibration of fluorescence images. Also, in **P2**, another factor that might affect the quality of the normals' reconstructions in the fluorescence mode is the signal-to-noise ratio (SNR). Due to the low-intensity nature of the fluorescence signal in comparison with reflectance, the SNR is higher for fluorescence images than for reflectance images. In the current acquisition setup, the SNR is controlled through a series of pre-processing and calibration operations (e.g. subtraction of ambient light image) similar for both reflectance and fluorescence. However, the SNR can be improved in the future by fine-tuning the acquisition parameters (e.g. integration time, camera aperture size) and/or by taking multiple captures of the same scene and averaging them.

The performance of the spatio-temporal simulation approach in **P7** depends on the quality of the data captured with a MFT and a hyperspectral camera. In particular, the microfading requires a careful design of experiment, in that the points chosen as samples need to include all the variation subtended by the surface to be mapped. For instance, the white areas in the lantern studied in **P7** were not measured with the MFT, and this affects the accuracy of the material distribution in the hyperspectral image, and implicitly, the spatio-temporal simulation.

4.4 RQ4: What are the ethical and legal implications of cultural heritage digitization and virtual restoration given the increasing accessibility of imaging sensors and the recent take-off of AI techniques?

This thesis presents digitization methods that, considering the value and fragility of cultural heritage objects, pose a certain risk. Because all the presented techniques are non-invasive, the risk is minimal, but present nonetheless. Every digitization requires the object to be handled and exposed to light. As tackled by some of the articles, such as **P5, P6, P7**, light exposure might accelerate the degradation of sensitive materials. Nevertheless, the capture and analysis is important to better understand the needs and singularities of an artwork, which helps determine conservation and exhibition policies. Although this seems like a vicious circle, the risks can be mitigated by following acquisition protocols that ensure the quality of the digitization while protecting the cultural heritage object as much as possible. Such guidelines are reviewed in **P10**. In addition to providing a survey of digitization methods, **P10** dwells on how the knowledge generated from the analysis of digitized artifacts can be put to good and bad use, in the context of art forgeries. The good use refers to digitization techniques as art forensic methods, while the bad use entails the increased awareness of forgers who learn how to fool the diagnostic methods.

Another contribution of **P10** is a brief overview of digital AI art methods. The essay touches on the subject of generative techniques and how they have a direct implication on virtual restoration or the creation of new paintings in the style of an artist. AI techniques offer a mimetic solution to the retouching problem, similar to the proposed technique in **P9**. Even though Brandi's "Theory of restoration" is targeted to the restoration of physical objects, it is interesting to ponder upon the utility of simulating the hatching techniques for digital restorations methods as well. Moreover, it is essential to other to ensure through metadata that the virtual reconstruction outcome is well documented and acknowledged as only a hypothesis to the real restoration. In conclusion, based on the above mentioned contributions, **RQ4** is answered by the essay elaborated in **P10** of this thesis.

Limitations

The ethical and legal considerations in **P10** are not exhaustive. For instance, the ethics of digital restoration is only glanced upon, but not presented with depth. In addition, the problem of the copyright for AI generated artworks is only discussed for particular instances and jurisdictions. Being a novel field whatsoever, the copyright rules are not yet well defined and standardized when it comes to AI-art tools.

4.5 Research Paradigms

The articles presented in this dissertation adhere to mainly three of the research philosophies described in Section 1.4: postpositivistic, pragmatic and transformative. Fig. 4.3 maps a distribution of the articles in relation to the research paradigms. Accordingly, **P1, P2, P3, P5, P9** have a postpositivistic lens because they use mathematical models as a hypothesis to approximate the real-world, and then validate the performance of these models based on quantitative comparison with a ground-truth baseline. The research approach in **P8** is postpositivistic as well, but different to the data-driven models employed in the previously mentioned articles, it proposes a method with a stronger foundation in physical laws.

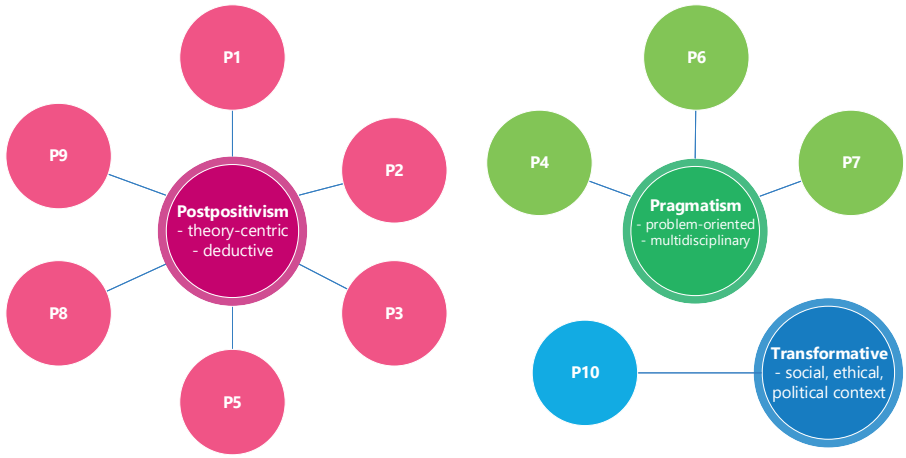

Figure 4.3: The research paradigms adopted in this thesis.

Although the core of **P4, P6, P7** lies in quantitative analysis, because they address specific case-studies, their research approach is a rather pragmatic one. In addition, for the task of pigment identification and spatio-temporal simulation in **P6** and **P7**, the ground-truth is unknown, so these articles rely on subjective assessment and interpretation, involving multidisciplinary cooperation with the conservation scientist co-author, to understand the quality of the exploratory data analysis.

Finally, **P10** zooms out and from a satellite perspective, takes a transformative stance on all the research topics addressed in this thesis, and discusses the ethical and legal implications of CH digitization, analysis and reconstruction.

4.6 Contributions to the CH field

The methods proposed in this dissertation bring specific contributions to the CH field, as follows:

- **Digitization** of CH objects with a wide range of materials, in on-site and off-site conditions, with multispectral, hyperspectral and RTI imaging setups.
- **Documentation and visualization** of appearance properties, such as reflectance, fluorescence, albedo, normal map.
- **Pigment unmixing**, in a semi-supervised way, based on microfading measurements. In other words, repurposing microfading from only assessing light sensitivity of pigments and establishing exhibition policies, to recover pure pigments in mixed samples.
- **Spatio-temporal simulation of fading mechanisms**, where the material and temporal characterization accomplished with microfading in small samples is extrapolated to the spatial dimension, by means of hyperspectral imaging.
- **Retouching of losses**, with an inpainting algorithm that follows a common artistic process, from first sketching the underdrawings to then applying color.
- **An ethical appraisal** of digitization practices, digital data integrity, image manipulation techniques, and new threats regarding authenticity of CH in the digital era.

Chapter 5

Conclusion and Perspectives

Atâta linişte-i în jur de-mi pare că
aud cum se izbesc de geamuri
razele de lună.

Lucian Blaga

Such a deep silence surrounds me,
that I think I hear moonbeams
striking on the windows.

English translation

In this last chapter, the overall outcome of this thesis is concluded, and thoughts regarding follow-up work and potential directions of future research are suggested.

5.1 Conclusions

This PhD dissertation aimed to bring advancements to appearance capture, material analysis and appearance reconstruction of cultural heritage objects through the application of spectral and multi-light imaging techniques.

Indeed, the research conducted in this PhD project brought contributions on multiple levels. Two acquisition setups were proposed for the multispectral and MLIC of objects with conventional (**P1**) and fluorescent materials (**P2**), respectively. In this setting, the shape and albedo of the various objects were reconstructed using

polynomial models. The real acquisition MLIC setup was virtually recreated in a spectral renderer that supports fluorescence to generate a synthetic dataset, similar to the physically captured data (**P3**). Based on this synthetic dataset, the influence of inter-reflections on the shape estimation was evaluated, comparing the cases of plain versus daylight fluorescent colored scenes. Furthermore, material properties for paper fixatives and pastel paintings were characterized in the spectral reflectance domain based on hyperspectral imaging (**P4**) and microfading data, respectively (**P6**). The microfading data became the source of two models for aging simulation. In the first model, the colorimetric degradation of pigment samples is forecasted by means of univariate time-series analysis (**P5**). The second model relies on multivariate tensor analysis (**P6, P7**) to perform aging simulation and digital rejuvenation for single points (1D) and for a surface (2D). The mapping of aging effects from 1D to 2D is called spatio-temporal simulation, and was achieved by merging a set of microfading measurements with a hyperspectral image of the same scene (**P7**). Afterwards, this thesis proposed an approach to the determination of optical properties of paints from pigment color charts, using Kubelka-Munk model (**P8**). Eventually, generative adversarial techniques were devised to conceive a color and structure consistent image inpainting approach for the virtual infilling of lacunae in wall paintings (**P9**). Finally, ethical aspects related not only to generative adversarial networks, but to all CH digitization, image analysis and synthesis techniques, were debated in a reflective essay (**P10**).

Therefore, the research outcomes in this thesis proposed novel solutions to several problems of appearance reconstruction, from the twofold perspective of the visual computing and CH fields. At the same time, the diversity of the objects included as case studies proved the versatility of the spectral and multi-light imaging techniques as non-destructive digitization methods of CH. In addition, the use of these imaging techniques produced a dataset that facilitated the characterization of material and appearance properties. Moreover, beyond the findings of this thesis, this dataset can be further explored, and represents a helpful testbed for future models and analyses.

5.2 Future Work

The body of work introduced in this dissertation can be continued in various directions. To begin with, starting from the introduced MLIC dataset of real and synthetic objects, models tailored to the relighting of fluorescent scenes can be designed and validated in an objective and subjective way [172]. In connection with the subjective assessment, another research gap that could be filled is to develop a tone mapping operator specifically optimized for fluorescent scenes. As highlighted in **P3**, such best tone mapping operator studies exists for conventional

colors, but not for fluorescent colors. Furthermore, the approaches to pigment unmixing and spatio-temporal simulation proposed in the series of articles **P6, P7** can be further validated on other artworks and control samples, and complemented by results gathered from analytical techniques such as microscopical examination, X-ray fluorescence, and fluorescence spectroscopy. Finally, perhaps the most popular research topics at the moment are covered by **P9** and **P10**, because of the fast pace at which AI image restoration are proposed in the literature. In this sense, there is room for improvement in integrating CH needs and particular scenarios. For instance, metamerism-aware generative inpainting techniques that operate in the spectral domain could be very helpful for art restorers and conservators in their preparation for physical retouching. Related to this, the recently proposed text-to-image formation algorithms, such as DALL-E 2[173], Midjourney [174] and Stable Diffusion [175] are highly relevant because they can directly involve art conservators and restorers in the process of AI-based image inpainting. Basically, in these methods, the art experts can edit and guide the inpainted result through text prompts. Due to the attractiveness and topicality of these techniques, in the following subsection, I will briefly demonstrate their basic potential through a series of examples and personal reflections.

5.3 Perspectives

Recent text-to-image AI models, such as DALL-E 2 [173], Midjourney [174] and Stable Diffusion [175] open new possibilities towards virtual artwork restoration and proposing creative image derivates of an artwork. These methods are already used for image inpainting and outpainting (i.e. extrapolating a scene beyond what is captured in an image) applications, where the editing is guided by a natural language caption. The example of outpainting highlighted on the website of DALL-E 2 [173], shows the girl in Vermeer's "Girl with Pearl Earring", surrounded by her room, filled with details of domestic intimacy (see Fig. 5.1). Of course, this is mainly a creative endeavour, the visualization of a hypothesis and not an attempt to claim with certainty a ground-truth that does not exist. For this reason, hereinafter, the results of these text-to-image tools will be referred to as "hallucination" or "generation" to emphasize the creative rather than the scientific side of the process.

Furthermore, these techniques have the potential to show something reminiscent of the original version of an artwork, in cases where descriptions of the original appearance exist in the form of text. Fig. 5.2 shows Midjourney's visual interpretation [174] Vincent van Gogh's painting "The Bedroom", based on the artist's own description, in his letter addressed to this brother. Thus, the caption used for the prompt in Midjourney was the following: *"The walls are pale violet. The floor is*

Figure 5.1: Example of outpainting. Is this how the house of the model in Vermeer's painting was decorated like? We don't know, but it's a possibility, as envisioned by DALL-E 2. Image courtesy: OpenAI [173].

of red tiles. The wood of the bed and chairs is the yellow of fresh butter, the sheets and pillows very light greenish-citron. The coverlet scarlet. The window green. The toilet table orange, the basin blue. The doors lilac. And that is all - there is nothing in this room with its closed shutters. The squareness of the furniture again must express inviolable rest. Portraits on the walls, and a mirror and a towel and some clothes." [176].

It is interesting that in three out of the four results, together with the fantasized image, the color palette of the pictures is summarized as well. In its default use, the Midjourney generates four possible results. Afterwards, it is possible to hallucinate additional variations of one of the results. While the results respect the colors and content of the description quite closely, the results is too photorealistic, in the sense that is resembles more a photography than a painting. To add a painting style, the words "a painting of a bedroom" were added to the prompt. In the new results displayed in Fig. 5.3, we can see that the perspective and the content is more similar to that of the artist. Actually, if we add "a painting of a bedroom in van Gogh's style", then the results approaches even more the current appearance of the original painting, as it can be visualized in Fig. 5.4. This is probably because in the training dataset that Midjourney employs to learn text-to-image associations, there are images of van Gogh's paintings, which influences the style of the output. Moreover, because the lilac colors are lost, there is an obvious bias to the images

Figure 5.2: *Left:* Midjourney's hallucination for van Gogh's description of his painting "The Bedroom". *Right:* variations of the second generated image.

of the current status of the painting. It seems that if we want to approach the virtual restoration of the painting with Midjourney, the results without indicating the name of the artist in the prompt remain closest to the original colors (Fig. 5.3).

Sometimes, the hallucinations unlocked by Midjourney can be helpful to visualize the artist's original intention (Fig. 5.3). However, as it based on a textual representation, the creativity can go even beyond the artist's final rendition of the intended scene and propose new, original variants that are sometimes triggered by the limitations of the tool in understanding expressions. For instance, when prompting the van Gogh's description of the "Starry Night", *"in short the starry sky painted by night, actually under a gas jet. The sky is aquamarine, the water is royal blue, the ground is mauve. The town is blue and purple. The gas is yellow and the reflections are russet gold descending down to green-bronze. On the aquamarine field of the sky the Great Bear is a sparkling green and pink, whose discreet paleness contrasts with the brutal gold of the gas. Two colorful figurines of lovers in the foreground."* [177], the Midjourney algorithm fails to understand that "The Great Bear" refers to the constellation, and instead paints an actual animal, while still creating a beautiful and fluid starry landscape (Fig. 5.5).

As with all AI-based techniques, the potential of image synthesis from text and in general, all generative approaches is huge for computer graphics and computer vision applications. However, it is accompanied by the risk of these methods to be used with malevolence. For this reason, it is crucial to regulate these tools and ensure the positive side of image generation approaches. Of course, when it

Figure 5.3: Midjourney's hallucination for van Gogh's description of his painting "The Bedroom", and adding a "A painting of a bedroom" to the prompt.

comes to art, it is not trivial to make the distinction between artistic intention and words that may carry a negative charge. For instance, Midjourney bans the use of the word "blood". This was discovered while trying to see how the tool imagines "The Scream" of Edward Munch based on his own words (Fig. 5.6: *"I was walking along a path with two friends – the sun was setting – suddenly the sky turned blood red – I paused, feeling exhausted, and leaned on the fence – there was blood and tongues of fire above the blue-black fjord and the city – my friends walked on, and I stood there trembling with anxiety – and I sensed an infinite scream passing through nature."* [178]. The word "blood" was replaced with "red" for the prompt to run. In a similar way, DALL-E [173], another platform for text-to-image generation bans the use of word "dissection", as discovered by [179]. Would the results have been more dramatic if the original words had been used? It is difficult to answer, but what is for sure, is that there is a concern against the misuse of these AI generated art tools, and there is room for fine-tuning the enforcement of ethics so that it does not become a technical limitation while shielding the malicious

Figure 5.4: Midjourney's hallucination when prompting van Gogh's description of his painting "The Bedroom", and adding a "A painting of a bedroom in van Gogh style" to the text.

users.

Although at the moment, text-to-image tools are mainly targeted for creative use, they can be repurposed to better meet the CH needs. This can achieved by including conservation scientists, art historians and restorers in the process of prompt engineering [180] and quality assessment of the results of the tools. For instance, for natural image inpainting, such a pipeline was proposed by Wang et al. [181], where the refinement of the restored image is guided by text input, allowing for specific editing of material and appearance properties, and in the end, the quality is evaluated by a group of human users. In addition, all inpainted outputs bear a watermark signature to elucidate that the image is generated by a computer algorithm, and not a digital reproduction of a real scene. To address CH needs, the work of Wang et al. could be extended by including a dataset of CH images in the training process, and by letting art conservators and restorers engineer a prompt according to their desired parameters.

Figure 5.5: Midjourney's hallucination for van Gogh's description of his painting "The Starry Night", and adding "a canvas painting" to the prompt. The tool fails to understand that the "Great Bear" in the artist's description refers to the constellation, not the animal.

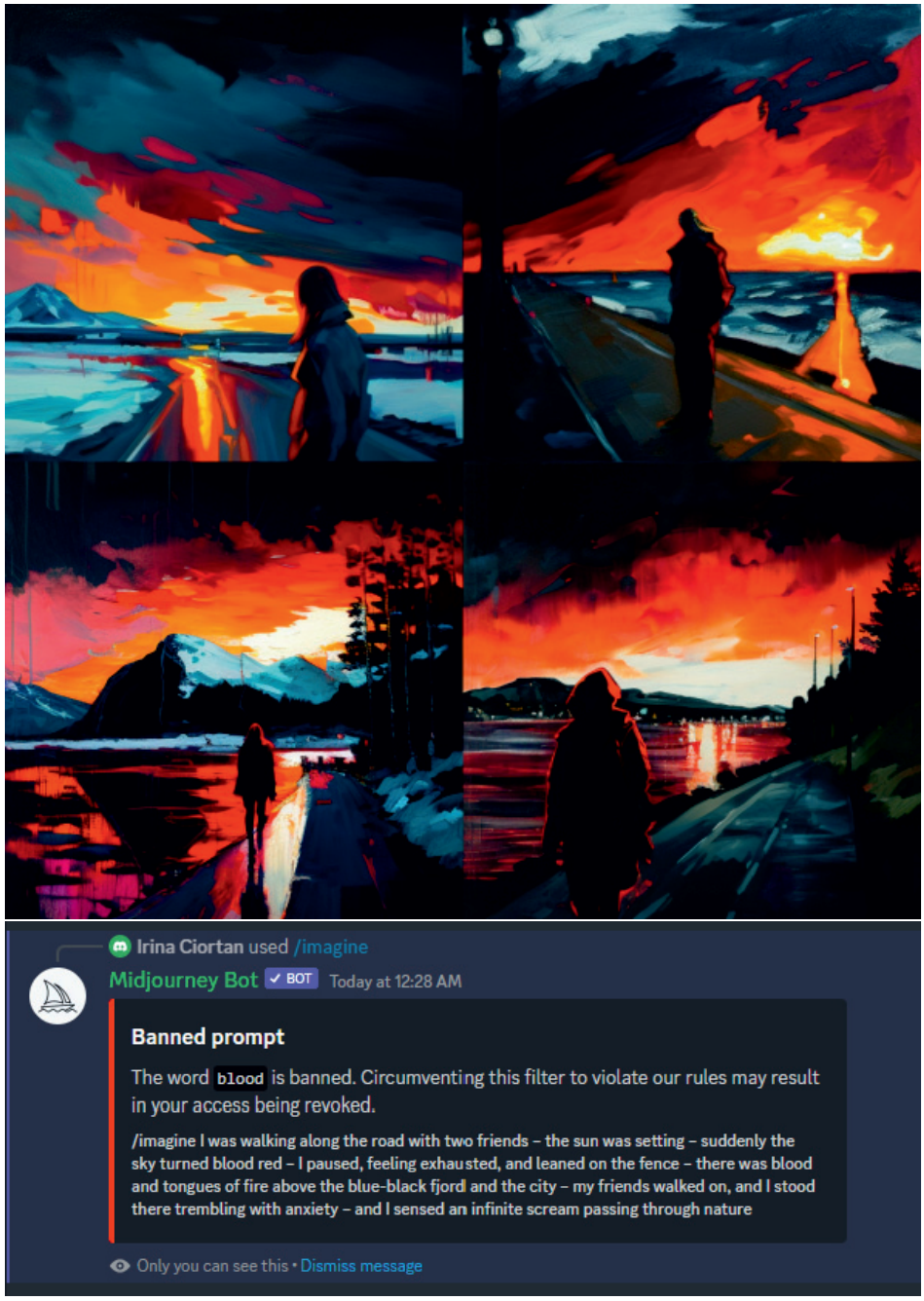

Figure 5.6: *Top:* Midjourney's result for Edward Munch's description of the scene that inspired his painting "The Scream". *Bottom:* alert against using the word "blood", showing implementation of ethical concerns in the Midjourney platform.

Bibliography

[1] E. Anziano, M. Elorza, and C. Roney, "Saving Florence from the next big flood," *Nature Italy*, Nov 2022.

[2] L. Pecchioli, F. Panzera, and V. Poggi, "Cultural heritage and earthquakes: bridging the gap between geophysics, archaeoseismology and engineering," *Journal of Seismology*, vol. 24, no. 4, p. 725–728, Aug 2020.

[3] D. Phillips, "Brazil museum fire: 'incalculable' loss as 200-year-old Rio institution gutted," *The Guardian*, Sep 2018, accessed 20 February 2023. [Online]. Available: https://www.theguardian.com/world/2018/sep/03/fire-engulfs-brazil-national-museum-rio

[4] UNESCO World Heritage Center, "Damage to Notre Dame Cathedral, resulting from the fire of 15 April 2019," accessed 20 February 2023. [Online]. Available: https://whc.unesco.org/en/collections/54/

[5] N. Winchester, "Targeting culture: The destruction of cultural heritage in conflict," Dec 2022, accessed 20 February 2023. [Online]. Available: https://lordslibrary.parliament.uk/targeting-culture-the-destruction-of-cultural-heritage-in-conflict/

[6] B. F. Lavoie, *The costs of digital preservation*. Facet, 2006, p. 106–132. [Online]. Available: https://www.cambridge.org/core/books/digital-preservation/costs-of-digital-preservation/31B8C84001567525B2F296C9B4A6C668

[7] K. L. Pendergrass, W. Sampson, T. Walsh, and L. Alagna, "Toward environmentally sustainable digital preservation," *The American Archivist*, vol. 82, no. 1, p. 165–206, Mar 2019.

[8] F. Nielsen, *Visual computing: Geometry, graphics, and vision (graphics series)*. Charles River Media, Inc., 2005.

[9] M. Strlič, "Heritage science: A future-oriented cross-disciplinary field," *Angewandte Chemie International Edition*, vol. 57, no. 25, p. 7260–7261, 2018.

[10] L. A. N. B. Broers *et al.*, *Science and Heritage: Report with Evidence; 9th Report of Session 2005-06*. The Stationery Office, 2006, vol. 256.

[11] H. Davy, "Some experiments and observations on the colours used in painting by the ancients," *Philosophical Transactions of the Royal Society of London*, no. 105, pp. 97–124, 1815.

[12] H. Davy, "Some observations and experiments on the papyri found in the ruins of herculaneum," *Philosophical Transactions of the Royal Society of London*, no. 111, pp. 191–208, 1821.

[13] A. Nanetti, "Defining Heritage Science: A Consilience Pathway to Treasuring the Complexity of Inheritable Human Experiences through Historical Method, AI, and ML," *Complexity*, vol. 2021, Feb 2021.

[14] B. Cornelis, A. Dooms, J. Cornelis, F. Leen, and P. Schelkens, "Digital painting analysis, at the cross section of engineering, mathematics and culture," in *2011 19th European Signal Processing Conference*, Aug 2011, p. 1254–1258.

[15] A. Bentkowska-Kafel and L. MacDonald, *Digital techniques for documenting and preserving cultural heritage*. Arc Humanities Press, 2018.

[16] C. R. Johnson, E. Hendriks, I. J. Berezhnoy, E. Brevdo, S. M. Hughes, I. Daubechies, J. Li, E. Postma, and J. Z. Wang, "Image processing for artist identification," *IEEE Signal Processing Magazine*, vol. 25, no. 4, p. 37–48, Jul 2008.

[17] N. van Noord, E. Hendriks, and E. Postma, "Toward discovery of the artist's style: Learning to recognize artists by their artworks," *IEEE Signal Processing Magazine*, vol. 32, no. 4, p. 46–54, Jul 2015.

[18] C. Florea, R. Condorovici, C. Vertan, R. Butnaru, L. Florea, and R. Vrânceanu, "Pandora: Description of a painting database for art movement recognition with baselines and perspectives," in *2016 24th European Signal Processing Conference (EUSIPCO)*, Aug 2016, p. 918–922.

[19] L. W. MacDonald, "Realistic visualisation of cultural heritage objects," PhD Thesis, UCL (University College London), 2015.

[20] S. Kenderdine, ""Pure Land": Inhabiting the Mogao Caves at Dunhuang," *Curator: The Museum Journal*, vol. 56, no. 2, p. 199–218, 2013.

[21] T. Cathcart and D. Klein, *Plato and a platypus walk into a bar...: Understanding philosophy through jokes*. Penguin, 2008.

[22] J. W. Creswell, *Research designs: Qualitative, quantitative, and mixed methods approaches*. Sage, California, 2014.

[23] L. Munck, L. Nørgaard, S. B. Engelsen, R. Bro, and C. A. Andersson, "Chemometrics in food science—a demonstration of the feasibility of a highly exploratory, inductive evaluation strategy of fundamental scientific significance," *Chemometrics and Intelligent Laboratory Systems*, vol. 44, no. 1, p. 31–60, Dec 1998.

[24] S. T. McAbee, R. S. Landis, and M. I. Burke, "Inductive reasoning: The promise of big data," *Human Resource Management Review*, vol. 27, no. 2, p. 277–290, Jun 2017.

[25] A. T. Jebb, S. Parrigon, and S. E. Woo, "Exploratory data analysis as a foundation of inductive research," *Human Resource Management Review*, vol. 27, no. 2, p. 265–276, Jun 2017.

[26] H.-C. Lee, *Introduction to color imaging science*. Cambridge University Press, 2005.

[27] H. G. Völz, *Industrial Color Testing: Fundamentals and Techniques*. Wiley-VCH New York, 2001, vol. 2.

[28] P. Kubelka and F. Munk, "Ein Beitrag zur Optik der Farbanstriche (Contribution to the optic of paint)," *Zeitschrift fur technische Physik*, vol. 12, pp. 593–601, 1931.

[29] R. Johnston-Feller, *Color science in the examination of museum objects: nondestructive procedures*. Getty Publications, 2001.

[30] G. G. Stokes, "On the change of refrangibility of light," *Philosophical Transactions of the Royal Society of London*, vol. 142, p. 463–562, May 1852.

[31] R. S. Berns, *Billmeyer and Saltzman's principles of color technology*. John Wiley & Sons, 2019.

[32] R. Donaldson, "Spectrophotometry of fluorescent pigments," *British Journal of Applied Physics*, vol. 5, no. 6, p. 210, Jun 1954.

[33] K. A. Dooley, A. Chieli, A. Romani, S. Legrand, C. Miliani, K. Janssens, and J. K. Delaney, "Molecular Fluorescence Imaging Spectroscopy for Mapping Low Concentrations of Red Lake Pigments: Van Gogh's Painting The Olive Orchard," *Angewandte Chemie International Edition*, vol. 59, no. 15, p. 6046–6053, 2020.

[34] J. Salvant, M. Walton, D. Kronkright, C.-K. Yeh, F. Li, O. Cossairt, and A. K. Katsaggelos, *Photometric Stereo by UV-Induced Fluorescence to Detect Protrusions on Georgia O'Keeffe's Paintings*, ser. Cultural Heritage Science. Cham: Springer International Publishing, 2019, p. 375–391.

[35] A. Rezaei, E. Aldea, P. Dondi, M. Malagodi, and S. L. Hégarat, "Detecting alterations in historical violins with optical monitoring," in *Fourteenth International Conference on Quality Control by Artificial Vision*, vol. 11172. SPIE, Jul 2019, p. 253–260.

[36] A. Álvarez Martín, S. De Winter, G. Nuyts, J. Hermans, K. Janssens, and G. Van der Snickt, "Multi-modal approach for the characterization of resin carriers in daylight fluorescent pigments," *Microchemical Journal*, vol. 159, p. 105340, Dec 2020.

[37] S. D. Winter, "Conservation problems with paintings containing fluorescent layers of paint," *CeROArt. Conservation, exposition, Restauration d'Objets d'Art*, no. EGG 1, Nov 2010.

[38] S. D. Winter, P. Moors, H. V. Gelder, and J. Wagemans, "Illusory depth based on interactions between fluorescent and conventional colours: A case study on frank stella's irregular polygons paintings," *Art & Perception*, vol. 6, no. 2–3, p. 116–150, Oct 2018.

[39] D. Duncan, "The colour of pigment mixtures," *Proceedings of the Physical Society*, vol. 52, no. 3, p. 390, 1940.

[40] R. S. Berns and M. Mohammadi, "Evaluating single-and two-constant Kubelka-Munk turbid media theory for instrumental-based inpainting," *Studies in conservation*, vol. 52, no. 4, pp. 299–314, 2007.

[41] G. Verri, C. Clementi, D. Comelli, S. Cather, and F. Piqué, "Correction of ultraviolet-induced fluorescence spectra for the examination of polychromy," *Applied spectroscopy*, vol. 62, no. 12, pp. 1295–1302, 2008.

[42] C. Clementi, C. Miliani, G. Verri, S. Sotiropoulou, A. Romani, B. G. Brunetti, and A. Sgamellotti, "Application of the Kubelka—Munk Correction for Self-Absorption of Fluorescence Emission in Carmine Lake Paint Layers," *Applied spectroscopy*, vol. 63, no. 12, pp. 1323–1330, 2009.

[43] L. Simonot, M. Thoury, and J. Delaney, "Extension of the Kubelka–Munk theory for fluorescent turbid media to a nonopaque layer on a background," *JOSA A*, vol. 28, no. 7, p. 1349–1357, Jul 2011.

[44] V. Duveiller, A. Gautheron, A. Cazier, L. Simonot, R. Clerc, J.-P. Salomon, and M. Hébert, "Estimation of the fluorescence emission spectrum of dental composite resin samples of varying thickness," in *IS&T International Symposium on Electronic Imaging 2023 Color Imaging XXVIII: Displaying, Processing, Hardcopy, and Applications*, vol. 35. Society for Imaging Science and Technology, 2023.

[45] UNESCO World Heritage Convention, "Mogao Caves," 1987, accessed 20 February 2023. [Online]. Available: https://whc.unesco.org/en/list/440/

[46] M. E. Ramos and M. G. Lagorio, "True fluorescence spectra of leaves," *Photochemical & Photobiological Sciences*, vol. 3, pp. 1063–1066, 2004.

[47] F. E. Nicodemus, J. C. Richmond, J. J. Hsia, I. W. Ginsberg, and T. Limperis, "Geometrical considerations and nomenclature for reflectance," *Final Report National Bureau of Standards*, 1977.

[48] J. H. Lambert, *Photometria*, 1760.

[49] M. B. Hullin, J. Hanika, B. Ajdin, H.-P. Seidel, J. Kautz, and H. P. A. Lensch, "Acquisition and analysis of bispectral bidirectional reflectance and reradiation distribution functions," in *ACM SIGGRAPH 2010 papers*, ser. SIGGRAPH '10. New York, NY, USA: Association for Computing Machinery, Jul 2010, p. 1–7.

[50] S. Tominaga, K. Hirai, and T. Horiuchi, "Measurement and modeling of bidirectional characteristics of fluorescent objects," in *International Conference on Image and Signal Processing*. Springer, 2014, pp. 35–42.

[51] M. Mohammadi, "Developing an imaging bi-spectrometer for fluorescent materials," Ph.D. dissertation, Rochester Institute of Technology, 2009.

[52] P. M. Whitmore, X. Pan, and C. Bailie, "Predicting The Fading of Objects: Identification of Fugitive Colorants Through Direct Nondestructive Lightfastness Measurements," *Journal of the American Institute for Conservation*, vol. 38, no. 3, pp. 395–409, Jan 1999.

[53] A. Lerwill, A. Brookes, J. H. Townsend, S. Hackney, and H. Liang, "Micro-fading spectrometry: investigating the wavelength specificity of fading," *Applied Physics A*, vol. 118, no. 2, pp. 457–463, Feb. 2015.

[54] H. Liang, R. Lange, A. Lucian, P. Hyndes, J. H. Townsend, and S. Hackney, "Development of portable microfading spectrometers for measurement of light sensitivity of materials," in *International Council of Museums, Committee for Conservation (ICOM-CC) Triennial Conference*. Lisbon, Portugal: Nottingham Trent University, Sep 2011.

[55] Instytut Fotonowy, "Micro fading tester," accessed 10 September, 2022. [Online]. Available: https://www.fotonowy.pl/products/micro-fading-tester/?lang=en

[56] G. Patin, R. G. Erdmann, F. Ligterink, J. G. Neevel, K. J. van den Berg, and E. Hendriks, "An enhanced optical micro-fading device," *Journal of Cultural Heritage*, vol. 57, pp. 276–285, 2022.

[57] B. Carrión-Ruiz, G. Riutort-Mayol, A. Molada-Tebar, J. L. Lerma, and V. Villaverde, "Color degradation mapping of rock art paintings using microfading spectrometry," *Journal of Cultural Heritage*, vol. 47, pp. 100–108, Jan. 2021.

[58] M. Aambø, M. Godzimirska, E. Chan, T. Lojewski, and I. C. Sandu, "Light Sensitivity of Pigments in Edvard Munch's Works on Paper," in *MUNCH2022: Understanding Munch and the Art at the turn of the Centuries - between the Museum and the Laboratory*, Oslo, Mar. 2022, p. 100.

[59] A. Haddad, L. Neufeld, and A. Martins, "Realizing sensations: analyzing paul cezanne's watercolors and assessing their light sensitivity with microfade testing," *Heritage Science*, vol. 11, no. 1, p. 39, 2023.

[60] B. Ford and J. Druzik, "Microfading: the state of the art for natural history collections," in *Collection Forum*, vol. 27, no. 1, 2013, pp. 54–7.

[61] C. Daher, A. Tournié, F. Sauvagnargues, C. Andraud, J. Cuisin, V. Illes, and É. Kissel, "Colored feathers in museum collections: A spectroscopic study of 3 bio-pigments and their lightfastness," *Journal of Cultural Heritage*, vol. 45, pp. 59–70, 2020.

[62] G. Vannucci, S. Joram, A. Beselin, and S. Röhrs, "Micro fading test for textile single yarns: a new methodology applied to the reformation tapestry to assess its sensitivity to light," *Heritage Science*, vol. 11, no. 1, pp. 1–11, 2023.

[63] S. Kogou, A. Lucian, S. Bellesia, L. Burgio, K. Bailey, C. Brooks, and H. Liang, "A holistic multimodal approach to the non-invasive analysis of watercolour paintings," *Applied Physics A*, vol. 121, no. 3, p. 999–1014, Nov 2015.

[64] J. M. del Hoyo-Meĺendez and M. F. Mecklenburg, "An Investigation of the Reciprocity Principle of Light Exposures Using Microfading Spectrometry," *Spectroscopy Letters*, vol. 44, no. 1, p. 52–62, Jan 2011.

[65] J. M. Amigo, *Hyperspectral imaging*, ser. Data handling in science and technology. Amsterdam: Elsevier, 2020, vol. 32.

[66] S. Birchfield, *Image processing and analysis*. Cengage Learning, 2016.

[67] B. E. Bayer, "Color imaging array," Jul 1976, accessed 20 February 2023. [Online]. Available: https://patents.google.com/patent/US3971065/en

[68] V. Kitanovski, J. B. Thomas, and J. Y. Hardeberg, "Reflectance estimation from snapshot multispectral images captured under unknown illumination," *Color and Imaging Conference*, pp. 264–269, 2021.

[69] I. M. **Ciortan**, *Chapter 6. Digitization of Cultural Heritage at the National Museum of Romanian History, Bucharest:*. ARC, Amsterdam University Press, Jan 2018, p. 107–120.

[70] F. H. Imai, M. R. Rosen, and R. S. Berns, "Multi-spectral Imaging of a van Gogh's Self-portrait at the National Gallery of Art Washington DC." in *PICS*, 2001, p. 185–189.

[71] D. Saunders and J. Cupitt, "Image processing at the National Gallery: The VASARI project," *National Gallery technical bulletin*, vol. 14, no. 1, pp. 72–85, 1993.

[72] G. Trumpy, J. Y. Hardeberg, S. George, and B. Flueckiger, "A multispectral design for a new generation of film scanners," in *Optics for Arts, Architecture, and Archaeology VIII*, vol. 11784. SPIE, Jul 2021, p. 138–146.

[73] P. Ricciardi, J. K. Delaney, M. Facini, J. G. Zeibel, M. Picollo, S. Lomax, and M. Loew, "Near infrared reflectance imaging spectroscopy to map paint binders in situ on illuminated manuscripts," *Angewandte Chemie*, vol. 124, no. 23, pp. 5705–5708, 2012.

[74] Norsk Elektro Optikk AS, "HySpex VNIR-1800," accessed 20 February 2023. [Online]. Available: https://www.hyspex.com/hyspex-products/hyspex-classic/hyspex-vnir-1800/

[75] S. Grusche, "Basic slit spectroscope reveals three-dimensional scenes through diagonal slices of hyperspectral cubes," *Applied Optics*, vol. 53, no. 20, p. 4594–4603, Jul 2014.

[76] L. Huang, R. Luo, X. Liu, and X. Hao, "Spectral imaging with deep learning," *Light: Science & Applications*, vol. 11, no. 11, p. 61, Mar 2022.

[77] H. Liang, "Advances in multispectral and hyperspectral imaging for archaeology and art conservation," *Applied Physics A*, vol. 106, no. 2, p. 309–323, Feb 2012.

[78] J. R. Gilchrist, T. Skauli, and C. Durell, "Developing the IEEE P4001 standard for characterisation and calibration of hyperspectral imaging devices," in *IGARSS 2022-2022 IEEE International Geoscience and Remote Sensing Symposium*. IEEE, 2022, pp. 4679–4682.

[79] A. Pelagotti, A. D. Mastio, A. D. Rosa, and A. Piva, "Multispectral imaging of paintings," *IEEE Signal Processing Magazine*, vol. 25, no. 4, p. 27–36, Jul 2008.

[80] H. Davies and A. J. Zawacki, "Making light work: Manuscripts and multispectral imaging," *Journal of the Early Book Society*, pp. 177–193, 2019.

[81] F. Gabrieli, J. K. Delaney, R. G. Erdmann, V. Gonzalez, A. van Loon, P. Smulders, R. Berkeveld, R. van Langh, and K. Keune, "Reflectance Imaging Spectroscopy (RIS) for Operation Night Watch: Challenges and Achievements of Imaging Rembrandt's Masterpiece in the Glass Chamber at the Rijksmuseum," *Sensors*, vol. 21, no. 20, p. 6855, Jan. 2021.

[82] H. Deborah, S. George, and J. Y. Hardeberg, "Pigment Mapping of the Scream (1893) Based on Hyperspectral Imaging," in *Image and Signal Processing*, A. Elmoataz, O. Lezoray, F. Nouboud, and D. Mammass, Eds. Cham: Springer International Publishing, 2014, p. 247–256.

[83] H. Deborah, S. George, J. Y. Hardeberg, J. S. Ferrer, and I. C. A. Sandu, "Old Man in Warnemunde (1907) colouring palette: A case study on the use of hyperspectral imaging for pigment identification," *Color and Imaging Conference*, vol. 25, no. 1, p. 339–344, Sep 2017.

[84] C. Cucci, J. K. Delaney, and M. Picollo, "Reflectance hyperspectral imaging for investigation of works of art: Old master paintings and illuminated manuscripts," *Accounts of Chemical Research*, vol. 49, no. 10, p. 2070–2079, Oct 2016.

[85] I. **Ciortan**, H. Deborah, S. George, and J. Y. Hardeberg, "Color and hyperspectral image segmentation for historical documents," in *Digital Heritage, 2015*, vol. 1. IEEE, 2015, p. 199–206.

[86] G. Trumpy, J. Y. Hardeberg, S. George, B. Flueckiger, B. Cattaneo, M. Picollo, F. Cherubini, and V. Marchiafava, "Multispectral capture of film colors with led," in *Colour photography and film : sharing knowledge of analysis, preservation, conservation, migration of analogue and digital materials*. Gruppo del Colore–Associazione Italiana Colore, March 2021, pp. 195–198.

[87] A. Babini, S. George, T. Lombardo, and J. Y. Hardeberg, "A portable set up for hyperspectral imaging of stained-glass panels," in *The Future of Heritage Science and Technologies: ICT and Digital Heritage: Third International Conference, Florence Heri-Tech 2022, Florence, Italy, May 16–18, 2022, Proceedings*. Springer, 2022, pp. 57–70.

[88] L. B. Pereira, "UV Fluorescence photography of works of art: replacing the traditional UV cut filters with interference filters," *International Journal of Conservation Science*, vol. 1, no. 3, pp. 161–166, 2010.

[89] O. Wang, P. Gunawardane, S. Scher, and J. Davis, "Material classification using BRDF slices," in *2009 IEEE Conference on Computer Vision and Pattern Recognition*. IEEE, 2009, pp. 2805–2811.

[90] R. Pintus, M. Ahsan, F. Marton, and E. Gobbetti, "Exploiting Neighboring Pixels Similarity for Effective SV-BRDF Reconstruction from Sparse MLICs," in *Eurographics Workshop on Graphics and Cultural Heritage*, V. Hulusic and A. Chalmers, Eds. The Eurographics Association, Nov 2021.

[91] I. M. **Ciortan**, R. Pintus, G. Marchioro, C. Daffara, A. Giachetti, and E. Gobbetti, "A Practical Reflectance Transformation Imaging Pipeline for Surface Characterization in Cultural Heritage," in *Eurographics Workshop on Graphics and Cultural Heritage*, C. E. Catalano and L. D. Luca, Eds. The Eurographics Association, 2016.

[92] L. Watteeuw, H. Hameeuw, B. Vandermeulen, A. Van der Perre, V. Boschloos, L. Delvaux, M. Proesmans, M. Van Bos, and L. Van Gool, "Light, shadows and surface characteristics: the multispectral Portable Light Dome," *Applied Physics A*, vol. 122, no. 11, p. 976, Oct 2016.

[93] V. Kitanovski and J. Y. Hardeberg, "Objective evaluation of relighting models on translucent materials from multispectral RTI images," *IS&T International Symposium on Electronic Imaging Science and Technology*, 2021.

[94] R. Luxman, Y. E. Castro, H. Chatoux, M. Nurit, A. Siatou, G. Le Goïc, L. Brambilla, C. Degrigny, F. Marzani, and A. Mansouri, "LightBot: A Multi-Light Position Robotic Acquisition System for Adaptive Capturing of Cultural Heritage Surfaces," *Journal of Imaging*, vol. 8, no. 55, p. 134, May 2022.

[95] Y. Castro, A. Siatou, M. Rossé, H. Chatoux, R. Luxman, G. Le Goïc, and A. Mansouri, "Extended Framework for Multispectral RTI," in *Archiving Conference, Society for Imaging Science and Technology Publisher Location : IS&T 7003 Kilworth Lane, Springfield, VA 22151 USA*, vol. 19, Springfield, United States, 2022, pp. 56 – 61.

[96] T. Hanneken, "The Jubilees Palimpsest Project," accessed 20 February 2023. [Online]. Available: https://jubilees.stmarytx.edu/

[97] T. Hanneken, "Integrating Spectral and Reflectance Transformation Imaging Technologies for the Digitization of Manuscripts and Other Cultural Artifacts," *National Endowment for the Humanities*, 2014, White Paper.

[98] S. E. Newman, "Applications of reflectance transformation imaging (RTI) to the study of bone surface modifications," *Journal of Archaeological Science*, vol. 53, p. 536–549, 2015.

[99] G. Palma, M. Baldassarri, M. C. Favilla, and R. Scopigno, "Storytelling of a coin collection by means of RTI images: The case of the Simoneschi collection in Palazzo Blu," in *Museums and the Web*, 2014.

[100] M. Mudge, T. Malzbender, C. Schroer, and M. Lum, "New Reflection Transformation Imaging Methods for Rock Art and Multiple-Viewpoint Display." in *VAST*, vol. 6. Citeseer, 2006, p. 195–202.

[101] M. Díaz-Guardamino, L. G. Sanjuán, D. Wheatley, and V. R. Zamora, "RTI and the study of engraved rock art: A re-examination of the Iberian south-western stelae of Setefilla and Almadén de la Plata 2 (Seville, Spain)," *Digital Applications in Archaeology and Cultural Heritage*, vol. 2, no. 2–3, p. 41–54, 2015.

[102] CDLI contributors, "Yale Babylonian Collection, New Haven, Connecticut, USA - Collections," accessed 24 March 2023. [Online]. Available: https://cdli.mpiwg-berlin.mpg.de/collections/6

[103] A. Cosentino, C. Koch Dandolo, A. Cristaudo, and P. Uhd Jepsen, "Diagnostics pre and post conservation on a 14th century gilded icon from Taormina, Sicily," *E-conserv. J.*, vol. 3, pp. 1–7, 2015.

[104] B. Vandermeulen, H. Hameeuw, L. Watteeuw, L. Van Gool, and M. Proesmans, "Bridging Multi-light & Multi-Spectral images to study, preserve and disseminate archival documents," in *Archiving Conference*, vol. 2018. Society for Imaging Science and Technology, 2018, p. 64–69.

[105] T. G. Dulecha, A. Giachetti, R. Pintus, I. **Ciortan**, A. J. Villanueva, and E. Gobbetti, "Crack Detection in Single- and Multi-Light Images of Painted Surfaces using Convolutional Neural Networks," in *Eurographics Workshop on Graphics and Cultural Heritage*, S. Rizvic and K. Rodriguez Echavarria, Eds. The Eurographics Association, 2019.

[106] E. Kotoula *et al.*, "Reflectance transformation imaging beyond the visible: ultraviolet reflected and ultraviolet induced visible fluorescence," in *Proceedings of the 43rd Annual Conference on Computer Applications and Quantitative Methods in Archaeology, Oxford*, 2015, pp. 909–919.

[107] Hoya, "Hoya filters," accessed 20 February 2023. [Online]. Available: https://hoyafilter.com/

[108] Schott, "Schott optical filter glass," accessed 20 February 2023. [Online]. Available: https://www.schott.com/en-id/products/optical-filter-glass

[109] Y. Panagakis, J. Kossaifi, G. G. Chrysos, J. Oldfield, M. A. Nicolaou, A. Anandkumar, and S. Zafeiriou, "Tensor methods in computer vision and deep learning," *Proceedings of the IEEE*, vol. 109, no. 5, p. 863–890, 2021.

[110] E. Acar and B. Yener, "Unsupervised multiway data analysis: A literature survey," *IEEE Transactions on Knowledge and Data Engineering*, vol. 21, no. 1, p. 6–20, Jan 2009.

[111] A. Cichocki, D. Mandic, L. De Lathauwer, G. Zhou, Q. Zhao, C. Caiafa, and H. A. Phan, "Tensor decompositions for signal processing applications: From two-way to multiway component analysis," *IEEE Signal Processing Magazine*, vol. 32, no. 2, p. 145–163, Mar 2015.

[112] N. D. Sidiropoulos, L. De Lathauwer, X. Fu, K. Huang, E. E. Papalexakis, and C. Faloutsos, "Tensor decomposition for signal processing and machine learning," *IEEE Transactions on Signal Processing*, vol. 65, no. 13, p. 3551–3582, Jul 2017.

[113] C. Zhao, M. Wang, N. Su, and S. Feng, "Dictionary Learning Hyperspectral Target Detection Algorithm Based on Tucker Tensor Decomposition," in *IGARSS 2020 - 2020 IEEE International Geoscience and Remote Sensing Symposium*, Sep 2020, p. 1763–1766.

[114] J. Christensen, E. M. Becker, and C. S. Frederiksen, "Fluorescence spectroscopy and PARAFAC in the analysis of yogurt," *Chemometrics and Intelligent Laboratory Systems*, vol. 75, no. 2, pp. 201–208, Feb. 2005.

[115] R. A. Harshman, "Foundations of the PARAFAC procedure: Models and conditions for an "explanatory" multi-modal factor analysis," *UCLA Working Papers in Phonetics*, vol. 16, pp. 1–84, 1970.

[116] H. Hotelling, "Analysis of a complex of statistical variables into principal components." *Journal of educational psychology*, vol. 24, no. 6, p. 417, 1933.

[117] R. Bro, "Multi-way analysis in the food industry," Ph.D. dissertation, University of Amsterdam, 1998.

[118] T. G. Kolda and B. W. Bader, "Tensor decompositions and applications," *SIAM Review*, vol. 51, no. 3, p. 455–500, Aug 2009.

[119] F. Yates, "The analysis of replicated experiments when the field results are incomplete," *Empire Journal of Experimental Agriculture*, vol. 1, no. 2, pp. 129–142, 1933.

[120] I. Goodfellow, J. Pouget-Abadie, M. Mirza, B. Xu, D. Warde-Farley, S. Ozair, A. Courville, and Y. Bengio, "Generative Adversarial Nets," in *Advances in Neural Information Processing Systems*, vol. 27. Curran Associates, Inc., 2014.

[121] D. P. Kingma, M. Welling *et al.*, "An introduction to variational autoencoders," *Foundations and Trends® in Machine Learning*, vol. 12, no. 4, pp. 307–392, 2019.

[122] M. Wang, Y. Panagakis, P. Snape, and S. P. Zafeiriou, "Disentangling the modes of variation in unlabelled data," *IEEE Transactions on Pattern Analysis and Machine Intelligence*, vol. 40, no. 11, p. 2682–2695, Nov 2018.

[123] R. J. Woodham, "Photometric stereo: A reflectance map technique for determining surface orientation from image intensity," in *Image Understanding Systems and Industrial Applications I*, vol. 155. International Society for Optics and Photonics, 1979, pp. 136–143.

[124] T. Malzbender, D. Gelb, and H. Wolters, "Polynomial texture maps," in *Proceedings of the 28th annual conference on Computer graphics and interactive techniques*, 2001, pp. 519–528.

[125] M. S. Drew, Y. Hel-Or, T. Malzbender, and N. Hajari, "Robust estimation of surface properties and interpolation of shadow/specularity components," *Image and Vision Computing*, vol. 30, no. 4-5, pp. 317–331, 2012.

[126] R. Pintus, A. Giachetti, G. Pintore, and E. Gobbetti, "Guided Robust Matte-Model Fitting for Accelerating Multi-light Reflectance Processing Techniques," *British Machine Vision Conference 2017*, Sep 2017.

[127] L. Wu, A. Ganesh, B. Shi, Y. Matsushita, Y. Wang, and Y. Ma, "Robust photometric stereo via low-rank matrix completion and recovery," in *Asian Conference on Computer Vision*. Springer, 2010, p. 703–717.

[128] S. Ikehata, D. Wipf, Y. Matsushita, and K. Aizawa, "Photometric Stereo Using Sparse Bayesian Regression for General Diffuse Surfaces," *IEEE Transactions on Pattern Analysis and Machine Intelligence*, vol. 36, no. 9, p. 1816–1831, Sep 2014.

[129] P. Gautron, J. Kivánek, S. N. Pattanaik, and K. Bouatouch, "A Novel Hemispherical Basis for Accurate and Efficient Rendering." *Rendering Techniques*, p. 321–330, 2004.

[130] G. Pitard, G. Le Goïc, H. Favrelière, S. Samper, S.-F. Desage, and M. Pillet, "Discrete Modal Decomposition for surface appearance modelling and rendering," in *Optical Measurement Systems for Industrial Inspection IX*, vol. 9525. International Society for Optics and Photonics, 2015, p. 952523.

[131] A. Giachetti, I. M. **Ciortan**, C. Daffara, R. Pintus, and E. Gobbetti, "Multispectral RTI Analysis of Heterogeneous Artworks," in *Eurographics Workshop on Graphics and Cultural Heritage*, T. Schreck, T. Weyrich, R. Sablatnig, and B. Stular, Eds. The Eurographics Association, 2017.

[132] H. Santo, M. Samejima, Y. Sugano, B. Shi, and Y. Matsushita, "Deep Photometric Stereo Network," in *Proceedings of the IEEE International Conference on Computer Vision (ICCV) Workshops*, Oct 2017.

[133] Z. Xu, K. Sunkavalli, S. Hadap, and R. Ramamoorthi, "Deep image-based relighting from optimal sparse samples," *ACM Transactions on Graphics (ToG)*, vol. 37, no. 4, pp. 1–13, 2018.

[134] T. Dulecha, "Surface analysis from Multi Light Image Collections," Ph.D. dissertation, University of Verona, Jun 2021.

[135] R. Pintus, T. G. Dulecha, I. **Ciortan**, E. Gobbetti, and A. Giachetti, "State-of-the-art in multi-light image collections for surface visualization and analysis," *Computer Graphics Forum*, vol. 38, no. 3, p. 909–934, 2019.

[136] H. R. Morris, ""Virtual Fading" of Art Objects: Simulating the Future Fading of Artifacts by Visualizing Micro-Fading Test Results," *Journal of the American Institute for Conservation*, vol. 46, no. 3, p. 215–228, 2007.

[137] R. S. Berns, S. Byrns, F. Casadio, I. Fiedler, C. Gallagher, F. H. Imai, A. Newman, and L. A. Taplin, "Rejuvenating the color palette of Georges Seurat's A Sunday on La Grande Jatte—1884: A simulation," *Color Research & Application*, vol. 31, no. 4, p. 278–293, 2006.

[138] J. E. Fieberg, P. Knutås, K. Hostettler, and G. D. Smith, ""Paintings fade like flowers": pigment analysis and digital reconstruction of a faded pink lake pigment in Vincent van Gogh's *Undergrowth with Two Figures*," *Applied Spectroscopy*, vol. 71, no. 5, p. 794–808, 2017.

[139] G. E. Box, G. M. Jenkins, and G. Reinsel, "Time series analysis: forecasting and control," *Holden Day, San Franciso*, 1970.

[140] B. G. Tabachnick and L. S. Fidell, *Using multivariate statistics*. Pearson Boston, MA, 2018, vol. 7.

[141] W. A. Fuller, "Introduction to statistical time series," *John Wiley, New York*, 1976.

[142] C. F. Baum and R. Sperling, "Tests for stationarity of a time series: Update," *Stata Technical Bulletin*, vol. 58, pp. 35–36, 2000.

[143] S. R. Eliason, *Maximum likelihood estimation: Logic and practice*. Sage, 1993, no. 96.

[144] M. L. Bagshaw, *Univariate and multivariate ARIMA versus vector autoregression forecasting*. Federal Reserve Bank of Cleveland, 1987, Working Paper No. 87-06.

[145] J. K. Sethi and M. Mittal, "Analysis of air quality using univariate and multivariate time series models," in *2020 10th International Conference on Cloud Computing, Data Science & Engineering (Confluence)*. IEEE, 2020, p. 823–827.

[146] van Noord, Nanne, "Learning visual representations of style," Ph.D. dissertation, Tilburg University, 2018, publication Title: TiCC Ph.D. Series Volume: 60.

[147] C. Brandi, *Teoria del restauro*. Ed. di Storia e Letteratura, 1963.

[148] C. Brandi, *Theory of Restoration*. Istituto centrale per il restauro, 2005.

[149] N. P. Stanley Price, M. K. Talley, A. Melucco Vaccaro, and G. C. Institute, *Historical and philosophical issues in the conservation of cultural heritage*, ser. Readings in conservation. Los Angeles, Calif: Getty Conservation Institute, 1996.

[150] G. W. R. Ward, *The Grove Encyclopedia of Materials and Techniques in Art*. Oxford University Press, 2008.

[151] U. Baldini, *Teoria del restauro e unità di metodologia*. Nardini Florence, 1978, vol. 1.

[152] U. Schädler-Saub, "Dealing with authenticity in the conservation and restoration of wall paintings and architectural surfaces," *Ochrona Dziedzictwa Kulturowego*, vol. Nr 8, 2019.

[153] E. Bouyer, "The bad reputation of neutral retouching," *Croatia 4^{th} International Meeting on Retouching of Cultural Heritage, RECH 4*, Jan 2018.

[154] V. Cappellini, M. Barni, M. Corsini, A. De Rosa, and A. Piva, "ArtShop: an art-oriented image-processing tool for cultural heritage applications," *The Journal of Visualization and Computer Animation*, vol. 14, no. 3, p. 149–158, 2003.

[155] L. Grementieri and E. Provenzi, "Selection of achromatic and non-neutral colors to fill lacunae in frescoes guided by a variational model of perceived contrast," in *Eighth International Conference on Graphic and Image Processing (ICGIP 2016)*, vol. 10225. SPIE, 2017, p. 398–402.

[156] S. Staniforth, "Retouching and Colour Matching: The Restorer and Metamerism," *Studies in Conservation*, vol. 30, no. 3, p. 101–111, 1985.

[157] R. S. Berns, J. Krueger, and M. Swicklik, "Multiple Pigment Selection for Inpainting Using Visible Reflectance Spectrophotometry," *Studies in Conservation*, vol. 47, no. 1, p. 46–61, 2002.

[158] R. S. Berns, M. Mohammadi, M. Nezamabadi, and L. A. Taplin, "A retouching palette that minimizes metamerism," in *Proc. Of The 14th Triennal ICOM-CC meeting*, 2005.

[159] H. Wei and W. Shuwen, "Dunhuang murals inpainting based on image decomposition," in *2010 3rd International Conference on Computer Science and Information Technology*, vol. 2, Jul 2010, p. 397–400.

[160] M. Bertalmio, G. Sapiro, V. Caselles, and C. Ballester, "Image inpainting," in *Proceedings of the 27th annual conference on Computer graphics and interactive techniques*. ACM Press/Addison-Wesley Publishing Co., 2000, p. 417–424.

[161] L. Calatroni, M. d'Autume, R. Hocking, S. Panayotova, S. Parisotto, P. Ricciardi, and C.-B. Schönlieb, "Unveiling the invisible: mathematical methods for restoring and interpreting illuminated manuscripts," *Heritage Science*, vol. 6, no. 1, p. 56, Sep 2018.

[162] P. Zhou, M. Hou, S. Lv, X. Zhao, and W. Wu, "Virtual Restoration of Stained Chinese Paintings Using Patch-Based Color Constrained Poisson Editing with Selected Hyperspectral Feature Bands," *Remote Sensing*, vol. 11, no. 11, p. 1384, 2019.

[163] C. Ballester, A. Bugeau, S. Hurault, S. Parisotto, and P. Vitoria, *An Analysis of Generative Methods for Multiple Image Inpainting*. Cham: Springer International Publishing, 2023, p. 773–820.

[164] H.-L. Wang, P.-H. Han, Y.-M. Chen, K.-W. Chen, X. Lin, M.-S. Lee, and Y.-P. Hung, "Dunhuang mural restoration using deep learning," in *SIGGRAPH Asia 2018 Technical Briefs*, ser. SA '18. Tokyo, Japan: Association for Computing Machinery, Dec 2018, p. 1–4.

[165] T. Yu, S. Zhang, C. Lin, and S. You, "Dunhuang Grotto Painting Dataset and Benchmark," *arXiv preprint arXiv:1907.04589*, 2019.

[166] A. Giachetti, I. M. **Ciortan**, C. Daffara, G. Marchioro, R. Pintus, and E. Gobbetti, "A novel framework for highlight reflectance transformation imaging," *Computer Vision and Image Understanding*, vol. 168, p. 118–131, 2018.

[167] R. Zhang, P. Isola, and A. A. Efros, "Colorful Image Colorization," in *Computer Vision – ECCV 2016*, ser. Lecture Notes in Computer Science, B. Leibe, J. Matas, N. Sebe, and M. Welling, Eds. Cham: Springer International Publishing, 2016, pp. 649–666.

[168] Z. Wang, A. C. Bovik, H. R. Sheikh, and E. P. Simoncelli, "Image quality assessment: from error visibility to structural similarity," *IEEE transactions on image processing*, vol. 13, no. 4, pp. 600–612, 2004.

[169] K. Nazeri, E. Ng, T. Joseph, F. Qureshi, and M. Ebrahimi, "EdgeConnect: Structure guided image inpainting using edge prediction," in *Proceedings of the IEEE/CVF International Conference on Computer Vision Workshops*, 2019.

[170] Laura's blog, "I do not crush the world's corolla of wonder," October 2010, accessed 20 February 2023. [Online]. Available: http://brinduc.blogspot.com/2010/10/i-do-not-crush-worlds-corolla-of-wonder.html

[171] UV Innovations™, "Ultraviolet Photography Color Standards for Visible Fluorescence," accessed 20 February 2023. [Online]. Available: https://www.uvinnovations.com/target-uv

[172] R. Pintus, T. Dulecha, A. Jaspe, A. Giachetti, I. **Ciortan**, and E. Gobbetti, "Objective and Subjective Evaluation of Virtual Relighting from Reflectance Transformation Imaging Data," in *Eurographics Workshop on Graphics and Cultural Heritage*, R. Sablatnig and M. Wimmer, Eds. The Eurographics Association, 2018.

[173] Open AI, "DALL·E 2," 2022, accessed 20 February 2023. [Online]. Available: https://openai.com/product/dall-e-2

[174] Midjourney, Inc., 2022, accessed 20 February 2023. [Online]. Available: https://www.midjourney.com/home/

[175] CompVis group LMU Munich, Runway, "Stability AI," 2023, accessed 20 February 2023. [Online]. Available: https://stability.ai/blog/stable-diffusion-public-release

[176] V. van Gogh, "Letter from Vincent van Gogh to Theo van Gogh, 16 October," 1888, accessed 24 March 2023. [Online]. Available: https://www.webexhibits.org/vangogh/letter/18/554.htm

[177] V. van Gogh, "Letter from Vincent van Gogh to Theo van Gogh, 28 September," 1888, accessed 24 March 2023. [Online]. Available: https://www.webexhibits.org/vangogh/letter/18/543.htm

[178] Z. Stańska, "The Mysterious Street from Edvard Munch's The Scream," Dec 2022. [Online]. Available: https://www.dailyartmagazine.com/the-mysterious-road-of-the-scream-by-edvard-munch/

[179] A. Gopnik, "What Can A.I. Art Teach Us About the Real Thing?" *The New Yorker*, Mar 2023, accessed 20 February 2023. [Online]. Available: https://www.newyorker.com/culture/cultural-comment/what-can-ai-art-teach-us-about-the-real-thing

[180] M. Ruskov, "Grimm in Wonderland: Prompt Engineering with Midjourney to Illustrate Fairytales," in *CEUR Workshop Proceedings*, vol. 3365, Bari, Italy, Feb 2023.

[181] S. Wang, C. Saharia, C. Montgomery, J. Pont-Tuset, S. Noy, S. Pellegrini, Y. Onoe, S. Laszlo, D. J. Fleet, R. Soricut *et al.*, "Imagen editor and editbench: Advancing and evaluating text-guided image inpainting," in *Proceedings of the IEEE/CVF Conference on Computer Vision and Pattern Recognition*, 2023, pp. 18 359–18 369.

Part II

Original Articles

Paper 1 - Artworks in the spotlight: Characterization with a multispectral LED dome

PAPER • **OPEN ACCESS**

Artworks in the spotlight: characterization with a multispectral LED dome

To cite this article: M Ciortan Irina *et al* 2018 *IOP Conf. Ser.: Mater. Sci. Eng.* **364** 012025

IOP Conf. Series: Materials Science and Engineering **364** (2018) 012025 doi:10.1088/1757-899X/364/1/012025

Artworks in the spotlight: characterization with a multispectral LED dome

M Ciortan Irina [1], G Dulecha Tinsae [1], Giachetti Andrea [1], Pintus Ruggero [2], Jaspe-Villanueva Alberto [2] and Gobbetti Enrico [2]

[1]University of Verona, Italy [2] Center for Research and Development, Sardinia, Italy

E-mail: irinamihaela.ciortan@univr.it

Abstract. We describe the design and realization of a novel multispectral light dome system and the associated software control and calibration tools used to process the acquired data, in a specialized pipeline geared towards the analysis of shape and appearance properties of cultural heritage items. The current prototype dome, built using easily available electronic and lighting components, can illuminate a target of size 20cm x 20cm from 52 directions uniformly distributed in a hemisphere. From each illumination direction, 3 LED lights cover the visible range of the electromagnetic spectrum, as well as long ultraviolet and near infrared. A dedicated control system implemented on Arduino boards connected to a controlling PC fully manages all lighting and a camera to support automated acquisition. The controlling software also allows real-time adjustment of the LED settings, and provides a live-view of the to-be-captured scene. We approach per-pixel light calibration by placing dedicated targets in the focal plane: four black reflective spheres for back-tracing the position of the LED lamps and a planar full-frame white paper to correct for the non-uniformity of radiance. Once the light calibration is safeguarded, the multispectral acquisition of an artwork can be completed in a matter of minutes, resulting in a spot-wise appearance profile, that stores at pixel level the per-frequency intensity value together with the light direction vector. By performing calibrated acquisition of multispectral Reflectance Transformation Imaging (RTI), with our analysis system it is possible to recover surface normals, to characterize matte and specular behavior of materials, and to explore different surface layers thanks to UV-VIS-IR LED light separation. To demonstrate the system features we present the outcomes of the on-site capture of metallic artwork at the National Archaeological Museum of Cagliari, Sardinia.

1. Introduction

Reflectance transformation imaging (RTI) is widely used in the Cultural Heritage field, first and foremost for documentation purposes [1], as well as for enhancing visibility of details with small relief [2] and for the extrusion of the three-dimensionality of the real-word object. The technique is based on capturing multiple images of an object from a fixed viewpoint under different directional illumination.

The acquisition setup can be quite simple, with a camera on a tripod and a hand-held torch that is freely moved around the scene, recovering the illumination direction from highlights on a spherical target (H-RTI). This method is cheap and flexible, but makes light calibration hard and requires careful manual procedures. The counterpart of H-RTI is the dome-based system with higher stability and precision, being based on fixed lights equally sampled in the shape of a hemisphere. Dome solutions are, however, expensive and not too practical to be used for

on-site acquisitions. In this paper we describe the design of a novel dome solution using low cost hardware and a reasonably portability making it suitable for both lab and on-site acquisitions. We describe our hardware and software choices, comparing them with prior work. We finally demonstrate the suitability of our system for Cultural Heritage applications, by showcasing an on-site acquisition carried out at the National Archeology Museum of Cagliari, Sardinia.

2. Related work

Several dome solutions have been introduced so far, with different cost requirements, dimensions and running environments [3, 4]. Schwartz et al. [5] presented a complex hardware design and the corresponding calibration and processing procedures for the "brute-force" sampling of a 6D approximation of Bidirectional Texture Functions (BTFs). In addition, their setup is capable of robustly and precisely reconstructing the mesoscopic material geometry, e.g. displacement maps, as well as capturing shape and reflectance of complete 3D objects. The system includes industrial digital video cameras, a rotation stage, LED lamps and projectors. The drawbacks of this arrangement are the high cost and high difficulty of handling outside the lab environment, as well as the need of complex calibration procedure due to many different hardware components. Hameeuw [4] proposed a portable solution extremely easy to use. It is almost a one-click solution that can provide a straightforward RTI acquisition pipeline. The dome is equipped with a 5 million pixel camera or a 29 million monochromatic sensor; it mounts 260 white LED light sources around a 80cm diameter dome. The main design purpose is to make it easy to assemble/disassemble the dome in less than half an hour. This requirement makes it operable both in museum collections or other in-situ scenarios. Recently, other domes have been presented that use both visible and invisible light wavelengths. One example is the Microdome with multispectral RTI capability presented by the RICH team [6]. It is equipped with 228 different LED light sources. Those LEDs are divided in five different spectra: ultraviolet (365 nm), blue (460 nm), red (523 nm), green (623 nm), and infrared (850 nm). A 28 megapixel monochromatic sensor is mounted on top of the dome.

In order to convert the raw image stack into shape and reflectance parameters or high quality relighted images, the calibration of light direction and intensity is required. Over the last decades a lot of methods have been published that deal with different kinds of acquisition setup, and several, non-ideal types of illuminants[7, 8, 9, 10]. Calibration should provide images and metadata suitable for the use with RTI processing/relighting pipeline.

In our work we propose an integrated dome solution coupled with our light calibration and processing software ([11]) able to recover reflectance parameters, relighted images and 3D models and we demonstrate its usefulness in CH applications.

3. Our system

Our dome (Figure 2) features 156 multi-spectral LEDs evenly distributed across 52 light positions over a 60cm diameter hemisphere. All the light sources have a wide aperture in order to stretch the homogeneity of the light intensity as much as possible. The light sources cover 5 bands (see Figure 1): two narrow in the ultraviolet (centered at 395nm) and infrared (centered at 850nm) regions and one broad in the visible to collect the RGB signals of the Nikon D810 DSLR camera with the infrared cut-off filter removed.

The camera is mounted on top of the hemisphere. The dome design has been thought in order to allow for its use in a fixed setup in an arbitrary orientation. This is achieved by integrating all the hardware components to the fixed dome structure, including the camera, as presented in Figure 3. It is possible to scan the objects horizontally, lying on a table by directly placing the dome on top of the acquisition surface (the most common setup for laboratory experiments or even on-site acquisitions, given that the cultural heritage objects allow to be moved) or

vertically, on a wall by mounting it on a tripod or other similar mounting accessory (appropriate for immutable objects, such as paintings, frescoes, etc.).

The control unit consists of some control boards (Arduino Mega 2560) and three constant voltage constant current programmable control supply power modules (DP20V2A). The boards drive the switch (on/off) of the single LEDs in the dome, while the power modules are used to tune the intensity of the three sets of LEDs (i.e., UV-VIS-IR). The Arduino boards are interconnected and can communicate with an external PC via USB cable using a serial protocol. This protocol allows a PC program to select and turn on one LED at a time; it is mandatory to wait until a LED is off before sending other commands.

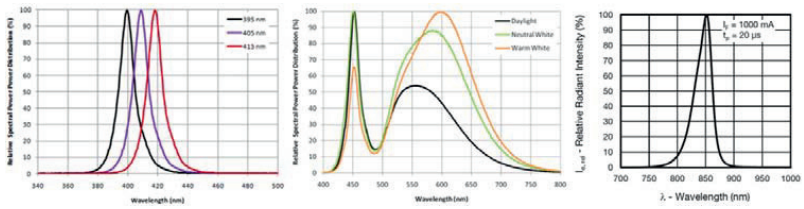

Figure 1. Spectral distribution of the LED spotlights in ultraviolet, visible and near infrared.

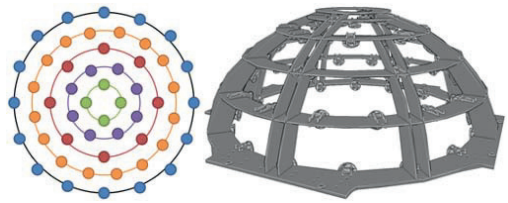

Figure 2. Light position distribution of the dome device.

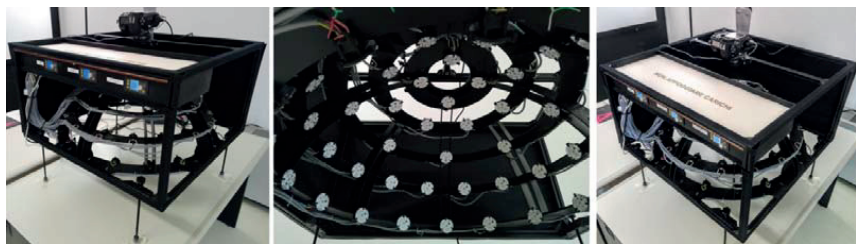

Figure 3. Several snapshots of the dome device.

3.1. Acquisition control software

An user friendly interface has been developed to control the image stack acquisition. The interface enables the easy control of both dome lights (sending commands to the Arduino according to the defined protocol) and of the digital camera by using a software library [12] with access to the camera settings. The GUI allows selection of predefined lights switch and synchronized camera

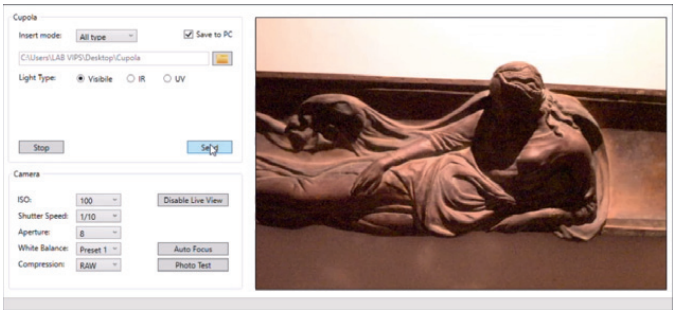

Figure 4. The graphical user interface of the dome system transmitting the live-view of a captured artwork, together with the camera settings.

capture sequences, or individual switches (Figure 4). The user can view in real-time the change of lights and the illuminated object during the acquisition thanks to the live-view window. The live-view feature is useful as well to visually check the image quality when adjusting the camera settings (ISO, shutter speed, aperture, white balance, image format and focus). The camera settings are optimally configured so as to capture sharp images of the object's surface.

3.2. Light calibration

The dome calibration method use methods and algorithms presented in [11], specifically adapted in order to obtain a preliminary estimation of per pixel light direction and reference illumination in the acquisition region that is then used to correct the image stack acquired during the actual object capture. This procedure consists in capturing two calibration targets at the same focal distance used for the object capture: the first includes four glossy spheres at the corners, and the second is a white Lambertian surface placed perpendicularly to the camera axis (Figure 5).

The image stack obtained capturing the first target is used to estimate per pixel interpolated light direction from the position of highlights on the spheres, as shown in [11]. The second image stack is used at the time of object image processing to correct original images with an intensity correction factors proportional to the measured illumination on the white target.

All these calibration procedures can be easily realized with a custom software tool (RTITool) freely available at *https://github.com/giach68/RTITool*. The tool allows semi-automatic sphere annotation and light direction estimate (Figure 6 (a)) as well as the intensity correction of the object images based on the reference images of the target (Figure 6 (b)). The tool features also

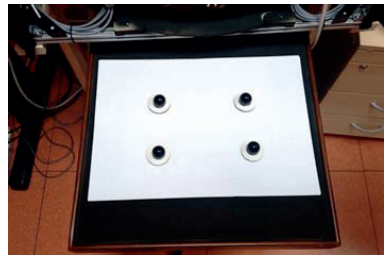

Figure 5. Target with reflective spheres being placed in the acquisition region for light direction calibration.

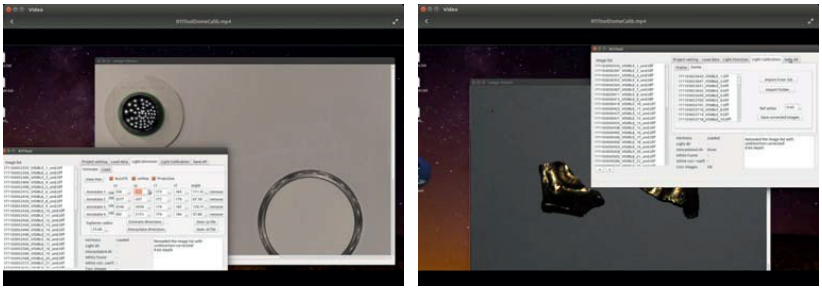

(a) (b)

Figure 6. Calibration software (RTItool) options for the dome system. (a) light direction estimation tab with the annotations of the four black reflective spheres; (b) intensity correction based on the loaded images of the white frame target.

several options for image preprocessing (e.g.undistortion) and on the fly calibration of RTI stacks based on targets directly added to the imaged scene (white frame and spheres).

The light calibration procedures and the interpolated light direction estimation proved to be effective in improving the accuracy of quantitative parameters that can be derived from the image stacks, e.g. normals and albedo [13].

4. Case Study

The dome has been tested on different artworks (paintings, bas-reliefs, coins). In this paper we present a particularly interesting case study related to an onsite acquisition of a metallic artwork at the National Archaeology Museum in Cagliari, Sardinia, Italy. The digitized object is an ancient gold lamina with historical inscriptions. Named "Lamina del Sulcis", it consists of two fragments of an inscription engraved on thin gold leaf "lamina" (a thin plaque or panel intended to be affixed to some other surface), that was found in the earliest stratum of the Sulcis tophet or infant cremation cemetery (West Sardinia). Only 1.4 cm x 1.5 cm x 0.05 cm in size, the whole lamina is thought to have once been attached to an iron object that has partially damaged its surface. The text has been dated to the 8th-7th centuries BCE on the basis of its paleographic features [14]. This makes the object extremely important for the Mediterranean archaeology [15].

In Figure 7 we show the acquisition setup. Before capturing the object images, the calibration procedure with the sphere target and the white target has been performed as described in Section 3. In the object acquisition setup, reflective spheres have been placed as well in order to allow a potential direct calibration from the acquired images. Different acquisition have been performed using different resolutions.

The RTI processing pipeline described in [11] has been used to extract albedo and normals of the lamina's surface, as shown in Figure 9.

Particularly valuable for the analysis of paintings, multispectral signal is also of great importance for metallic objects, and can increase the amount of information provided for a particular artwork. Looking at albedo and normal maps obtained with the three different lights it is possible to see that they capture slightly different information.

From the reflectance properties of the object it is possible to obtain useful information about it, in this case, for example, reading inscriptions. In [11] we have shown that measures like the Outlier Direction map (Figure 10), counting the number of incoming light directions causing non Lambertian reflection in the target object can reveal surface details. Estimating this map from

Figure 7. The acquisition setup: the dome is placed in order to have the object near the center of its sphere with its flatter part perpendicular to the camera axis.

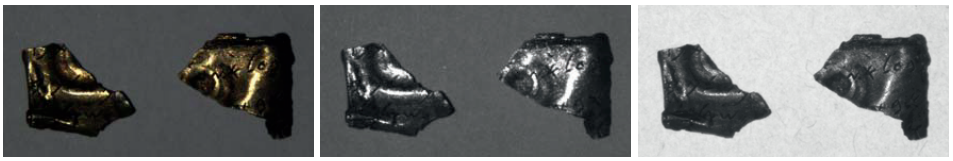

(a) (b) (c)

Figure 8. Example captured images with the different ligths. (a) visible. (b) IR. (c) UV.

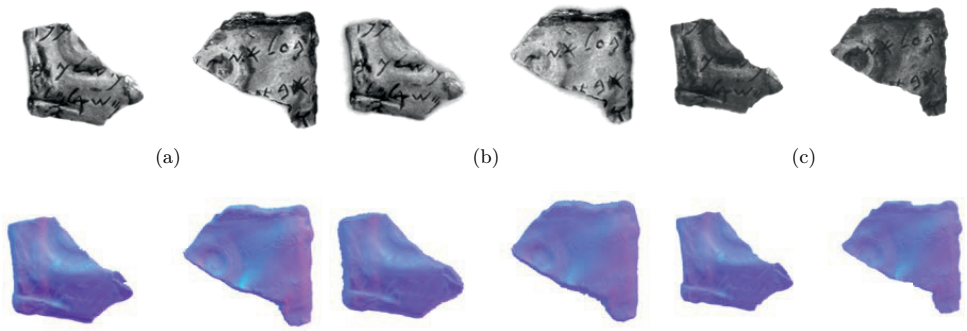

(a) (b) (c)

(d) (e) (f)

Figure 9. Albedo and normals of the lamina, estimated with Photometric Stereo on Visible (a,d), IR (b,d) and UV (c,f) images.

PS fitting and mosaicking (manually) image patches in order to obtain an approximate object reconstruction it is possible to visualize the enhanced inscription as shown in Figure 10. It is possible to see that the map obtained with the IR images better enhances the characters, possibly due to the different shape of the specular highlight in the IR frequency reflectance function.

By relighting the image and simulating the appearance of the object from a virtual light direction, an enhanced visualization of the inscriptions is obtained (see Figure 11). In this case we performed relighting with Radial Basis Function interpolation as shown in [16], allowing a

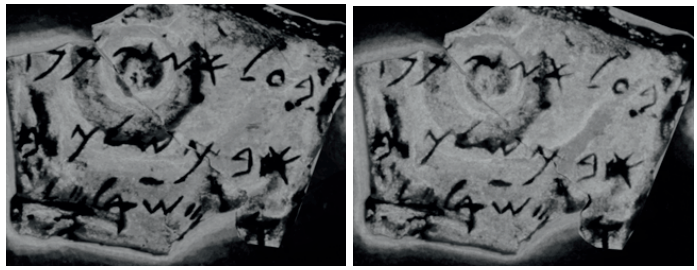

(a) (b)

Figure 10. Outlier Directions maps enhancing local specularity of the surface can enhance useful detail. In this case the IR-based enhancement results in more readable characters.

good representation of the specular component of the reflectance.

Moreover, the recovery of the normals allows for a 3D reconstruction that further on leads to the identification of matching points between the two fragments of the lamina. The shape of the object has been obtained by integrating the input normal vector field. A mask identifies the object within the normal map images (Figure 9). Two types of integral have been performed. The first is a one-dimensional integral along the object/mask contour. Since the integral is defined up to a constant, a random point on the contour is chosen to have depth equal to zero. The boundary condition of the linear integral is the depth value of this point, which is the first and last point on the integration curve. Then a surface integral is computed, using the depth of the contour as the boundary condition. In both cases, an approximation of the second derivatives of the surface is employed to build a sparse Poisson based linear system, and it has been solved through a multidimensional Conjugate Gradient method. Figure 12 shows the re-attachment of the two parts into a whole piece, based on the corresponding points with highest matching probability.

5. Conclusion

The dome system presented in this paper is a flexible and reliable solution that can be extremely useful for the digitization of various types of artworks and underlying materials. By our multiple acquisition experiments both in laboratory and on-site, we have proved that our system is highly portable and this is thanks to the integrated hardware components that can be controlled by a single tool. Apart from the all-in-one controlling software, we have showed how the image stack delivered by the dome is easily compatible with image calibration and visualization tools developed in previous work for different RTI setups, by adding only minor tweaks. Above all, we

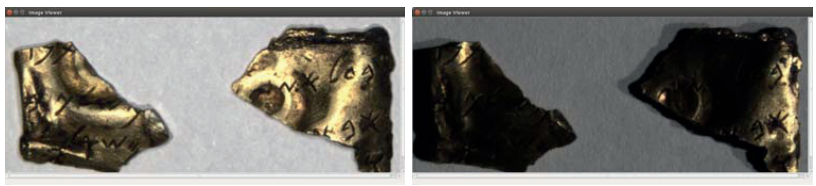

(a) (b)

Figure 11. Lamina images relighted from top center position (lx, ly) = (0,0) and with raking light from right (lx, ly) = (0,0.85) using Radial Basis Function interpolaton.

Figure 12. Shaded (left) and textured (right) rendering of the 3D model of the lamina obtained with 3D stitching of the two meshes recovered by normal map integration.

have seen that the multispectral dome in combination with reflectance fitting algorithms leads to revealing results for artworks, from detail visibility enhancement to 3D reconstruction and fragment reassembly.

As future work, we intend to enlarge the portfolio of acquisitions with the dome, by testing it on more artworks, with other properties than what was covered so far. At the same time, we are planning to continuously improve the supporting image processing tools, according to new challenges that may arise, and to extract more visual information based on the multi-light image stacks captured by the dome.

Acknowledgments
This work was partially supported by the Scan4Reco project funded by European Union's Horizon 2020 Framework Programme for Research and Innovation under grant agreement no 665091 and by the DSURF project (PRIN 2015) funded by the Italian Ministry of University and Research. We also acknowledge the contribution of Sardinian Regional Authorities. We thank Plumake SRL, Opificio delle Pietre Dure and the National Archaeological Museum of Cagliari for their collaboration.

References
[1] Mudge M, Voutaz J P, Schroer C and Lum M 2005 *VAST* vol 6 pp 29–40
[2] Palma G, Corsini M, Cignoni P, Scopigno R and Mudge M 2010 *Journal on Computing and Cultural Heritage (JOCCH)* **3** 6
[3] CHI 2017 Cultural heritage imaging URL `http://culturalheritageimaging.org`
[4] Hameeuw H 2015 *Bulletin van de Koninklijke Musea voor Kunst en Geschiedenis* **84** 5–48
[5] Schwartz C, Sarlette R, Weinmann M and Klein R 2013 *Material Appearance Modeling* pp 25–31
[6] LEUVEN K *URL: https://portablelightdome. wordpress. com/2015/04/29/rich-presents-the-new-multispectral-microdome* **2**
[7] Powell M W, Sarkar S and Goldgof D 2001 *IEEE Transactions on Pattern Analysis and Machine Intelligence* **23** 1022–1027
[8] Ackermann J, Fuhrmann S and Goesele M 2013 *VMV* pp 161–168
[9] Takai T, Maki A, Niinuma K and Matsuyama T 2009 *Computer Vision and Image Understanding* **113** 966–978
[10] Wong K Y K, Schnieders D and Li S 2008 *European conference on computer vision* (Springer) pp 631–642
[11] Giachetti A, Ciortan I, Daffara C, Marchioro G, Pintus R and Gobbetti E 2017 *Computer Vision and Image Understanding*
[12] Nikon 2017 Sdks for digital imaging products URL `https://sdk.nikonimaging.com/apply/`
[13] Giachetti A, Daffara C, Reghelin C, Gobbetti E and Pintus R 2015 *SPIE Optical Metrology* 95270B–95270B
[14] Barreca F 1965 *OA», IV* **1** 1–5
[15] Dixon H M 2013 *Phoenician Mortuary Practice in the Iron Age I-III (ca. 1200-ca. 300 BCE) Levantine" Homeland"* Ph.D. thesis University of Michigan
[16] Giachetti A, Ciortan I M, Daffara C, Pintus R and Gobbetti E 2017 *Eurographics Workshop on Graphics and Cultural Heritage* ed Schreck T, Weyrich T, Sablatnig R and Stular B (The Eurographics Association) ISBN 978-3-03868-037-6 ISSN 2312-6124

Paper 2 - Fluorescence Transformation Imaging

Fluorescence transformation imaging

Irina-Mihaela Ciortan, Andrea Giachetti, Sony George, Jon Yngve Hardeberg

Irina-Mihaela Ciortan, Andrea Giachetti, Sony George, Jon Yngve Hardeberg, "Fluorescence transformation imaging," Proc. SPIE 11784, Optics for Arts, Architecture, and Archaeology VIII, 1178416 (20 June 2021); doi: 10.1117/12.2593651

SPIE.

Event: SPIE Optical Metrology, 2021, Online Only

Fluorescence Transformation Imaging

Irina-Mihaela Ciortan[a], Andrea Giachetti[b], Sony George[a], and Jon Yngve Hardeberg[a]

[a]Department of Computer Science, NTNU - Norwegian University of Science and Technology, Gjøvik, Norway
[b]Department of Computer Science, University of Verona, Verona, Italy

ABSTRACT

Fluorescent or luminescent materials absorb light at shorter wavelengths and re-emit at longer wavelengths. In terms of appearance, this translates to a increased color vividness, as well as a glowing effect. Thanks to these properties, the study of fluorescent materials is of interest for Cultural Heritage applications, where fluorophores are incorporated in many pigments and varnishes. This paper proposes a variant to Reflectance Transformation Imaging (RTI) technique, namely Fluorescence Transformation Imaging (FTI), that handles luminescent objects. Reflectance Transformation Imaging method outputs a single-camera multi-light image collection of a static scene, which can be used to model the reflectance of the scene as a polynomial of the illumination directions. Similarly, Fluorescence Transformation Imaging aims to model the fluorescent signal based on a series of images with fixed scene and viewpoint and varying incident light directions - what changes with respect to RTI is that fluorescence is recorded instead of reflected radiation. In the literature, there are works that explore the isotropic property of fluorescence in low-dimension multi-light imagery methods (such as Photometric Stereo) to model the appearance of an object with a first-order polynomial. This is based on the assumption that in the fluorescent mode the object gets closer to a Lambertian surface than in the reflective mode where non-Lambertian effects such as highlights are more likely to appear. Nonetheless, this assumption stands for single-object scenes, with uniform albedo and convex geometries. When there are multiple fluorescent objects in the scene, with concavities and non-uniform fluorescent component, then the fluorescence can become secondary light to the object and become a source of interreflections. Through quantitative and qualitative analysis, this paper explores the Reflectance and Fluorescence Transformation Imaging methods and the resulting texture maps towards appearance rendering of heterogeneous non-flat fluorescent objects.

Keywords: Fluorescence, Reflectance Transformation Imaging, Interreflections, Appearance Rendering

1. INTRODUCTION

Fluorescence is a photoluminescence phenomenon where light is absorbed at lower wavelengths and re-emitted at longer wavelengths. For classic artworks, this phenomenon is useful for detecting several resin-based aged varnishes or restorations. At the same time, modern artworks sometimes employ synthetic fluorescent pigments because of their special appearance properties. To name a few of these properties, highly bright and vivid colors that reflect more than the incoming light due to self-luminescence, as well as hidden details that gain visibility when illuminated by specific short-wavelength fluorescence-inducing light installations. For these reasons, fluorescent materials have received a lot of recent attention in the computer graphics and cultural heritage communities.

Nonetheless, fluorescent objects are challenging to measure, model and render. Due to the shift in the excitation-emission wavelengths they need to be measured by a bispectrometer, where for each illumination wavelength, the reflectance and emission response are recorded distinctly for each spectral band. The bispectral nature of fluorescent materials adds another layer of complexity to bidirectional reflectance distribution functions used in computer graphics to model the change in appearance with changing viewing angles and changing illumination angles. For this reason, most of the works make assumptions towards the type of fluorescence

Further author information: (Send correspondence to I.M.C.)
I.M.C..: E-mail: irina-mihaela.ciortan@ntnu.no

Optics for Arts, Architecture, and Archaeology VIII, edited by Haida Liang, Roger Groves, Proc. of SPIE
Vol. 11784, 1178416 · © 2021 SPIE · CCC code: 0277-786X/21/$21 · doi: 10.1117/12.2593651

exhibited by materials (uniform fluorescent composition, not reflecting the same color they fluoresce) to simplify the appearance modelling.

At the same time, Reflectance Transformation Imaging (RTI) has become an established multi-light image technique used for 2.5D reconstruction, appearance modelling and relighting with numerous active applications in the Cultural Heritage community.[1–5] The methods designed under the RTI umbrella have been tested for opaque and diffuse objects, as well as opaque and shiny surfaces. Even though there are a few works on using RTI for the rendering of translucent[6] and fluorescent materials,[7] the literature is still scarce on multi-light imagery of special materials. Moreover, for fluorescent materials, usually a low-dimensionality RTI stack of only 3-4 images has been investigated.[8,9]

This work aims to study the appearance of challenging scenes with fluorescent objects: with a heterogeneous distribution and concentration of fluorescent content; prone to interreflections by being reflective in the same wavelengths they fluoresce and by containing a mix of convex and concave geometries. For the study, single-camera multi-light images are collected with traditional Reflection Transformation Imaging and a proposed Fluorescence Transformation Imaging (FTI) method, and polynomial models are used to recover appearance coefficients.

2. RELATED WORK

Photometric Stereo and Reflectance Transformation Imaging. Photometric stereo was a method first proposed by Woodham et al.[10] for recovering shape from only few images acquired by a static viewpoint of a static object scene illuminated by different light directions. This pioneering work was aimed for Lambertian objects, that are diffuse and flat. The minimally optimal number of images to be acquired was defined as three, so that the linear system of equations composed by three unknowns (a coefficient for each of the x, y, z components of the light directions) can be overdetermined and uniquely solved. The coefficients in this case represent the components of the normal vector.

After photometric stereo was established as an image-based shape recovery technique, other models have been proposed as an improvement by relaxing the Lambertian assumption. In this sense, a groundbreaking work was the formulation of Polynomial Texture Maps (PTM) introduced by Malzbender et al.,[11] which fit a multi-light image collection to a quadratic polynomial, where instead of only the normal vector, 6 coefficients are reconstructed that account for the shape as well as other more complex non-Lambertian appearance phenomena: interreflections, shadow, highlights. Moreover, they coined a new term - Reflectance Transformation Imaging - as a general term for referring to the conversion of multi-light image collections to reflectance to maps that describe a surface appearance. In Drew et al.,[12] a modified second-order polynomial with different terms was proposed as an improvement to the original PTM[11] so that in case a purely Lambertian surface is captured, the three shape-related coefficients can be extracted from the model in a straightforward way without having to apply any non-linear operation to recover one of them, as it's the case with.[11] In addition, many robust methods have been designed to handle irregularities that break the Lambertian rule such as shadows and specularities.[12–14]

Fluorescence-based Photometric Stereo. One of the studies to empirically prove the isotropic property of fluorescence was carried out by Tominaga et al.,[15] where fluorescent samples were measured in a goniometric fashion. Their findings showed that the fluorescence radiance factor was changing with the variation of incident light with a trend very close to a cosine function, while there was little change with the viewing angles. The first works to exploit the Lambertian behaviour of fluorescence in a photometric stereo setup, completed by Treibitz et al.[8] and Sato et al.[9] were developed contemporarily. Both these works have similar findings. More precisely, they show that shape reconstruction from photometric stereo can be improved for fluorescent objects, because the specularities disappear in the fluorescent state making the surface more diffuse. They separate the fluorescent signal from the reflective signal through multispectral imaging. In,[8] a yellow filter is mounted on a trichromatic sensor to extract only the fluorescent signal excited by the blue light, while in,[9] they isolate fluorescence by working only with red and green channels. This assumption that fluorescence appears only in the red and green channels, exploited as well by Fu et al.[16] for developing an interreflection removal technique, is based on the physical properties of fluorescence of absorbing the light at lower wavelengths and re-emitting at higher wavelengths. However, this assumption perfectly stands in case of complete separation between the

sensitivites of the red, green and blue channels of the CCD sensors, while in the real case the trichromatic Bayer filter has broad-brand spread in the electromagnetic space. In addition, another aspect this assumption is that the fluorescence of the object has no overlap between the excitation and emission spectra, which is not true for all objects. The authors in[9] acknowledge this last considerations as limitation of their work. Moreover, they use it as justification for explaining why their method is prone to be less affected by interreflections: in their fluorescent state, materials with little to no overlap between their excitation and emission spectra are less likely to be excited by their own self-emission and thus, there are less mutual illumination effects in the fluorescent state than in the non-fluorescent reflective state. As pointed out by the authors in,[9] this is valid only for simple scenes containing only one objects. However, in more complex scenes with more objects with both concave and convex geometries, fluorescent components can become a second, indirect source of illumination for the scene. Especially if these materials reflect light in the same wavelengths where they fluoresce. Both[9] and[8] have minimized the problem of interreflection by studying simple scenes of materials that don't reflect the color they fluoresce. Under the same assumption, the work of[16] manages to decompose the direct and indirect illumination components from fluorescent images so that it later feeds the photometric stereo reconstruction only the interreflection-free direct light component images. Nonetheless, their approach requires homogeneous only materials.

To the best of our knowledge, Koutula et al.[7] are the only ones to have exploited the angularity of the light to visualize the relief of the fluorescent signal in museum ceramic artifacts. More precisely, Kotoula et al.[7] show the benefits of capturing reflectance transformation imaging in the UV-reflected (UVR) and UV-fluorescent (UVF) ranges for visualizing traces of conservation on two real ceramic vases from a museum. The filters proposed in their setup are off-the-shelf solutions for UV imaging: for the UVR, the UV-transmitter (HOYA 330) and IR barrier filter (SCHOTT BG 38); for the UVF, an UV and IR barrier filters were used (B+W 021). In the UVF RTI mode, traces of conservation, like previous repair of the ceramics become noticeable, because common adhesives are luminescent when lit by the UV light, revealing details otherwise obscure in the visible light. Actually, the authors in[7] argue that UVF RTI is basically an efficient way of recording a good practice of conservators when they visually inspect an artifact with UV light: they position the light around the artifact, at different raking lights and statically inspect the change in the appearance of the object at each distinct position of the light. In this way, UVF RTI becomes a way of documenting this process of dynamic inspection by stacking together all the static frames at each light direction into a single relightable file. In contrast with UVF, the UVR mode highlights the subtle variations in the surface, such as scratches and smudges, as well as traces remains of glaze and salt encrustations. Even though such variations might be revealed as well in the visibile RTI, the contrast is enhanced under UV reflected light and the variations gain clarity. Therefore, the paper of[7] shows effectively how the combined forces of RTI and UV imaging can export visualizations and rendering useful for the analysis of Cultual Heritage objects.

3. MATERIALS AND METHOD

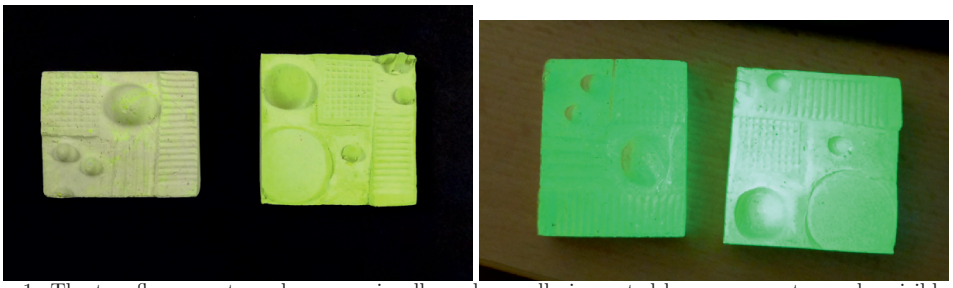

Figure 1: The two fluorescent mockups, as visually and casually inspected by a conservator under visible light and, respectively, ultraviolet light in uncontrolled conditions.

In this paper, we compare normal and appearance maps recovered with four representations of the Photometric Stereo model, based on multi-light image collections of two handmade fluorescent objects, shown in

Fig. 1. The fluorescent objects were designed to have complex convex and concave geometries, a heterogeneous composition and to reflect the same color as they fluoresce. The mockups are made of gesso mould mixed with a commercial UV-induced lime green, fluorescent pigment. One of the mockups has a higher overall concentration of the fluorescent pigment and the mixing was done in several iterations until achieving a more homogeneous material (referred to in the paper as highly fluorescent mockup). The other mockup contains a lower overall concentration of the fluorescent pigment and it is mixed in a rougher way, having a more heterogeneous composition (from now on, referred to in the paper as low fluorescent mockup). The two mockups were acquired with a multispectral light dome system in visible mode and fluorescent mode. Based on the two stack of images for each mode, surface normals and albedo maps are reconstructed using four methods. In the rest of this section, a brief theoretical background for these methods is outlined.

A multi-light image collection can be formalized as a system of linear equations, where on one side we have the intensity values and on the other side we have the polynomial based on the light direction vector. The terms and order of the polynomial depend on the assumptions made with respect to the surface appearance. In the case of classic Photometric Stereo (PS),[10] the assumption is that the material is perfectly Lambertian and the polynomial has a first-order and is modelled as follows:

$$anl = I_k \tag{1}$$

where a represents the albedo, n the normal, l the light direction vector, I the intensity and k the number of images taken at different illumination angle. If we split the light direction into the x, y, z components, and given that the albedo is a constant that can be computed as the norm of the normal vector, eq. 1 becomes:

$$n_{1k}lx + n_{2k}ly + n_{3k}lz = I_k \tag{2}$$

There are 3 unknowns so in order for the system to be determined and reach a unique solution, at 3 equations are needed, given by the capture of 3 intensity images under varying light directions. To ensure accuracy, common practice is to acquire more than 3 images, where the overdetermined system is solved with Least-Squares regression.

Since most of the real-world objects are not perfectly Lambertian, the reconstruction of albedo and normal maps with classic Photometric Stereo is affected by more complex appearance effects such as specularities, shadows or interreflections. Many methods that were proposed to extend this limitation focus on extending the number of parameters of the surface model and/or design robust strategies for solving the system of equations. The increased complexity of the models requires a higher number of images and hence, a multi-light image collection. One of the first methods to extend the classic Photometric Stereo, by increasing the number of modelled coefficients other than normal and albedo, PTM,[11] replaced the first-order polynomial with a second-order polynomial. This results in the recovery of 6 appearance descriptor maps.

One constraint of the PTM polynomial is that in case the analyzed object has a subset of its surface that is perfectly Lambertian, then the regression of the biquadratic polynomial will not directly output the normal vectors. This limitation is accounted for by the modified polynomial terms proposed by Drew et al. (PTMD) in:[12]

$$c_{1k}lx + c_{2k}ly + c_{3k}lz + c_{4k}lxly + c_{5k}lz^2 + c_{6k} = I_k \tag{3}$$

where $lz = \sqrt{1 - lx^2 - ly^2}$ and the normal vectors are given by the first three coefficients. Simultaneously with the straightforward recovery of the normal vectors for Lambertian parts, PTMD models as well high-frequency and low-frequency non-Lambertian components (4th and 5th coefficients). However, the distinction between the nature of these components (highlights, interreflection, shadows) is not trivial.

Furthermore, the influence of the outliers can be accounted for with robust fitting strategies that solve the system of equations bypassing the Least Squares method. For instance, one such approach reformulates the regression problem as the task of matrix rank minimization,[14] assuming that the full set of observations explains the Lambertian component of the material with a low-rank matrix and the outlier with a sparse matrix. In

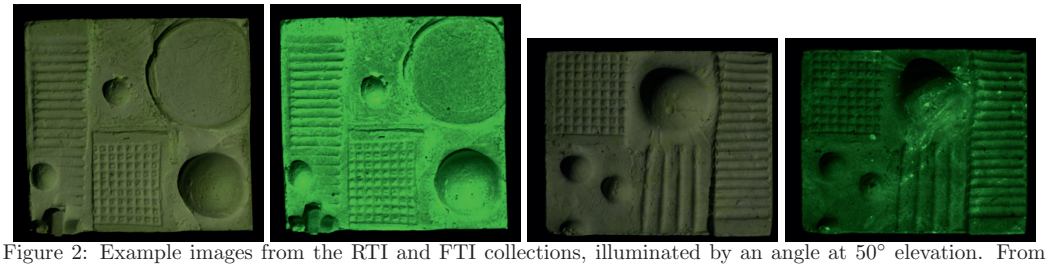

Figure 2: Example images from the RTI and FTI collections, illuminated by an angle at 50° elevation. From left to right: mockup with higher and almost uniform fluorescent component in the reflective, then fluorescent mode; mockup with lower and heterogeneous fluorescent component in the reflective, then fluorescent mode.

addition, a per-pixel estimation of the light directions, was proved to be more effective at estimating surface normals with polynomial models as opposed to assuming a constant light direction for all the scene.[17]

In the experimental part of our paper, we discuss the results obtained with four variants of the classic Photometric Stereo algorithm: the first-order polynomial in Eq. 1, with constant light direction vector and solved with Least-Squares; the first-order polynomial in Eq. 1, with constant light direction vector and solved with low-rank matrix minimization;[14] the second-order polynomial in Eq. 1, with per-pixel light direction vector and solved with Least-Squares; the second-order polynomial in Eq. 3 with per-pixel light direction and solved with Least-Square.

4. RESULTS

4.1 RTI and FTI Data Acquisition

The two fluorescent mockups that contain impressions of convex spherical objects as well as concave patterns were acquired with a multispectral RTI light dome,[4] with lights distributed at different elevation (50°, 30° and 10°) and azimuth angles. The ambient light was controlled by covering the dome in black non-reflective clothing. The sensing device was a Nikon D810 RGB camera, with a 50 mm lens. The objects were captured in two modes (see Fig. 2): reflective mode, under visible light (illuminated by white LEDs), and fluorescent mode, under ultraviolet light (illuminated by ultraviolet LEDs) in combination with a filter attached to the camera that separates the fluorescent signal from the UV-reflected signal.

Because filtering individually the visible radiation emitted by each UV LED was impractical, we tested different filters assembly for filtering the UV-reflected radiation during the fluorescence analysis. Fig. 3 shows the normalized transmittance curves of the measured filters compared with the spectral power distribution of the UV LEDs of the dome as reported by the manufacturer. Hoya Pro1Digital UV filter was used for blocking the internal fluorescence of the tested coloured filters: Nikkon Y44 and Hoya K2. Hoya K2 filter was chosen for the experiments reported in this paper, cuts wavelengths lower than 500 nm, filtering most of the visible emission tail of the UV LED.

At each light direction, a picture was shot sequentially, in the visible and fluorescent modes.The multi-light image collections were converted from the raw signal to linear tiff using dcraw. Afterwards, the stacks of images were processed with RTItool,[18] where firstly, geometric undistortion was applied. Then, the light-direction vectors were recovered assuming a perspective projection based on the semi-automatic annotation of the calibration targets (4 glossy spheres). Given the polygonal arrangement of the 4 spheres (enclosing the object), an interpolation was made between the 4 light direction vector and so, the light directions were locally estimated for each pixel in the image. In addition to the per-pixel light direction, a constant light direction for all image can be computed as the average of the 4 light direction vectors estimated from the 4 spheres. Finally, an appearance profile is generated for the two mockups, where for each pixel, the color information is encoded for each light direction.

Once the appearance profile is obtained, the surface coefficients are recovered with four fitting models: classic Photometric Stereo, with constant light direction and Least-Squares fitting (PS-L2),[10] Photometric Stereo with

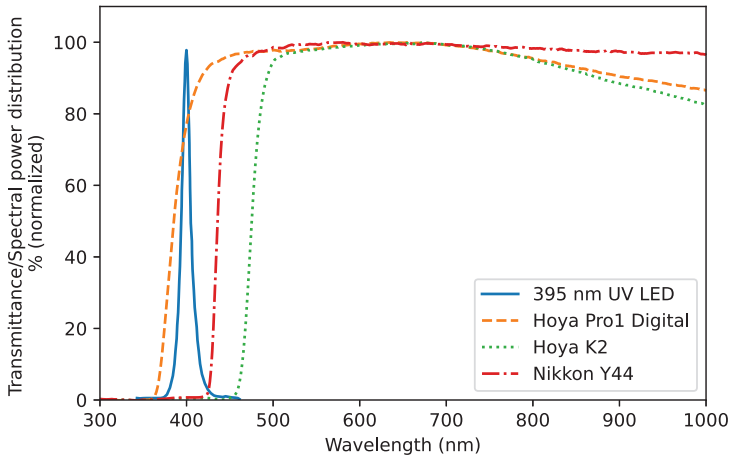

Figure 3: Normalized transmittance curve measured for off-the-shelf fluorescence-pass filters, together with the spectral distribution of the UV LED light of the dome.

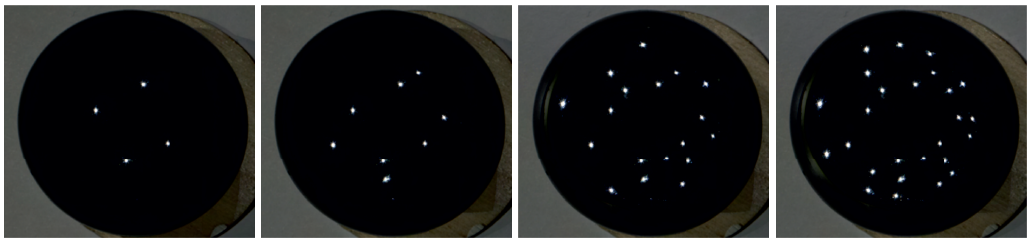

(a) 1 (4 lights) (b) 2 (8 lights) (c) 3 (18 lights) (d) 4 (26 lights)

Figure 4: We use four different light distributions to evaluate the quality of the Reflectance and Fluorescence Transformation modes. As mirrored on the reflective sphere, in each of the four distributions, the lights are sampled in approximately radially symmetric way.

per-pixel light direction and Least-Squares fitting (PS-4-L2), Photometric Stereo based on low-rank matrix minimization (PS-RPCA),[14] Polynomial Texture Maps with Drew terms[12] with per-pixel light direction and Least-Squares fitting (PTMD-4-L2). The fitting is performed based on various light distributions (see Fig. 4) in order to investigate the impact of the number of light directions and their spatial arrangement on the quality of appearance reconstruction. The 4 light constellations are sampling increasing number of lights at different elevation angles with approximately opposite azimuth distancing.

4.2 Ground-truth Shape Scanning and Registration

In order to compare the surface normals maps estimated with RTI and FTI, we scan the shape of the mockups with an off-the-shelf structured light 3D scanner.[19] Once the mesh of the surfaces is recovered, we align the two coordinate systems using mutual information algorithm[20] as implemented in Meshlab.[21] Mutual information algorithm optimizes the roto-translation matrix in an iterative fashion based on the statistical similarity between the normal map obtained with the camera (from RTI anf FTI modes) and various renderings of the 3D model (normal map, ambient occlusion map and specular map). After alignment has converged, the 3D model is

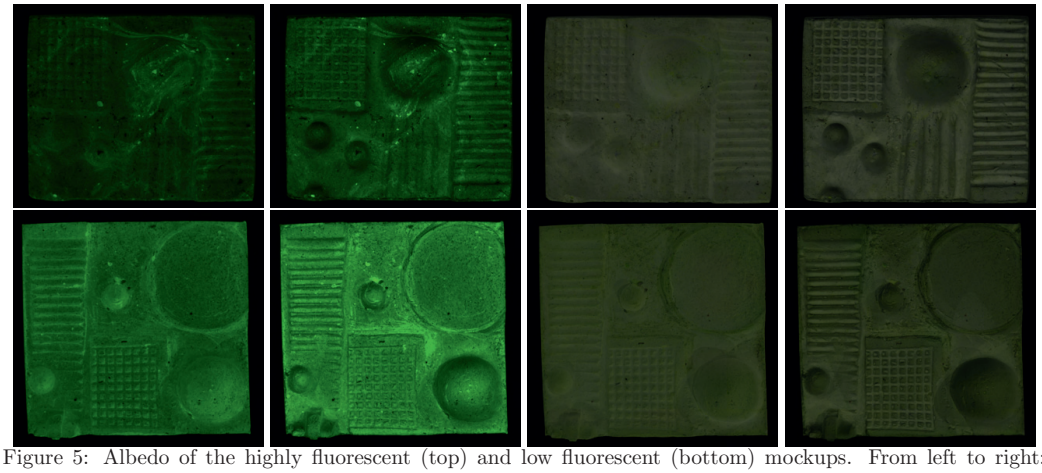

Figure 5: Albedo of the highly fluorescent (top) and low fluorescent (bottom) mockups. From left to right: reconstruction with FTI PS-4-L2, FTI PTMD-4-L2, RTI PS-4-L2, RTI PTMD-4-L2 for light configuration 4. The PS-4-L2 model seems to perform better at discarding the shading effects from the albedo map than PTMD-4-L2.

rendered with the camera parameters and the transformation matrix using Mitsuba renderer.[22] This protocol of shape-to-image alignment has been employed before in analogous task.[23,24]

4.3 Quantitative and Qualitative Analysis

Appearance maps, such as albedo and normal maps are recovered from the FTI and RTI multi-light image collections. The albedos of the two mockups reconstructed with PS-4-L2 and PTMD-4-L2 models in the fluorescent and visible modes are shown in Fig. 5. For both mockups, we can notice that the two models reconstruct a different albedo, while PS-4-L2 manages to better isolate the shading effects from the reflectance.

Surface normal maps given by RTI and FTI are compared with the normal maps derived from the 3D scans. Fig. 6 shows a visual comparison of the normal maps recovered with RTI next to the ground-truth ones. While the normal maps rendered from the 3D scanned models are overall sharper than the RTI surface normals, they present horizontal line artifacts. Moreover, in the highly fluorescent mockup, fine details of the coin imprint are better defined in the RTI surface normals. Even though the quality of the 3D scan normals is not impeccable, they still represent a common reference ground for comparison between the different RTI and FTI modes.

Angular difference is computed between the normal orientation vectors of ground-truth against those reconstructed with RTI and FTI as $arccos(n_{gt}^{T}n)$ for each of the 4 light distributions. The results are presented in the form of box-and-whiskers plots in Fig. 7 and 8, as well as difference maps in the Appendix A. Overall, the models that consider per-pixel light direction estimation show lower error than the models with constant light direction. Similarly, the former category exhibit more invariance to the change of number of lights than the latter.

For the low fluorescent mockup 7, the angular error is higher in the fluorescent mode than it is in the visible modes for all light configurations, as obtained with PS-L2, PS-RPCA and PS4-L2 models. The lowest median angular difference is given by the PTMD-4-L2 model, in particular for the 4^{th} light configuration with $10.95°$ for the visible mode and $11.46°$ for the fluorescent mode. Nevertheless, there is a general high overlap between the distributions of the angular error difference in visible or fluorescent modes, meaning that the difference between the two modes is not significantly large for this object. The impact of the light distribution varies according to the fitting model, but is constant between fluorescent/visbile modes: for PS-L2 and PS-RPCA, it seems that the best light configuration is configuration 2 (8 lights), while for per-pixel methods, PS-4-L2 and PTMD-4-L2,

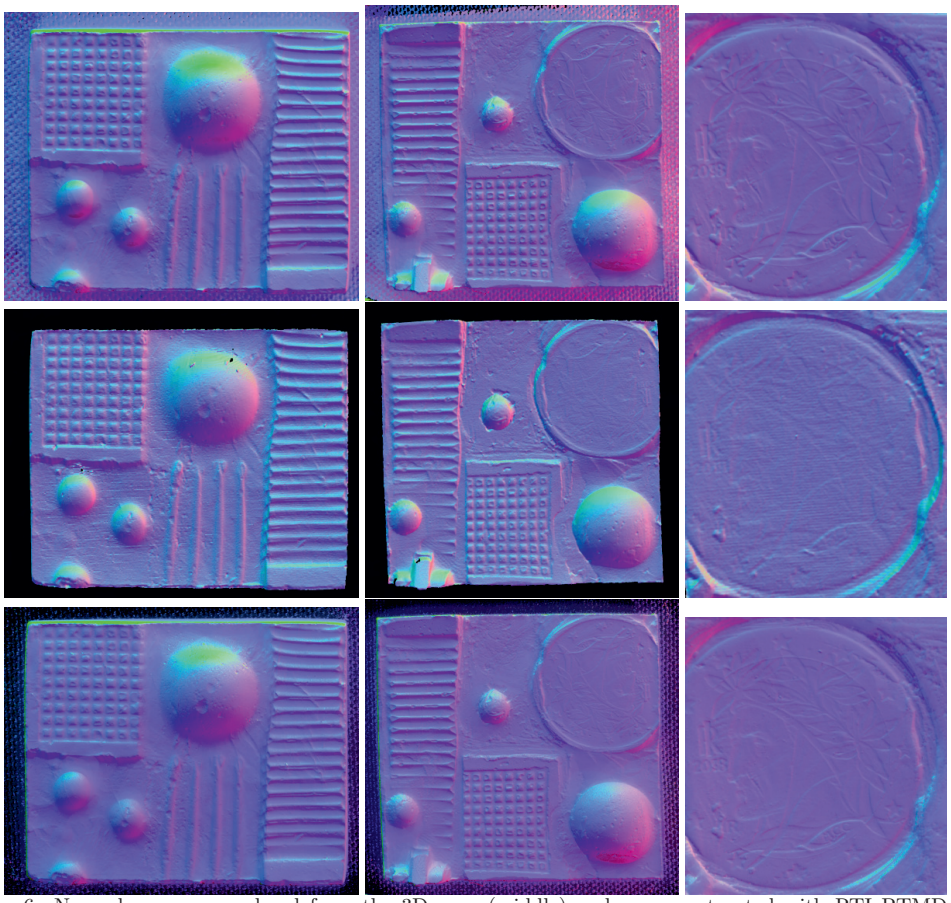

Figure 6: Normal maps as rendered from the 3D scan (middle) and as reconstructed with RTI PTMD-4-L2 (top) and FTI PTMD-4-L2 (bottom) based on light configuration 4. From left to right: low fluorescent mockup, highly fluorescent mockup, rotated detail of the coin imprint from the right upper corner of the highly fluorescent mockup. The RTI and FTI normal maps manage to render fine elements of the coin imprint (such as the issue year and the contours of the portrait) more accurately than the 3D scan. Nonetheless, they have poorer estimation for the elements with higher depth.

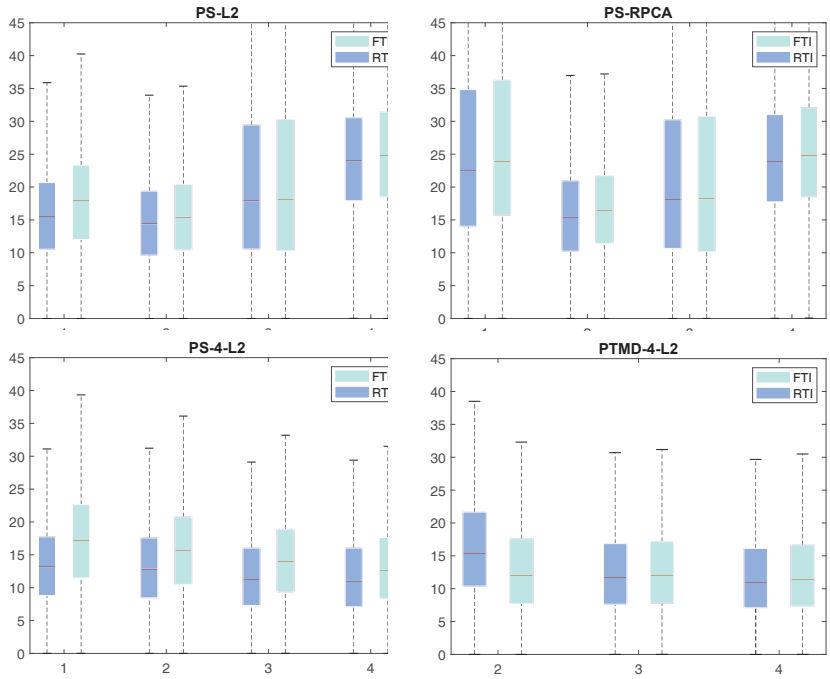

Figure 7: Angular error in degrees (Y-axis) between the ground-truth normal of the low fluorescent mockup and the normals reconstructed with RTI and FTI methods with varying light distributions (X-axis). The angular errors were computed only for the area corresponding to the object, background was discarded.

configuration 4 (26 lights). It is noteworthy to point out that in the fluorescent mode, PTMD-4-L2 seems to be more stable across varying light distributions than it is the case for the visible mode.

The differences between visible and fluorescent modes are more salient for the highly fluorescent object. Similar to the low fluorescent case, the higher angular differences correspond to the fluorescent mode. Moreover, this time, given the lower extent of the overlap between the two distributions, the discrepancy between visible and fluorescent modes is more significant. For the visible mode, the lowest angular error is provided by the PS-4-L2 and 4th light configuration with a median value of 9.12°, while for the fluorescent mode the lowest median angular difference is 17.82° given by the PTMD-4-L2 and the same 4^{th} light configuration. A descending trend is observed for the error as the number of lights increases, which stops at the the 3^{rd} light distribution for PS-L2 and PS-RPCA, while continues up until the 4^{th} light distribution for PS-4-L2 and PTMD-4-L2.

The fact that, for the given case studies, higher errors correspond to the normals recovered in the fluorescent mode contravene the expectation given by previous findings in the scientific literature[8,9] where due to its presumable isotropic property, fluorescence is more accurately approximated by the classic photometric stereo model than signal in the visible light reflective mode. Moreover, the modulation of the angular error with varying light distributions in the fluorescence mode further indicates the presence of deviations from a perfectly Lambertian behaviour. It is true that in[8] and,[9] they exploit the fluorescence mode for objects that are highly specular in the visible mode, while in our case, the objects are diffuse in the visible mode. In addition,[8] and[9] work with single-geometry scenes and objects with uniform albedo that don't fluoresce the same color they reflect, ensuring the lack of interreflections provoked by the luminescence becoming a secondary light source in the scene. We specifically designed our mockups to break the above-mentioned assumptions. The results of our proposed experiments imply that heterogeneous, non-flat and cluttered fluorescent scenes exhibit more non-Lambertian

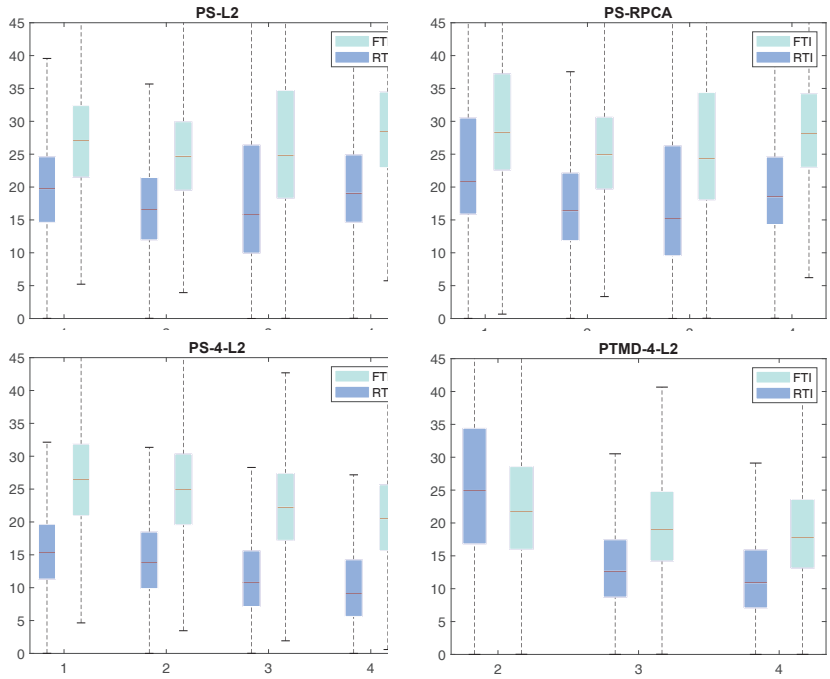

Figure 8: Angular error in degrees (Y-axis) between the ground-truth normal of the highly fluorescent mockup and the normals reconstructed with RTI and FTI methods with varying light distributions (X-axis). The angular errors were computed only for surface corresponding to the object, background was discarded.

effects in the fluorescent mode. This might be partly explained by the higher number of interreflections provoked by the luminescence becoming a secondary light that gets reflected by the object (that both reflects and emits green color).

In an attempt to further assess the presence of non-Lambertian effects in the mockups, we visually compare the 4^{th}, 5^{th} and 6^{th} coefficient maps in Fig. 9 of the PTMD-4-L2 polynomial, as expressed in Eq. 3, for the Green color channel, which is the most relevant for investigating the cross-signal between fluorescence and visible reflectance. The 6^{th} is the constant, ambient term, while the 4^{th} and 5^{th} coefficients model non-Lambertian high and low frequency effects such as highlights, interreflections and shadows. However, it is not obvious and immediate how to separate between the various effects. Nonetheless, we can notice that these non-Lambertian effects are present in visible mode and are definitely not lacking in the fluorescent mode. Moreover, since the mockups reflect the color that they emit in fluorescence mode, we expect that the mutual illuminations effects are higher in the fluorescent mode. Indeed, the green channel of the 4^{th} and 5^{th} PTMD-4-L2 coefficients show more variation in the fluorescent mode than for the visible mode in the case of the high fluorescent mockup. This is valid for the low fluorescent mockup, spread of differences is overall lessened and more limited to certain areas like edges and concavities.

However, in order to find out the precise nature and cause of higher angular errors for the normal maps in the fluorescence method, further investigation is needed, and ideally, validated with synthetic data, where ground-truth with respect to each outlier (shadows, interreflections and highlights) are known in advance and can be discarded from the pipeline. We plan to explore these aspects in-depth in future work.

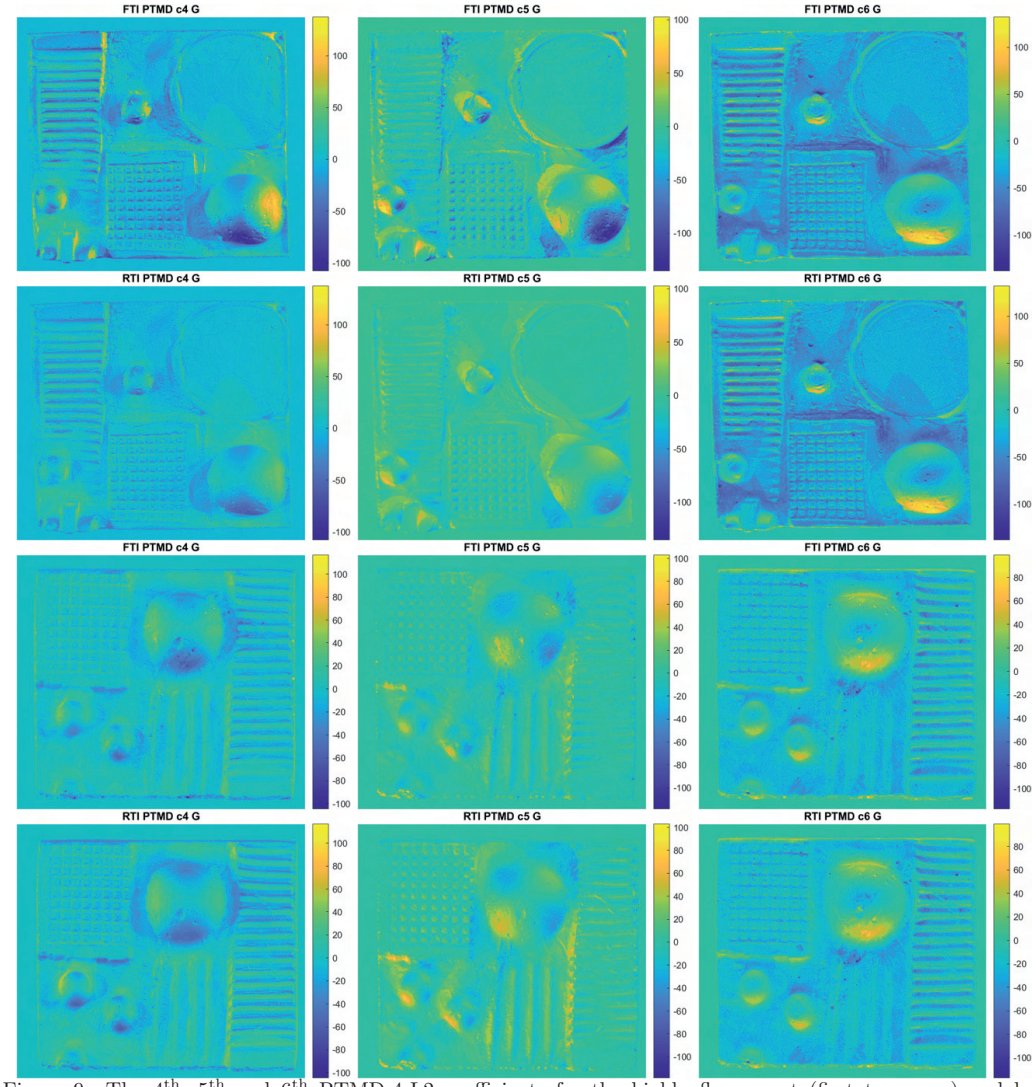

Figure 9: The 4^{th}, 5^{th} and 6^{th} PTMD-4-L2 coefficients for the highly fluorescent (first two rows) and low fluorescent (last two rows) mockups, plotted for the Green color channel, in both visible and fluorescence modes. These coefficients model the non-Lambertian behaviour as encoded by the quadratic and constant terms of the second-order polynomial, as expressed in Eq. 3. Overall, the highest difference between RTI and FTI is registered by coefficients 4 and 5, while the constant term stays invariant.

5. CONCLUSION

In this work, the estimation of normal and appearance maps of heterogeneous fluorescent scenes with non-flat geometries and multiple objects have been investigated under a Reflectance and Fluorescence Transformation Imaging setup. Through qualitative and quantitative analysis of the normal vectors recovered with first and second-order polynomial models, it was shown that contrary to the expectation given by the presumably ideal isotropic property of fluorescence, the surface reconstruction error was higher in the fluorescent mode than in the reflective visible mode. This might be due to the higher number of interreflections provoked by the luminescence becoming a secondary light that gets reflected by the object (that both reflects and re-emits the same color). Our findings show that is important to further investigate the appearance of complex fluorescent scenes with Fluorescence Transformation Imaging, going beyond the assumption of a perfectly Lambertian behaviour of luminescent materials. This is important for accurate appearance modelling and relighting of real-world fluorescent materials.

ACKNOWLEDGMENTS

We would like to acknowledge Giacomo Marchioro (University of Verona), who designed and manufactured the two fluorescent mockups, and helped with the data acquisition process.

REFERENCES

[1] Castro, Y., Pitard, G., Le Goïc, G., Brost, V., Mansouri, A., Pamart, A., Vallet, J.-M., and De Luca, L., "A new method for calibration of the spatial distribution of light positions in free-form rti acquisitions," in [*Optics for Arts, Architecture, and Archaeology VII*], **11058**, 1105813, International Society for Optics and Photonics (2019).

[2] Ponchio, F., Lamé, M., Scopigno, R., and Robertson, B., "Visualizing and transcribing complex writings through rti," in [*2018 IEEE 5th International Congress on Information Science and Technology (CiSt)*], 227–231, IEEE (2018).

[3] Vanweddingen, V., Vastenhoud, C., Proesmans, M., Hameeuw, H., Vandermeulen, B., Van der Perre, A., Lemmers, F., Watteeuw, L., and Van Gool, L., "A status quaestionis and future solutions for using multi-light reflectance imaging approaches for preserving cultural heritage artifacts," in [*Euro-Mediterranean Conference*], 204–211, Springer (2018).

[4] Irina, M. C., Tinsae, G. D., Andrea, G., Ruggero, P., Alberto, J.-V., and Enrico, G., "Artworks in the spotlight: characterization with a multispectral LED dome," *IOP Conference Series: Materials Science and Engineering* **364**, 012025 (June 2018).

[5] Kotoula, E. and Kyranoudi, M., "Study of ancient greek and roman coins using reflectance transformation imaging," *E-conservation magazine* **25**, 74–88 (2013).

[6] Kitanovski, V. and Hardeberg, J. Y., "Objective evaluation of relighting models on translucent materials from multispectral rti images," (2021).

[7] Kotoula, E. et al., "Reflectance transformation imaging beyond the visible: ultraviolet reflected and ultraviolet induced visible fluorescence," in [*Proceedings of the 43rd Annual Conference on Computer Applications and Quantitative Methods in Archaeology, Oxford*], 909–919 (2015).

[8] Treibitz, T., Murez, Z., Mitchell, B. G., and Kriegman, D., "Shape from fluorescence," in [*European Conference on Computer Vision*], 292–306, Springer (2012).

[9] Sato, I., Okabe, T., and Sato, Y., "Bispectral photometric stereo based on fluorescence," in [*2012 IEEE Conference on Computer Vision and Pattern Recognition*], 270–277 (Jun 2012).

[10] Woodham, R. J., "Photometric stereo: A reflectance map technique for determining surface orientation from image intensity," in [*Image Understanding Systems and Industrial Applications I*], **155**, 136–143, International Society for Optics and Photonics (1979).

[11] Malzbender, T., Gelb, D., and Wolters, H., "Polynomial texture maps," in [*Proceedings of the 28th annual conference on Computer graphics and interactive techniques*], 519–528 (2001).

[12] Drew, M. S., Hel-Or, Y., Malzbender, T., and Hajari, N., "Robust estimation of surface properties and interpolation of shadow/specularity components," *Image and Vision Computing* **30**(4-5), 317–331 (2012).

[13] Ikehata, S., Wipf, D., Matsushita, Y., and Aizawa, K., "Robust photometric stereo using sparse regression," in [*2012 IEEE Conference on Computer Vision and Pattern Recognition*], 318–325, IEEE (2012).
[14] Wu, L., Ganesh, A., Shi, B., Matsushita, Y., Wang, Y., and Ma, Y., "Robust photometric stereo via low-rank matrix completion and recovery," in [*Asian Conference on Computer Vision*], 703–717, Springer (2010).
[15] Tominaga, S., Hirai, K., and Horiuchi, T., "Measurement and modeling of bidirectional characteristics of fluorescent objects," in [*International Conference on Image and Signal Processing*], 35–42, Springer (2014).
[16] Fu, Y., Lam, A., Matsushita, Y., Sato, I., and Sato, Y., "Interreflection removal using fluorescence," in [*European Conference on Computer Vision*], 203–217, Springer (2014).
[17] Ciortan, I. M., Pintus, R., Marchioro, G., Daffara, C., Giachetti, A., and Gobbetti, E., "A Practical Reflectance Transformation Imaging Pipeline for Surface Characterization in Cultural Heritage," in [*Eurographics Workshop on Graphics and Cultural Heritage*], Catalano, C. E. and Luca, L. D., eds., The Eurographics Association (2016).
[18] "Rtitool." https://github.com/giach68/RTITool/. (Accessed on 2021-05-30).
[19] "Gocator 3210 large field of view 3d snapshot sensor." https://lmi3d.com/series/gocator-3210/. (Accessed on 2021-05-30).
[20] Corsini, M., Dellepiane, M., Ponchio, F., and Scopigno, R., "Image-to-geometry registration: a mutual information method exploiting illumination-related geometric properties," in [*Computer Graphics Forum*], **28**(7), 1755–1764, Wiley Online Library (2009).
[21] Cignoni, P., Ranzuglia, G., Callieri, M., Corsini, M., Ganovelli, F., Pietroni, N., and Tarini, M., "Meshlab," (2011).
[22] Nimier-David, M., Vicini, D., Zeltner, T., and Jakob, W., "Mitsuba 2: A retargetable forward and inverse renderer," *ACM Transactions on Graphics (TOG)* **38**(6), 1–17 (2019).
[23] Shi, B., Wu, Z., Mo, Z., Duan, D., Yeung, S.-K., and Tan, P., "A benchmark dataset and evaluation for non-lambertian and uncalibrated photometric stereo," in [*Proceedings of the IEEE Conference on Computer Vision and Pattern Recognition*], 3707–3716 (2016).
[24] Shi, B., Mo, Z., Wu, Z., Duan, D., Yeung, S.-K., and Tan, P., "A benchmark dataset and evaluation for non-lambertian and uncalibrated photometric stereo," *IEEE Transactions on Pattern Analysis and Machine Intelligence* **41**(2), 271–284 (2019).

APPENDIX A. ANGULAR DIFFERENCE MAPS

Angular differences maps between normals from all models and light configurations (Lc) with respect to ground truth are presented on a scale from 0° to 40° for the highly fluorescent and low fluorescent mockups.

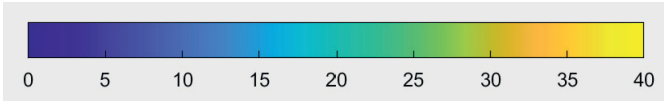

FTI PS-L2 Lc1

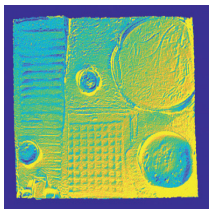

FTI PS-L2 Lc2

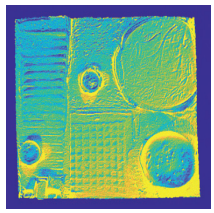

FTI PS-L2 Lc3

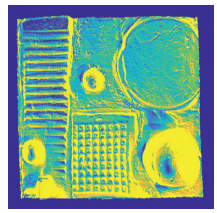

FTI PS-L2 Lc4

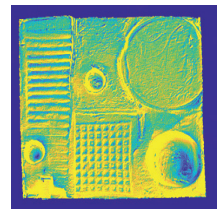

RTI PS-L2 Lc1

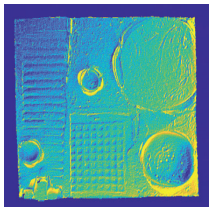

RTI PS-L2 Lc2

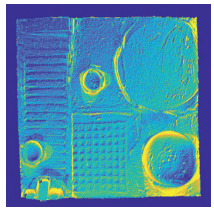

RTI PS-L2 Lc3

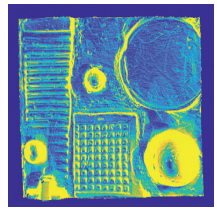

RTI PS-L2 Lc4

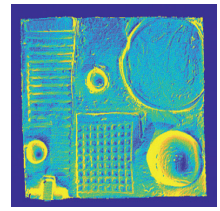

FTI PS4-L2 Lc1

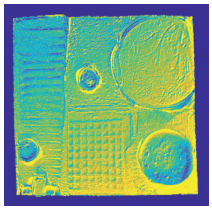

FTI PS4-L2 Lc2

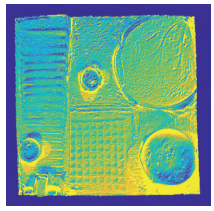

FTI PS4-L2 Lc3

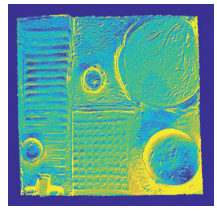

FTI PS4-L2 Lc4

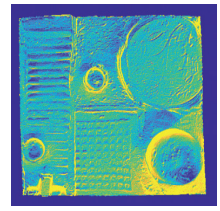

RTI PS4-L2 Lc1

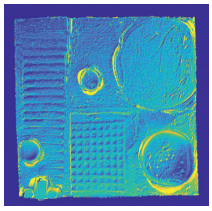

RTI PS4-L2 Lc2

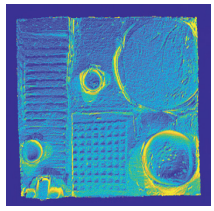

RTI PS4-L2 Lc3

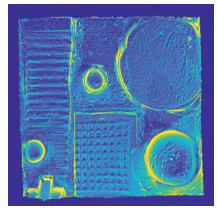

RTI PS4-L2 Lc4

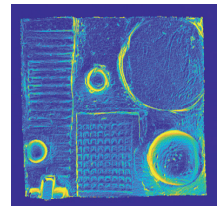

FTI PS-L2 Lc1

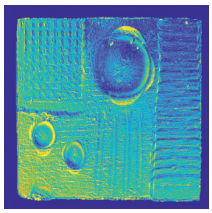

FTI PS-L2 Lc2

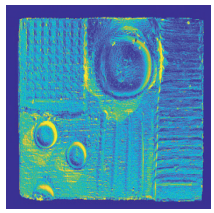

FTI PS-L2 Lc3

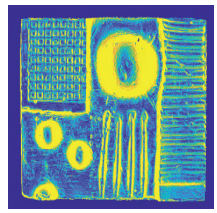

FTI PS-L2 Lc4

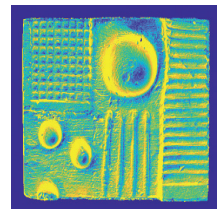

RTI PS-L2 Lc1

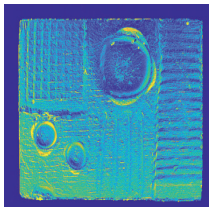

RTI PS-L2 Lc2

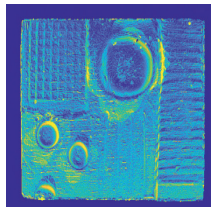

RTI PS-L2 Lc3

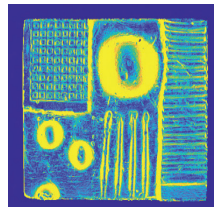

RTI PS-L2 Lc4

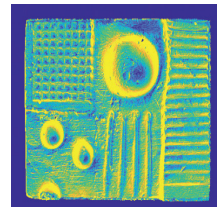

FTI PS4-L2 Lc1

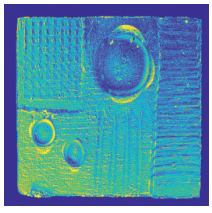

FTI PS4-L2 Lc2

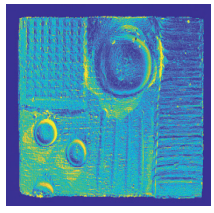

FTI PS4-L2 Lc3

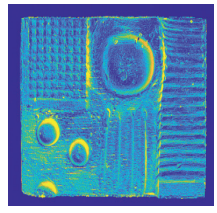

FTI PS4-L2 Lc4

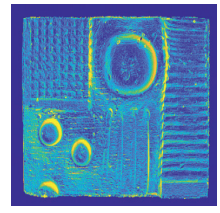

RTI PS4-L2 Lc1

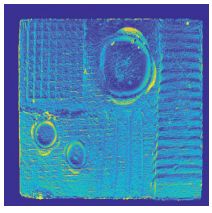

RTI PS4-L2 Lc2

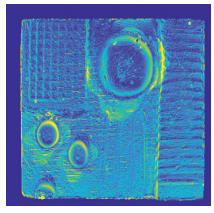

RTI PS4-L2 Lc3

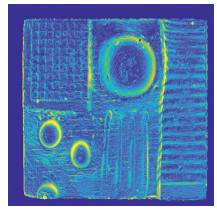

RTI PS4-L2 Lc4

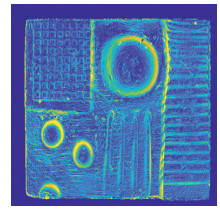

FTI PS-RPCA Lc1

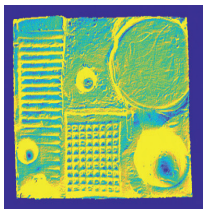

FTI PS-RPCA Lc2

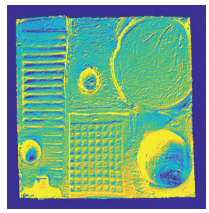

FTI PS-RPCA Lc3

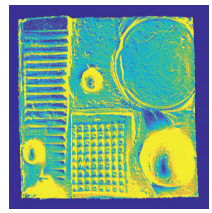

FTI PS-RPCA Lc4

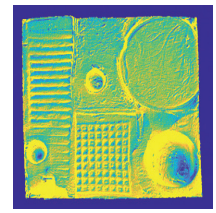

RTI PS-RPCA Lc1

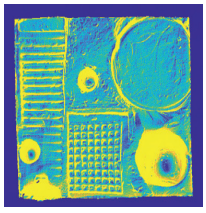

RTI PS-RPCA Lc2

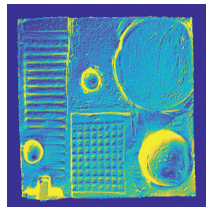

RTI PS-RPCA Lc3

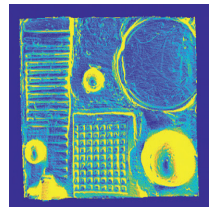

RTI PS-RPCA Lc4

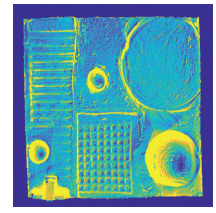

FTI PS-RPCA Lc1

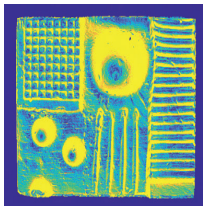

FTI PS-RPCA Lc2

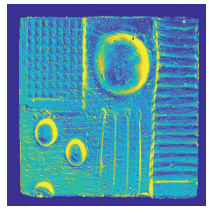

FTI PS-RPCA Lc3

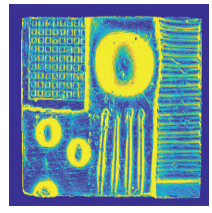

FTI PS-RPCA Lc4

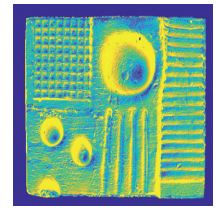

RTI PS-RPCA Lc1

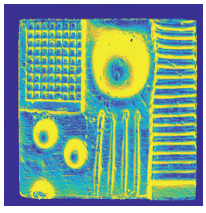

RTI PS-RPCA Lc2

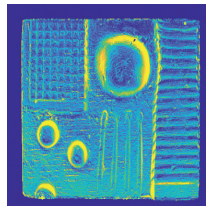

RTI PS-RPCA Lc3

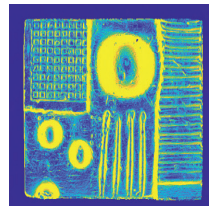

RTI PS-RPCA Lc4

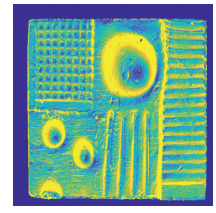

FTI PTMD-4-L2 Lc2

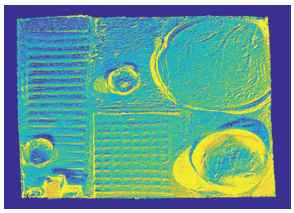

FTI PTMD-4-L2 Lc3

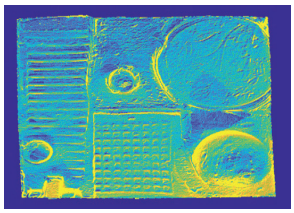

FTI PTMD-4-L2 Lc4

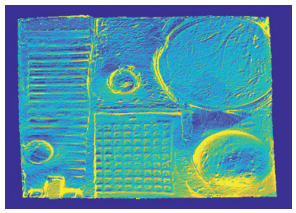

RTI PTMD-4-L2 Lc2

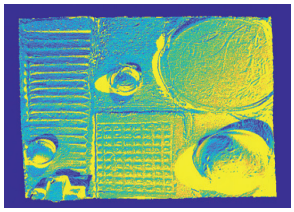

RTI PTMD-4-L2 Lc3

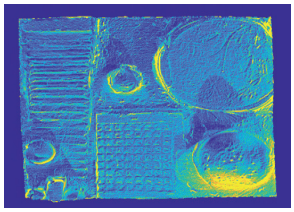

RTI PTMD-4-L2 Lc4

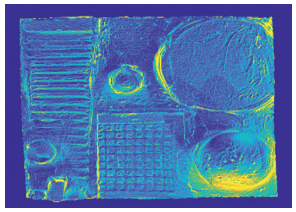

FTI PTMD-4-L2 Lc2

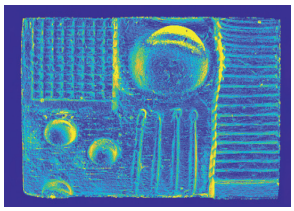

FTI PTMD-4-L2 Lc3

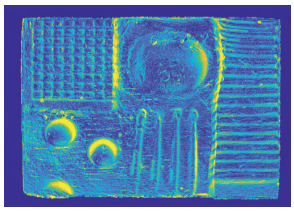

FTI PTMD-4-L2 Lc4

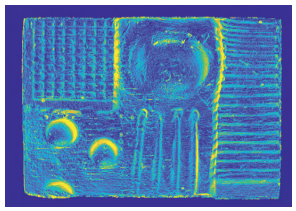

RTI PTMD-4-L2 Lc2

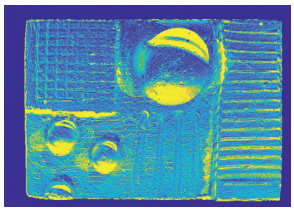

RTI PTMD-4-L2 Lc3

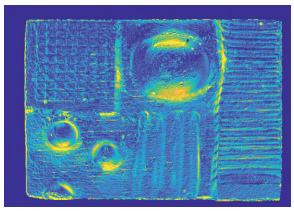

RTI PTMD-4-L2 Lc4

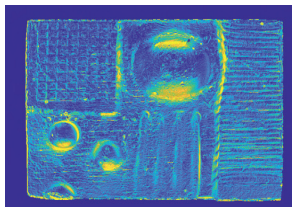

Paper 3 - The Influence of Interreflections on Shape from Fluorescence

This paper is submitted for publication and is therefore not included.

Paper 4 - Spectral Classification of Paper Fixatives: A Case Study on Thomas Fearnley's Drawings

Available at: http://dx.doi.org/10.2352/issn.2168-3204.2022.19.1.18

Paper 5 - Predicting Pigment Color Degradation with Time Series Models

Paper 6 - Tensor Decomposition for Painting Analysis. Part 1: Pigment Characterization

Ciortan *et al. Heritage Science* (2023) 11:76
https://doi.org/10.1186/s40494-023-00910-x

Heritage Science

RESEARCH

Open Access

Tensor decomposition for painting analysis. Part 1: pigment characterization

Irina M. Ciortan[1*], Tina G. Poulsson[2], Sony George[1] and Jon Y. Hardeberg[1]

Abstract

Photo-sensitive materials tend to change with exposure to light. Often, this change is visible when it affects the reflectance of the material in the visible range of the electromagnetic spectrum. In order to understand the photo-degradation mechanisms and their impact on fugitive materials, high-end scientific analysis is required. In a two-part article, we present a multi-modal approach to model fading effects in the spectral, temporal (first part) and spatial dimensions (second part). Specifically, we collect data from the same artwork, namely "A Japanese Lantern" by Norwegian artist, Oda Krohg, with two techniques, point-based microfading spectroscopy and hyperspectral imaging. In this first part, we focus on characterizing the pigments in the painting based on their spectral and fading characteristics. To begin with, using microfading data of a region in the painting, we analyze the color deterioration of the measured points. Then, we train a tensor decomposition model to reduce the measured materials to a spectral basis of unmixed pigments and, at the same time, to recover the fading rate of these endmembers (i.e. pure, unmixed chemical signals). Afterwards, we apply linear regression to predict the fading rate in the future. We validate the quality of these predictions by spectrally comparing them with temporal observations not included in the training part. Furthermore, we statistically assess the goodness of our model in explaining new data, collected from another region of the painting. Finally, we propose a visual way to explore the artist's palette, where potential matches between endmembers and reference spectral libraries can be evaluated based on three metrics at once.

Keywords Multivariate analysis, Microfading spectroscopy, Color photodegradation, Pastel painting, Bubble chart

Introduction

Light-sensitive pigments may irreversibly change the appearance of an artwork after exposure to light. For this reason, special research and efforts are dedicated to keep in control the exhibition conditions and choose the optimal lighting policy. While traditionally, broad categories of materials were established depending on assumed light sensitivity, more recently microfading has come into use to make more individual assessments. In this way, less sensitive objects may be displayed for longer, while the most sensitive objects will be better protected.

Furthermore, the degradation of pigments might interfere with the accurate recognition of materials in paintings. This is because fading might cause the disappearance or transformation of some highly sensitive elements in the materials. In such cases, state-of-the-art non-invasive optical techniques used for the task of pigment identification, such as reflectance imaging spectroscopy can be helpful to find residual pigments, by sensing their known responses to certain incident light [1]. Nevertheless, knowledge of the pigments' fading behaviour can contribute towards their recognition.

The sensitivity to light applies not only to pigments, but to all colorants, dyes included and other materials, such as wood. This has a practical implication and general applicability in a wide range of fields beyond

*Correspondence:
Irina M. Ciortan
irina-mihaela.ciortan@ntnu.no
[1] Department of Computer Science, NTNU - Norwegian University of Science and Technology, Teknologivegen 22, 2815 Gjøvik, Norway
[2] Collection Management, National Museum, Oslo, St. Olavs plass, 0130, Norway

cultural heritage, such as printing, automotive industries, fashion and textile, architecture, etc. Because photodegradation is such a widespread concern, it has even been approached by the computer graphics community in an attempt to synthesize the spectral aging effects of multi-layered surfaces [2].

In this first part of a two-series article, we are proposing an approach based on microfading spectroscopy, coupled with multivariate data analysis to model pigment fading effects along the spectral and temporal dimensions. We show the performance of our model on a pastel painting, where specific research questions are answered.

Related work

Spectroscopic analysis for pigment identification

Spectral response of a pigment to electromagnetic radiation represents a distinctive signature. For this reason, the spectroscopic signal is often studied for pigment identification tasks. While it is fruitful to operate in the reflectance domain [3], some works in the literature point out that the absorption spectra [4, 5] or the first-derivative of the reflectance might be more helpful for discriminating pigments with similar composition [6–8]. Johnston and Feller [4] used the additive property of the constituents of a mixture in the absorption domain to subtract the absorption spectra of a pigment before and after aging. The difference absorption spectrum preserved the peaks characteristic of a certain red lake pigment that were attenuated in the individual absorptions. Fonseca et al. [7] designed a decision support system to distinguish between plant (madder root) and animal (cochineal insects) red lake pigments based on inflection points of the reflectance curve and its first-order derivative. Recently, Gabrieli et al. [8] used derivative analysis to identify the palette of Rembrandt's "Night Watch".

Given a spectral library, i.e. a dataset of reference pigments, it is possible to assess the similarity between a standard specimen of a pigment and the measurements in an artwork, by comparing their reflectances as vectors in the spectral space. The spectral similarity can be computed for reflectance or its variants: absorption and first derivative [8]. While there are various distance metrics that can be used, with spectral angle mapper being the most common [8], there are works in the literature that argue for the higher performance of spectral correlation mapper [9] and Kullback Leibler pseudo-divergence [10]. Nevertheless, to find good matches, it is important to design the spectral libraries in such a way that they resemble the target in terms of chemical composition, concentration and binding media [11].

Pigment unmixing

In the case of image spectroscopy also known as hyperspectral imaging, where the spectra is documented at every spatial location of an artwork, it becomes feasible to map the existence of a pigment in two dimensions by thresholding the spectral similarity between a reference material and the measured painting [8]. In addition, hyperspectral imaging also allows for pigment unmixing, where traces of an endmember and their abundance are found at every spatial location. The pigment identification based on the spectral signal can be affected due to mixing mechanisms. Thus, it is a common practice to perform pigment unmixing before computing spectral similarities with a databases. Given a collection of measurements, pigment unmixing finds a set of endmembers, and the abundance of all endmembers in each sample. An endmember is a pure pigment that forms the basis of a palette in a painting, implying that all the other signals in the painting can be represented as a mixture of the endmembers. Nonetheless, the task of finding the endmembers is not a trivial one because of the nature of mixing mechanisms. There is a lot of literature for material unmixing in the remote sensing field, where hyperspectral imagery is used as well [12–14]. However, the spatial resolution in remote sensing applications is lower than close-range imaging as is the case in the cultural heritage field. In the former case, optical mixing occurs, at the sensor level, where a pixel is formed by a linear combination of the radiances of endmembers. Hence, linear unmixing models work acceptably for the remote sensing field [13] and examples of known linear unmixing methods are pixel purity index (PPI) [15], N-FINDR [16], vertex component analysis [17]. PPI is the default unmixing method implemented in the Spectral Hourglass Wizard functionality of the ENVI software [18], which gave good results for painting analysis while complemented by experts' input [8] or automated algorithms to find meaningful spectral features in the endmembers' reflectance [11].

When it comes to close-range reflectance image spectroscopy, intimate mixing and layered mixing effects are of higher concern. Intimate mixing refers to the heterogeneous chemical composition of a material, while layered mixing refers to the blended stacks of materials, where due to translucency, the material in the background has a contribution to the surface material that is recorded at pixel level. In these cases, non-linear unmixing models are more appropriate to find the endmembers. Kubelka-Munk [19] is an example of a non-linear model, that describes the physical interaction of turbid media and it characterizes a medium with two optical coefficients, absorption and scattering. Unmixing in the Kubelka-Munk space has proven especially effective

for the analysis of pigments [20–22]. While physically-based models such as Kubelka-Munk are accurate and offer an analytical solution to the radiative transfer equation, several data-driven methods for non-linear unmixing were shown to be successful as well. For instance, Kleynhans et al. [23] trained a convolutional neural network to associate 1D spectra of pigments to their labels, given a dataset of illuminated manuscripts, scanned with a hyperspectral camera and with known chemical composition.

A common pre-processing step in the pigment unmixing pipeline is represented by dimensionality reduction [24], typically achieved by principal component analysis, non-negative matrix factorization or clustering techniques such as k-means and t-SNE [25]. In several studies, tensor decomposition [26], in particular Parallel Factor Analysis (PARAFAC) [27], also known as canonical decomposition [28], was employed to achieve dimensionality reduction, clustering and classification of hyperspectral images in a trilinear fashion without resorting to flattening to a 2D array [29, 30]. The main advantages of tensor (i.e. multidimensional array) analysis over matrix processing consist in the preservation of data structure, the ability to retrieve latent variables in the multi-linear space and the uniqueness of the base factors [31]. Thus, operations in the tensor space have a wide applicability in signal processing [32] and computer vision tasks [31]. Moreover, tensor computation was often been coupled with the sparse representations in dictionary learning methods towards speech recognition [33] and spectral unmixing [34].

In the field of chemometrics, numerous articles stand as evidence for the capabilities of PARAFAC [27] to extract unique pure spectra in a completely unsupervised manner from multi-way data such as fluorescence spectroscopy [35, 36], chromatography [37], laser-induced breakdown spectroscopy [38] and nuclear magnetic resonance spectroscopy [39]. For example, PARAFAC was effective in extracting the emission and excitation functions of the fluorophores and their concentration in a set of bispectral measurements of sugar samples [36].

Fading analysis of pigments

Beside their spectral reflectance, pigments are also characterized by their lightfastness properties. The behaviour of pigments to light exposure is used to judge the quality of a pigment by artists, paint manufacturers and art historians alike [40]. So much so, that in compendiums describing pigments [41–43], fugitivity to light is included to assess the permanence of a pigment. Starting as early as the second half of the nineteenth century [44], art historians together with conservation scientists designed fading experiments in a controlled environment that surpassed visual observation, and quantified the light-induced degradation of pigments in the color [45] and spectral domain [4]. For instance, Saunders et al. [45] prepared samples of organic pigments following historical recipes and aged them in an accelerated way by exposure to artificial daylight fluorescent lamps at an illuminance of 10,000 lux inside a chamber with constant temperature and relative humidity levels. They measured the samples colorimetrically in a gradual way, at every predefined interval of time during the fading procedure. The samples were exposed for 3000 h. The CIE ΔE_{ab} color difference was computed to quantify the extent of the fading. In addition, the color change was compared to that of ISO blue wool (BW) standards 1–3 [46], that have increasing lightfastness. This controlled fading experiment showed that the most fugitive red lake is brasilwood lake followed by lac lake, cochineal, kermes madder and alizarin. Moreover, the authors discovered several important factors that impact the fading: the lake extraction method (raw, directly from insects as opposed to colored textile patches), lake precipitation methods (aluminum, aluminum with calcium carbonate and tin), pigment concentration, content of ultraviolet radiation in the light source.

Several studies investigate the relation between the photo-permanence of pigments and the spectral power distribution of the light source used in the fading process. Earlier on, Saunders et al. [45] showed that ultraviolet radiation strongly accelerates the fading pattern of organic pigments. The same finding was later confirmed by Hattori et al. [47] who noticed that ultraviolet radiation contributed to the fading of blue wool standards [46] with a higher share than visible light. As far as the visible range of the electromagnetic spectrum is concerned, the fading seems to be positively impacted by the amount of overlap between the absorption of the pigment and the spectral distribution of incident light [48]. Saunders et al. [48] were among the first to model the light-induced color change of red lake pigments as a function of the incoming wavelength. They adjusted the fading experiment in [45] by coupling the light source with seven broad-band filters with peak transmittances sampled every 50 nm between 400 and 700 nm. Because red lakes absorb more in the lower wavelengths, their photo-degradation increases when exposed to light in the blue side of the spectrum. Lerwill et al. [49] reiterated a similar experiment, with an improved setup based on narrow-band filter for separating the incident light signal and examining more pigments. While they agreed to the conclusion of [48], i.e. damage increases with increasing absorption, they found out that Prussian blue is an exception. In other words, Prussian blue is less affected by the light it absorbs and more by the light it reflects.

The impact of the light source spectrum in accelerated aging experiments was acknowledged as well by Pintus et al. [50]. In an attempt to characterize the formation of cadmium soaps in oil paints, they discovered that LED light impinged more aging effects than a halogen lamp and a natural light source.

It is important to make the distinction between fading and other related terms such as light bleaching and photobleaching. In art conservation and material research, the first term is commonly adopted to refer to the process of yellowness and stain removal and it has been encountered in applications on aged paper [51], film artifacts [52], textile [53] and teeth enamel [54]. The second term is typically used in biology to refer to the process by which fluorophores are removed from a molecule through light excitation [55]. While photobleaching may relate to the light-induced chemical alteration of a colorant that affects its color attributes, its meaning is mainly tailored to the loss of fluorescence. For this reason, in the current study, we use the term fading which covers the general alteration of a colorant with exposure to any type of light.

Microfading analysis

Microfading is a fading process performed at a smaller scale, that concentrates light over spots of submillimetric size, thus minimizing the extent of the damage. For this reason, it can be considered an almost non-destructive technique and can therefore be applied on real artworks. Whitmore et al. [56] were the first to propose a microfading protocol for measuring real art objects. The non-invasiveness is ensured by terminating the procedure before a noticeable color difference or a maximum number of iterations is reached.

In the recent years, thanks to the accessibility of portable microfadeometers (MFT) such as the one proposed by Lojewski [57], there has been an increased interest to analyse the light sensitivity of pigments directly on artworks. Chan et al. [58] measured with the MFT the litographic print and the painted version (from 1910) of "The Scream", both belonging to Munch museum. The most fugitive pigment in both artworks was revealed to be vermilion, with a light-sensitivity comparable to that of BW 1. The lightfastness analysis inspired the museum to design an intermittent display that lowers the display time for each artwork. Grimstad et al. [59] microfaded 27 paintings of Edvard Munch and similar to [58], they noticed that reds are the most sensitive colors, and all of these reds contain vermilion. Aambø et al. [60] gathered microfaded observations from 63 paper-based artworks in the Munch museum collection and discovered intricate light-induced change mechanisms for pigments with apparently the same color and/or chemical composition. In one case, for two reproductions of a woodcut plate supposedly made of the same material, two samples that appeared to have the identically same green color showed a different fading pattern. This implies the use of two different pigments.

While the study of lightfastness in the color domain gives a first intuition on whether similar materials were used in a sample, it is the knowledge of the spectral composition that adds more precision. Even when a set of measurements share one pigment, the photo-degradation can have different dynamics because of the rest of the materials in the mixture. In [60], the red colors were found to be the most fugitive, approaching BW 1 fading rate, a finding similar to that of [58 and 59]. While analytical techniques discovered traces of vermilion in all the highly sensitive reds in [60], vermilion wasn't the only pigment in the composition. In addition, other red colors were found to be more light resistant (BW 2–3 category), even though they contained vermilion as well. Moreover, other red points, with both similar pigments (vermilion) and similar color sensitivity, manifested a slightly different change rate. In most of these studies, the microfading experiments are usually performed in the visible range of the spectrum, which better aligns with the current exhibition conditions in museums and galleries [61].

Method

In many of the above mentioned related articles, the pigment's composition is sometimes known apriori, and the microfading analysis is mainly performed with the purpose of implementing a more or less protective lighting policy for artworks displayed in museum exhibitions. To the best of our knowledge, there are no works that use the microfading analysis in the reverse way, i.e. to use the lightfastness behaviour aside from the spectroscopic features for characterizing and identifying an unknown pigment. In our work, we propose a linear unmixing method based on microfading single-point measurements, by modelling changes in the spectral domain and extracting endmembers using multivariate algebra analysis. We represent the light-induced measurements as a 3D tensor (samples*time step*spectra), where every sample is described by the spectral reflectance at different points in time during the photo-degradation process. With trilinear tensor decomposition, we are then able to recover chemically relevant endmembers that best explain the data, their concentration in every sample and the temporal change provoked by light exposure. While still a linear unmixing technique, by preserving the trilinear data structure, the tensor decomposition is able to recover more latent variables than a traditional bilinear setting [31].

Figure 1 shows an overview of our method. Given a set of spectral microfading measurements, we create a 3D array, where the first dimension corresponds to the

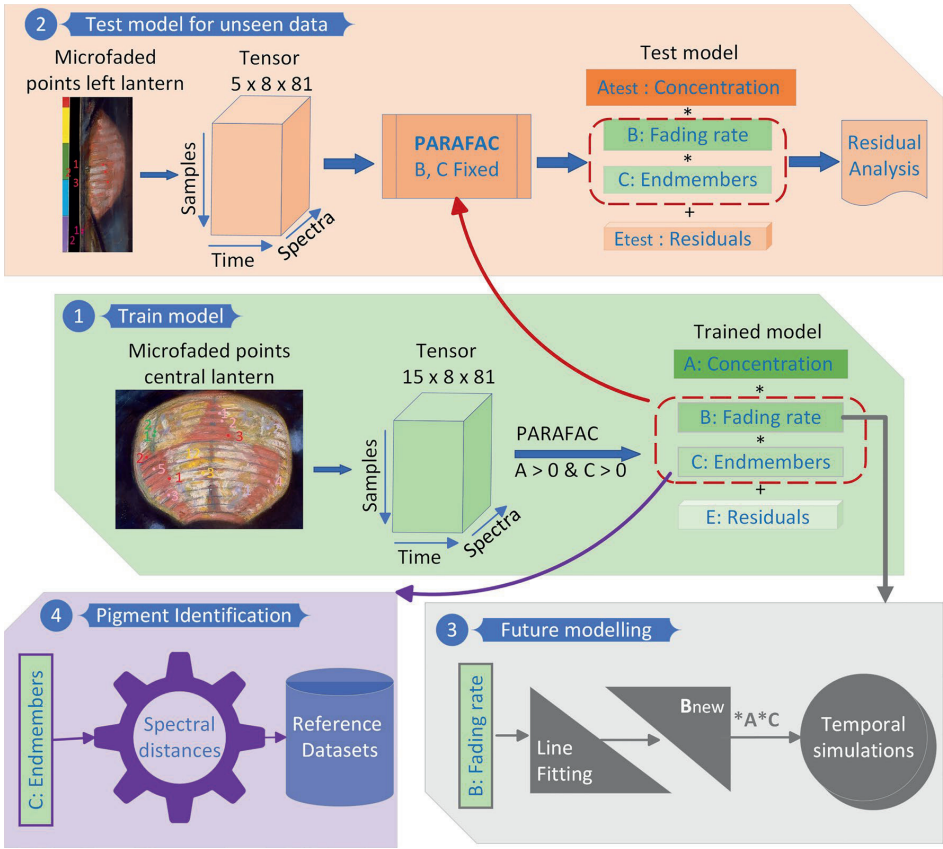

Fig. 1 The diagram of our method. The module **1** is the core model, where we extract the endmembers and their fading rate with three-way tensor decomposition from a collection of microfading observations. Using this trained model, we verify how well we can explain new microfaded data (**2**). Also, we apply regression on the fading rates and extrapolate the behaviour for future temporal modelling (**3**). Finally, we spectrally compare our endmembers with databases of pigments to identify the materials used in the painting (**4**).

number of observations, the second dimension corresponds to temporal changes and the third to the spectral reflectance. Then, we use PARAFAC in order to retrieve the loadings for each of the three dimensions, also called modes in our data representation. The PARAFAC analysis gives the pure spectra underlying the sample, the concentration of all pure components for each sample, and the degradation rate of every principal component. Once we get the trained model, we can test whether it can explain new samples, unseen at the calibration stage, by keeping fixed the loadings corresponding to the spectral composition and the alteration rate. Moreover, by using regression on the temporal change loadings, we can predict unmeasured future values.

Tensor decomposition with parallel factor analysis

PARAFAC is a tensor decomposition method that was initially proposed by Harshman [27] to increase interpretability of multivariate data. PARAFAC can be considered as a generalization of the bilinear PCA method [36] in the sense that both methods assume the input data can be explained as a linear combination of basis factors. These factors are also called scores and loading vectors. However, one of the most important aspects is that PARAFAC doesn't require unfolding the data into bilinear form, thus maintaining the structure of the multivariate data. This way, there is a one-to-one mapping between the effects of a variable and a loading vectors, which is relevant for describing an underlying chemical or physical phenomena. Moreover, PCA doesn't give an unique

solution, because all rotations of the orthogonal loading vectors can be good fits of the data. Thus, while PCA scores and loadings are still meaningful for deciphering the data, it is difficult to draw a direct association with pure chemical components. On the contrary, PARAFAC loadings have the property of being unique, where the unique loadings resemble loyally the actual pure spectra in a material [62]. At the same time, the scale of the loading vectors resulting from tensor decomposition is unidentifiable and has no immediate correspondence with units of measure unless a scaling factor to a ground-truth can be determined [62].

Let $X^{M \cdot K \cdot N}$ be a 3D tensor, where M is the number of samples, K the number of time steps and N the number of spectral bands of the input microfading data. Then, using three-way decomposition, we can model this tensor as the outer product of 3 factor matrices, A, B, C:

$$\hat{X}^{M \cdot K \cdot N} = A^{M \cdot F} \otimes B^{K \cdot F} \otimes C^{N \cdot F}, \tag{1}$$

where F is the user-defined number of components to split the tensor into. Using the Kathri-Rao product $\odot$, Eq. 1 can be re-written in the following flattened form:

$$\hat{X}^{M \cdot KN} = A^{M \cdot F} \times (C^{N \cdot F} \odot B^{K \cdot F})^T, \tag{2}$$

where $\times$ denotes the conventional matrix multiplication. The flattened array can then be easily reshaped to the original size of the tensor.

The decomposition is solved with the alternating least squares algorithm [63] where the objective is to minimize the squared residuals between the actual data and the model. If E is the tensor corresponding to the residuals, defined by $E^{M \cdot K \cdot N} = X - \hat{X}$, then the loss function is $\underset{A,B,C}{min} E^2$. Alternating least squares algorithm implies that the factors A, B, C will be conditionally estimated on each other. To determine A, B and C will be initialized and then, the minimization function will be solved for A given the B and C priors. Afterwards, the same operation is repeated to get B with the previously fitted A and initialized C. Subsequently, the optimization function is run again for C with the already fitted A and B loadings. Finally, based on the values of the 3 factors obtained after the first iteration, the least-square optimization is repeated in the same conditional fashion until convergence is reached, i.e. there is negligible improvement in the newly fitted values with respect to the previous. While numerically there is no difference between scores and loadings, it is common practice to consider that the first factor, A refers to the scores of the model and B and C to the loadings. In this article, C represents the endmembers, A the concentration of each endmember $f = \{1\ F\}$ in all the input samples and B the fading rate for each endmember. Moreover, because we are dealing with physical and chemical feasible data, the constraints of non-negativity for A and C are enforced during the decomposition process.

The choice of number of components F is not trivial. Typically, if no previous knowledge is known about the tensor's rank, then experiments are done starting from a very small number of components in increments of 1. For each trained model, residual analysis is performed and the chemical meaningfulness of the loadings is interpreted. The model that gives the most sensible fitting from a chemical point of view and has good residual metrics is then selected.

Testing the PARAFAC model for new data

It is possible to test new data based on a trained model. Let's consider a test tensor $X_{test}^{W \cdot K \cdot N}$ with different size in the $1st$ dimension but identical size in the $2nd$ and $3rd$ dimensions with respect to the tensor used for training. Then we can fit the new data by keeping the B and C loadings fixed in Eq. 1 and solving only for the new concentration matrix $A_{test}^{W \cdot F}$. This makes sense under the assumption that the test data has similar chemical content as the data used for training.

Future modelling

The fading rate R_f of each pure pigment is given by the loadings of the $2nd$ mode, B. Mathematically, it could be approximated by a line equation, implying that the reflectance of a pure pigment changes linearly with time:

$$R_f = ak + b, \tag{3}$$

where $k = \{1\ K\}$ are the modelled time steps, a the slope and b the intercept of the line. Once the slope and intercept are computed, we can replace k in Eq. 3 with values higher than K and get the values of the change for future times. These new values can then be input in Eq. 2 to predict the spectra of the original samples for future times other than those modelled. If there are samples in the original data, for which there are microfading spectra recorded for more than K time steps included in the training model, then the future modelling can be validated quantitatively. It is important to mention that the linear approximation in Eq. 3 is a simplification of the real change mechanisms and it assumes that the fading rate of each pigment evolves independently from that of other pigments. However, the fading rate R_f was extracted as one of the factors from the tensor decomposition method, which considers the tandem change of all the microfaded measured samples. Thus, it can be argued

that the interaction between pigments is included to a certain extent in the fading rate curve.

Pigment identification

The endmembers extracted with our proposed method are described spectrally, which facilitates the comparison with reference datasets using established distances in the spectral domain towards pigment identification. We use spectral correlation and spectral angle as comparison metrics with databases of known pigments. Given two spectra s_1, s_2, the spectral angle treats them as vectors and computes the angle between these two vectors as the inverse cosine function of their dot product:

$$\mathrm{SA} = cos^{-1} \frac{\sum s_1 s_2}{\sqrt{\sum s_1^2} \sqrt{\sum s_2^2}} \tag{4}$$

A smaller angle indicates a smaller difference between the spectra. On the other hand, spectral correlation [64] computes the similarity of two spectra as the dot product of their mean-centered signals:

$$\mathrm{SC} = \frac{\sum (s_1 - \overline{s_1})(s_2 - \overline{s_2})}{\sqrt{\sum (s_1 - \overline{s_1})^2} \sqrt{\sum (s_2 - \overline{s_2})^2}} \tag{5}$$

A higher correlation indicates higher resemblance of the two spectra.

Data collection and results

Case study: Oda Krohg's painting "A Japanese Lantern"

In this article, we show the performance of our method on the pastel painting "A Japanese Lantern", also known as "By the Christiania Fjord". (see Fig. 2) created by the Norwegian painter Oda Krohg in 1886 and present in the collection of the National Museum of Norway (inventory number NG.M.00879). The painting is made of pastels applied on canvas and it is not very well documented from a scientific conservation point of view. Thus, the exact materials are unknown, and there is no record of the initial color appearance so as to make any immediate assumption about visible changes in the current version. This leads to the first research objective of our case study: to assess the light sensitivity of the painting materials. Typically, pastel sticks come in a wide range of hues and saturations [65] and are essentially composed of colored pigment powders in combination with white pigments, a white filler and binder [66]. To achieve a certain desired colour, pastel stick might contain a single pigment or a mixture [65]. While various binders can be used for the preparation of pastels [66], art conservators assume that the ones in Oda Krohg's painting are soft pastels and so, probably mixed with aqueous binder in rather small amount. In terms of artistic technique, soft pastel paintings are often built up in layers, which combined with the pluralistic composition of pastel sticks, results in complex pigment mixing mechanisms. Therefore, the second research question for the case study is: can we surpass these complex mixing mechanisms and extract the pure pigments used in the pastel painting?

Fig. 2 Oda Krohg's painting "A Japanese Lantern". Pastel on canvas (1886). Courtesy of photographers Børre Høstland/Lathion, Jacques, National Museum

In order to address these research questions, two areas of interest in the painting were selected by the museum conservator for the analysis: the central lantern and the lantern in the left upper edge. Stylistically, the latter is actually depicting the reflection of the central lantern on the window. In particular, the area along the left edge is of special interest because it has been partially covered by the rebate of the frame, which prevented part of the pigments in the left lantern being exposed to light. Therefore, we are investigating if our approach can detect similar materials in the two lanterns.

Microfading data collection

Specific locations on the central and left were faded using the microfadeometer provided by FotoNowy Institute [67]. The MFT illuminated spots of 0.5 mm diameter, with a white LED at an irradiance of 12.585 MegaLux and a power of 3.44 mW, for a 0°/45°

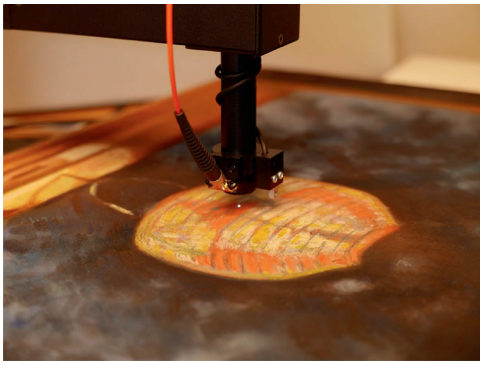

Fig. 3 Microfading measurement setup. Light is incident on the surface at 0° and the colorimeter is collecting the signal at 45°

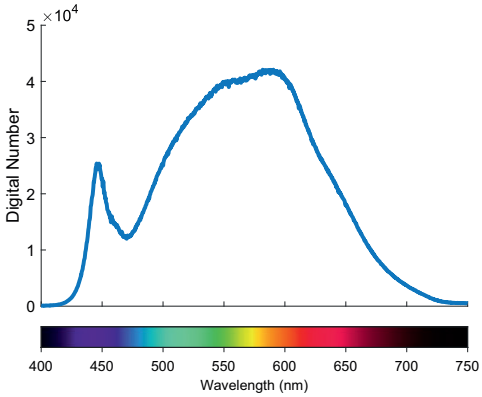

Fig. 4 Spectral power distribution of the white LED of the microfadeometer

geometry, as shown in Fig. 3. The light source was apriori calibrated by the manufacturers with a white standard card [68] and, as can be seen in the spectral power distribution in Fig. 4, it has a stronger emission in the middle and right parts of the electromagnetic spectrum. The measurement was stopped when the ΔE_{00} color difference with respect to the original reached 2 units or after 600 s. For this reason, the cardinality of the observations is uneven, depending on the sensitivity of the pigment: some are measured for 77 s, others for 600, etc. The L*, a*, b* color coordinates are recorded for D65 standard illuminant and CIE 1931 2° observer after every fading iteration. Apart from the color change, the instrument records the spectral reflectance every $11th$ second with a spectral resolution of 2.5 nm in the 400–730 nm range. To reduce the noise, the spectral data was smoothed with a Savitzky-Golay filter [69] of order 2 and window size 17, and then further downsampled. In addition, the spectral range has been restricted to 440 and 680 nm due to the high noise in the data at both far ends of the measured spectrum.

As shown in Fig. 5, for the central lantern, 15 locations were microfaded that cover 5 apparent color groups (pink, green, red, pale blue/violet, orange). The minimum common number of recorded spectral changes is 8 (including the initial reflectance before fading), equivalent to 77 s of light exposure. As far as the left lantern is concerned, 5 locations were selected for investigation, that correspond to red and dark pink colors. The dark pink points have been protected by the painting's frame, which was removed during the microfading measurements. Thus, one hypothesis that we try to verify with our model, is whether the dark pink and the red spots were initially applied from the same stroke, but they now differ in color because fading has occurred in areas unprotected by the frame.

Colorimetric analysis

Before diving into the tensor decomposition specifications and findings, we applied exploratory analysis techniques to get a first-hand overview of the microfading data. The straightforward outcome from a microfading experiment is the color change of the samples as a function of time. This is a primary hint to the stability of the pigments. Figure 6 depicts the ΔE_{00} color difference for central lantern points measured with MFT and shows how the pink samples have the fastest change rate, while the green ones seems to be more stable.

Another immediate analysis from the microfading is to assess the color change for a*, b* coordinates, where a^*_+ corresponds to the red quadrant in the CIE L*a*b* space, a^*_- to green, b^*_+ to yellow, and b^*_- to blue. As shown in 7, the change occurs in the negative direction. This entails that all samples lose the yellow and red chromatic components. It is interesting to note that Red 2 after fading has the same a*b* coordinates as Pink 5 before fading.

Specification of PARAFAC model fitting

The microfaded observations of the central lantern were structured into a 15*8*81 (samples * time steps * spectra) tensor. The three-way array was then decomposed using parallel factor analysis (PARAFAC) with the Matlab implementation of the N-Way toolbox [70]. In Additional file 1, we inserted a code snippet to exemplify basic operations. Setting the number of components in the PARAFAC analysis is not a trivial task. We adopted a trial-and-error approach starting from 5 components and stopping where the loadings of the endmember resembled impossible reflectances. Our rationale was rooted in the typical formulation

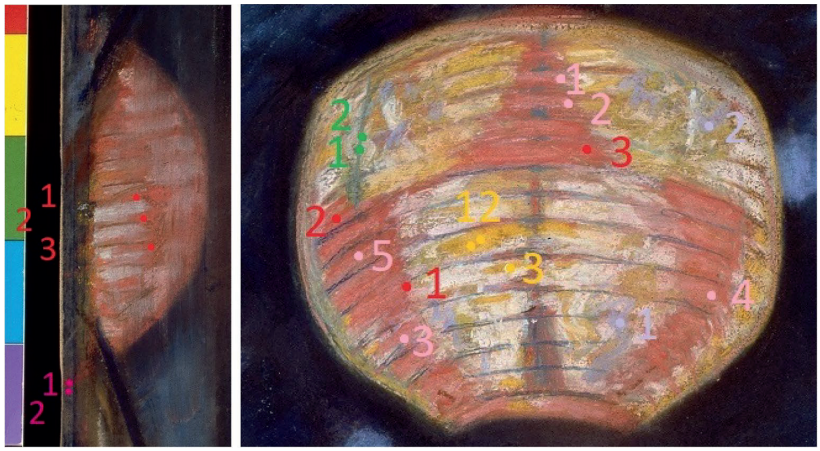

Fig. 5 Locations measured with the MFT for the left lantern and the central lantern. Courtesy of Børre Høstland, National Museum

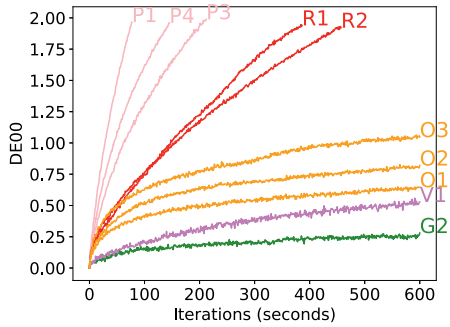

Fig. 6 ΔE_{00} as a function of time for selected microfaded samples in the central lantern, representatives of each colour group

of pastels: they are manufactured as saturated color, where typically there would be a dominant pure pigment combined with others in smaller quantities. Given that samples collected in the microfading experiment roughly represent 5 colour groups, we assumed there should be at least 5 pure pigments. Figure 8 depicts the endmembers extracted when fitting the model with 5, 6 and 7 components. We can see that in the latter case, the spectra become noisier. Also, correlated spectra seem to appear (orange and cyan curves) and the orange curve resembles a composite multi-lobe signal rather than a realistic reflectance. On the other hand, the 5 and 6-component case output smooth and similar reflectances. Nonetheless, the 6-component case introduces an additional component in the red end of the spectrum (cyan curve in Fig. 8b), which is a realistic reflectance resembling a typical red lake. As a matter of fact, in a later subsection 4.7, we will prove that indeed, this endmember has a high similarity with a crimson carmine lake, when comparing with a reference database of pigments. Thus, we continued the analysis with the factors of the tensor decomposition model fitted for 6 components. The model converged in 1099 iterations, retaining 99.99% variance in the data while achieving a sum-of-squared residuals of 0.0145. Moreover, the histogram of the residuals shows a bell-shaped curve around 0 (see Fig. 9), suggesting that the variance follows a normal distribution, which is a good quality indicator of the regression process.

Figure 10 plots the three modes of the resulting model: endmembers, fading rate of each endmember, and concentration of each endmember in the input samples in the central lantern collected with the microfadeometer. In Additional file 1: Figure S1 displays the measured and modelled spectra for all the 15 samples, at time steps 1 and 8. The endmembers have the same color code in the three plots. One of the first comments that emerges is that the Pink 1–5 samples seem to be predominantly made of the endmember 2 (magenta curve), which also fades the most rapidly because it has the steepest descent in Fig. 10b. This is in conformity with the colorimetric analysis of the color degradation, where the Pink samples change most rapidly, reaching 2 ΔE_{00} units before the other samples. Another interesting outcome is given by the concentration of the endmember in each sample. As the microfading experiment

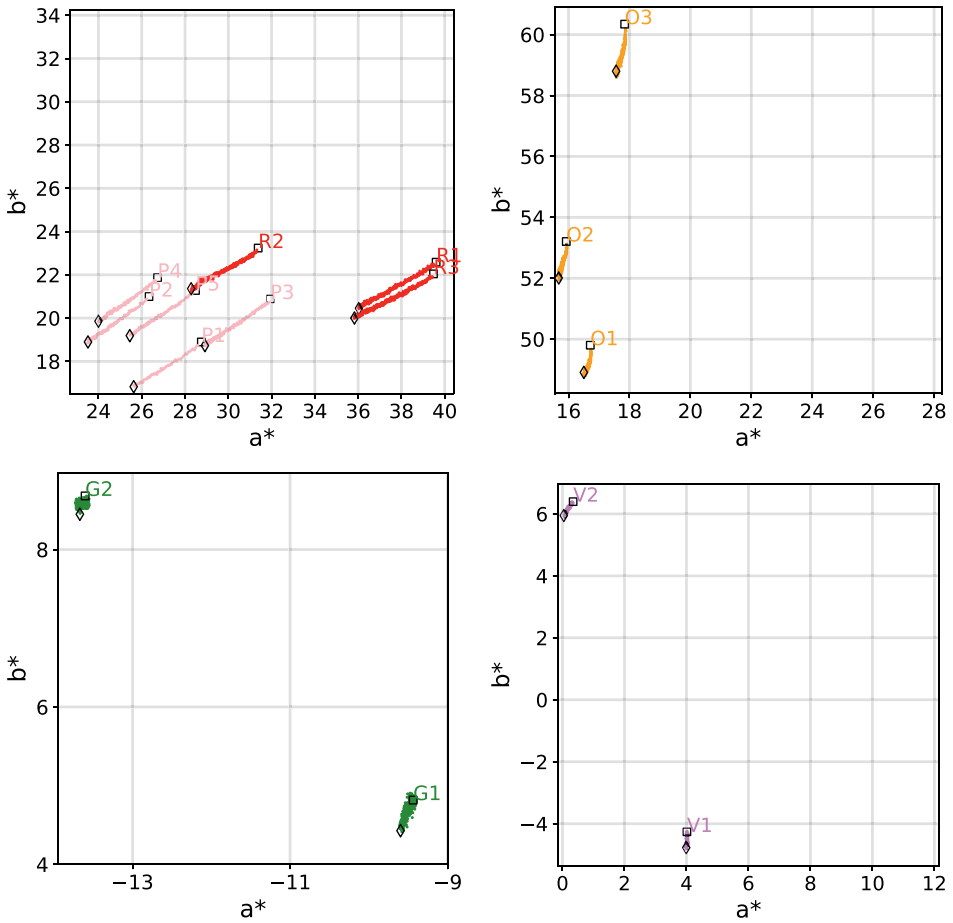

Fig. 7 The chromatic changes of the microfaded samples in the central lantern. The black square marks the initial value, before fading, while the diamond marks the final value, after fading

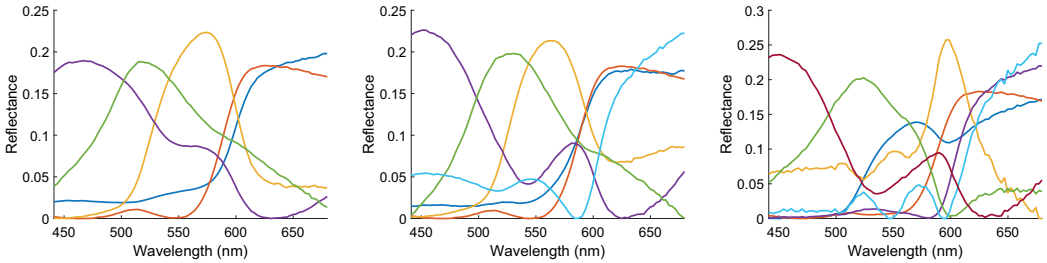

(a) 5 components (b) 6 components (c) 7 components

Fig. 8 Endmembers obtained when fitting the tensor decomposition model with 5 (**a**), 6 (**b**) and 7 (**c**) components. In the 7 component case, the some spectral curves are noisy (cyan and orange curves) and seems to have a mixed rather than pure chemical composition. While both 5 and 6 component cases give smooth curves and similar members, it seems that the latter is able to extract a different pigment (cyan curve), that with the sudden growth close to 600nm, shows the characteristic of an organic red lake pigment

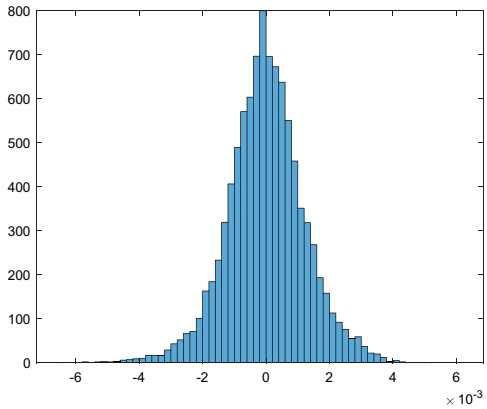

Fig. 9 Histogram of the residuals for the PARAFAC model fitted with the microfaded observations in the central lantern

proceeds, we can infer that the underneath pastel layers get revealed as the top layer fades. This effect should be stronger for the pigments that are more fugitive. However, given the composite nature of the pastel sticks, we should also take into account that dominant concentrations in a sample hint to the multiple pigments present in a single pastel stick.

Future modelling

In the trained model, we included only a subset of the measured time steps, which is the minimum number of measurements common to all 15 samples. However, except Pink 1 sample, there are more measurements for the rest of the samples. Hence, another way to validate the goodness of the model is to test how well the excluded measurements can be explained by the trained model. To this purpose, we need to extend the fading rates for future time steps. As explained in subsection 3.3, we generated the fading rate for more than 8 time steps, by applying linear regression on the loadings in Fig. 10b. This gives as a slope and an intercept for the temporal change rate of each endmember, that we can use to further compute the fading rate for new time steps using Eq. 3. Table 1 summarizes the line equations for the fading rates of the 6 endmembers and Fig. 11 exemplifies the goodness of the linear fit to the changing trend of endmember 1.

Using these fits, we generate the fading rate for time steps higher than 8 with Eq. 3. Then, we input these new values in Eq. 2 to recover the spectra of the samples.

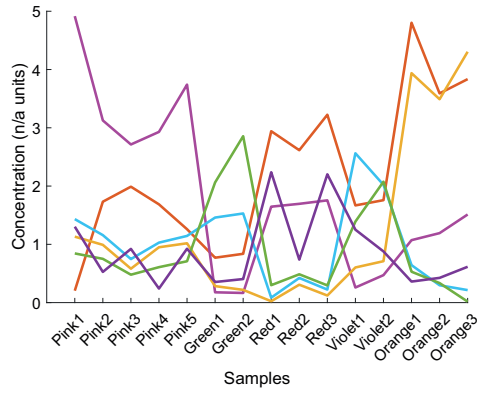

(a) Concentration

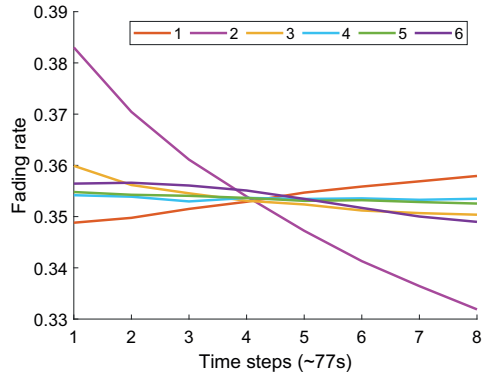

(b) Fading rate

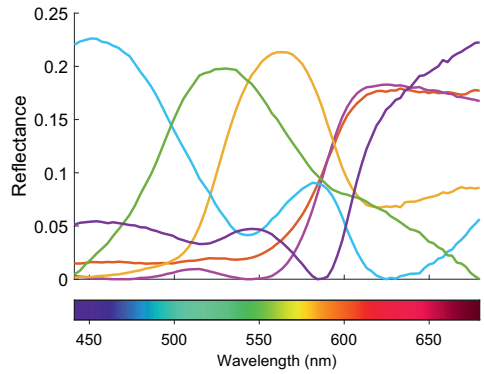

(c) Endmembers

Fig. 10 Loadings of the three factors (**A**, **B**, **C**) in our tensor decomposition model, fitted for 6 components

Table 1 Slope, intercept and coefficient of determination for fitting the fading rate of the 6 endmembers to a line

	1	2	3	4	5	6
Slope	0.0014	−0.0071	−0.0013	−0.0001	−0.0031	−0.0012
Intercept	0.3474	0.3850	0.3592	0.3539	0.3549	0.3589
R^2	99.26 %	97.17 %	88.90 %	24.91 %	96.06 %	93.98 %

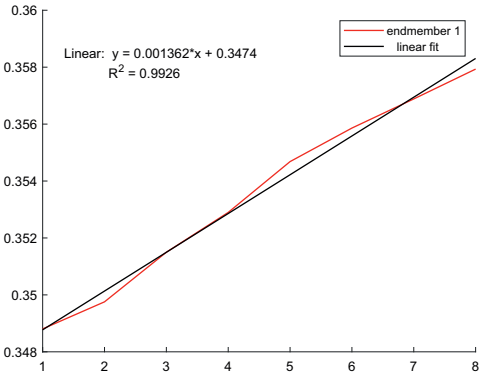

Fig. 11 Linear regression fit for the fading rate of endmember 1. *y* -axis represents the fading rate, while *x*-axis stands for the time step

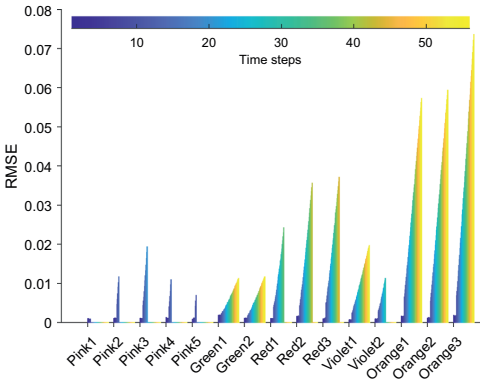

Fig. 12 The RMSE between measured and reconstructed spectra for future time steps. The RMSE is computed for each measured time step, hence the different cardinality of bars plotted per sample. Overall, the RMSE has small values, suggesting that our model is able to reconstruct future reflectances with good quality. However, the higher the time step values, the larger the RMSE, showing a limitation of the linear approximation of the fading rate

Afterwards, we compare the simulated reflectances with the measured ones with the root mean square error metric (RMSE). The barplot in Fig. 12 shows

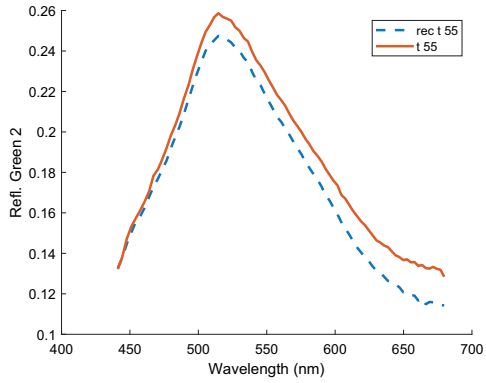

Fig. 13 Example of future spectral simulation for Green 2 sample for time step 55 (594 s). The reconstruction presents slight changes in amplitude, but follows well the spectral shape of the original. In this case, linear approximation of the fading rate seems to be more robust for high values of the time steps with respect to other samples

RMSE values for all the simulated time steps available for every sample. To be noted that the reconstructions for the first 8 time steps are done with the fading rate of the trained model, not using the linear approximation in eq. 3. Overall, the RMSE values are very low, proving a good performance of our model in estimating the future reflectance of the samples. Nevertheless, it is clear from the plot that the error increases with higher values of the time steps. This suggests a lower accuracy of the line fitting in approximating the fading rate when the gap between the modelled and simulated time steps is too high, especially for orange samples. It seems that the linear regression is most robust for the green samples. Indeed, Fig. 13 shows the measured and reconstructed spectra for Green 2 sample at time step 55 (594 s), which are very similar in shape and only slightly vary in amplitude.

Even though the linear regression gives the lowest coefficient of determination for endmember 4's fading rate (see Table 1), the future simulation of the samples with a high concentration of endmember 4 (Violet 1, Violet 2) is not severely affected as the corresponding RMSEs are among the lowest numbers. The visual analysis of the reconstructed reflectance of Violet 1 at time step 16

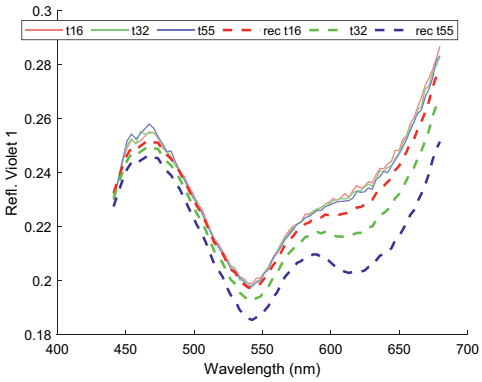

Fig. 14 Example of future spectral simulation for Violet 1 sample for time steps 16 (165 s), 32 (341 s) and 55 (594 s). The reconstruction at time step 16 slightly exaggerates the decrease of the spectra at 600–650 nm, but otherwise closely follows the measured reflectance. The reconstructions worsen in this spectral range for time step 32 and for time step 55

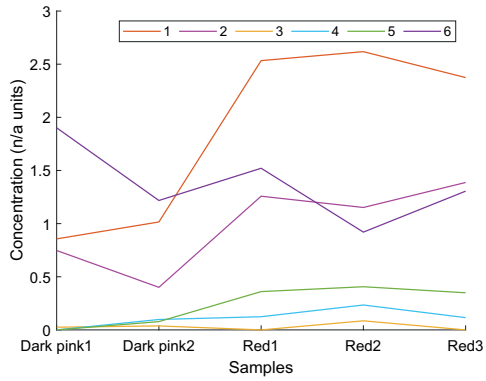

Fig. 15 The estimated concentration of the 6 endmembers in the left lantern samples. The estimation was achieved by using the endmembers and fading rates apriori obtained through training the PARAFAC model on the central lantern samples

in Fig. 14 confirms the accuracy of the simulation with respect to the measurement. However, as previously mentioned, the reconstructions further deviate from the original for time step 32 (341 s), and especially time step 55 (594 s). The deviation happens mostly in the region 600–650 nm, which might also indicate unexplained variation of the tensor decomposition model in this spectral range. In future, other approaches to model the fading rate can be implemented towards improvement, such as spline interpolation or time-series models [71].

Model validation for the left lantern

In the previous sections we proved that our proposed tensor decomposition model is statistically valid and works fine for future modelling of the samples with the same chemical composition as those included in the training stage. Now, we'll verify the performance of our model for unseen microfaded samples, taken from the left lantern in the pastel painting (see Fig. 5). It is assumed that the same materials were used to render the red and pink colors in the central and left lantern, since actually the left lantern depicts the reflection of the central lantern. If so, then the trained model should be able to explain the variance in the left lantern data. To test this hypothesis, we arrange the 5 microfaded measurements into a three-way tensor, similar to the central lantern, which results into a 5*8*81 tensor. Then, we fitted a PARAFAC model to this new data, by keeping fixed the loadings of the B (fading rate) and C (endmembers) factors extracted with the previously trained model (for details, revise subsection 3.2). The model thus fitted achieved a sum of squared residuals of 0.0476. As a result, we obtain a new set of loadings, the A factor, (shown in Fig. 15) that gives the concentration of the already known endmembers in the left lantern samples. All 5 samples have as major constituents endmember 1, 2 and 6, but in different proportions. It appears that Red 1–3 samples in the left lantern are predominantly made of endmember 1, similar to the red samples from the central lantern. On the other hand, it seems that the two Dark Pink samples are richest in endmember 6. Additional file 1: Figure S2 displays the measured and modelled spectra at time steps 1 and 8, for the 5 samples in the left lantern.

To assess the quality of the reconstruction, we graphically analyze the residuals of the model fitted on the test data. Figure 16 shows the histogram of the residuals for each of the 5 samples, and the surface plots of the residuals distributed along the spectral and temporal dimensions. We'd expect the histograms to have a Gaussian distribution and the surface plots to be as flat as possible. The histogram for Red 1–3 samples are centered around 0 and fairly symmetric, even though they are slightly skewed towards the left. While the magnitude of the left-side skewedness and asymmetry are more evident for the Dark Pink samples, the normal distribution pattern does not get disrupted to a far extent. At the same time, while the surface plots are not completely flat, showing some variation that the model did not capture from the data, the magnitude of this unexplained structure is however of a very low order. Thus, the model has statistical relevance in explaining the left lantern samples, and we can conclude that the materials used in the central lantern are most likely the same as the ones in the left lantern.

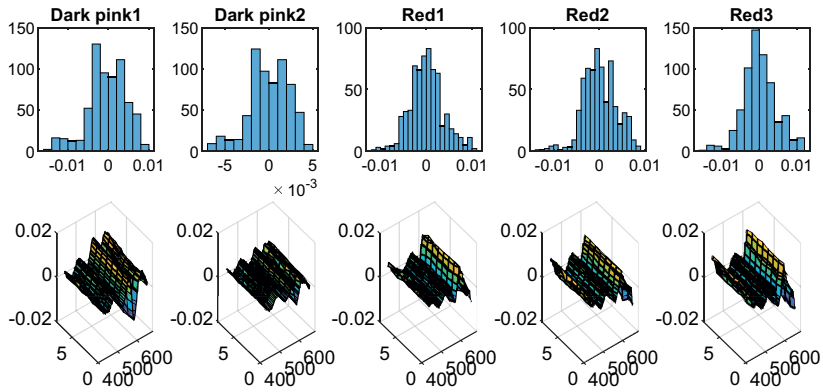

Fig. 16 Visualization of the residuals when testing the model on the left lantern. The residuals are plotted for the first factor, A, i.e. concentration of endmembers in each sample. The histogram of the residuals (top) show a fairly symmetric spread around the mean and the distribution is close to a Gaussian one. The surface plots (bottom) distribute the residuals ($z-$ axis) along the spectral ($x-$ axis) and temporal dimension ($y-$ axis) hint that there's little chemical structure in the test samples that the model is not able to explain

Another research question is whether the 5 samples on the left lantern correspond to the same materials, since in the painting it looks as if they were part of the same strokes. In this regard, it is noteworthy to mention that the resulting factor A loadings point to a sensible layering pattern of the pastels. Considering that the samples Dark Pink 1 and Dark Pink 2 were collected from an area in the painting that was covered by the frame, we know they were less exposed to less light than the rest of the left lantern. Assuming that all the 5 samples represent the same material, the uneven exposure to light would explain the difference in the dominant pigment component. For instance, if the initial material was made of a layer of endmember 1 covered by a layer of endmember 6, the fact that Red 1–3 samples were exposed to light for a considerably higher extent, would explain why they have less concentration of endmember 6 as opposed to Dark Pink 1 and Dark Pink 2. In addition, this theory can be corroborated by a common artistic practice, namely that of covering a base red pigment (endmember 1) with a lake glaze (endmember 6) [45]. Even though this theory seems plausible, in order to fully validate it, we would need to complement our study with analytical data such as XRF, that would shed further light on the chemical composition of the pigments. We plan to pursue such an extended analysis in our future work.

Pigment identification

We compared the spectra of our endmembers with three reference datasets of known pigments using spectral angle and spectral correlation. The first dataset includes spectrophotometric measurements of 54 pigments combined with various binders: gum Arabic, gum Arabic measured with a reflection probe (that discards specularities from the measurement), egg-tempera, acrylic and fresco [72]. From here on, this dataset will be called FORS-CHO. It is believed that the pastels used in the painting are soft, and most probably an aqueous binder was used in small quantities. For this reason, out of the binders in the FORS-CHO dataset, we chose the pigments bound with gum Arabic (and measured with a reflection probe for higher precision), because this pigment-binder combination is considered to be the most sensible with respect to the soft pastels in the painting. The second dataset consists of hyperspectral measurements with the HySpex camera of a pigment panel, called ENST, that was prepared by National Gallery in London for the VASARI project [73]. It contains 64 unvarnished patches of historical pigments bound with egg-tempera and applied on a panel primed with gesso. Even though the binder is egg-tempera, which is not typically used for the preparation of soft pastels, we still used this dataset as standard for comparison because it contains a higher variety of historical pigments than the first dataset. Finally, the third reference collection is the only spectral database of pastels applied on paper and measured with a spectrophotometer, and it is published by Centore [74]. While this database includes both modern brands (Blue Earth, Unison, Great American, Mount Vision) and historical pastel manufacturers (Girault, Sennelier, Schmincke), nowadays all the manufactures most probably use modern materials for the pastels' preparation. Usually, these recipes are not revealed by the manufacturers so the chemical composition is unknown making it

difficult to interpret and validate the results in a pigment identification task. Nonetheless, we deemed it interesting to explore the resemblance with our endmembers especially because it is a pastel-to-pastel comparison. To be noted that among the pastel manufacturers present in this dataset, Girault and Schmincke were already producing pastels when Oda Krohg painted "A Japanese Lantern" in the late $19th$ century.

We have to keep in mind that the painting in our study has a more intricate formulation than the patches measured in the three spectral libraries. This is expected to negatively impact the quality of the spectral matches [11]. While for future work, we plan to collect a spectral reference dataset of a mockup that is carefully designed to mirror the materials and technique of the studied painting, we are still interested to see if the comparison with the currently available libraries leads to sensible matches.

The spectral sampling of the pigments in the reference databases varies with the measuring instruments, so they were interpolated to align to the sampling of the endmembers. After the interpolation, the spectral metrics in Eq. 4 and 5 were computed in a two-folded way: for the original reflectance vector and for the first derivative of the reflectance. The first derivative better captures the inflection points (minima and maxima) of the spectral reflectance curve. As a result, the spectral distance comparison will be more sensitive to big shifts in reflectance, which has more discriminative power than reflectance alone for pigment analysis, as proved in previous works [8]. In order to simultaneously visualize the similarity according to the reflectances, and both spectral metrics, we are visualizing the distances with a bubble chart in the following way. For each reference dataset, the lowest 5 spectral angles with respect to the endmembers, are chosen for the reflectance and first derivative mode, giving a total pool of maximum 10 best matches. Then, we define a 2D coordinate system of the bubble chart with the spectral angle in the reflectance mode as the $x-$axis and the spectral angle in the derivative mode as the $y-$axis. We plot each of the 10 best matches in this coordinate system. It can happen that the first derivative and reflectance comparisons give overlapping matches. For this reason, we actually have less than 10 bubbles plotted for each pigment. Furthermore, the diameter of the bubbles is scaled with the spectral correlation value between of the endmembers with the reflectances in the reference datasets. We chose to vary the size of the bubbles with the diameter instead of the area because previous research [75] showed that the human visual system better appreciates changes in the diameter of a disk as opposed to its area.

Hence, in the bubble chart visualization, an ideal candidate would be represented by a big size bubble located in the bottom left corner of the chart, which translates to the following attributes: big correlation, low spectral angle for the reflectance, low spectral angle for the first derivative. Figure 17 displays the similarities of our endmembers (1–6) with the pigments in the ENST dataset, while Fig. 18 features the FORS-CHO dataset. It is easy to notice that overall, the spectral angles computed for the first derivative have a higher magnitude than those computed in the reflectance mode. This is because the first derivative is sensitive to any change of growth in the reflectance curve, and so it amplifies the noise of the initial signal. At the same time, the values of the spectral metrics are lower for the comparison with the ENST library. This might be due to the use of historical recipes in the manufacturing of the ENST target. At a quick perusal of the charts, we can see that there is a certain clustering of the endmembers, meaning that some endmembers have better matches than others. For instance, endmember 1 (red) has closer matches than endmember 3 (orange) since the candidates for the former are located in the bottom left corner, while those of the latter are in the top right corner. For endmember 1, we can see that the reflectance comparison with ENST suggest the *red lead* pigment as the best match, because it's situated in the left-most corner, while the first derivative spectral angle picks *red ochre* as having the lowest value in the y dimension. Interestingly, *red lead* is designated as the best candidate for endmember 1 by the FORS-CHO dataset as well, followed by *vermilion* and *red ochre*. Moreover, we can see that all candidates for the red endmember have bubbles of similar size, so in this case, spectral correlation does not bring clarification to distinguishing between candidates. ENST shows as secondary matches vermilion, cadmium red and rose madder, which are positioned very close to each other, with cadmium red being slightly better than the other two. Following the same reasoning, the most valid choices from ENST dataset for endmember 2 (pink) seem to be *red lead* and *vermilion*. Nonetheless, *mercuric iodide* arises as the best match according to the first derivative comparison, but it jumps more than 2 orders of magnitude along the $x-$axis. Out of the FORS-CHO pigments, *red lead* comes atop with the highest similarity.

It is interesting to note here several known aging attributes of the red lead pigment. It has been documented [41] that when exposed to sunlight, rain and carbon dioxide, red lead can cause the formation of lead carbonate, giving it a whiter, thus pinkish appearance. Hence, if we follow the theory that both endmembers are red lead, the difference in their spectra might be due to this aging phenomena. On the contrary, if we were to judge by inflection peaks only, endmember 1 and 2 have maxima at 590 nm and, respectively, 587 nm, which were associated to

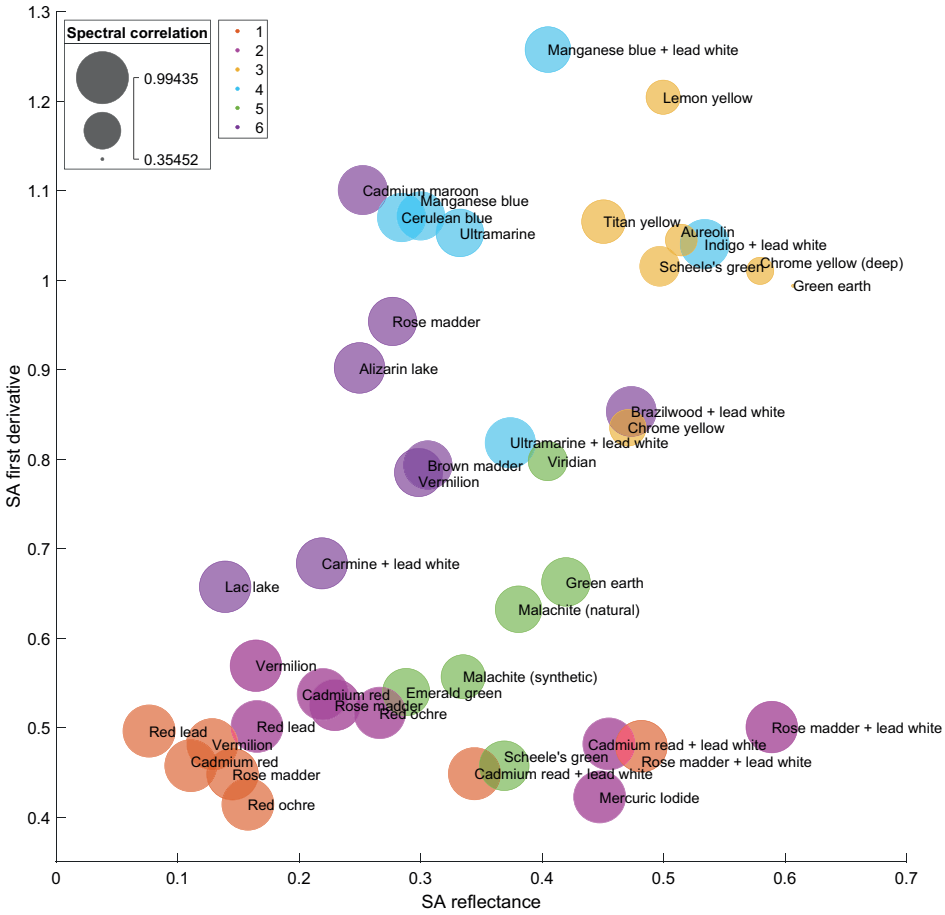

Fig. 17 Matches of the endmembers with the pigments in the ENST dataset, visualized as a bubble chart. The x-coordinate represents the spectral angle in radians computed on reflectance spectra between endmembers and reference dataset, while the y-coordinate is the spectral angle in radians computed on the first derivative. The diameter of the bubble is proportional with the spectral correlation between the reflectance spectra. Bigger bubbles in the bottom left indicate a higher confidence of the match

vermilion in a previous multi-analytical study of pigments [76]. In the same study, red lead was associated with a peak shifted towards 565 nm. However, we believe this might be to a great extent influenced by the media (the previous study was performed for an illuminated manuscript) and the binder. Actually, as we can see in Fig. 19, the reference vermilion has a peak at 600nm, while red lead reaches its maxima at 578 nm. At the same time, the peaks of endmembers 1 and 2 are approximately equally distant to the reference red lead and vermilion in the ENST dataset.

As far as endmember 3 is concerned, *chrome yellow* surfaces as the most reasonable option from the ENST dataset, while FORS-CHO leads to *saffron* and *cobalt yellow* as best compromise along the two dimensions. By studying the reflectance of endmember 3, we can actually see that it doesn't have the characteristics of a pure orange, because the curve has a depression in the red region of the spectrum. This means that the color is shifting to green, which is a well known aging behaviour of the chrome yellow pigment [41]. The shift to green of chrome yellow has been encountered in other paintings, such

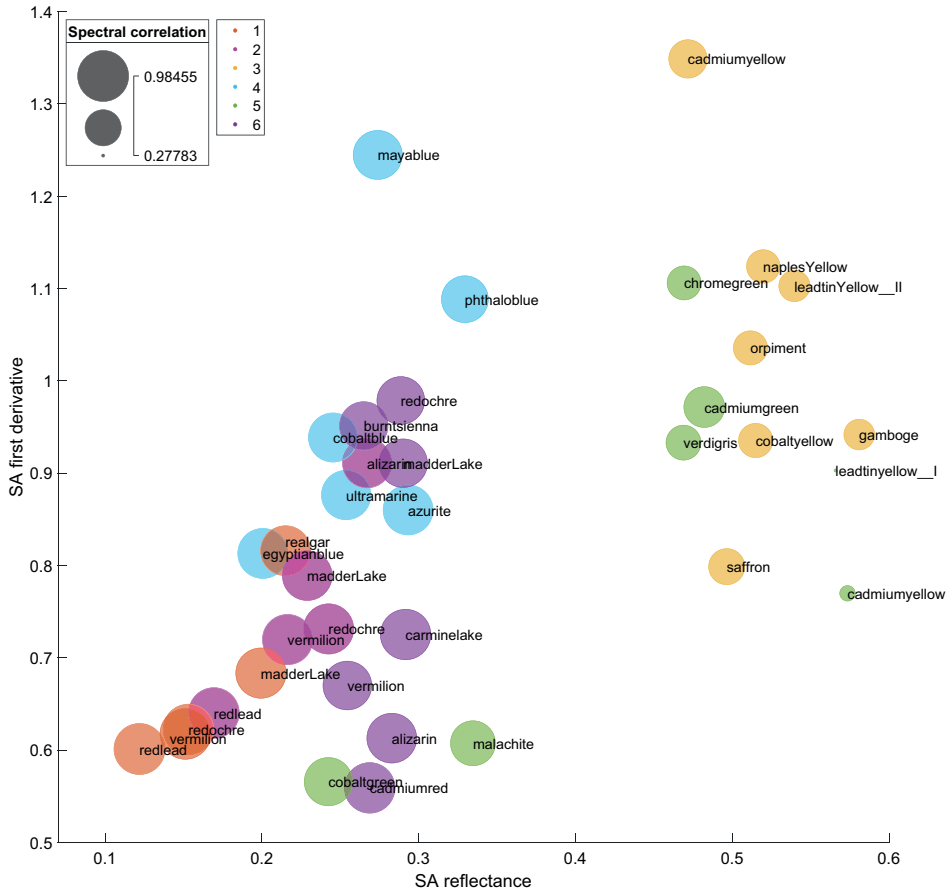

Fig. 18 Matches of the endmembers with the pigments in the FORS-CHO dataset, visualized as a bubble chart. The x-coordinate represents the spectral angle in radians computed on reflectance spectra between endmembers and reference dataset, while the y-coordinate is the spectral angle in radians computed on the first derivative. The diameter of the bubble is proportional with the spectral correlation between the reflectance spectra. Bigger bubbles in the bottom left indicate a higher confidence of the match

as Van Gogh's "Field with Irises", as recorded by Geldof et al. [77]. Figure 20 displays the reflectance of the aged chrome yellow from Van Gogh's painting together with the spectra of our endmember. While we can see that the two spectra are similar, it appears that in the case of our endmember, the aging is more advanced. However, we should keep in mind that it is possible for this accentuated loss of the red color to be rooted in the limitations of our model in perfectly unmixing the components. Nonetheless, chrome yellow classifies as a feasible option for endmember 3 and the shift to green would also explain why the spectral metrics give generally higher errors for this component.

Top choices for endmember 4 (blue) from ENST seem to be *cerulean blue*, *manganese blue* and *ultramarine mixed with lead-white*. At the same time, the most similar pigments from FORS-CHO are *Egyptian blue*, *cobalt blue* and *ultramarine*. Regarding endmember 5 (green), *emerald green*, *synthetic malachite* and *Scheele' s green* are nominated as the most similar pigments among ENST group. On the other hand, *cobalt green* and *malachite* are the most salient with respect to the FORS-CHO group. As for endmember (violet), it is obvious from the sudden and steep growth of the reflectance curve close to 600 nm that it is a red lake. Red lakes surface as good options from the bubble charts as well. However, a very

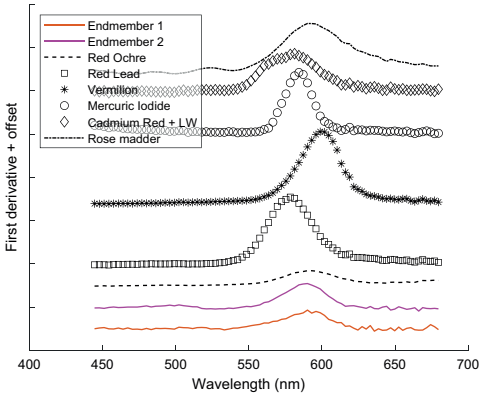

Fig. 19 First derivative spectra of endmembers 1 and 2 together with best matches from the ENST spectral library. Offset was added for clarity

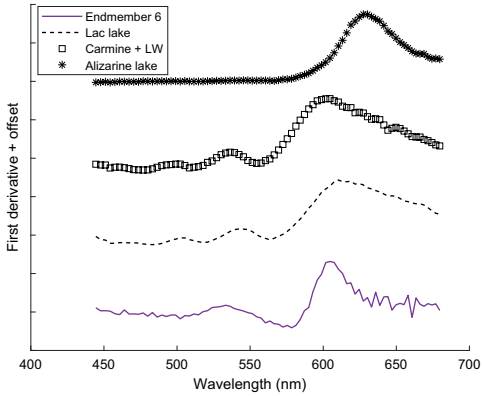

Fig. 21 First derivative spectra of endmember 6 together with potential candidates from the ENST spectral library. Offset was used for clarity. Endmember 6 has two minima between 400–600 nm, with the second one at 578 nm. Also, the maximum overlaps with that of carmine lake, while the lac lake has the maximum more towards the right

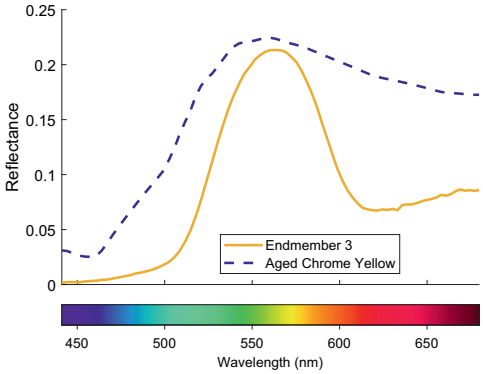

Fig. 20 Solid line: the 3*rd* endmember in our model, which is found in highest concentration in the yellow samples. Dashed line: chrome yellow in an aged version, as identified in Van Gogh's "Field with Irises near Arles" by Geldof et al. [77]. Chrome yellow has the characteristic of turning green over time and so lose the longer-wavelength components. For our endmember, which is likely a chrome yellow, this tendency is obvious

helpful tool in identifying the actual type of lake is the protocol proposed by Fonseca et al.[7]. According to this protocol, the presence of two minima between 450–600 nm prove that it is a *carmine lake*. Moreover, the proximity of second minimum to 600 nm, as shown in Fig. 21 gives additional information about the preparation of the carmine lake in that it was precipitated on aluminum.

Out of the comparison with the Centore dataset (See Fig. 22), we can see that historic pastel brands emerge among top 5 matches for the endmembers: Girault 36 and Schmincke 042B for endmember 1; Girault 196 and Sennelier 930 for endmember 2; Girault 195 for endmember 3; Sennelier 290 for endmember 4; Girault 229 and Schmincke 076 H for endmember 5; and lastly Schmnicke 048B for endmember 6. While the chemical formulation of the pastels included in the Centore database is unknown, it is still possible that historic manufacturers might have preserved a formula close to the traditional formulations.

With the bubble chart visualization approach, we aim to shortlist possible pigments and to alleviate the task of conservators of assessing the potential candidates for identification. It is up to the conservator to give weights to the two spectral metrics (SA in reflectance or derivative mode, and SC in reflectance mode). We believe with this visualization, it is also easy to spot and discard anachronistic pigments (as long as there are no suspicions of forgery), albeit high votes from the spectral metrics. For example, titanium yellow could be discarded as an option for endmember 3, because it is a pigment that was created more than 60 years after the painting was created. Nonetheless, pigment identification is a complex task, hence multiple data, visualizations and knowledge about the pigment aging behaviour should all be weighed by an expert. Also, for full validation, analytical data such as XRF should be added to the spectral analysis, which we plan to collect in the future.

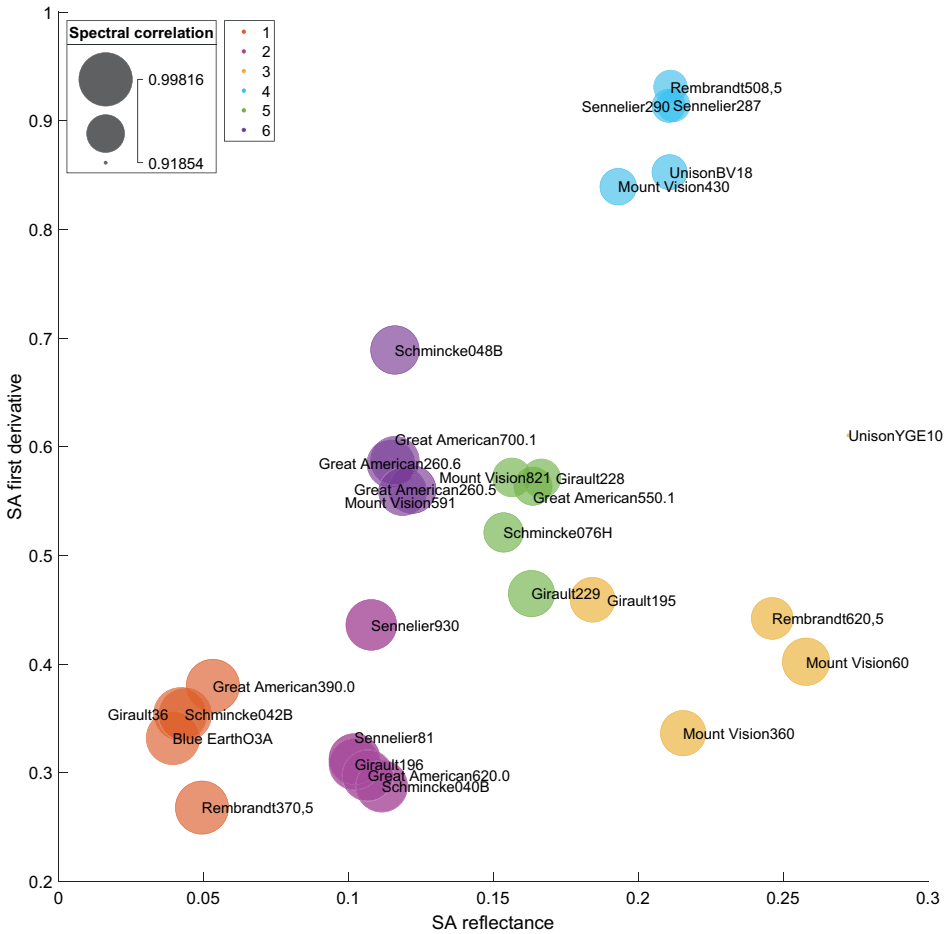

Fig. 22 Matches of the endmembers with the pastels in the Centore dataset, visualized as a bubble chart. The x-coordinate represents the spectral angle in radians computed on reflectance spectra between endmembers and reference dataset, while the y-coordinate is the spectral angle in radians computed on the first derivative. The diameter of the bubble is proportional with the spectral correlation between the reflectance spectra. Bigger bubbles in the bottom left indicate a higher confidence of the match

Discussion

To summarize our results, we showed how microfading spectrometry can be useful to the analysis of an artwork beyond assessing pigments' sensitivity to light and summarizing their color degradation. Namely, we use the microfading data to perform pigment unmixing and identification. Moreover, we model the photodegradation phenomena in a spectral not only color dimension, and for all wavelengths in one go as opposed to a tedious recovery of the fading rate for each wavelength taken separately. This is achieved with multivariate data techniques, such as the tensor decomposition model that is the pillar of our work. This model is trained on the microfading data and decouples signals to get pure pigments (endmembers) on a spectral basis, together with their fading rates. As a byproduct, we can solve the pigment identification task by comparing the endmembers with reference spectral datasets of pigments.

While the results look promising, our approach is not without limitations. Above all, we lack ground-truth to fully validate our results. For the pigment identification task, we plan to solve this in the future by collecting XRF data of the painting. In addition, our method requires user input, as long as the number of components

(endmembers) is concerned. This is common to other traditional pigment unmixing methods, such as PPI. Indeed, with pigment unmixing being such a complex task, we believe that art conservators and art historians should remain in the loop and ascertain the chemical meaningfulness of the endmembers. Moreover, it is important to mention that the tensor decomposition is a linear unmixing method that might not manage to capture all the non-linearities present in a pastel painting, where both intimate and layered mixing mechanisms exist. While the accuracy of tensor decomposition for spectral unmixing tasks is supported by previous findings in chemical [37] and computer vision [31] applications, in future, we plan to compare the performance of our approach with that of non-linear unmixing models. Finally, although we show results for a single case study, our method can be applied on any other type of colorant data (ink, dyes, etc.) and artworks given a set of overlapping microfading measurements and we intend to test this on mockups and additional artworks.

Conclusion

In this article, we presented an approach to pigment characterization in a painting. Our method is based on a tensor decomposition model that, from a set of microfading measurements, disentangles in one shot, the reflectances of pure pigments, their concentration and their fading rate as a function of time.

We statistically validate our model on the training data, as well as for unseen, test data. In addition, we compare the endmembers with reference datasets of pigments and we present our results with a bubble-chart visualization that is capable of combining the result of three spectral metrics. This way, we ease the decision of art conservators in shortlisting the best pigment matches.

In conclusion, we showed how microfading, which is traditionally used only for assessing sensitivity to light, can be useful as well for the task of pigment characterization. In this context, it appears that parallel factor analysis shows promising results for pigment unmixing.

Abbreviations

CIE	Commission Internationale de l'Éclairage (International Commission on Illumination)
MFT	Microfadeometer
LED	Light-emitting diode
PARAFAC	Parallel factor analysis
PCA	Principal component analysis
PPI	Pixel purity index
RMSE	Root mean square error
SA	Spectral angle
SC	Spectral correlation
XRF	X-Ray fluorescence

Supplementary Information

The online version contains supplementary material available at https://doi.org/10.1186/s40494-023-00910-x.

Additional file 1: The supplementary file attached to this paper includes a code snippet for a better understanding of the implementation details, as well as plots with all the measured and modelled spectra of the samples in the central and left lantern.

Acknowledgements
No acknowledgement.

Author contributions

IMC: conceptualization, methodology design, software implementation, formal analysis, investigation, results' visualization and interpretation, writing of the main manuscript; TGP: conceptualization of conservation-related research questions, collection of the microfading data, investigation and interpretation, revision of the final manuscript; SG and JYH: supervised the research, ensured the funding acquisition, revision of the final manuscript. All authors read and approved the final manuscript.

Funding
Open access funding provided by Norwegian University of Science and Technology. This work has not received additional funding.

Availability of data and materials

The datasets used and/or analysed during the current study are available from the corresponding author on reasonable request.

Declarations

Competing interests

The authors declare that they have no competing interests.

Received: 13 December 2022 Accepted: 19 March 2023
Published online: 13 April 2023

References

1. Dooley KA, Chieli A, Romani A, Legrand S, Miliani C, Janssens K, Delaney JK. Molecular fluorescence imaging spectroscopy for mapping low concentrations of red lake pigments: Van Gogh's painting The Olive Orchard. Angew Chem Int Ed. 2020;59(15):6046–53. https://doi.org/10.1002/anie.201915490.
2. Kimmel BW, Baranoski GVG, Chen TF, Yim D, Miranda E. Spectral appearance changes induced by light exposure. ACM Trans Gr. 2013;32(1):10–11013. https://doi.org/10.1145/2421636.2421646.
3. Bacci M, Orlando A, Picollo M, Radicati B, Laterna G. Colour analysis of historical red lakes using non-destructive reflectance spectroscopy. PACT. 2000;58:21.
4. Johnston RM, Feller RL. The use of differential spectral analysis in the study of museum objects. Dyestuffs. 1963;44(9):1–10.
5. Aceto M, Agostino A, Fenoglio G, Idone A, Gulmini M, Picollo M, Ricciardi P, Delaney JK. Characterisation of colourants on illuminated manuscripts by portable fibre optic UV-visible-NIR reflectance spectrophotometry. Anal Methods. 2014;6(5):1488–500. https://doi.org/10.1039/C3AY41904E.
6. Bisulca, C., Picollo, M., Bacci, M., Kunzelman, D.: UV-Vis-NIR reflectance spectroscopy of red lakes in paintings. In: 9th International Conference on NDT of Art, Citeseer, Jerusalem, Israel; 2008. pp. 25–30.
7. Fonseca B, Schmidt Patterson C, Ganio M, MacLennan D, Trentelman K. Seeing red: towards an improved protocol for the identification of madder- and cochineal-based pigments by fiber optics reflectance spectroscopy (FORS). Herit Sci. 2019;7(1):92. https://doi.org/10.1186/s40494-019-0335-1.

8. Gabrieli F, Delaney JK, Erdmann RG, Gonzalez V, van Loon A, Smulders P, Berkeveld R, van Langh R, Keune K. Reflectance Imaging Spectroscopy (RIS) for operation night watch: challenges and achievements of imaging rembrandt's masterpiece in the glass chamber at the rijksmuseum. Sensors. 2021;21(20):6855. https://doi.org/10.3390/s21206855.
9. Deborah H, George S, Hardeberg JY. Pigment mapping of the scream (1893) based on hyperspectral imaging. In: Elmoataz A, Lezoray O, Nouboud F, Mammass D, editors. Image and signal processing. Cham: Springer; 2014. p. 247–56.
10. Deborah H, Ferrer J, Sandu I, George S, Hardeberg J. Old Man in Warnemunde (1907) colouring palette: A case study on the use of hyperspectral imaging for pigment identification. 2017;25:339–344. https://doi.org/10.2352/ISSN.2169-2629.2017.25.339.
11. Kleynhans T, Messinger DW, Delaney JK. Towards automatic classification of diffuse reflectance image cubes from paintings collected with hyperspectral cameras. Microchem J. 2020;157: 104934. https://doi.org/10.1016/j.microc.2020.104934.
12. Heylen R, Parente M, Gader P. A review of nonlinear hyperspectral unmixing methods. IEEE J Sel Top Appl Earth Obs Remote Sens. 2014;7(6):1844–68.
13. Bioucas-Dias JM, Plaza A, Dobigeon N, Parente M, Du Q, Gader P, Chanussot J. Hyperspectral unmixing overview: geometrical, statistical, and sparse regression-based approaches. IEEE J Sel Top Appl Earth Obs Remote Sens. 2012;5(2):354–79. https://doi.org/10.1109/JSTARS.2012.2194696.
14. Keshava N, Mustard JF. Spectral unmixing. IEEE Signal Process Mag. 2002;19(1):44–57. https://doi.org/10.1109/79.974727.
15. Boardman JW, Kruse FA, Green RO. Mapping target signatures via partial unmixing of AVIRIS data. In: Summaries of the Fifth Annual JPL Airborne Earth Science Workshop. 1995;1:23–26.
16. Winter ME. A proof of the n-findr algorithm for the automated detection of endmembers in a hyperspectral image. Algorithm Technol Multispectr Hyperspectr Ultraspectr Imag X. 2004;5425:31–41.
17. Nascimento JM, Dias JM. Vertex component analysis: a fast algorithm to unmix hyperspectral data. IEEE Trans Geosci Remote Sens. 2005;43(4):898–910.
18. L3Harris geospatial solutions: ENVI spectral hourglass wizard. 2022. https://www.l3harrisgeospatial.com/docs/spectralhourglasswizard.html. Accessed 03 Feb 2023.
19. Kubelka P, Munk F. An article on optics of paint layers. Z Tech Phys. 1931;12(593–601):259–74.
20. Zhao Y. Image segmentation and pigment mapping of cultural heritage based on spectral imaging. PhD thesis, Rochester Institute of Technology. 2008. https://scholarworks.rit.edu/theses/3029
21. Kirchner E, Ivd Lans, Ligterink F, Geldof M, Gaibor ANP, Hendriks E, Janssens K, Delaney J. Digitally reconstructing Van Gogh's Field with Irises near Arles. Part 2: pigment concentration maps. Color Res Appl. 2018;43(2):158–76. https://doi.org/10.1002/col.22164.
22. Rohani N, Pouyet E, Walton M, Cossairt O, Katsaggelos AK. Nonlinear unmixing of hyperspectral datasets for the study of painted works of art. Angew Chem. 2018;57(34):10910–4. https://doi.org/10.1002/anie.201805135.
23. Kleynhans T, Schmidt Patterson CM, Dooley KA, Messinger DW, Delaney JK. An alternative approach to mapping pigments in paintings with hyperspectral reflectance image cubes using artificial intelligence. Herit Sci. 2020;8(1):84. https://doi.org/10.1186/s40494-020-00427-7.
24. Amigo JM. Hyperspectral imaging. Amsterdam: Elsevier; 2019.
25. Grabowski B, Masarczyk W, Glomb P, Mendys A. Automatic pigment identification from hyperspectral data. J Cult Herit. 2018;31:1–12.
26. Hitchcock FL. The expression of a tensor or a polyadic as a sum of products. J Math Phys. 1927;6(1–4):164–89. https://doi.org/10.1002/sapm192761164.
27. Harshman RA. Foundations of the PARAFAC procedure: models and conditions for an "explanatory" multimodal factor analysis. UCLA Work Pap Phon. 1970;16:1–84.
28. Carroll JD, Chang J-J. Analysis of individual differences in multidimensional scaling via an N-way generalization of "Eckart-Young" decomposition. Psychometrika. 1970;35(3):283–319.
29. Bilius L-B, Pentiuc SG. Improving the analysis of hyperspectral images using tensor decomposition. In: 2020 international conference on development and application systems (DAS). 2020; pp. 173–176. IEEE . https://doi.org/10.1109/DAS49615.2020.9108935.
30. Veganzones MA, Cohen JE, Farias RC, Usevich K, Drumetz L, Chanussot J, Comon P. Canonical polyadic decomposition of hyperspectral patch tensors. In: 2016 24th European Signal Processing Conference (EUSIPCO). 2016; pp. 2176–2180. IEEE.
31. Panagakis Y, Kossaifi J, Chrysos GG, Oldfield J, Nicolaou MA, Anandkumar A, Zafeiriou S. Tensor methods in computer vision and deep learning. Proc IEEE. 2021;109(5):863–90.
32. Chen P, Cheng L, Zhang T, Zhao H, Li J. Tensor dictionary learning for representing three-dimensional sound speed fields. J Acoust Soc Am. 2022;152(5):2601–16. https://doi.org/10.1121/10.0015056.
33. Zubair S, Wang W. Tensor dictionary learning with sparse TUCKER decomposition. In: 2013 18th international conference on Digital Signal Processing (DSP). 2013; pp. 1–6 . https://doi.org/10.1109/ICDSP.2013.6622725
34. Zhao C, Wang M, Su N, Feng S. Dictionary learning hyperspectral target detection algorithm based on tucker tensor decomposition. In: IGARSS 2020 - 2020 IEEE international geoscience and remote sensing symposium. 2020; pp. 1763–1766. https://doi.org/10.1109/IGARSS39084.2020.9324144
35. Christensen J, Becker EM, Frederiksen CS. Fluorescence spectroscopy and PARAFAC in the analysis of yogurt. Chemom Intell Lab Syst. 2005;75(2):201–8. https://doi.org/10.1016/j.chemolab.2004.07.007.
36. Bro R. Multi-way analysis in the food industry. PhD thesis, University of Amsterdam. 1998
37. Smilde AK, Geladi P, Bro R. Multi-way analysis: applications in the chemical sciences. Hoboken: John Wiley & Sons; 2005.
38. Castro JP, Pereira-Filho ER, Bro R. Laser-induced breakdown spectroscopy (LIBS) spectra interpretation and characterization using parallel factor analysis (PARAFAC): a new procedure for data and spectral interference processing fostering the waste electrical and electronic equipment (WEEE) recycling process. J Anal At Spectrom. 2020;35(6):1115–24. https://doi.org/10.1039/D0JA00026D.
39. Jansen JJ, Bro R, Hoefsloot HCJ, van den Berg FWJ, Westerhuis JA, Smilde AK. Parafasca: Asca combined with parafac for the analysis of metabolic fingerprinting data. J Chemom. 2008;22(2):114–21. https://doi.org/10.1002/cem.1105.
40. Feller RL. Studies on the darkening of vermilion by light. Rep Stud Hist Art. 1967;1:99–111.
41. Feller RL. Artist's pigments: a handbook of their history and characteristics. National gallery publications: London, UK; vol. 1 1986. https://doi.org/10.1186/s40494-023-00910-x.
42. Rutherford J, Fitzhugh West E, Kuhn H, Plesters J, Chase W, Muhlethaler B, Thissen J, Feller R. Artists' pigments: a handbook of their history and characteristics, vol. 2. National Gallery of Art: Washington, DC; 1993.
43. FitzHugh EW. Artists' pigments: a handbook of their history and characteristics. National Gallery of Art: Washington, DC; vol. 3 1997.
44. Russell WJ, de Wiveleslie Abney W. Report to the Science and Art Department of the Committee of Council on Education on the Action of Light on Water Colours: Presented to Both Houses of Parliament by Command of Her Majesty. HM Stationery Office. 1888
45. Saunders D, Kirby J. Light-induced colour changes in red and yellow lake pigments. Natl Gallery Tech Bull. 1994;15(1):79–97.
46. International Organization for Standardization: ISO 105-B02:2014 Textiles - Tests for colour fastness - Part B02: Colour fastness to artificial light. 2014. https://www.iso.org/obp/ui/#iso:std:iso:105:-B02:ed-6:v1:en. Accessed 10 Sept 2022.
47. Hattori H, Yoshizumi K, Crews PC. Wavelength sensitivity of AATCC Blue wool lightfastness standards under light radiation. Dyes Pigments. 2012;92(3):936–41.
48. Saunders D, Kirby J. Wavelength-dependent fading of artists' pigments. Stud Conserv. 1994;39:190–4. https://doi.org/10.1179/sic.1994.39.
49. Lerwill A, Brookes A, Townsend JH, Hackney S, Liang H. Micro-fading spectrometry: investigating the wavelength specificity of fading. Appl Phys A. 2015;118(2):457–63. https://doi.org/10.1007/s00339-014-8645-3.
50. Pintus V, Garrappa S, Baragona AJ, Hradil D, Szabo F, Sterflinger K. Different Shades of Cadmium Soaps in Light Aged Modern Oil Mock-up Paints: First Multi-Analytical Investigation. In: MUNCH2022: Understanding Munch and the Art at the Turn of the Centuries - Between the Museum and The Laboratory, Oslo. 2022; p. 104

51. Kirschner B. Light bleaching with light emitting diodes (led): evaluation of treatment procedure and bleaching potential. J Pap Conserv. 2020;21(4):151–65. https://doi.org/10.1080/18680860.2020.2009704.
52. Whitmore PM, Colaluca VG, Morris HR. The light bleaching of discolored films of an acrylic artists' medium. Stud Conserv. 2002;47:228–36. https://doi.org/10.1179/sic.2002.47.4.228.
53. Lennox FG, King MG. Studies in wool yellowing: part XXIII: UV yellowing and blue-light bleaching of different wools. Text Res J. 1968;38(7):754–61. https://doi.org/10.1177/004051756803800711.
54. Zhang B, Huo S, Liu S, Zou L, Cheng L, Zhou X, Li M. Effects of cold-light bleaching on enamel surface and adhesion of Streptococcus mutans. BioMed Res Int. 2021;2021:3766641. https://doi.org/10.1155/2021/3766641.
55. Diaspro A, Chirico G, Usai C, Ramoino P, Dobrucki J. Photobleaching. Handbook of biological confocal microscopy. New York: Springer; 2006. p. 690–702.
56. Whitmore PM, Pan X, Bailie C. Predicting the fading of objects: identification of fugitive colorants through direct nondestructive lightfastness measurements. J Am Inst Conserv. 1999;38(3):395–409. https://doi.org/10.1179/019713699806113420.
57. Lojewski T. Lightfastness studies with MFT. In: MUNCH2022: Understanding Munch and the Art at the Turn of the Centuries - Between the Museum and The Laboratory, Oslo. 2022; p. 87
58. Chan E, Aambø M, Godzimirska M, Grimstad I, Lojewski T, Sandu ICA. Light-induced Color Changes on "The Scream"Versions in the Munch Museum Collection. In: MUNCH2022: Understanding Munch and the Art at the Turn of the Centuries - Between the Museum and The Laboratory, Oslo. 2022; p. 91
59. Grimstad I, Lojewski T, Sandu ICA. Is the interpretation and application of collected microfading data straight forward? In: MUNCH2022: Understanding Munch and the Art at the Turn of the Centuries - Between the Museum and The Laboratory, Oslo. 2022; p. 103
60. Aambø M, Godzimirska M, Chan E, Lojewski T, Sandu ICA. Light Sensitivity of Pigments in Edvard Munch's Works on Paper. In: MUNCH2022: Understanding Munch and the Art at the Turn of the Centuries - Between the Museum and The Laboratory, Oslo. 2022; p. 100
61. Beltran VL. Advancing microfading tester practice. Los Angeles: Getty Conservation Institute; 2019.
62. Kolda TG, Bader BW. Tensor decompositions and applications. SIAM Rev. 2009;51(3):455–500. https://doi.org/10.1137/07070111X.
63. Yates F. The analysis of replicated experiments when the field results are incomplete. Emp J Exp Agric. 1933;1(2):129–42.
64. De Carvalho OA, Meneses PR. Spectral correlation mapper (SCM): an improvement on the spectral angle mapper (SAM). In: Summaries of the 9th JPL Airborne Earth Science Workshop, JPL Publication 00-18, vol. 9. JPL publication Pasadena, CA, USA. 2000
65. Shelley M. Joseph Wright's pastel portrait of a woman part III: technique and aesthetics. Metrop Mus J. 2009;44:113–20.
66. Townsend JH. Analysis of pastel and chalk materials. Paper Conserv. 1998;22(1):21–8. https://doi.org/10.1080/03094227.1998.9638605.
67. Instytut Fotonowy: Micro fading tester. 2022. https://www.fotonowy.pl/products/micro-fading-tester/?lang=en. Accessed 10 Sept 2022.
68. Instytut Fotonowy: Fotolon, white standard reference. 2022. https://www.fotonowy.pl/products/wzorzec-bieli/?lang=en. Accessed 10 Sept 2022.
69. Savitzky A, Golay MJ. Smoothing and differentiation of data by simplified least squares procedures. Anal Chem. 1964;36(8):1627–39.
70. Rasmus Bro: The N-way Toolbox for Matlab. 2023. https://ucphchemometrics.com/186-2/algorithms/. Accessed 03 Feb 2023.
71. Ciortan I, Poulsson TG, George S, Hardeberg J. Predicting pigment color degradation with time series analysis. In: Color and Imaging Conference, vol. 2022. Society for Imaging Science and Technology. 2022.
72. Cosentino A. FORS spectral database of historical pigments in different binders. E Conserv J. 2014;2:54.
73. Saunders D, Cupitt J. Image processing at the National Gallery: the VASARI project. Natl Gallery Tech Bull. 1993;14(1):72–85.
74. Centore P. A colour survey of artist's pastels. J Int Colour Assoc. 2016;15:42–59.
75. Raidvee A, Toom M, Averin K, Allik J. Perception of means, sums, and areas. Atten Percept Psychophys. 2020;82(2):865–76.
76. Delaney JK, Ricciardi P, Glinsman LD, Facini M, Thoury M, Palmer M, Rie ER. Use of imaging spectroscopy, fiber optic reflectance spectroscopy, and X-ray fluorescence to map and identify pigments in illuminated manuscripts. Stud Conserv. 2014;59(2):91–101. https://doi.org/10.1179/2047058412Y.0000000078.
77. Geldof M, Proano Gaibor AN, Ligterink F, Hendriks E, Kirchner E. Reconstructing Van Gogh's palette to determine the optical characteristics of his paints. Herit Sci. 2018. https://doi.org/10.1186/s40494-018-0181-6.

Publisher's Note

Tensor Decomposition for Painting Analysis. Part 1: Additional File 1

1. CODE SNIPPET

The following code snippet shows the basics of the tensor decomposition model, implemented in Matlab using N-way toolbox.

```
% Let T be the 15*8*81 tensor, created from the MFT measurements

% Options for running the model. In order: convergence; initialization;
% plotting options; scaling; showfit; max. iterations.
opts = [1e-6, 0, 1, 0, 10, 4000];
% Activate constraints for non-negativity for the concentration and the
% endmembers.
constr = [2,0,2];
% Specify number of components and run PARAFAC.
Factors  = parafac(T,6, opts, constr);
% Separate the factors in the 3 loadings A,B,C corresponding to
% concentration, fading rate, endmembers.
[A,B,C] = fac2let(Factors);

%Recreate the modelled tensor using Khatri-Rao product
M = A*kr(C,B)';
% Reshape M (15*648) to the original tensor dimensions
M = reshape(M, [size(T,1) size(T,2) size(T,3)]);
```

2. MEASURED VERSUS RECONSTRUCTED SPECTRA

A. Training: Central lantern

Fig. S1 shows the reconstructions of the tensor decomposition model for the spectra used as training, at time steps 1 and time steps 8 (equivalent to 77 seconds). As it can be seen from the plots, the reconstructions are very loyal to the the original spectra.

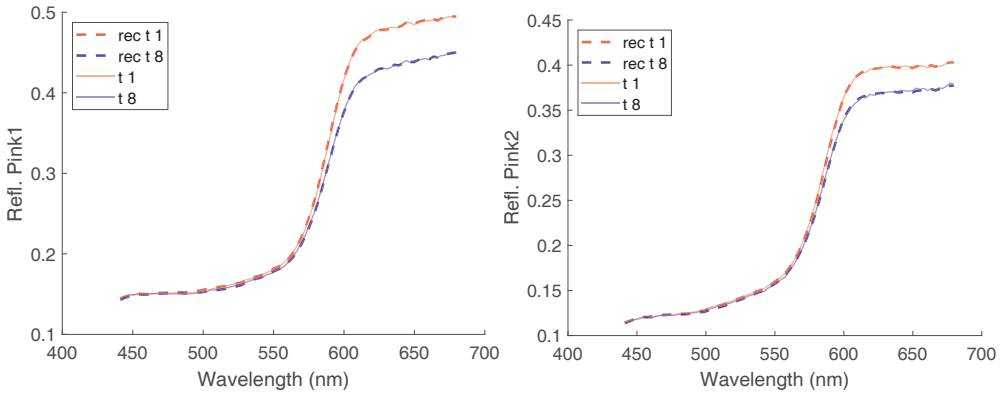

Fig. S1. The reflectances of the 15 samples in the central lantern, as measured with the microfadeometer and reconstructed with the tensor decomposition model, trained for 8 time steps.

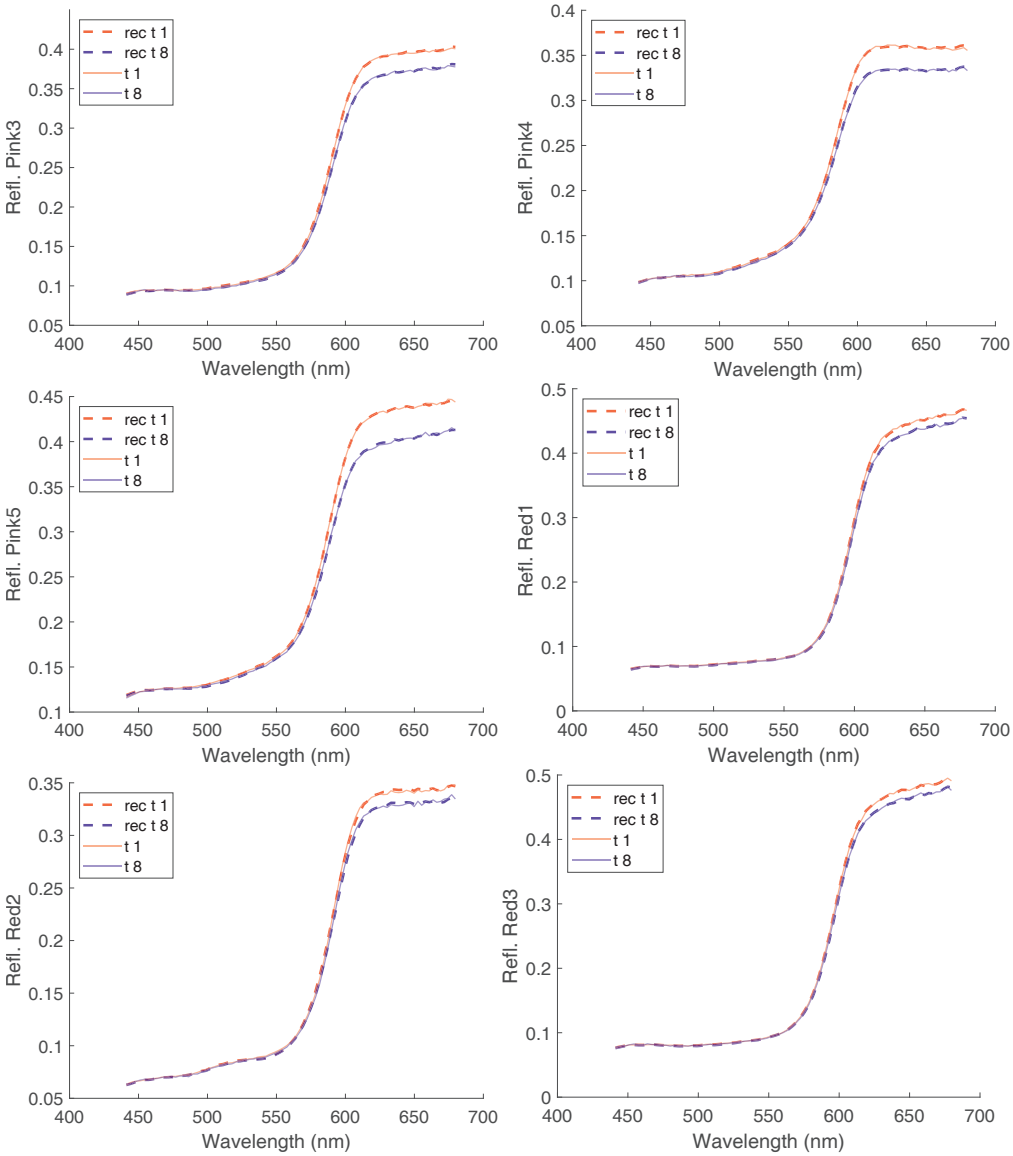

Fig. S1. The reflectances of the 15 samples in the central lantern, as measured with the microfadeometer and reconstructed with the tensor decomposition model, trained for 8 time steps.

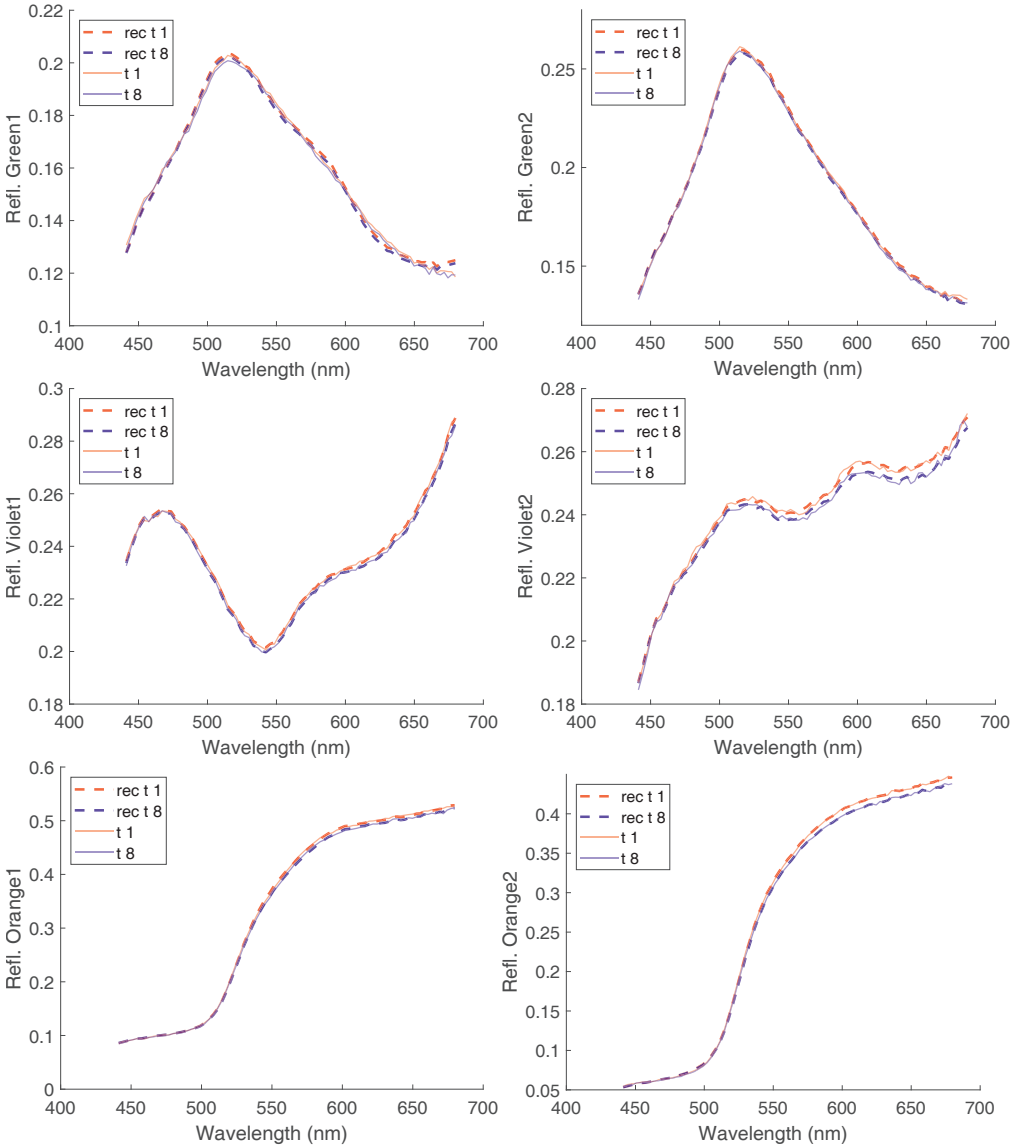

Fig. S1. The reflectances of the 15 samples in the central lantern, as measured with the microfadeometer and reconstructed with the tensor decomposition model, trained for 8 time steps.

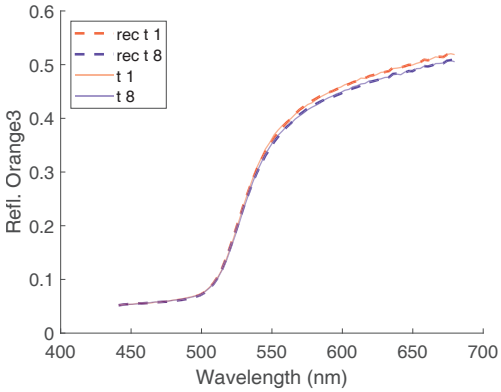

Fig. S1. The reflectances of the 15 samples in the central lantern, as measured with the microfadeometer and reconstructed with the tensor decomposition model, trained for 8 time steps.

B. Test case: Left lantern

Fig. S2 graphically represent the reflectances of the 5 measured point from the left lantern and their reconstruction s with the model trained with the data from the central lantern. The curves are very similar, implying that the model manages to explain well the test samples.

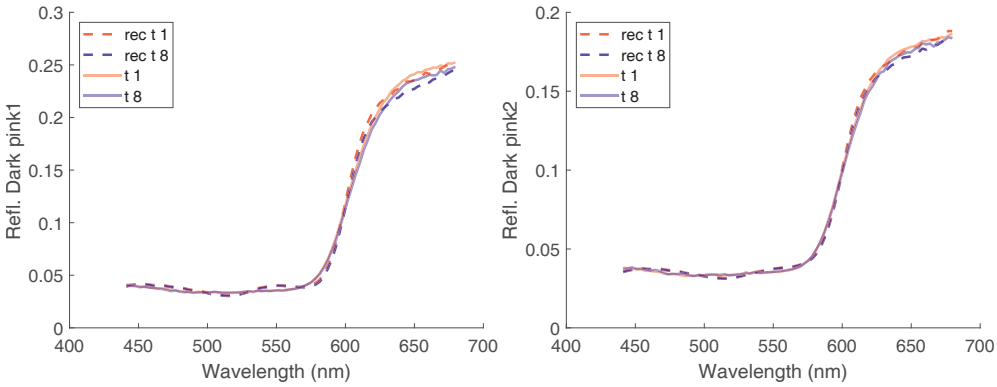

Fig. S2. The reflectances of the 5 samples in the left lantern, as measured with the microfadeometer and reconstructed with the tensor decomposition model trained on the central lantern.

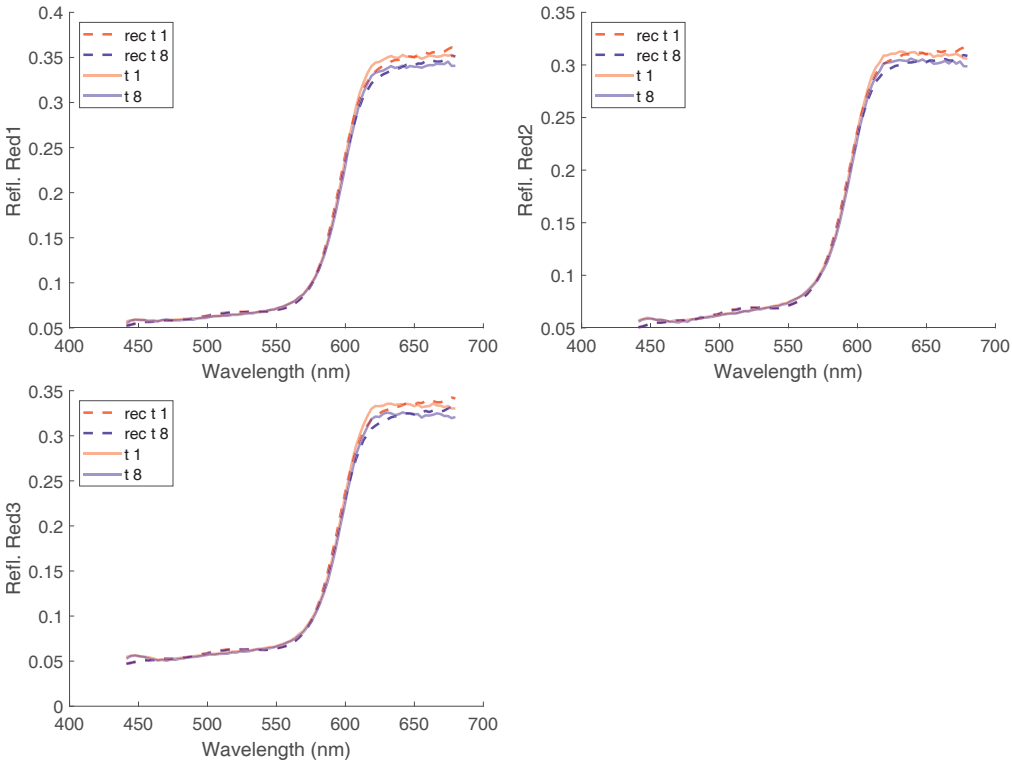

Fig. S2. The reflectances of the 5 samples in the left lantern, as measured with the microfadeometer and reconstructed with the tensor decomposition model trained on the central lantern.

Paper 7 - Tensor Decomposition for Painting Analysis. Part 2: Spatio-temporal Simulation

Ciortan *et al. Heritage Science* (2023) 11:84
https://doi.org/10.1186/s40494-023-00913-8

Heritage Science

RESEARCH Open Access

Tensor decomposition for painting analysis. Part 2: spatio-temporal simulation

Irina M. Ciortan[1*], Tina G. Poulsson[2], Sony George[1] and Jon Y. Hardeberg[1]

Abstract

In a previous article, we modelled the spectral and temporal dimensions of the photodegradation behaviour of pigments in the painting "A Japanese Lantern" by Oda Krohg. In particular, we extracted the endmembers and spectral fading rate of pigments by applying tensor decomposition on a time-series of spectroscopic point measurements. Now, we capture the same painting with a hyperspectral imaging setup and propose an approach to render the fading effects as 2D images. More precisely, from the hyperspectral image, we compute the concentration maps of each previously identified endmember with a least-squares unmixing method. Subsequently, by using tensor algebra, we multiply the concentration maps with the endmembers and their corresponding fading rate and obtain a 4D tensor where each pixel in the image is described by a spectrum and a fading function. This way, we generate past and future spatio-temporal simulations of the painting's appearance by reversing and elevating light exposure, respectively.

Keywords Spatio-temporal simulation, Tensor algebra, Microfading, Spectral photodegradation

Introduction

A wide range of materials manifests light-induced appearance changes. To name only a few: wood [1], paper [2], dyed textiles [3], pigments [4]. For this reason, it is of general interest to create models that are able to predict future degradation as a function of light exposure. In the field of cultural heritage, for older paintings where damage has already occurred, there is also an interest to reverse these changes, either through physical restoration or through digital image processing techniques. The latter are non-invasive methods because there is no intervention on the real object, and they offer a good playground for the implementation of various scenarios of degradation. Thus, digital rejuvenation has been employed for the reconstruction of Georges Seurat's "La Grande Jatte" [5], van Huysum's "Flowers in an Urn" [6], Vincent van Gogh's "Field with Irises near Arles" [7] and other drawings and paintings by van Gogh [4]. In some of the previous works, the proposed solutions are based on physical-based models such as Kubelka–Munk that considers the absorption and scattering of pigments, and the non-linear mixing of the various pictorial layers [2, 5, 7]. Other approaches are hybrid, combining physical models with data-driven methods [4]. There are also purely data-driven approaches, where analytical data and measurements of accelerated aging are combined with linear regression methods to virtually restore and/or age an artwork [7, 8].

Our novel approach for spatio-temporal simulation of paintings is also a data-driven method. In a previous article [10], we showed how from a set of microfading measurements, we created a tensor decomposition model and extracted the spectral curve of the pure pigments, together with their temporal evolution. Now, we link the loadings of the tensor decomposition model with a hyperspectral capture of the same scene. More

*Correspondence:
Irina M. Ciortan
irina-mihaela.ciortan@ntnu.no
[1] Department of Computer Science, NTNU - Norwegian University of Science and Technology, Teknologivegen 22, 2815 Gjøvik, Norway
[2] Collection Management, National Museum, St. Olavs plass, 0130 Oslo, Norway

specifically, we unmix the hyperspectral image with the endmembers previously obtained by minimizing the least square error under a linear mixing assumption. Once the concentration maps are retrieved, backward and forward spatio-temporal simulations are proposed.

Related work

Microfading analysis

Microfading refers to the accelerated aging process, where gradual light-induced changes in color and spectra are gathered. While accelerated photodegradation of pigments has been studied long before [11, 12], usually on mockups, it was not until the introduction of microfading that such experiments were performed on real objects. The main advantage of microfading is its minimal invasiveness. Light is cast over an area so small, that the fading effect is almost unperceivable by the naked eye, making this technique appropriate for the measurement of real artworks. Since the pioneering work of Whitmore et al. [13], who was the first to design a microfading setup, several other systems with increased spectral accuracy and higher portability for in-situ handling have been proposed [14–16]. As a consequence, microfading has enabled the color degradation analysis of a series of artworks from museum collections [17, 18] and even outdoor rock art specimens [19]. In many cases, this has determined museums to improve the light policy and better control the display time of sensitive artworks, such as Islamic Ardabil carpets [3], natural history artifacts [20], paintings [18], and heterogeneous collections including prints, watercolors, curtains [21].

Mapping of photodegradation

The point-based specificity of microfading experiments poses a challenge for the holistic visualization of the light-induced damage for an artwork's entire surface. The lack of ground-truth regarding the aging of the artwork's surface adds to the complexity of the task. There are several publications with a rather artistic approach to this challenge, where data from accelerated aging is used in combination with image manipulation software such as Photoshop to simulate faded variants of artworks in the color domain [22–24]. For instance, Morris and Whitmore [22] collect microfading data of mockups that include different painting media. They transform the spectroscopic data to color coordinates, that are later fed to Photoshop to create uniformly colored swatches where the evolution of the photo-degradation becomes easier to visualize. Moreover, by using the same data and procedure, the authors render fading effects for images with variation in the spatial content. In particular, the spatial structure is taken from scans of real paintings. To avoid damage, the paintings are not measured with the microfadeometer and so, the color behaviour is borrowed from the mockups' measurement. In addition, the authors automate the spatial rendering process in a scientific software, where a look-up table is created from the fading measurements of the mockup, connecting a color group with its faded variants at all light dosages. Hence, when the simulation at a certain dosage is queried, the closest corresponding color in the look-up table is retrieved. However, no interpolation method is applied to fill in the gaps between unmeasured values. Hendriks et al. [23] generated forecasts of the red and yellow colors in van Gogh's "The Bedroom", given a light exposure of up to 30 Mlux hr. The authors incorporated microfading data from aged mockups of red lakes and chrome yellow paints and based on these, altered the image of the painting in Photoshop. In a similar way, Brokerhof et al. [24] made a prognosis of color changes for a collection of Dutch city maps from the 17th century, by running various light fading scenarios in the same image editing software. While in these works the fading experiments allowed for high dosages of light, this might not be possible when the analysis is performed on real artifacts. In these latter cases, the future change could be predicted from the set of measured data using linear regression [9] or time-series models [25].

Riutort-Mayol et al. [8] proposed an interpolation method based on a multivariate Gaussian process, that correlates the set of microfaded points with a trichromatic image of the same scene. The Gaussian process considers the covariance between the faded spots and the pixels in color image based on their similarity in the HSV (hue, saturation, value) color space and spatial proximity. This way, the color fading values are extrapolated to the entire image, facilitating spatio-temporal analysis. Moreover, the sign of the partial derivative is used to ensure that the temporal change function is monotonically increasing. This method was applied to predict color changes for Spanish Levantine rock art paintings [19]. While potentially, given a hyperspectral image, the Gaussian process interpolation could be extended to the spectral domain as well, no such feasibility prospects were discussed in the papers [8] and [19].

Thomas et al. [9] suggested an interdisciplinary approach for the spatial mapping of the color degradation in "The Scream" painting in the National Museum of Norway collection. The pigments in the artwork had been previously analysed with, among other methods, X-ray fluorescence, and test points for microfading were chosen based on previous test points. Microfading data were combined with knowledge of the paintings' support, pigments and surface layer to create digital simulations of the painting after 10 dose values ranging from 0.5 to

25 MLux hr. Moreover, unrealistic colors were eliminated based on color rendering index values. It was pointed out that it is reasonable to extrapolate up to 3 times the applied dose. If we assume that 1.5 Mlux hr were applied, this allows for projections up to 4.5 Mlux hr. Beyond this limit, the authors claim that the model performs less well. For many artworks, simulations such as these may not be possible, as they require a combination of different methods of analysis and data processing that may not be viable to carry out for most objects.

Method

Figure 1 displays the workflow of our approach. The first and core module is represented by the tensor decomposition model (thoroughly described in Part 1 of this two-article series) [10]. This model takes as input a collection of microfaded samples, and employs parallel factor analysis (PARAFAC) to find the spectra of the unmixed pigments (endmembers), their concentration in each sample and their fading rate. In the second module, we capture a hyperspectral image of the same scene to obtain the concentration of the endmembers for the full spatial dimension, beyond the microfaded points. Then, we can reconstruct each pixel in the image as a tensor product between the concentration, endmembers and the fading rate. This way, we generate spatio-temporal simulations of the whole surface, for the time steps included in the model. In the third module, we go beyond the measured time steps, by applying linear regression on the fading rates. As a result, the fading rate of each endmember is characterized by two coefficients (slope and intercept) and a given time step. Hence, fading rates for past and future moments can be computed. In tensor algebra, these new fading rates can be multiplied with the endmember and their concentration maps to render the analyzed surface backwards and forward in time.

Spatio-temporal modelling

For the sake of brevity, we will not insist here on the tensor decomposition model as it was described in the "Method" section of Part 1 of this article series [10]. Thus, we take for granted that matrix C represents the endmembers, A the concentration of each endmember $f = \{1 \dots F\}$ in all the input samples and B the fading rate for each endmember.

Let us consider a hyperspectral image $H^{I \cdot J \cdot U}$ of the same scene from which the microfading samples were collected. Instead of sampling the scene at only few locations as the microfadeometer does, the hyperspectral image measures the scene holistically, where for every pixel at location i, j with $i = \{1 \dots I\}$ and $j = \{1 \dots J\}$ its reflectance spectrum is recorded with a dense bandwidth for a total of U bands. Given the endmembers defined by the loadings of factor C of the trained PARAFAC model, we can unmix the hyperspectral image assuming the same endmembers. The unmixing is formulated as a least-square optimization problem, where the linear combination of the F endmembers that best explains the image with the minimum sum of squared residuals is chosen. The result of the unmixing is given by the abundance maps, which are essentially the concentration

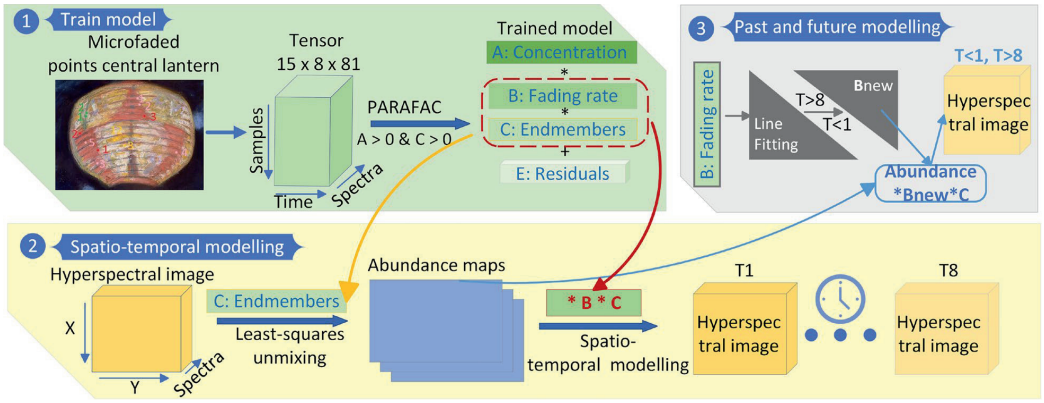

Fig. 1 The diagram of our method. The module (1) is the core model, where we extract the endmembers and their fading rate with three-way tensor decomposition from a collection of microfading observations. Then we perform spatio-temporal fading simulation by capturing a hyperspectral image of the same microfaded scene (2). We unmix the hyperspectral image to get the concentration map for each endmember, and then recompose it as a tensor product with the fading rate for each of the modelled time steps. Finally, we extend the time span of the spatial simulations by extrapolating the fading rate for time steps not included in the trained model (3)

of each pure spectrum defined at pixel level. By flattening the abundance maps A_{map} into a matrix of cardinality $IJ \cdot F$, we can then replace it in Eq. 2 of Part 1 [10] and obtain spatial simulations of fading for each k time step modelled with PARAFAC:

$$H_{sim}^{IJ \cdot KN} = A_{map}^{IJ \cdot F} \times (C^{N \cdot F} \otimes B^{K \cdot F})^T \quad (1)$$

Then we can reshape $H_{sim}^{IJ \cdot KN}$ to $I \cdot J \cdot K \cdot N$ to access the fading simulations of the hyperspectral image at each time step k.

The loadings of the 2nd mode, B define the fading rate of every endmember. In Part 1 [10], Eq. 3 we showed how the fading rate can be expressed as a linear function of the light exposure. By replacing k in that equation with values lower than 1 or higher than K (the total numbers of steps included in the model), we can estimate new values for the fading rate R_f backward or forward in time. These new values can then substitute B in Eq. 1 to get the spatial simulations for time steps other than those measured. It is important to note that while from a mathematical standpoint the backward prediction holds, from a physical perspective, it is not entirely legitimate, as the modelling was achieved with data describing only the present and future state of the artwork. Thus, in this paper, we present a rather mathematically valid modelling of the past appearance.

Data collection and results

Case study: Oda Krohg's painting "A Japanese Lantern (By the Christiania Fjord)"

In this article as well as its prequel, Part 1 [10], we show the performance of our method on the painting "A Japanese Lantern" created by the Norwegian painter Oda Krohg in 1886 and present in the collection of the National Museum of Norway (inventory number NG.M.00879). The painting is made on canvas, and with pastel media. The highlight of the painting, as indicated by its title, is the Japanese lantern in the top central part (see Fig. 2). The lantern is interesting from a scientific point as well, because it has an intricate color composition. For this reason, in this two-part series of articles, the lantern was chosen as the region of interest to characterize the reflectance and lightfastness of the constituent pigments, based on microfading spectrometry. In this article, we present an approach to visualize the fading effects for the entire surface of the lantern.

Microfading analysis

In Part 1 [10] of this two-series article, we explained how we collected a set of measurements (see Fig. 2) from a fragment of the painting, i.e. the lantern in the top central part, with a portable microfadeometer (MFT) [26].

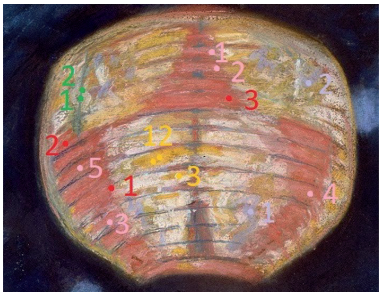

Fig. 2 Locations measured with MFT on the central lantern. The samples correspond to five colour groups: pink (P), red (R), green (G), orange (O), violet blue (V). Courtesy of Børre Høstland, National Museum

The temporal evolution of the color coordinates shows an overview of the color degradation mechanisms. As it emerges from the plots in Fig. 3, the tendency is for the colors to darken (the negative change of lightness) and desaturate (negative change of chroma). The desaturation effect is evident for the pink, red and orange samples. However, in the case of the green samples, it seems that chroma remains stable. Similarly, the chroma of the violet samples has a rather small shift in comparison to the red, pink and orange. In addition, V1 saturates, while V2 desaturates. This contrasting trend is probably related to the underlying materials that albeit similar in color, have different spectral composition.

Hyperspectral image capture

The painting was imaged with the HySpex VNIR-1800 [27]. HySpex VNIR-1800 is a pushbroom hyperspectral scanner, with a CMOS sensor that records the spectral response every 3.2 nm between 400 and 1000 nm for a line of 1800 pixels at a time. In order to acquire a full surface, either the camera or the object needs to be moved so that sequential frames are acquired. This results in a 3D data array with size equal to (number of frames) * 1800 pixels * 186 spectral bands. In this case, the camera was set on a rotational stage, parallel to the painting that was held in a vertical position with a motorized easel, as shown in Fig. 4. A lens focusing at 1 m was mounted on the camera, resulting in a pixel size equivalent to that of 0.2 mm. The distance between the camera and the painting was approximately 1 m. To maximize the signal, two halogen studio lamps were placed on the left and right side of the camera, at 45° with respect to the painting. To account for the light non-uniformity of the captured line and to obtain the reflectance factor, a standard gray target with known reflectance of approximately 60% was

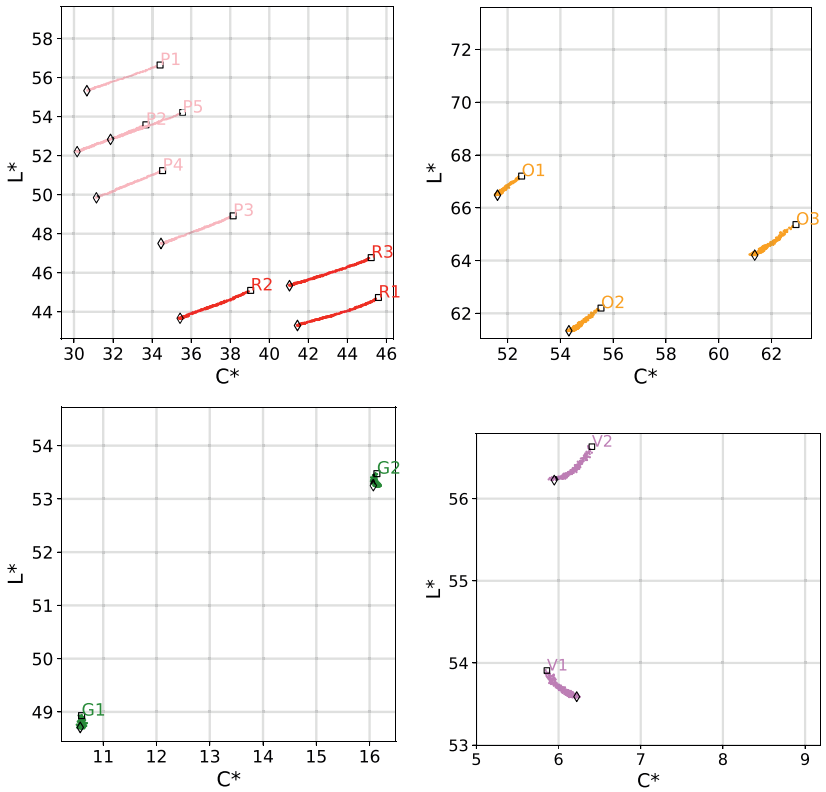

Fig. 3 Alteration of L*, C* coordinates for the microfaded samples in the central lantern. The black square marks the initial value, before fading, while the diamond marks the final value, after fading. The lightness of all samples decreases after fading. While the red, pink and orange sample desaturate, the chroma of the green samples keeps constant. Interestingly, the two violet samples have opposite behaviours, where chroma increases for V1, whereas it decreases for V2

placed alongside the painting. Each pixel in the captured line is corrected for the dark current noise. Then, to get the reflectance factor, the pixels in the region of interest are divided by the response of the gray target and multiplied by the known reflectance of the target. Similar to the microfaded data, the hyperspectral signals were smoothed with a Savitzky–Golay filter [28] of order 2 and window size 17 to reduce the noise.

Due to various constraints related to the in-situ measurements and museum logistics, the microfading was performed before the hyperspectral imaging. Moreover, at the time of the imaging campaign, the painting was reframed, whereas it was without frame during the microfading experiment. The framing includes a thin sheet of Optium acrylic [29] overlaid on the painting. The acrylic sheet blocks 99% of the UV

Fig. 4 In-situ setup for hyperspectral imaging

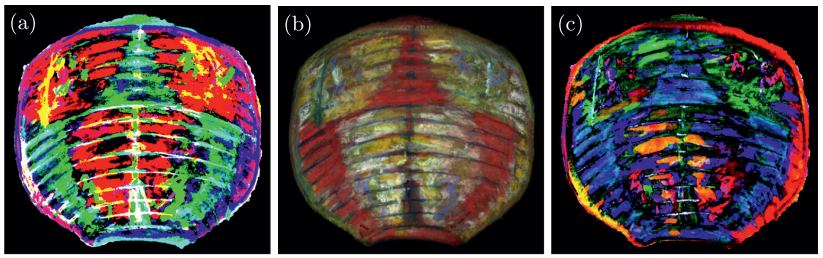

Fig. 5 True color visualization of the central lantern based on the hyperspectral image (**b**), together with PCA false color renderings (**a**, **c**). **a** R, G, B correspond to: PC1—45.23% retained variance, PC2—36.55% variance, PC3—7.3% variance. **b** R, G, B correspond to the most informative spectral bands: 650 nm, 551 nm and 470 nm. **c** R, G, B correspond to: PC5—2.47% retained variance, PC6—10.97% variance, PC4—5.53% variance

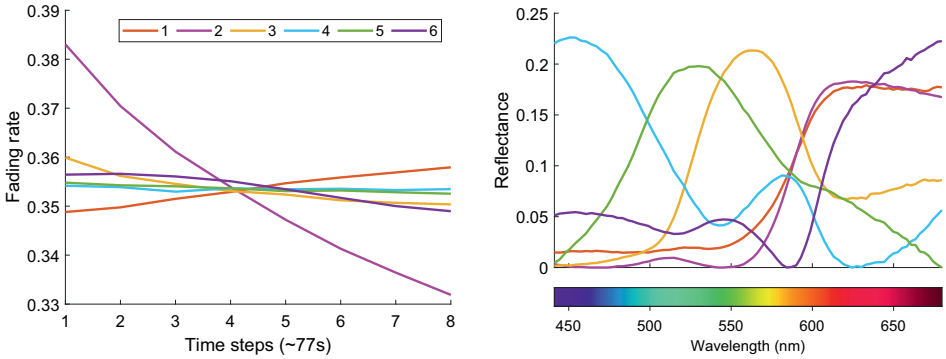

(a) B: Fading rate of each endmember (b) C: Endmembers

Fig. 6 Loadings of the two factors (B, C) in our tensor decomposition model, fitted for 6 components

light, is anti-reflective and is transparent, so it should have minimal to no impact on the imaged signal of the painting's reflectance in the visible range. It could be implied that during the gap in-between the two measurements, some intermediate fading might have occurred. Nonetheless, the painting was not on display during this period, so there should have been very little light exposure mostly due to the reframing after the microfading experiment, packing, and setting up for the hyperspectral scanning.

Exploratory analysis

In order to get a quick understanding of the hyperspectral image, principal component analysis (PCA) was computed to compress and visualize the significant variation in the spectral data for the full spectral range (400–1000 nm). Before PCA was applied, the data was normalized along the spectral dimension with the standard normal variate preprocessing technique [30], to reduce the influence of the spectral signal's intensity in favour of its shape. The data was split into 10 principal components, where the components are sorted descendingly by the amount of data variance they explain. By nature, principal components (PC) are orthogonal, and they could suggest distinct materials in the data. However, it is difficult to give chemical meaning to the spectra of the PC especially since the mean-centering in pre-processing implies loadings with negative values. Fig. 5a, c display false color visualizations of the first 6 principal components in the central lantern, where we can see a spatial distribution of different materials. We can parallel these distributions with the true color rendering of the central lantern (Fig. 5b) to attribute more meaning to the components. For example, the red in Fig. 5a seems to correspond to the yellow areas in the true color image, while green segments the violet-blue strokes and cyan covers the pink regions. Moreover, the false green color in Fig. 5c delineates stripes that overlap with the false red color regions in Fig. 5a. Actually, considering the known

fact that pastels are usually applied in layers, we could hypothesize that PCA manages to separate some of the layers in the painting, even though it is difficulty to quantify the order. Nonetheless, if we carefully inspect the true color image, we can notice areas of yellow covered with green in the top left and right sides of the lantern.

Spatio-temporal spectral fading simulation

One of the advantages given by our tensor decomposition model and facilitated by the multi-modal acquisition, is the possibility to spatially map the temporal changes triggered by fading. For generating spatio-temporal simulations, we first recover the concentration maps of the endmembers (factor C loadings extracted with the PARAFAC model, displayed in Fig. 6b) in the hyperspectral image using least-squares method. We enforce the non-negativity constraint so that we get realistic, positive concentrations. Also, we interpolate the spectral sampling of the hyperspectral image to match that of the microfading data. The resulting abundance maps have the same spatial dimension as the input hyperspectral image, 736*790 (height*width), and are shown in Fig. 7. A clustering effect can be noticed, where the same endmember is present in contiguous and adjacent regions, which indicates that the abundance maps are realistic. The most spatially predominant pigment is endmember 1, while the least extensive is endmember 6. The uniformity of endmember 1 seems to confirm the likelihood of our previously mentioned layering theory, suggesting the presence of a common bottom red layer applied on the central lantern before the other colors.

The abundance maps with size 736*790*6 are then flattened to 581,440*6 arrays so that they can be combined with the fading rate and endmember loadings (see Fig. 6) using the Khatri-Rao product, as formulated in Eq. 1. The result is a 2D matrix with dimensions 581,440*648, where the second dimension corresponds to the number of time steps (8) multiplied by the number of wavelengths (81). This is then reshaped to a 4D array with size 736*790*8*81, that contains the spectral simulations along the 81 wavelengths for the 8 time steps, spatially distributed for the entire surface of the central lantern. We then separate the images at each temporal slice, and transform them to CIE L*a*b* using CIE 1931 2° standard observer and D65 standard illuminant. This way, we can check whether the degradation pattern of the spatio-temporal simulations fits with the findings of the colorimetric analysis in "Microfading analysis" section.

Figure 8 shows the ΔE_{00} difference between the spatio-temporal simulations at time step 8 and time step 1. We would expect that the maximum difference is 2 ΔE_{00} units, since this is the span of the microfading data used to train the tensor decomposition model. While, indeed, the range is mostly below 2 ΔE_{00} units, the maximum difference reaches 2.5 units for few isolated groups of pixels. This can be caused by a number of factors: the imperfections of our model in finding all the endmembers; the

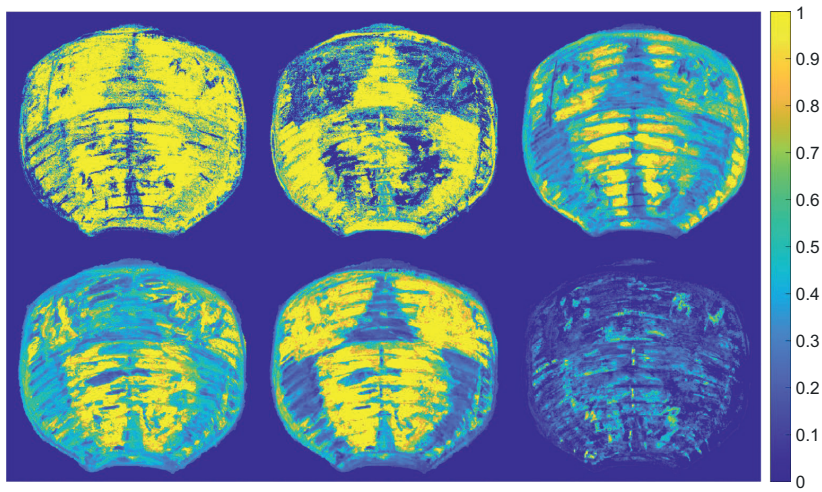

Fig. 7 Abundance maps, estimated with the least-square method, of endmembers 1–6 (previously extracted with the tensor decomposition model from the microfading data) in the hyperspectral image of the central lantern. Endmember 1 seems to be the pigment most uniformly distributed. This hints to its application as an underneath layer, beneath the rest of the colors

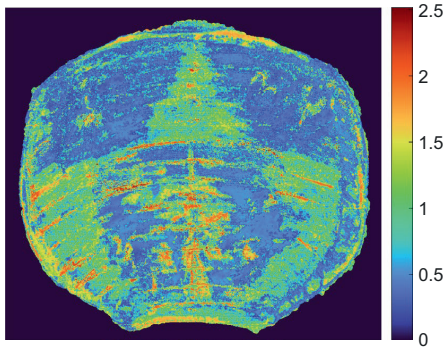

Fig. 8 ΔE_{00} between the spatio-temporal simulations at time step 1 and time step 8, where the exposure is equivalent to 0.027 Mlux hr

least-square fitting error in the estimation of the abundance maps; the setup differences between the microfading and hyperspectral measurements that might generate a difference of scale when computing the abundance maps. In addition, we graphically represented the subtraction of the color coordinates L* and C* between the simulations at time step 1 and time step 8. Hence, in Fig. 9 the false colors red and green stand for positive and negative change, respectively. The previous colorimetric analysis (see "Microfading analysis" section) revealed a negative trend for the L* and C* coordinates for almost all of the single point measurements. This trend seems to be preserved for the spatial simulations as well. Nonetheless, we can notice small red areas in Fig. 9, indicating a positive change, which is contrary to the colorimetric analysis of the individual microfaded samples. This may be explained by the fact that those areas in the hyperspectral image simulations that change positively in the L* and C* coordinates were not measured with the microfadeometer. Actually, this raises one potential limitation of our spatio-temporal simulation model: if the microfading experiment doesn't sample the full range of the materials spatially present, then the performance and accuracy of the model might be affected.

We know that the hyperspectral image was captured 1 year after the microfading experiment. In this period, the painting was not on display. Hence, the exposure should have been minimal, mostly occurring during the reframing process after the microfading data collection and during the hyperspectral scanning. By comparing the spatio-temporal simulations with the hyperspectral image, it is possible to estimate the amount of light exposure in-between the two measurements. Therefore, we computed the ΔE_{00} and root mean square error (RMSE) between the hyperspectral image and the spatio-temporal simulations for time steps 1–8. According to both metrics, the simulation at time step 2 is the one with the highest colorimetric and spectral similarity with the original image, as shown in Fig. 10. This implies that in the gap between the two acquisitions, the painting was exposed for approximately 0.0385 Mlux hr. However, there are a number of factors other than light exposure that may influence the precision of this result. For instance, there were a number of differences between the microfading data collection and hyperspectral imaging: the state of the painting (without and with the acrylic

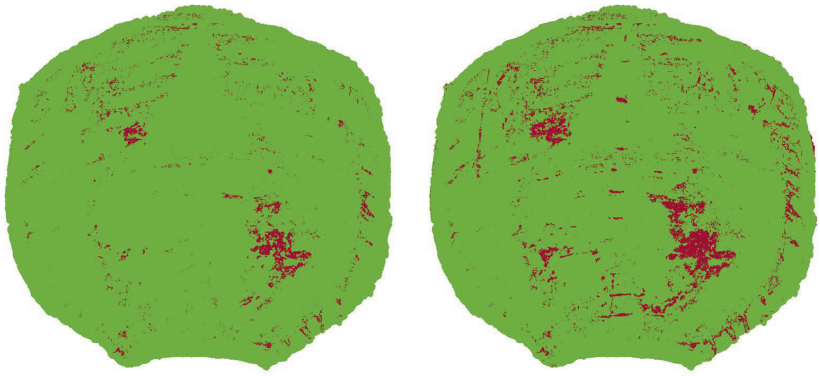

(a) L_8^* -L_1^* (b) C_8^* -C_1^*

Fig. 9 Comparison of the CIE L*, C* coordinates between the spatio-temporal simulations at time step 8 (equivalent to 77 s of light exposure) and time step 1. Red depicts a positive change, while green a negative change. The negative difference prevails, which is in agreement with the colorimetric analysis of the microfading data ("Exploratory analysis" section)

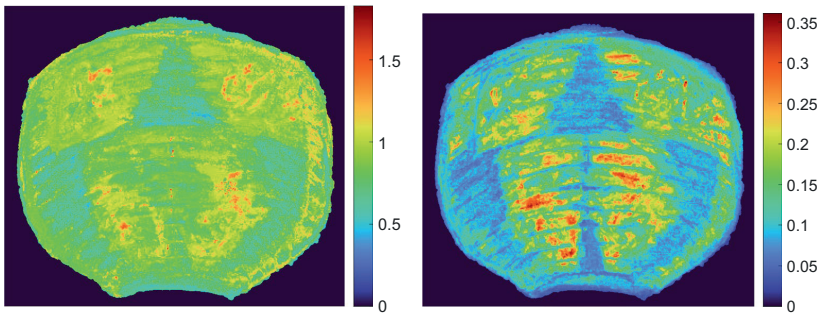

(a) ΔE_{00} (b) RMSE

Fig. 10 The spatio-temporal simulation at time step 2 is most similar to the hyperspectral image, both colorimetrically and spectrally, with an average ΔE_{00} of 0.86 and an average RMSE of 0.13. This indicates that light-induced aging happened in-between the two measurements (microfading and hyperspectral). However, there are other factors, mainly related to the differences between the two acquisitions setups, that could influence the accuracy of this result

sheet), illumination (LED vs. halogen) and acquisition geometry. In addition, the neutral reference tiles used to calibrate the light sources for the two instruments were different. Moreover, there is the problem of unidentifiable scale of the endmembers extracted with the parallel factor analysis (see "Tensor decomposition with parallel factor analysis" section in Part 1 [10] prequel). To account for these variations in magnitude, before computing the difference between the simulations with respect to the hyperspectral image, we applied normalization in each case by division with the maximum values.

Rendering of past and future appearance

In a previous article we derived the linear approximations of the fading rates characteristic to each endmember and estimated the slope and intercept, (see Eq. 3 and Table 1 of Part 1) [10]. In addition, the goodness of the linear approximations was proved based on a test dataset. To visually acknowledge the effect of reversed and increased fading, we computed new fading rates for $k = \{-31 \dots 0\}$ and $k = \{9 \dots 32\}$, which together with the measured $k = \{1 \dots 8\}$, cover a light exposure range of ± 341 seconds or ± 1.19 Mlux hr. The number of 32 time steps was inspired from the analysis of future modelling of the point measurements in Part 1 [10], section "Data collection and results", where the reconstruction error was showed to increase proportionally with the extent of the temporal range. For this reason, we chose a moderate value as a way to cap the amount of error and at the same time, achieve the visible effect of aging. Then, we input the new fading rates in Eq. 1 and created a total of 64 hyperspectral images for $k = \{-31 \dots 32\}$. In Fig. 11, we show sRGB renderings (based on the CIE L*, a*, b* coordinates integrated for D65 illuminant and 2° observer)

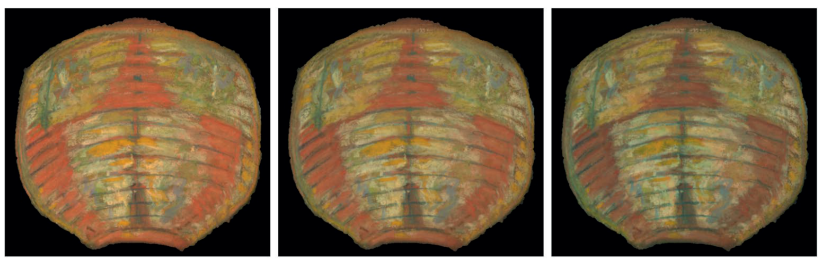

(a) -341 s of light exposure (b) 0 s (c) +341 s of light exposure

Fig. 11 Spatio-temporal sRGB renderings of the lantern, for D65 illuminant and 2° observer. For simulating the past, we reverse the light exposure, up to -1.19 Mlux hr (equivalent to -341 s or $k = -31$ time steps). Present refers to 0 Mlux hr ($k = 1$) and future to $+1.19$ Mlux hr ($k = 32$ or $+341$ s). We can see that the overall appearance turns darker due to photodegradation. Also we can notice the shift to greener hues of the orange colours in the center (corresponding to points O1, O2, O3 in the microfaded samples). For a more gradual display of the change, for intermediate time steps, please watch the animation in the Additional file 1

of the past, present and future appearance of the Japanese lantern. The past, simulated for the smallest k can be considered a digital rejuvenation and shows a brighter and more colorful appearance than the consequent renderings. Indeed, the future appearance (Fig. 11c) looks darker and less colorful. This means that the color degradation trend, previously discussed in the case of a sparser spatial sampling (Fig. 3) or for a more confined period of time (Fig. 9) is consistent for bigger cutouts in the spatio-temporal volume. The animation in Additional file 1 portrays a more gradual visualization of the change, that takes into account the intermediate time steps between the past and future simulations in Fig. 11. We chose these boundaries for the light exposure $k = \{-31 \dots 32\}$ because they are sufficient to show the aging process. Mathematically, we have no clear boundaries and potentially, we could generate simulations far beyond this range. However, from a physical point of view, simulations might get unrealistic beyond a certain threshold. Defining this threshold requires precise knowledge about long-term kinetics of the pigments and a full monitoring of the painting's storage and display conditions, and it is out of scope for our current work.

Every 2D rendering for a certain time step has a full spectral representation. This facilitates the visualization of the degradation for particular wavelengths. For instance, Fig. 12 shows the difference between the rejuvenation (-1.19 Mlux hr) and aged ($+1.19$ Mlux hr) versions of the lantern, in RGB composite images. Each R, G, B channel corresponds to the most representative spectral bands in the long-wave, mid-wave and short-wave parts of the visible electromagnetic spectrum according to the correlation coefficient metric. These informative bands are 650 nm, 551 nm and 470 nm. By visualizing the difference hyperspectral image between past and future, we can see which wavelengths change most for certain areas in the lantern. For example, in the areas surrounding the O1 and O2 microfaded points, we can see the predominant color in Fig. 12 is yellow, meaning that the most significant shift happens in G and R channels, corresponding to 551 nm and 650 nm. A full animation highlighting the photodegradation as the per-wavelength difference between the rejuvenation and aged simulations is included in Additional file 2.

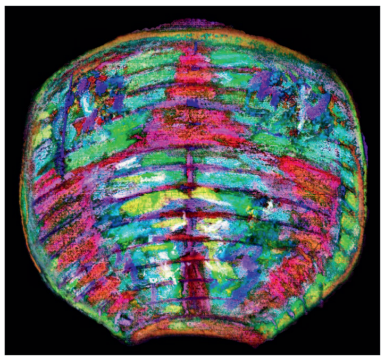

Fig. 12 RGB image of the difference between past and future simulation of the lantern. The R, G, B channels correspond to the most informative spectral bands in the ranges 600–700 nm, 500–600 nm, 400–500 nm, namely 650 nm, 551 nm and 470 nm. The contrast of the image is stretched for visualization purposes

Discussion

To summarize our results, we showed how the fusion of microfading spectrometry with reflectance image spectrometry can be useful to the analysis of an artwork on various levels. First, both acquisition methods enable informative preliminary analysis. Microfading gives us an overview of the color degradation of the materials, while the spatio-spectral dimension of the hyperspectral imaging enables principal component analysis that shows a distribution of probably distinct materials, even though the components have low interpretability with regard to the chemical meaningfulness. However, these techniques alone have a number of limitations. Microfading doesn't have a spatial component making it a difficult task to extrapolate the degradation behaviour to other points on a surface. On the other hand, hyperspectral imaging, while having a good resolution in the spatial and spectral dimensions contains little information about the fading mechanisms of the pigments. Also, while pigment classification and unmixing techniques can be applied, hyperspectral imaging has a limited reach beyond the surface layer of a painting. In our case, the hyperspectral system is sensitive in the near-infrared region, and able to see through several pigments that are transparent in the near-infrared. In addition, we can argue that the microfading, based on an accelerated aging procedure, can reach as well layers underneath the superficial pictorial layer. In other words, through fading, some components disappear, uncovering pigments from underneath layers. Seeing beyond the surface turns out to be a useful property when it comes to pigment unmixing.

Given all these considerations, by fusing microfading data with hyperspectral image analysis we get a more holistic representation of an artwork and its constitutive pigments together with their fading mechanisms. In other words, we get a spatio-spectro-temporal representation.

Towards future validation of our approach, we intend to conduct psycho-physical studies where more experts could assess if the spatio-temporal simulations look realistic. Moreover, because the tensor decomposition method is sensitive to the training data, we are aware that

with a limited sampling of the microfading observations, some pure pigments might be disregarded, which in turn affects the spatial mapping. This could be accounted for with a more thorough sampling during the microfading experiment. In addition, the tensor decomposition method is ultimately a linear unmixing method, which might not capture all the non-linear mixing mechanisms in the current pastel painting. Because this has an impact on the spatial representation, non-linear models such as Kubelka–Munk are under consideration for further evaluation. Finally, although we show results for a single case study, our method can be applied on any other type of colorant (ink, dyes, etc.) and artworks given a set of overlapping microfading and hyperspectral measurements.

Conclusion

In this study, we elaborated a method that combines microfading spectrometry with hyperspectral image analysis towards spatio-temporal simulations of an artwork. The current approach builds on our previous work, where we distilled a time-series of point spectroscopic measurements into the spectral signals of pure pigments and their fading functions. In this follow-up article, by coupling the basis factors recovered beforehand with a hyperspectral image of the same scene, we are able to render the appearance of the artwork by modulating the amount of light exposure. As a result, we can undo the fading and achieve a digital rejuvenation. Similarly, we can simulate the future photodegradation by virtually increasing the light exposure. Our proposed spatio-temporal simulations have a full spectral representation, meaning that they can be rendered for specific wavelengths, as well as adapted to the color response of various illuminants.

Abbreviations

CIE	Commission Internationale de l'Éclairage (International Commission on Illumination)
CMOS	Complementary metal-oxide semiconductor
LED	Light-emitting diode
MFT	Microfadeometer
Mlux hr	Megalux hours
PARAFAC	Parallel factor analysis
PC	Principal component
PCA	Principal Component Analysis
RGB	Red, green, blue color space
RMSE	Root mean square error

Supplementary Information

The online version contains supplementary material available at https://doi.org/10.1186/s40494-023-00913-8.

Additional file 1. Animation showing the gradual color degradation of the lantern.

Additional file 2. Animation showing the spectral difference between past and future simulations of the lantern.

Acknowledgements

We would like to thank all the colleagues from NTNU and the National Museum who helped with the logistics during the hyperspectral image acquisition campaign.

Author contributions

IMC: conceptualization, methodology design, hyperspectral image acquisition, formal analysis, investigation, results' visualization and interpretation, writing of the main manuscript; TGP: collection of the microfading data, investigation, revision of the final manuscript; SG and JYH: supervised the research, ensured the funding acquisition, revision of the final manuscript. All authors read and approved the final manuscript.

Funding

Open access funding provided by Norwegian University of Science and Technology. This work has not received additional funding.

Availability of data and materials

The datasets used and/or analysed during the current study are available from the corresponding author on reasonable request.

Declarations

Competing interests

The authors declare that they have no competing interests.

Received: 13 December 2022 Accepted: 22 March 2023
Published online: 26 April 2023

References

1. Cirule D, Kuka E, Andersone I, Andersons B. Wood discoloration patterns depending on the light source. Herit Sci. 2022;10(1):158. https://doi.org/10.1186/s40494-022-00795-2.
2. Kimmel BW, Baranoski GVG, Chen TF, Yim D, Miranda E. Spectral appearance changes induced by light exposure. ACM Trans Graph. 2013;32(1):10–11013. https://doi.org/10.1145/2421636.2421646.
3. Pretzel B. Now you see it, now you don't: lighting decisions for the Ardabil carpet based on the probability of visual perception and rates of fading. In: Proceedings of the 15th triennial conference on ICOM committee for conservation, New Delhi, India; 2008. p. 22–6.
4. van Gogh Museum. REVIGO project (REassessing VIncent van GOgh). 2017. https://www.vangoghmuseum.nl/en/about/knowledge-and-research/completed-research-projects/revigo. Accessed 10 Sept 2022.
5. Berns RS, Byrns S, Casadio F, Fiedler I, Gallagher C, Imai FH, Newman A, Taplin LA. Rejuvenating the color palette of Georges Seurat's A Sunday on La Grande Jatte-1884: a simulation. Color Res Appl. 2006;31(4):278–93. https://doi.org/10.1002/col.20223.
6. Trumpy G, Conover D, Simonot L, Thoury M, Picollo M, Delaney JK. Experimental study on merits of virtual cleaning of paintings with aged varnish. Opt Express. 2015;23(26):33836–48. https://doi.org/10.1364/OE.23.033836.
7. Kirchner E, Lans Ivd, Ligterink F, Geldof M, Megens L, Meedendorp T, Pilz K, Hendriks E. Digitally reconstructing Van Gogh's field with Irises near Arles part 3: determining the original colors. Color Res Appl. 2018;43(3):311–27. https://doi.org/10.1002/col.22197.
8. Riutort-Mayol G, Gómez-Rubio V, Lerma JL, del Hoyo-Meléndez JM. Correlated Functional Models with Derivative Information for Modeling Microfading Spectrometry Data on Rock Art Paintings. Mathematics. 2020;8(1212):2141. https://doi.org/10.3390/math8122141.
9. Thomas J, Poulsson TG, Ford T. The changing face of Munch's scream. In: MUNCH2022: understanding Munch and the art at the turn of the centuries—between the museum and the laboratory, Oslo; 2022. p. 88.
10. Ciortan IM, Poulsson TG, George S, et al. Tensor decomposition for painting analysis. Part 1: pigment characterization. Herit Sci 11;76 (2023). https://doi.org/10.1186/s40494-023-00910-x.

11. Feller RL. Studies on the darkening of vermilion by light. Report and Studies in the History of Art 1; 1967. p. 99–111.
12. Saunders D, Kirby J. Light-induced colour changes in red and yellow lake pigments. Natl Gallery Tech Bull. 1994;15(1):79–97.
13. Whitmore PM, Pan X, Bailie C. Predicting the fading of objects: identification of fugitive colorants through direct nondestructive lightfastness measurements. J Am Inst Conserv. 1999;38(3):395–409. https://doi.org/10.1179/019713699806113420.
14. Lerwill A, Brookes A, Townsend JH, Hackney S, Liang H. Micro-fading spectrometry: investigating the wavelength specificity of fading. Appl Phys A. 2015;118(2):457–63. https://doi.org/10.1007/s00339-014-8645-3.
15. Lojewski T. Lightfastness studies with MFT. In: MUNCH2022: understanding munch and the art at the turn of the centuries—between the museum and the laboratory, Oslo; 2022. p. 87.
16. Patin G, Erdmann RG, Ligterink F, Neevel JG, van den Berg KJ, Hendriks E. An enhanced optical micro-fading device. J Cult Herit. 2022;57:276–85. https://doi.org/10.1016/j.culher.2022.08.012.
17. Aambø M, Godzimirska M, Chan E, Lojewski T, Sandu ICA. Light sensitivity of pigments in Edvard Munch's works on paper. In: MUNCH2022: understanding Munch and the art at the turn of the centuries—between the museum and the laboratory, Oslo; 2022. p. 100.
18. Chan E, Aambø M, Godzimirska M, Grimstad I, Lojewski T, Sandu ICA. Light-induced color changes on "The Scream" versions in the Munch museum collection. In: MUNCH2022: understanding Munch and the art at the turn of the centuries—between the museum and the laboratory, Oslo; 2022. p. 91.
19. Carrión-Ruiz B, Riutort-Mayol G, Molada-Tebar A, Lerma JL, Villaverde V. Color degradation mapping of rock art paintings using microfading spectrometry. J Cult Herit. 2021;47:100–8. https://doi.org/10.1016/j.culher.2020.10.002.
20. Ford B, Druzik J. Microfading: the state of the art for natural history collections. In: Collection forum, vol. 27; 2013. p. 54–7.
21. Beltran V, Pesme C, Freeman S, Benson M. Microfading tester: light sensitivity assessment and role in lighting policy. Los Angeles: Getty Conservation Institute; 2021.
22. Morris HR. "Virtual fading" of art objects: simulating the future fading of artifacts by visualizing micro-fading test results. J Am Inst Conserv. 2007;46(3):215–28.
23. Hendriks E, Brokerhof AW, van den Meiracker K, Bridgland J, et al. Valuing van Gogh's colours. In: ICOM-CC 18th triennial conference Copenhagen. International Council of Museums; 2017.
24. Brokerhof A, Kuiper P, Scholten S. Spread or sacrifice: dilemma for lighting policies. Stud Conserv. 2018;63(sup1):28–34. https://doi.org/10.1080/00393630.2018.1504439.
25. Ciortan IM, Poulsson TG, George S, Hardeberg J. Predicting pigment color degradation with time series analysis. In: Color and Imaging Conference, vol. 30. Society for Imaging Science and Technology; 2022. p. 250–257.
26. Instytut Fotonowy: micro fading tester. 2022. https://www.fotonowy.pl/products/micro-fading-tester/?lang=en. Accessed 10 Sept 2022.
27. Norsk Elektro Optikk AS: HySpex. 2022. https://www.hyspex.com/hyspex-products/hyspex-classic/hyspex-vnir-1800/. Accessed 10 Sept 2022.
28. Savitzky A, Golay MJ. Smoothing and differentiation of data by simplified least squares procedures. Anal Chem. 1964;36(8):1627–39.
29. Vue T. Optium museum acrylic. 2022. https://tru-vue.com/solution/optium-museum-acrylic/. Accessed 31 Oct 2022.
30. Barnes RJ, Dhanoa MS, Lister SJ. Standard normal variate transformation and de-trending of near-infrared diffuse reflectance spectra. Appl Spectrosc. 1989;43(5):772–7.

Publisher's Note

Terms and Conditions

Springer Nature journal content, brought to you courtesy of Springer Nature Customer Service Center GmbH (“Springer Nature”).
Springer Nature supports a reasonable amount of sharing of research papers by authors, subscribers and authorised users (“Users”), for small-scale personal, non-commercial use provided that all copyright, trade and service marks and other proprietary notices are maintained. By accessing, sharing, receiving or otherwise using the Springer Nature journal content you agree to these terms of use (“Terms”). For these purposes, Springer Nature considers academic use (by researchers and students) to be non-commercial.
These Terms are supplementary and will apply in addition to any applicable website terms and conditions, a relevant site licence or a personal subscription. These Terms will prevail over any conflict or ambiguity with regards to the relevant terms, a site licence or a personal subscription (to the extent of the conflict or ambiguity only). For Creative Commons-licensed articles, the terms of the Creative Commons license used will apply.
We collect and use personal data to provide access to the Springer Nature journal content. We may also use these personal data internally within ResearchGate and Springer Nature and as agreed share it, in an anonymised way, for purposes of tracking, analysis and reporting. We will not otherwise disclose your personal data outside the ResearchGate or the Springer Nature group of companies unless we have your permission as detailed in the Privacy Policy.
While Users may use the Springer Nature journal content for small scale, personal non-commercial use, it is important to note that Users may not:

1. use such content for the purpose of providing other users with access on a regular or large scale basis or as a means to circumvent access control;
2. use such content where to do so would be considered a criminal or statutory offence in any jurisdiction, or gives rise to civil liability, or is otherwise unlawful;
3. falsely or misleadingly imply or suggest endorsement, approval , sponsorship, or association unless explicitly agreed to by Springer Nature in writing;
4. use bots or other automated methods to access the content or redirect messages
5. override any security feature or exclusionary protocol; or
6. share the content in order to create substitute for Springer Nature products or services or a systematic database of Springer Nature journal content.

In line with the restriction against commercial use, Springer Nature does not permit the creation of a product or service that creates revenue, royalties, rent or income from our content or its inclusion as part of a paid for service or for other commercial gain. Springer Nature journal content cannot be used for inter-library loans and librarians may not upload Springer Nature journal content on a large scale into their, or any other, institutional repository.
These terms of use are reviewed regularly and may be amended at any time. Springer Nature is not obligated to publish any information or content on this website and may remove it or features or functionality at our sole discretion, at any time with or without notice. Springer Nature may revoke this licence to you at any time and remove access to any copies of the Springer Nature journal content which have been saved.
To the fullest extent permitted by law, Springer Nature makes no warranties, representations or guarantees to Users, either express or implied with respect to the Springer nature journal content and all parties disclaim and waive any implied warranties or warranties imposed by law, including merchantability or fitness for any particular purpose.
Please note that these rights do not automatically extend to content, data or other material published by Springer Nature that may be licensed from third parties.
If you would like to use or distribute our Springer Nature journal content to a wider audience or on a regular basis or in any other manner not expressly permitted by these Terms, please contact Springer Nature at

onlineservice@springernature.com

Paper 8 - Estimating Optical Properties of Pigments from Color Charts with Multi-contrast Background

This paper is submitted for publication and is therefore not included.

Paper 9 - Colour-Balanced Edge-Guided Digital Inpainting: Applications on Artworks

sensors

MDPI

Article

Colour-Balanced Edge-Guided Digital Inpainting: Applications on Artworks

Irina-Mihaela Ciortan *, Sony George and Jon Yngve Hardeberg

Department of Computer Science, NTNU—Norwegian University of Science and Technology, 2815 Gjøvik, Norway; sony.george@ntnu.no (S.G.); jon.hardeberg@ntnu.no (J.Y.H.)
* Correspondence: irina-mihaela.ciortan@ntnu.no

Abstract: The virtual inpainting of artworks provides a nondestructive mode of hypothesis visualization, and it is especially attractive when physical restoration raises too many methodological and ethical concerns. At the same time, in Cultural Heritage applications, the level of details in virtual reconstruction and their accuracy are crucial. We propose an inpainting algorithm that is based on generative adversarial network, with two generators: one for edges and another one for colors. The color generator rebalances chromatically the result by enforcing a loss in the discretized gamut space of the dataset. This way, our method follows the modus operandi of an artist: edges first, then color palette, and, at last, color tones. Moreover, we simulate the stochasticity of the lacunae in artworks with morphological variations of a random walk mask that recreate various degradations, including craquelure. We showcase the performance of our model on a dataset of digital images of wall paintings from the Dunhuang UNESCO heritage site. Our proposals of restored images are visually satisfactory and they are quantitatively comparable to state-of-the-art approaches.

Keywords: inpainting; colorization; generative adversarial networks; dunhuang wall paintings

Citation: Ciortan, I.-M.; George, S.; Hardeberg, J.Y. Colour-Balanced Edge-Guided Digital Inpainting: Applications on Artworks. *Sensors* **2021**, *21*, 2091. https://doi.org/10.3390/s21062091

Academic Editors: Anastasios Doulamis and Eui Chul Lee

Received: 30 December 2020
Accepted: 11 March 2021
Published: 17 March 2021

1. Introduction

Image restoration is a classical task in computer vision, where the objective is to enhance the quality of an image, by removing noise, undoing irreversible damage, increasing the resolution, or recovering lost information. Inpainting, which is also known as image completion, is one of the instances of the image restoration problems that aims to fill gaps in a digital image, by reconstructing the color and structural elements. Colorization is highly related to inpainting, the task of hallucinating colors in black-and-white and neutral-toned visual material, where the semantics is preserved but the color clues are non-existent. As a matter of fact, the choice of possible infilling colors is more confined in image completion cases, since assumptions can be extrapolated from the area surrounding the missing region.

Centuries old artworks with historical and cultural values are among the surfaces that most suffer from severe degradations due to aging and mishandling. In most cases, the damage represents a complete lacuna, where ground-truth is missing and/or the number of unknowns is too high to allow the generation of a fully validated reconstruction. Retouching the physical objects might result in a risky operation and it is perceived with very careful and conservative views in the Cultural Heritage (CH) community. Nonetheless, the desire to visualize the hypothesis of how the undamaged original might have looked like is still present, and the possibility to do this digitally without altering the original is very attractive to art conservators. This places CH among the first applications to benefit from digital inpainting. As a matter of fact, the pioneering work on digital inpainting [1] was built around the scope of artwork reconstruction.

Traditional solutions to inpainting fill the missing region while using the statistics of the image and the structure and texture synthesis from the neighbourhood. However, such traditional approaches require ad-hoc feature engineering and they are seldom semantic-aware. The take-off of deep learning techniques has leveraged the performance of image

restoration solutions, including inpainting. End-to-end convolutional neural network (CNN) models infer complex image understanding processes and they account for low-level characteristics and high-level semantics of the image in one-go without the need to break the image and feature computation into sub-components treated as single cases.

The interest for virtually repairing damaged artworks with deep learning approaches is rising. As a matter of fact, the e-heritage Workshop of the International Conference on Computer vision in 2019 [2] organized an image restoration challenge for image inpainting that is tailored to CH scans, releasing a dataset of wall paintings (visualized in Figure 1 from the Dunhuang cultural site [3]). There are not numerous such attempts in the computer vision world, partly because CH datasets are yet not perceived as a baseline in the deep learning community and partly because they are not widespread. For this reason, most of the deep learning approaches are not made to solve the specific problems of art images. Moreover, most of the solutions for the CH field are deployed by means of transfer learning from approaches that were developed for natural images (ImageNet [4], Places [5]), buildings and streets (Paris Street View [6]), celebrities faces (CelebA [7]), etc.

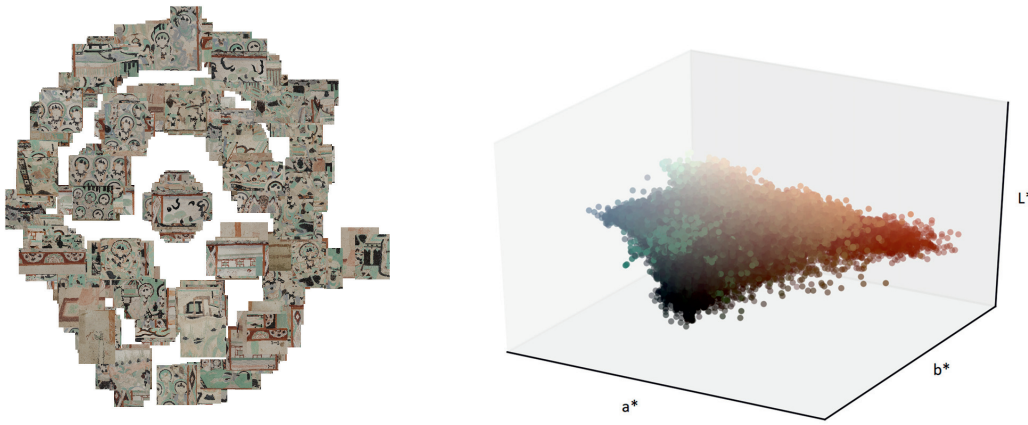

Figure 1. Left: Dunhuang dataset visualized in a two dimensional space with Barnes-Hut Stochastic Neighbour Embedding (BH-SNE) [8]. The clustering is done based on the activations of the first fully connected layer of the pretrained VGG19 network [9] that outputs a vector of 4096 features (color, size, semantics, etc.) for each image. Images are displayed exactly at their embedded location in the two-dimensional (2D) projection space. **Right**: color gamut of the Dunhuang dataset. The L*a*b* coordinates are rendered with the corresponding RGB colour.

In this work, we propose an inpainting algorithm for artworks, where two convolutional models are learned in a generative adversarial fashion: an edge generator and a color generator. The purpose of the first model is to learn the edges in the missing region based on a monochrome-only representation of the input image. To complement the structural information, the second model fills in the gap with color information. It does so by enforcing that the infilled chromatic information respects a balanced palette, based on priors that were computed in the quantized chromatic channels, so that the generator doesn't get biased to only overly-used colors. With this workflow, we are traversing the usual steps that an artwork usually undergoes: first the under-drawings are sketched (edges), then the main color palette is chosen (priors), and, finally, the color tones are painted. We test our approach on digital images of the Dunhuang murals, part of an UNESCO heritage site in North China [3].

2. Related Work

In this literature review, we only focus on learning-based solutions to digital inpainting. We start with works on natural images, which are the state-of-the-art in field and, then, we carry on to cultural heritage applications.

2.1. Deep Learning Approaches for Image Inpainting

The seminal work of Pathak et al. [10] addressed the inpainting of natural images with an encoder-decoder CNN. The encoder part is based on AlexNet architecture [11], trained on an input image size of 227×227. The missing area amounts to 1/4 of the image and it is simulated by either a rectangular shaped mask originated at the center or several rectangular areas randomly positioned. Such solutions that involve rectangular masks are categorized as region inpainting. By adding the adversarial loss to the L2 Euclidean reconstruction function, [10] claim a substantially improved accuracy.

The approach of Iizuka et al. [12] is inspired by [10], while adding the following contribution: holes are simulated by arbitrary forms, as opposed to only rectangular shapes, a training process in the adversarial fashion that ensures multi-scale resolution and global as well as local consistency and applications to more challenging data, such as faces. In order to increase the quality of the resolution, they also use dilated convolution layers, which allows for increasing the receptive field without placing a burden on the number of parameters or the computational complexity. These methods are however dependent on the initialization of the missing pixels and might need post-processing refinements. The work of Liu et al. [13] proposes an end-to-end inpainting pipeline with partial convolutions arranged in a U-Net architecture, where convolutions affects only non-hole pixels and where the mask gets updated after each convolution, by getting thinner and thinner, until its total disappearance. This way, the content to be infilled is learned only from the contextual information provided by the valid pixels. Moreover, the masks have no constraints on the shape and the approach gives good results, even if the missing information is present around the edges (image extrapolation).

Isola et al. [14] and Shu et al. [15] both employ generative adversarial networks (GAN) to solve a more general problem, that of "image to image translation", which can be adjusted to inpainting as well. In the former paper, the inputs are pairs of images, while the latter extends the work for cases when pairs of images do not exist by introducing a cycle consistency loss. The work of [16] offers multiple plausible solutions for the completion of natural images, faces and buildings and trains in parallel two networks (reconstructive and generative) supported by the generative adversarial setting.

Inspired by the image-making process from an artist's perspective "lines first, color after", the network that was proposed by Nazeri et al. [17] uses a three-stage GAN network: firstly, the edges are learned in the missing region from the grayscale input; secondly, the color information in the missing area is learned from the RGB input; and, thirdly, the joint edge and color information are trained in conjunction.

There is a body of works that focus on the accurate inpainting of complex structural information [18–20]. These works exploit landmarks in the geometry of the human body [18,20] and human faces [19] in order to estimate parsing maps. Parsing maps encode the components that define the objective structure, together with each part's labeled location that constrain the subsequent color completion step. While these methods go beyond learning edge information, since they deal with a more specific and geometric definition of structure, they require a dataset that is uniform and deterministic in its shape representations, be it human body, animal body, or human faces. In this sense, the Dunhuang dataset is rich in content, varying from Buddha representations to architectural elements and decorative patterns [3].

2.2. Deep Learning Approaches for Paintings Retouching

One of the first attempts to address image restoration problem with a dedicated interest for paintings and for big missing regions was made by van Noord [21]. The

method is mainly based on the context encoder of [10], but it uses dilated convolutions instead and different loss functions. In order to repair damaged wall paintings of the Dunhuang site, Yu et al. [22] utilize transfer learning from [13] and bring modifications that adapt to the specificity of the data, such as the use of masks that have a random walk configuration and, thus, resemble more the stochastic damage process of the wall paintings surface. More specifically, the dusk-like masks (based on random walk) emulate deterioration by molds and salty erosion, while jelly-like masks (which is a dilated random walk) simulate physical damages or sabotages.

Wang et al. [23] offer a method for the digital restoration of Tibetan Thanka murals, based on Unet Partial Convolution Network. Their main contributions are related to the mask and training loss design. Thus, they analytically summarize the frequent type of damage in the murals as scratches and spots and simulate the damage with masks that contain lines and elliptical shapes with various size parameters and of random distribution. These masks are similar to the irregular masks that were proposed by [12], while adding the elliptical elements as variation. Nonetheless, this mask design is tailored to the type of damage observed in the Thanka murals. Further on, they train their model in two stages: in the first stage, higher weight is given to losses that characterize per-pixel reconstruction, while, in the second stage, higher weight is given to perceptual losses.

In their work [24], Wang et al. identify the problems of low-resolution, color discrepancy, and blurriness in image inpainting for general applications, and they stress that these problems are more critical for CH surfaces. Thus, their methodology is rooted in the unpaired image-to-image translation implemented with a fully-convolutional CycleGAN architecture [15]. Nonetheless, they bring minor improvements to account for the above-mentioned problems. They address the high-resolution by diving the symmetrically-padded input images (8912×8912) into patches of the maximum size allowed by memory (2048×2048) and then recompose the patches into a high-resolution image. However, this results in a loss of local color accuracy that is compensated by adding a color constraint to the high-resolution mosaic. This constraint is derived from a low resolution reconstruction with the same network, where the input image is resized to the maximum possible size (2048×2048). The constraint is verified by means of an identity loss. As far as the sharpness is concerned, it is solved with a Gaussian–Poisson editing in the post-processing stage.

Weber et al. [25] also include refinements in the post-processing stage, by inserting human expertize in their inpainting solution to the Dunhuang murals and benchmark dataset [3]. More precisely, they introduce an interactive extension to the Deep Image Prior (DIP) work [26], where an initial restoration is given by the DIP method, that requires no training process. Through an interactive tool, the initial restoration is then edited by human experts, which generates an improved result that is further fed back into the DIP algorithm. This process continues iteratively until the user is satisfied with the inpainted image. While such an interactive approach is very attractive, especially because of bridging the domain-specific expert knowledge with the input provided by computer vision technologies, this work does not challenge the internal learning mechanisms of a deep-learning model.

2.3. Research Gaps and Contributions

There is still room for improvement for deep learning approaches for artworks inpainting. Many of the imperative improvements to be made are on color consistency and high-resolution. For strengthening the color consistency, new losses have been formulated in the GAN setting, such as identity loss, Wasserstein loss [27], etc. A successful approach was developed by Zhang et al. [28] for the recolorization of natural images, where the color accuracy is not verified with an Euclidean distance (that is minimized by the mean value), but formulated as multinomial classification, where the ground-truth image's gamut is represented in a quantized L*a*b* color space. Moreover, each of the discrete values of the quantized color space receives rebalancing weights to account for the natural images' bias to desaturated colors (due to the higher frequency of skies and landscapes in the dataset). A similar color-palette constraint was also used in [29], without the rebalancing

weights. Even though these color-palette constrained CNN have been developed for the recolorization tasks, they can be easily adopted in the inpainting task.

Several actions can be taken for reaching sharper results and higher-definition. If computing power allows, training on bigger image size can help. Otherwise, the result of the inpainting can be improved by being fed to super-resolution model. The resolution is increased when the receptive field of a CNN is increased, so dilated convolutions are good practice, because they expand the receptive field without an echo on the number of the parameters included in the model [21].

In addition, the size of the receptive field is also affected by the size and shape of the holes. As a matter of fact, in [30], they studied how the size, shape, and orientation of masks influence the performance of digital inpainting.

Based on all of these insights, we bring the following contributions in our proposed model: (1) we complement the edge-guided multi-stage network introduced by [17] with a color-aware loss that rebalances the chromatic elements to avoid the bias of dull colors from the core of the gamut; (2) we use four morphological variations of the random-walk mask, so as to target different receptive fields of the network. While the work of Nazeri et al. [17] is guided by the principle "lines first, color after", our work's underlying principle is "lines first, color palette after, color tones at last" by resembling even more the modus operandi of an artist.

3. Method

Our approach to solve inpainting for artworks is both edge and color aware. Building on the work of [17], we train two generative adversarial networks (see the diagram of our approach in Figure 2): one that learns the edges in the lacunae (Section 3.2) and a second one that learns the color information (Section 3.3). The two networks are trained in a multi-stage fashion: first, separately and then combined, as detailed in in Figure 3. Contrary to the work of [17], instead of the RGB colour space, we work in the L*a*b* space, which is a more perceptual chromatic space. Besides enforcing the computation of the convolutional neural features in a perceptual space, the use of L*a*b* space serves the scope of rebalancing colors, so that they fit into the overall palette of the dataset. In order to improve the color coherence, we smooth the effect of L1 loss in GANs—that of filling in empty spaces with the mean colour of the gamut, which results in inaccurate and desaturated colors—by adding a color rebalancing loss similar to [28,31].

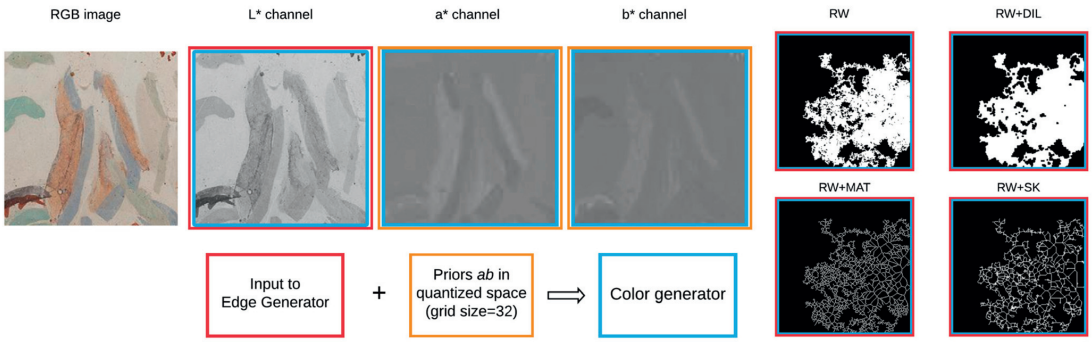

Figure 2. Our model converts the RGB images to L*a*b* color. The edge generator receives as input only the monochrome luminance channel and the binary masks of missing pixels (that follow variations of a random walk pattern). Subsequently, color rarity weights are computed on the a* and b* channels and then used in the loss function of the color generator. The edge map, the multichannel L*a*b* image and the priors are fed to the color generator.

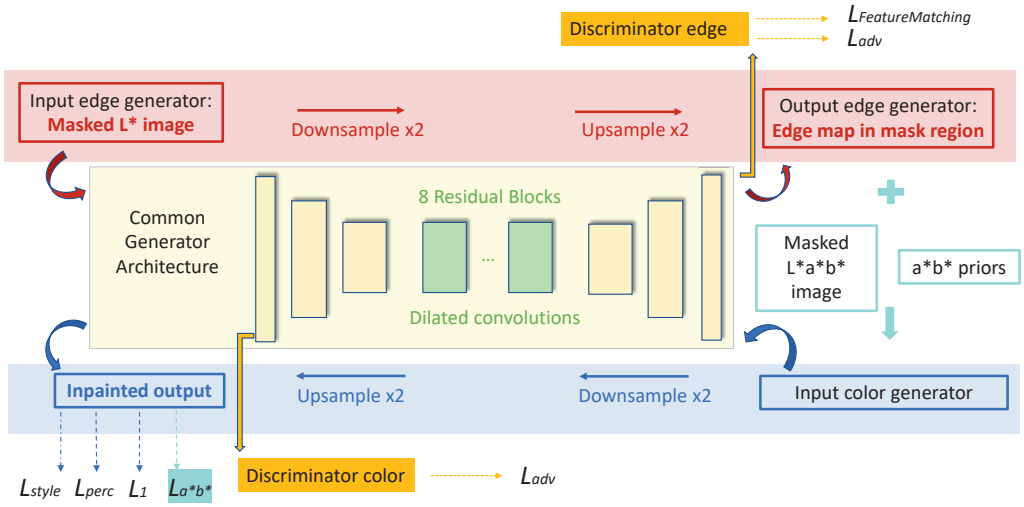

Figure 3. Both color and edge generators have the same underlying convolutional architecture, composed of encoder–decoder blocks and eight residual blocks with dilated convolution in between. Different from [17], we introduce the L_{a*b*} loss for the color generator to lower the bias towards mean values of the dataset's gamut.

3.1. Masks

The performance of learned image completion is influenced by the network activations and the receptive field, especially when training for a resolution twice or four times the test image resolution. Based on this insight, we take the following measures to modulate the size of the receptive field: we incorporate dilated convolutions and we use irregular masks of different size and orientations. We start with a mask that simulates a random walk: starting from a random seeding position, each next move is decided by a random choice between the pixels in the four-connected neighbourhood. There can be multiple seeding positions and, at the same time, a pixel can be re-traversed multiple times, which decides the overall spread of the mask. We use the convention 1 values for holes, 0 values for non-hole region. Each base random walk mask is then further processed into morphological derivates (see Figure 4) by applying the following operations: dilation, skeletonization and medial axis transform. The random walk mask was proposed in the Dunhuang challenge [2,3]. This pattern was adopted in [22], where the authors call the normal random-walk dusk-mask and the dilated random walk jelly mask, claiming the former to be characteristic of mold and erosion and the latter of physical damages. Nonetheless, to the best of our knowledge, we are the first to introduce the skeletonization and medial axis transforms of the random walk. Through these operations, we are synthesizing a fine craquelure-like structure, a common aging effect of artworks.

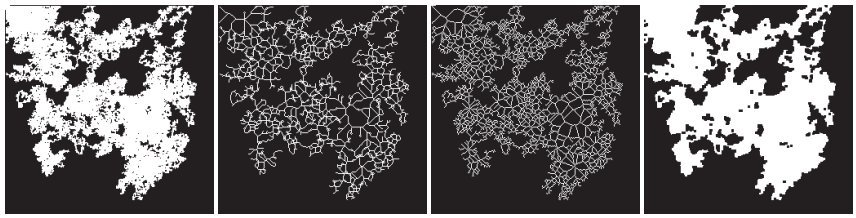

Figure 4. Random walk (RW) mask (leftmost) with three morphological variations: skeletonization (RW + SK), medial axis transform (RW + MAT) and dilation (RW + DIL). Besides covering different areas of missing pixels, these masks simulate various patterns characteristic to artwork degradation: moist and pest formation, craquelure, and mechanical damage.

3.2. Edge Inpainting Model

The edge model receives three inputs: the Luminance channel of the ground-truth data, the mask image, and the edge map obtained with the Canny operator from the luminance channel. The threshold for Canny edge detection was empirically set to 1.1 to discount as much as possible noise and only select the relevant edges. As sketched in Figure 3, we preserve the network architecture that was proposed in [17] with dilated convolutions and residual blocks, followed by spectral normalization. Beside the adversarial loss, the loss function for the edge hallucinator includes feature-matching loss that compares activation maps at intermediate layers of the discriminator.

3.3. Color Inpainting Model

The input to the color inpainting model is the masked L*a*b* image and the edge map. In a first phase, when the color model is trained independently from the edge model, the edge map is given by the Canny operator. Subsequently, when the two models are jointly trained, the edge map is inferred by the edge model. The architecture of the network is the same as in [17], consisting of dilated convolutions and residual blocks, followed by instance normalization. As in [17], the loss function for the generator includes the adversarial loss, the L_1 distance, the perceptual loss, and the style loss $L_1, L_{adv}, L_{perc}, L_{style}$. In addition, we inserted a new loss term, L_{ab}, which only operates on the chromatic channels.

The L_{ab} loss is computed as multi-class cross-entropy in the quantized *ab* space between the target and predicted image, multiplied by color rebalancing priors. The priors are extracted before the training process, by saving the discretized *ab* space (where number of quantiles q = 32) for each training image. Subsequently, these priors are smoothed with a Gaussian filter and finally, they are mapped to a probability distribution between $[0, 1]$ in the discretized space of possible colors. This loss is computed separately for a and b channel, and then averaged as the final L_{ab} loss that contributes to the generator loss. The full mathematical formulation for the color rebalancing loss can be followed in Equations (1)–(4). The parameter p was chosen as in [31]. The weight for the losses are as follows: $w_{L_1} = 0.05, w_{L_{adv}} = 0.1, w_{L_{perc}} = 0.1, w_{L_{style}} = 250, w_{L_{ab}} = 0.9$. We did not completely exclude the L_1 distance, instead we opted for a very small weight, since we want the model to still be aware of the global differences that are provided by L_1 norm.

$$priors_{a,b} = ((1-p)(Filt_{gaussian} \times q_{train}) + p)^{-1} \tag{1}$$

$$l_{a,b} = priors_{a,b} * MCE(q_{a,b}(target), q_{a,b}(pred)) \tag{2}$$

$$L_{ab} = mean(l_a, l_b) \tag{3}$$

$$Loss_{GC} = w_{L_1} L_1 + w_{L_{adv}} L_{adv} + w_{L_{style}} L_{style} + w_{L_{perc}} L_{perc} + w_{L_{ab}} L_{ab} \tag{4}$$

Finally, the output of the network is rendered from L*a*b* to RGB and merged with the non-masked original pixels.

4. Results

4.1. Dataset and Training Specifications

Our model was trained and tested for the Dunhuang dataset, released for the ICCV e-Heritage workshop challenge [3]. The images represent digital scans of the mural paintings inside one of the Mogao caves in North China. Generally, the Dunhuang caves were painted across many centuries by various artists and under various dynasties, covering more than one artistic style. They display figurative symbols that were taken from Buddhist mythology. The ICCV e-Heritage challenge released 500 train images with ground-truth and 100 masked test images, for which the reference has not yet been released to the best of our knowledge. The images have non-uniform dimensions across the dataset. Therefore, for our work, we split the available 500 images into 465-10-25 images as base for training-validation-test experiments. Further on, we cropped the test and validation images in blocks of 256×256 with minimal overlap, so as to take advantage of the full resolution of the images. This totalled to 5596 ground-truth images for training and 96 for validation. The test images were left at their original size.

Each image in the training and validation collections was accompanied by a random walk mask and its 3 morphological variations, so the total training load was 22,384 images. Meanwhile, for each image in the test set, two base masks plus the derivates were generated, amounting to a total of 200 images for inference. The masks cover from 0 to 60% of the image size. The training images were randomly flipped horizontally and vertically with a random factor that is decided by a binomial distribution.

The model was implemented in PyTorch1.1 [32] and then trained on a single CUDA-enabled GPU with a memory capacity of 11 GB. Training was performed on images of size 256×256, with batch size of 4. The model was optimized with ADAM optimizer [33], and the hyperparameters β_1 and β_2 set to 0 and 0.9. We followed the training strategy of [17]. In a first stage, the color generator was trained separately from the edge generator and then, the input from the edge model was added as input to the color-only based model to improve the infilling of edges. For the separate training phase of the generators, we set the learning rate to 10^{-4} and stopped the training after observing a flatness in the oscillation of the loss values. Afterwards, for the joint training, we reduced the learning rate to 10^{-5} to push the weights of the model to update for smaller changes, and continued training until the losses plateaued. In each case, the discriminators were learned at a rate that was ten times lower than the generators' rate. Figure 5 displays the intermediate results of the jointly trained model on the Dunhuang validation dataset. An interesting highlight of these intermediate maps are the edge maps, which show how the edge generator is able to infill structure in the missing regions in a way that follows the edge lines in the original image.

4.2. Qualitative and Quantitative Assessment

The test images were reconstructed at the original resolution. In most of the state-of-the-art papers on image restoration, the results are presented at the same size as train size or only slightly bigger. However, in our case, the scaling factor is between two to four times the training size.

For visual inspection, we selected four images that are displayed in Figure 6, that we consider challenging cases for inpainting. Figure 7 shows two random walk degradations over a scene that contains a character (Figure 6a). The first deterioration hides most of the details of the face and decorations above the head of the character. Faces contain fine structural details that are challenging for an inpainting task. Our result is able to recover the details for the aura, the left eye, the lip, and the base of the nose. In the same way, the second deterioration occludes the palms and fingers that are recovered in the inpainted image. Nonetheless, a downside of this reconstruction is that the orange wings in the top center are not completely free from color artifacts.

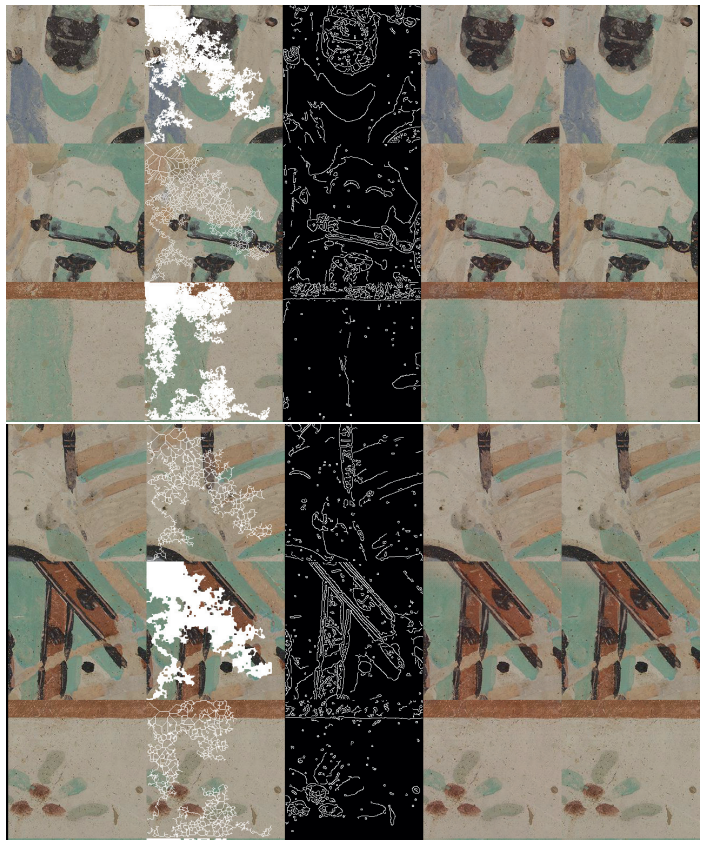

Figure 5. Intermediate results generated for a subset of random six images from the validation set (original size of the images is 256 × 256, scaled to fit in the page). For each of the six instances, five images are shown, in order from left to right: ground-truth; ground-truth with deterioration; edge map in the missing region; output inpainted image with both edge and color information as generated by the network; and, output of the model merged with the non-masked input pixels.

(**a**) (**b**) (**c**) (**d**)

Figure 6. Ground-truth images selected for discussion. (**a**) First image (697 × 701 pixels) was chosen because it contains a face, that we consider a challenging case for inpainting. (**b**) Second image (681 × 674) is very color diverse. (**c**) Third image (828 × 800) is a homogenous colour, where it will be easy to check for color artifacts in the inpainted result. (**d**) Fourth image (582 × 841) is a scene with decorating motifs, where edges reconstruction can be inspected.

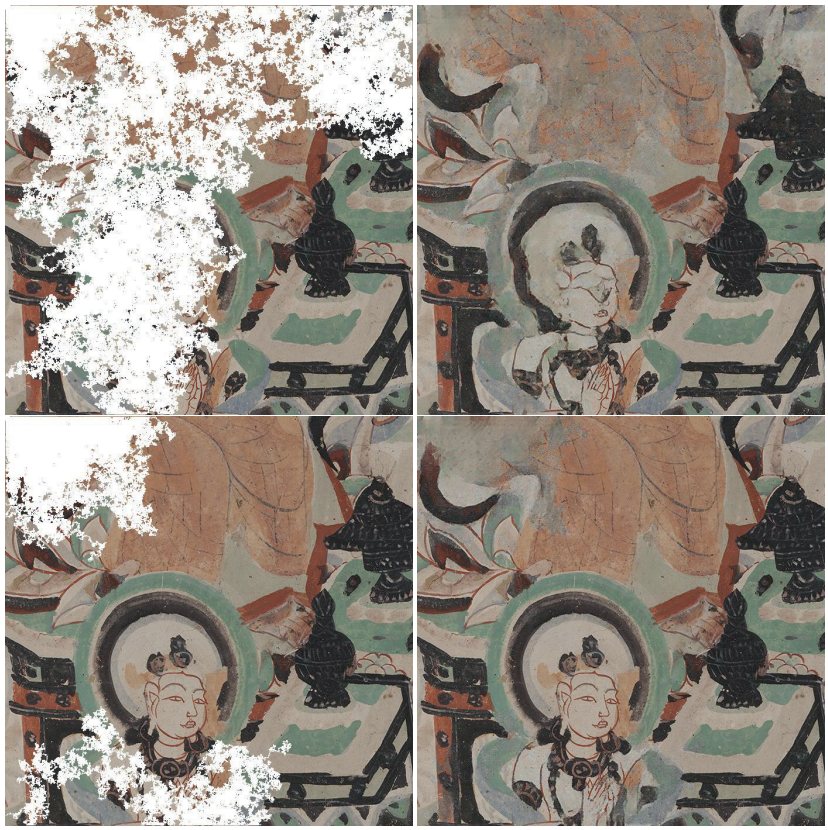

Figure 7. Inpainting results for random walk deterioration with different coverage of the same scene (ground-truth is Figure 6a). The inpainted images were generated at full resolution, however they are shrinked for display purposes here. Even though, in the first deteriorated example, the face of the character is mostly covered, the inpainted version manages to reconstruct some structural details with good accuracy, such as the aura, the lips and the left eye.

On the other hand, Figures 8 and 9 show an accurate restoration of the color content. The gap shown in Figure 8 cover distinct color tones from Figure 6b that are well retrieved in the restored result. Similarly, Figure 9 retouches Figure 6c, which lies as a patch of homogeneous color where chromatic inaccuracy would be easily detected. However, the infilling adds color of a hue similar to the original. The last example (Figure 6d) is a painting of a temple that is rich in structural details. The color coherence is maintained in the beige roof in the middle of the image, but it shows greenish artifacts in the orange stripe in the bottom of the image, as depicted in Figure 10.

Figure 8. Pairs of inpainting results for morphological variations of random walk masks with different coverage of the same scene (ground-truth is Figure 6b). The colors are well preserved in the restored version. In the second pair (top third and fourth images), where dilated random walk deterioration is used, we can notice more blurriness.

Figure 9. Inpainting result for Figure 6c. The restoration does not disrupt the color homogeneity with respect to the non-corrupted part of the image.

We have quantitatively evaluated the performance of our method with traditional image quality metrics (IQM), as well as CNN-enhanced IQMs. These metrics are computed starting from the RGB rendering of the output of our approach in comparison to that of [17] trained from scratch on our dataset. Out of the traditional IQMs, we present Structural Similarity Index (SSIM) [34] with a window size 11, Peak Signal-to-Noise Ratio (PSNR), colorimetric difference with the CIEDE2000 formula [35], as well as the spatial extension of the CIELAB colorimetric difference (S-CIELAB) [36]. The results in Table 1 are reported for each mask type. The results are better for the gap that occupies less space in the image. Accordingly, the metrics indicate that the highest quality of reconstruction is achieved on holes that simulate craquelure due to the minimal corruption they bring to the original image. Meanwhile, the lowest performance of the metrics corresponds to the dilated random walk masks, because of their increased coarseness of the pattern and a higher take-over of the image. Even though, numerically, our approach does not outperform [17] for the four traditional IQMs, the differences are not significantly apart. Actually, the differences between the compared methods for the color metrics quantified as CIEDE2000 and S-CIELAB are under the "just noticeable difference" ΔE unit. Meanwhile, PSNR and SSIM are known to be low estimators of the human perception and, in addition, they have very low sensitivity to color (as a matter of fact the input to SSIM is grayscale) and spatial effects (such as blur or constrast). By visually assessing selected images that are inpainted

by the two approaches (see Figure 11), we can see that the restoration that is generated with our approach appears to be more color coherent and sharper in localized areas with respect to the results obtained with [17]. The pictures in the third and fourth rows, last column exemplify color hue artifacts where beige color gets replaced with green tones, which are not produced by the proposed method. We would like to suggest that for the color metrics, a more meaningful representation than numeric values that are aggregated over all images and pixels, is actually a distance map, where the chromatic differences are correlated with their spatial context. As a matter of fact, in order to enforce the above-mentioned visual hints perceived in Figure 11, we computed Spatial-CIELAB [36] distance maps between the original, our proposed method and the method in [17]. S-CIELAB computes the color difference between images, after applying a spatial processing step as a simulation of the human vision bandpass filtering. This way, instead of considering pixel-only variations, it measures the color distance on more semantically meaningful spatial patterns. Figure 12 depicts the difference in ΔE error between our approach and [17] based on S-CIELAB computed for the selected images in Figure 6. We visualize these differences as contour plots, where positive values (yellow) highlight areas in the images where our method performs better colorimetrically while negative values (blue) show where the other method works better. The contour plots display isolines of ΔE differences at specific levels defined as -2σ, $-\sigma$, σ, 2σ, where σ is the standard deviation of each case's distribution. These comparisons are consistent with the visual observation of images shown in Figure 11 and they prove that both models have selective performance. For more visual assessments of these two approaches, please refer to the Supplementary Material to this article.

Figure 10. Inpainting result for Figure 6d. The beige structure in the middle of the image remains color coherent in the infilled image. Similarly, the two leftward black poles. However, the reconstruction is more blurry in the top left corner, which corresponds to a bigger and more contiguous lacuna.

Table 1. Peak Signal-to-Noise Ratio (PSNR), Structural Similarity Index (SSIM), CIEDE2000, and S-CIELAB metrics between the ground-truth test images and the inpainted results, presented for each mask type. For PSNR & SSIM, higher values mean better closer resemblance to the ground-truth. For CIEDE2000 and S-CIELAB, higher values correlate with a higher colorimetric distance with respect to ground-truth.

Mask Type	Missing Pixels (%)	PSNR		SSIM		CIEDE2000		S-CIELAB	
		Ours	[17]	Ours	[17]	Ours	[17]	Ours	[17]
RW	28.42	26.57	26.86	0.74	0.76	4.09	4.05	3.75	3.71
RW + SK	6.93	29.89	30.12	0.81	0.82	3.19	3.10	2.30	2.19
RW + MAT	7.60	29.81	30.04	0.81	0.81	3.21	3.12	2.38	2.26
RW + DIL	31.20	24.75	25.18	0.72	0.73	4.44	4.34	4.24	4.13

Recent works in the field of image quality evaluation have demonstrated the effectivenes of CNN-based IQMs [37–39]. In other words, measuring the similarity in the feature space extracted by convolutional neural networks is in more agreement with the human subjective scores than by directly comparing end-level images. In [37], Amirshahi et al. compute the similarity of feature maps extracted from CNNs (AlexNet and VGG19 networks pretrained on ImageNet dataset). They compute the self-similarity of feature maps at each convolutional layer and at multiple levels of spatial resolution inspired by the Pyramid Histogram of Oriented Gradients (PHOG) approach. The final aggregate metric is given by the geometric mean of the single metrics determined for each convolutional layer. They test their method on four image quality datasets of natural images with various distortions and show that the CNN-based self-similarity measure has more correlation with human subjective scores than PSNR, SSIM, and S-CIELAB metrics. This work is extended in [38], where CNN feature maps are compared with traditional IQMs (such as PSNR and SSIM). Similar to [37], the finding is that the CNN-enhancement of IQMs (computed on CNN feature maps) is significantly more correlated with human perception than their traditional variant (applied on end-level image). In addition, the performance of all the proposed CNN metrics is not affected by changing the CNN network [37,38].

Hence, drawing from the insights of [37,38], we validate our method with three metrics that measure the similarity between features maps that were extracted with the pretrained AlexNet for the ground-truth and inpainted images; Self-Similarity based on Pyramid Histogram of Oriented Gradients [37], CNN-enhanced PSNR, and CNN-enhanced SSIM [38]. Figure 13 displays the global performance of these metrics (pooled from the intermediate results at each convolutional layer). Based on CNN-enhanced PHOG self-similarity (Figure 13a), our method slightly outperforms [17] for bigger areas of damage (RW, RW+DIL). However, the overall values of CNN-enhanced PSNR and SSIM for [17] are better than ours. Nonetheless, we continue the analysis by exploring the internal representations of these metrics and study their performance for each convolutional layer. In this sense, one important finding of [37,38] is the proportionality between the order of the convolutional layer and the correlation with subjective scores. Thus, the first convolutional layer, because of embedding lower-level features, is farther away from human perception than the fifth convolutional layer that embeds higher-level features. Figures 14b,c show that the CNN-enhanced SSIM and PSNR for convolutional layers 2–5 are better for our method in comparison with [17], even for larger missing content (RW, RW + DIL). We could further infer that what draws back the pooled overall results for our method (Figures 13c and 14b) is explained by the poorer performance of the first convolutional layer only. This suggests that our method preserves more of the mid-level and higher-level features in restoring the original images. It is noteworthy to relate these findings with a study on color responsivity of AlexNet [40], where it is claimed that all layers have color responsivity in a trend that decreases from first convolutional layer to the fourth one and then rises back in the fifth layer. Accordingly, the highest color responsivity is given by the first and last layer. Nonetheless, the first layer deals with a basic encoding of the color signal, while the last

layer responds to more complex color encodings. Therefore, we could extrapolate that, based on the higher performance of all CNN-based metrics for the last convolutional layer, our method handles better complex entanglements between spatial and chromatic signals.

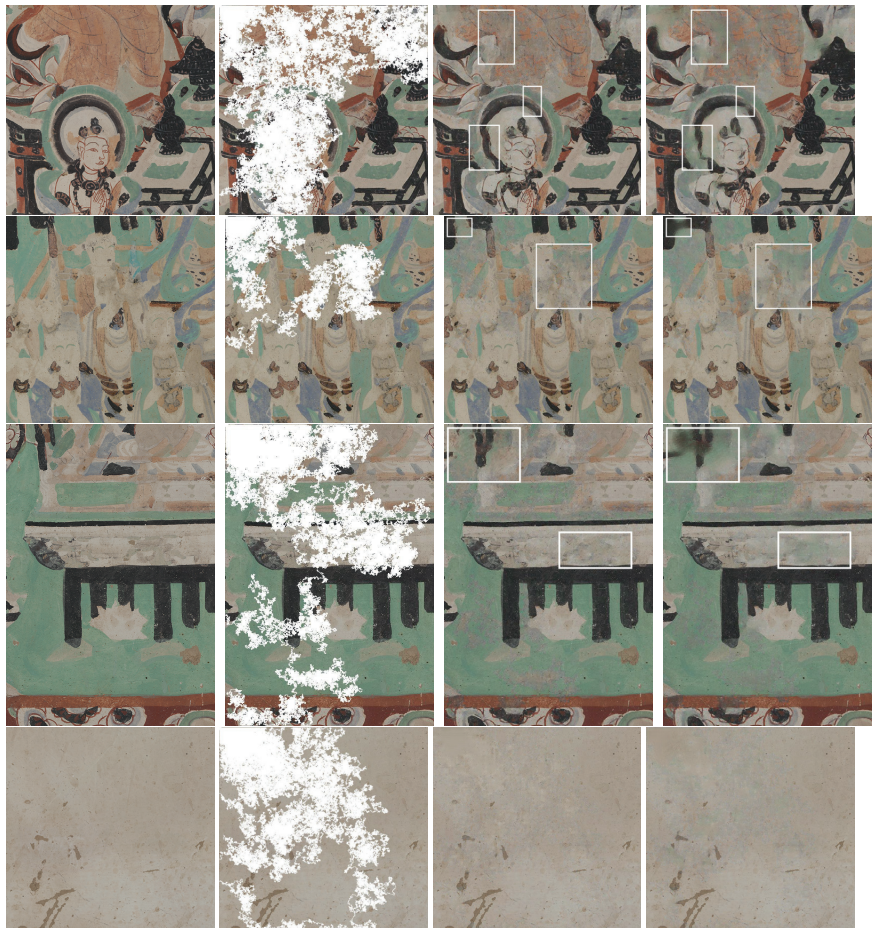

Figure 11. The columns represent in order, from left to right: original image, deteriorated image with RW mask, inpainted image with our approach, inpainted image with the approach of [17]. In the highlighted regions of interest, our approach outputs more color coherent and sharper results.

Regarding the performance of all image quality metrics, it is noteworthy to mention that compression artifacts (the dataset is available as JPEG images) might represent an error factor in the pipeline. Similarly, the conversion back and forth from RGB to L*a*b* color space might introduce some numerical loss in the quantitative analysis. This transformation takes place more times than in the method of [17] due to the way our pipeline is designed.

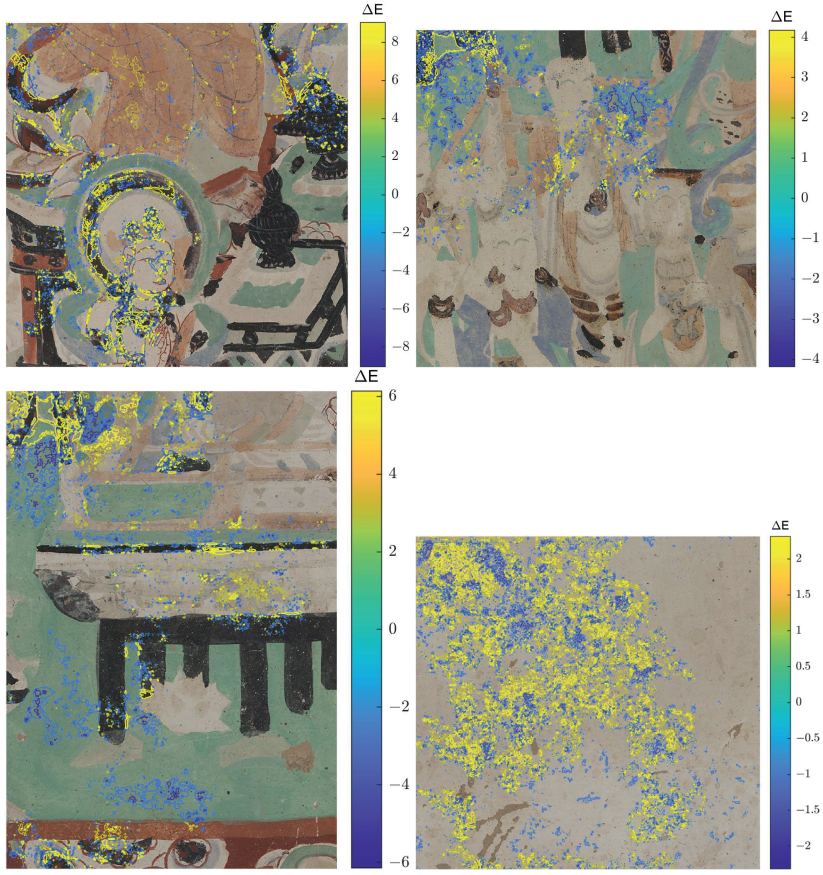

Figure 12. Contour plots showing the isolines of difference in ΔE error between images inpainted with the proposed method minus the method in [17]. For each method, ΔE was computed with the S-CIELAB distance metric, where the reference was the original, undamaged image. A positive value (yellow) for the contour plots show areas where our proposed method is more color coherent with the original, whereas negative values (blue) represent regions where the other algorithm performs better.

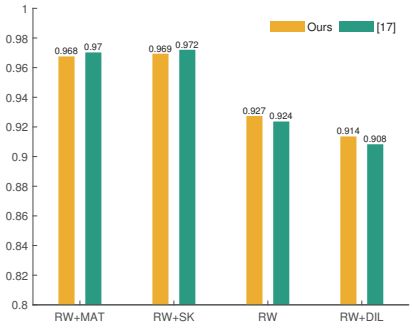

(**a**) Convolutional neural network (CNN)-enhanced Self-similarity

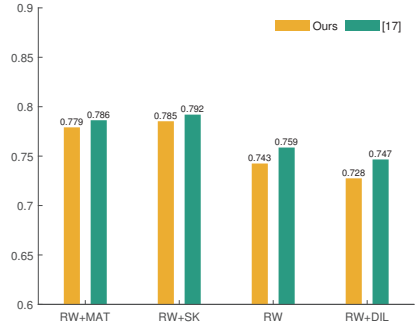

(**b**) CNN-enhanced SSIM

Figure 13. *Cont*.

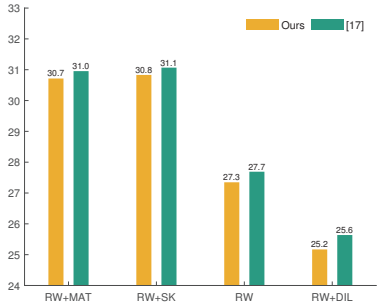

(**c**) CNN-enhanced PSNR

Figure 13. Bar plots showing the overall performance of three CNN-based mage quality metrics (IQMs) for groups of damage. These metrics measure the similarity of the feature maps given by the activations of AlexNet (pretrained on ImageNet) for the ground-truth test images and images inpainted by our approach and [17]. The overall metrics are aggregated as the geometric mean of the result at each convolutional layer.

It is not trivial to draw a straightforward and fair comparison with other relevant state-of-the-art models, such as [3,23,25], where the exact dataset, train-test split, and model implementation are not available to perform a one-to-one mapping to our approach. So much so, we provide a rough comparison in Table 2, where we outline key aspects of every method, including the minima and maxima of PSNR and SSIM metrics where applicable. Letting aside the variations in data, mask type, and precise extent of missing pixels reported for each method, we can compare these results by identifying their common purpose: solving the digital inpainting task for Buddhist mural paintings with deep learning approaches. With these considerations in mind, Wang et al., in [23], simulate four levels of damage as is our case, even though the ratio of corrupted pixels to non-corruped pixels per level remains unknown. Compared to the IQMs reported by [23], our work achieves higher PSNR extremes, while lower SSIM extremes. It seems that the user input in the interactive Deep Image Prior method of [25] leverages the SSIM to a value of 0.78 for random-walk type of damage, which is higher than our results for the RW category (0.74). Nonetheless, [25] pool their results from only 10 images. At the same time, Yu et al. [22] include no quantitative result, so we are not able to draw any numeric comparison with their method. While our method does not outperform the SSIM and PSNR reported by [17,23], it is noteworthy to emphasize that the proposed approach works selectively better than [17] for certain areas in the image, as presented in the color difference maps of Figure 12. This selective performance is reinforced by the CNN-based metrics that prove our method handles better the processing of higher level combinations of spatial and chromatic features.

It should be stated that our method is not restricted to only wall paintings and it can be applied to more types of paintings, as long as there is a sufficient dataset of digital color images to train the model. As far as the simulation of damage is concerned, our approach can be improved by considering more shapes and sizes for the loss patterns other than the already explored morphological variations of random walks. Moreover, there are several configurations of that might limit the performance of the results and that could potentially be changed and tuned in future work, such as: the input image size for the training process that could be increased to achieve higher resolution, the number of quantization levels for the prior color palette fed to the network, and the use of image formats other than JPEG to mitigate the effect of the compression artifacts.

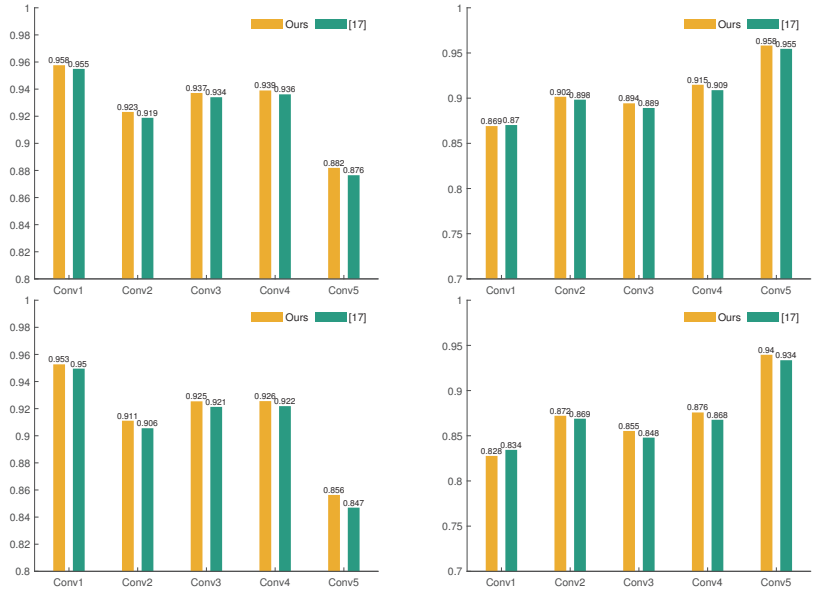

(**a**) CNN-based Self-similarity (**b**) CNN-based SSIM

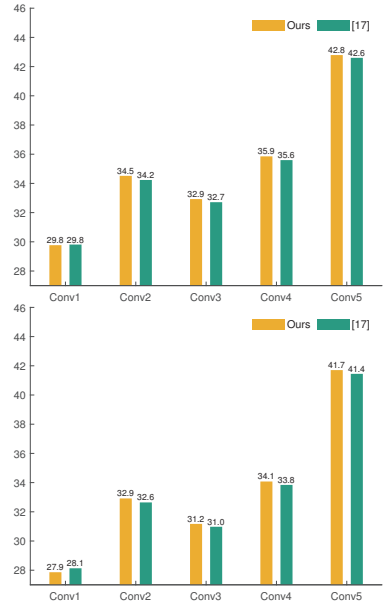

(**c**) CNN-based PSNR

Figure 14. Bar plots showing the performance of three CNN-based IQMs for each convolutional layer. These metrics measure the similarity of the feature maps given by the activations of AlexNet (pre-trained on ImageNet) for the ground-truth test images and images inpainted by our approach and [17]. **Top for each pair:** the results for RW damage. **Bottom for each pair:** results for RW+DIL damage.

Table 2. Rough comparison between our method and other relevant related works solving the restoration of wall paintings.

Approach	Dataset	Mask Type	Damage Levels	Nr. Images Evaluated Quantitatively	Quantitative Results			
					PSNR		SSIM	
					Lowest	Highest	Lowest	Highest
Ours	Dunhuang	RW, RW + DIL, RW + MAT, RW + SK	4	200	24.75	29.89	0.72	0.81
Yu et al. [22]	Dunhuang	Dusk-like (∼RW), Jelly-like (∼RW+DIL)	2	-	-			
Weber et al. [25]	Dunhuang	RW	1	10	-		0.78	
Wang et al. [23]	Thanka	Irregular lines and elliptical shapes	4	1391	21.23	33.12	0.74	0.98

5. Conclusions

The virtual inpainting of artworks is an attractive application for art restorers as well as for the general public. Deep learning techniques and, in particular, generative adversarial networks, open new horizons for increasing accurate and sensible solutions in this application.

This paper evaluated an inpainting algorithm for a set of digitizations of the Dunhuang murals. By jointly learning edge and color content, the proposed algorithm is able to produce results, where these two features are coherent with the original. Moreover, it accounts for four types of deterioration patterns by employing various irregular mask that essentially follow a random walk trajectory. The limitations to our model are partially due to the discrepancy between the (lower) train and (higher) test resolution, partially due to JPEG compression artifacts and not entirely lossless conversion between RGB and CIELAB color spaces. Even so, there seems to be a miscoordination between the visual and quantitative appreciation of our results as a consequence of the imperfect integration of human perception factors in the existing image quality metrics.

Supplementary Materials: The following are available online at https://www.mdpi.com/1424-8220/21/6/2091/s1. The damaged test images used for evaluation and the corresponding inpainted images obtained with our model.

Author Contributions: Conceptualization, I.-M.C.; methodology, I.-M.C.; software, I.-M.C.; validation, I.-M.C.; formal analysis, I.-M.C.; writing—original draft preparation, I.-M.C.; writing—review and editing, I.-M.C., S.G., J.Y.H.; visualization, I.-M.C.; supervision, S.G. and J.Y.H.; project administration, S.G. and J.Y.H.; funding acquisition, S.G. and J.Y.H. All authors have read and agreed to the published version of the manuscript.

Funding: This research received no external funding.

Institutional Review Board Statement: Not applicable.

Informed Consent Statement: Not applicable.

Data Availability Statement: The images used for evaluating our method are available as the Supplementary Material.

Acknowledgments: Special thanks to Ahmed Kedir Mohammed for the helpful support and advice in the early stages of this work.

Conflicts of Interest: The authors declare no conflict of interest.

Abbreviations

The following abbreviations are used in this manuscript:

S-CIELAB	Spatial extension of the CIELAB colorimetric difference
JPEG	Joint Photographic Experts Group
PHOG	Pyramid Histogram of Oriented Gradients
PSNR	Peak Signal-to-Noise Ratio
SSIM	Structural Similarity Index Measure
CNN	Convolutional Neural Network
DIL	Dilation
DIP	Deep Image Prior
GAN	Generative Adversarial Network
IQM	Image Quality Metric
MAT	Medial Axis Transform
CH	Cultural Heritage
RW	Random Walk
SK	Skeletonization

References

1. Bertalmio, M.; Sapiro, G.; Caselles, V.; Ballester, C. Image inpainting. In Proceedings of the 27th annual Conference on Computer Graphics and Interactive Techniques, New Orleans, LA, USA, July 2000; ACM Press/Addison-Wesley Publishing Co.: New York, NY, USA, 2000; pp. 417–424.
2. International Conference on Computer Vision. ICCV Workshop on E-Heritage 2019. 2019. Available online: http://www.eheritage-ws.org/ (accessed on 20 November 2020).
3. Yu, T.; Zhang, S.; Lin, C.; You, S. Dunhuang Grotto Painting Dataset and Benchmark. *arXiv* **2019**, arXiv:1907.04589.
4. Russakovsky, O.; Deng, J.; Su, H.; Krause, J.; Satheesh, S.; Ma, S.; Huang, Z.; Karpathy, A.; Khosla, A.; Bernstein, M.; et al. Imagenet large scale visual recognition challenge. *Int. J. Comput. Vis.* **2015**, *115*, 211–252. [CrossRef]
5. Zhou, B.; Lapedriza, A.; Khosla, A.; Oliva, A.; Torralba, A. Places: A 10 million image database for scene recognition. *IEEE Trans. Pattern Anal. Mach. Intell.* **2017**, *40*, 1452–1464. [CrossRef] [PubMed]
6. Doersch, C.; Singh, S.; Gupta, A.; Sivic, J.; Efros, A. What makes Paris look like Paris? *ACM Trans. Graph.* **2012**, *31*, 1–9. [CrossRef]
7. Liu, Z.; Luo, P.; Wang, X.; Tang, X. Deep learning face attributes in the wild. In Proceedings of the IEEE International Conference on Computer Vision, Santiago, Chile, 7–13 December 2015; pp. 3730–3738.
8. van der Maaten, L.; Hinton, G. Visualizing data using t-SNE. *J. Mach. Learn. Res.* **2008**, *9*, 2579–2605.
9. Simonyan, K.; Zisserman, A. Very deep convolutional networks for large-scale image recognition. *arXiv* **2014**, arXiv:1409.1556.
10. Pathak, D.; Krahenbuhl, P.; Donahue, J.; Darrell, T.; Efros, A.A. Context encoders: Feature learning by inpainting. In Proceedings of the IEEE Conference on Computer Vision and Pattern Recognition, Las Vegas, NV, USA, 27–30 June 2016; pp. 2536–2544.
11. Krizhevsky, A.; Sutskever, I.; Hinton, G.E. Imagenet classification with deep convolutional neural networks. *Adv. Neural Inf. Process. Syst.* **2012**, *25*, 1097–1105. [CrossRef]
12. Iizuka, S.; Simo-Serra, E.; Ishikawa, H. Globally and locally consistent image completion. *ACM Trans. Graph. (ToG)* **2017**, *36*, 1–14. [CrossRef]
13. Liu, G.; Reda, F.A.; Shih, K.J.; Wang, T.C.; Tao, A.; Catanzaro, B. Image inpainting for irregular holes using partial convolutions. In Proceedings of the European Conference on Computer Vision (ECCV), Munich, Germany, 8–14 September 2018; pp. 85–100.
14. Isola, P.; Zhu, J.Y.; Zhou, T.; Efros, A.A. Image-to-image translation with conditional adversarial networks. In Proceedings of the IEEE Conference on Computer Vision and Pattern Recognition, Honolulu, HI, USA, 21–26 July 2017; pp. 1125–1134.
15. Zhu, J.Y.; Park, T.; Isola, P.; Efros, A.A. Unpaired image-to-image translation using cycle-consistent adversarial networks. In Proceedings of the IEEE International Conference on Computer Vision, Venice, Italy, 22–29 October 2017; pp. 2223–2232.
16. Zheng, C.; Cham, T.J.; Cai, J. Pluralistic image completion. In Proceedings of the IEEE Conference on Computer Vision and Pattern Recognition, Long Beach, CA, USA, 15–21 June 2019; pp. 1438–1447.
17. Nazeri, K.; Ng, E.; Joseph, T.; Qureshi, F.; Ebrahimi, M. EdgeConnect: Structure guided image inpainting using edge prediction. In Proceedings of the IEEE/CVF International Conference on Computer Vision Workshops, Seoul, Korea, 27–28 October 2019.
18. Cai, H.; Bai, C.; Tai, Y.W.; Tang, C.K. Deep video generation, prediction and completion of human action sequences. In Proceedings of the European Conference on Computer Vision (ECCV), Munich, Germany, 8–14 September 2018; pp. 366–382.
19. Song, L.; Cao, J.; Song, L.; Hu, Y.; He, R. Geometry-aware face completion and editing. *Proc. AAAI Conf. Artif. Intell.* **2019**, *33*, 2506–2513. [CrossRef]
20. Wu, X.; Li, R.L.; Zhang, F.L.; Liu, J.C.; Wang, J.; Shamir, A.; Hu, S.M. Deep Portrait Image Completion and Extrapolation. *IEEE Trans. Image Process.* **2020**, *29*, 2344–2355. [CrossRef] [PubMed]
21. van Noord, N. Learning Visual Representations of Style. Ph.D. Thesis, Tilburg University, Tilburg, The Netherlands, 2018.
22. Yu, T.; Lin, C.; Zhang, S.; You, S.; Ding, X.; Wu, J.; Zhang, J. End-to-end partial convolutions neural networks for Dunhuang grottoes wall-painting restoration. In Proceedings of the IEEE/CVF International Conference on Computer Vision Workshops, Seoul, Korea, 27–28 October 2019.
23. Wang, N.; Wang, W.; Hu, W.; Fenster, A.; Li, S. Damage Sensitive and Original Restoration Driven Thanka Mural Inpainting. In *Chinese Conference on Pattern Recognition and Computer Vision (PRCV)*; Springer: Cham, Switzerland, 2020; pp. 142–154.
24. Wang, H.L.; Han, P.H.; Chen, Y.M.; Chen, K.W.; Lin, X.; Lee, M.S.; Hung, Y.P. Dunhuang mural restoration using deep learning. In *SIGGRAPH Asia 2018 Technical Briefs*; Association for Computing Machinery: Tokyo, Japan, 2018; pp. 1–4. [CrossRef]
25. Weber, T.; Hußmann, H.; Han, Z.; Matthes, S.; Liu, Y. Draw with me: Human-in-the-loop for image restoration. In Proceedings of the 25th International Conference on Intelligent User Interfaces, Cagliari, Italy, 17–20 March 2020; pp. 243–253.
26. Ulyanov, D.; Vedaldi, A.; Lempitsky, V. Deep image prior. In Proceedings of the IEEE Conference on Computer Vision and Pattern Recognition, Salt Lake City, UT, USA, 18–23 June 2018; pp. 9446–9454.
27. Arjovsky, M.; Chintala, S.; Bottou, L. Wasserstein GAN. *arXiv* **2017**, arXiv:1701.07875.
28. Zhang, R.; Isola, P.; Efros, A.A. Colorful Image Colorization. In *Computer Vision–ECCV 2016*; Leibe, B., Matas, J., Sebe, N., Welling, M., Eds.; Lecture Notes in Computer Science; Springer International Publishing: Cham, Switzerland, 2016; pp. 649–666. [CrossRef]
29. Cho, J.; Yun, S.; Mu Lee, K.; Young Choi, J. PaletteNet: Image recolorization with given color palette. In Proceedings of the IEEE Conference on Computer Vision and Pattern Recognition Workshops, Honolulu, HI, USA, 21–26 July 2017; pp. 62–70.
30. Köhler, R.; Schuler, C.; Schölkopf, B.; Harmeling, S. Mask-specific inpainting with deep neural networks. In *German Conference on Pattern Recognition*; Springer: Cham, Switzerland, 2014; pp. 523–534.

31. van Noord, N.; Postma, E. A learned representation of artist-specific colourisation. In Proceedings of the IEEE International Conference on Computer Vision Workshops, Venice, Italy, 22–29 October 2017; pp. 2907–2915.
32. PyTorch. An Open Source Machine Learning Framework that Accelerates the Path from Research Prototyping to Production Deployment. 2020. Available online: https://pytorch.org/ (accessed on 20 November 2020).
33. Kingma, D.P.; Ba, J. Adam: A method for stochastic optimization. *arXiv* **2014**, arXiv:1412.6980.
34. Wang, Z.; Bovik, A.C.; Sheikh, H.R.; Simoncelli, E.P. Image quality assessment: From error visibility to structural similarity. *IEEE Trans. Image Process.* **2004**, *13*, 600–612. [CrossRef] [PubMed]
35. Sharma, G.; Wu, W.; Dalal, E.N. The CIEDE2000 color-difference formula: Implementation notes, supplementary test data, and mathematical observations. *Color Res. Appl.* **2005**, *30*, 21–30. [CrossRef]
36. Zhang, X.; Wandell, B.A. A spatial extension of CIELAB for digital color image reproduction. In *SID International Symposium Digest of Technical Papers*; Citeseer Online Library: Princeton, NJ, USA, 1996; Volume 27, pp. 731–734.
37. Amirshahi, S.A.; Pedersen, M.; Yu, S.X. Image quality assessment by comparing CNN features between images. *J. Imaging Sci. Technol.* **2016**, *60*, 60410-1–60410-10. [CrossRef]
38. Amirshahi, S.A.; Pedersen, M.; Beghdadi, A. Reviving traditional image quality metrics using CNNs. In *Color and Imaging Conference*; Society for Imaging Science and Technology: Springfield, VA, USA, 2018; Volume 2018, pp. 241–246.
39. Zhang, R.; Isola, P.; Efros, A.A.; Shechtman, E.; Wang, O. The unreasonable effectiveness of deep features as a perceptual metric. In Proceedings of the IEEE Conference on Computer Vision and Pattern Recognition, Salt Lake City, UT, USA, 18–22 June 2018; pp. 586–595.
40. Flachot, A.; Gegenfurtner, K.R. Processing of chromatic information in a deep convolutional neural network. *J. Opt. Soc. Am. A* **2018**, *35*, B334–B346. [CrossRef] [PubMed]

Paper 10 - Better Sensors, Better Forgers: An Adversarial Loop

AUTHENTICITY
STUDIES
International Journal of Archaeology and Art

ISSN 2785-7484
Issue n. 1 / 03.2022
https://authenticity-studies.padovauniversitypress.it/issue/1/1

/1.0

PADOVA UP

Università degli Studi di Padova
Dipartimento dei Beni Culturali: archeologia, storia dell'arte, del cinema e della musica
Piazza Capitaniato, 7 - 35139 Padova (PD)

AUTHENTICITY STUDIES
International Journal of Archaeology and Art

Iniziativa sostenuta dalla
Fondazione Cassa di Risparmio di Padova e Rovigo
Nell'ambito del Progetto
eccellenza

Progetto MemO

PADOVA UP

Authenticity Studies. International Journal of Archaeology and Art is an international and independent journal based on a peer review system and dedicated to studying the methods of attribution and authentication of authentic archaeological and historical-artistic artefacts. *Authenticity Studies* is an **open-access electronic journal** (with ISSN). It is based on an anonymous and **international double peer review system**.
Authenticity Studies does not foresee any financial contribution from the Authors or any expenses for the Readers.

Founded by Monica Salvadori (Editor in Chief), Federica Toniolo, Andrea Tomezzoli, Marta Nezzo, Monica Baggio and Luca Zamparo, *Authenticity Studies*. *International Journal of Archeology and Art* is a journal of the **Department of Cultural Heritage of the University of Padova** and is published by **Padova University Press**.

In copertina
Vista frontale del frammento di parapetto messo in vendita il 20 luglio 2020. © HVMC / Bianca Massard.

ISSN 2785-7484
Rivista scientifica in fase di registrazione presso il Tribunale di Padova

Università degli Studi di Padova
Via 8 Febbraio 1848, 2 - 35122 Padova (PD)
Tel. +39 049 8273748, Fax +39 049 8273095
padovauniversitypress@unipd.it - authenticity.studies.dbc@unipd.it
www.padovauniversitypress.it

Progettazione ed elaborazione grafica: www.publicad.it

AUTHENTICITY STUDIES
International Journal of Archaeology and Art

Issue n. 1 / 03.2022
https://authenticity-studies.padovauniversitypress.it/issue/1/1

Index

AUTHENTICITY STUDIES
International Journal of Archaeology and Art

Issue n. 1 / 03.2022
DOI: 10.14658/pupj-as-2022-1-12

Irina-Mihaela Ciortan, Sony George, Jon Yngve Hardeberg. Department of Computer Science, NTNU – Norwegian University of Science and Technology
irina-mihaela.ciortan@ntnu.no / jon.hardeberg@ntnu.no / sony.george@ntnu.no

Better Sensors, Better Forgers: An Adversarial Loop

ABSTRACT

This essay zooms into the topic of art forgeries and how the refinement of authentication methods and the dissemination of the resulting expert knowledge has led to detectives and forgers alike being better prepared. Following a brief navigation into the mechanics of art forensics, it discusses several relevant case studies that display the importance of authority delegation in solving the puzzle of authentication.
In art attribution, a consensus needs to be reached between the main forgery detection "sensors": the eyes of art historian for stylistic diagnostic; the eyes of hardware analytical and optical devices that gather scientific evidence; the eyes of the scientific experts to interpret the latter properly. Particular focus is given to the correlated effects activated by the increasing popularity of digitization of cultural heritage (CH) objects. Digital repositories of cultural heritage scientific data have themselves become a subject for forgery and contamination. This introduces the need to dive into a new typology of sensors: forensic software, that can identify the alteration of scientific images. Nonetheless, software may also be employed by forgers to maliciously modify digital data in order to influence a certain diagnostic. This essay frames all the above-mentioned aspects in a cyclic adversarial process, where the progress of sensors determines that of forgers and vice versa. Finally, ethical and legal considerations are explored with respect to the prevention of art forgeries and the reciprocal influence between researchers and forgers.

KEYWORDS. Sensors, Adversarial Framework, Cultural Heritage, Digitization, Artificial Intelligence.

I. INTRODUCTION

Given the high numbers and turnover that are at stake in the art market, authentication studies and forgery detection have sparked the interest of not only the research and scholarship community (Craddock 2009, Scott 2007, Khan *et alii* 2018), but that of the general public as well. So much so, that the British Broadcasting Corporation sponsored a documentary/investigation series called "Fake or Fortune?", where a journalist and art dealer investigate cases of authentication of works of art (mostly paintings) by resorting to multidisciplinary analyses, so as to track the provenance, as well as the stylistic similarities and scientific coherence (BBC 2019). Furthermore, two feature movies are conveying different shades of forgeries: Giuseppe Tornatore's "The Best Offer" (2013) and Philip Martin's "The Forger" (2014). Even though the movies are fictional stories, the underlying morals include a big share of reality. The latter is an art heist case whose target is Monet's "Woman with parasol" displayed during a temporary exhibition. The original painting is stolen from the museum and replaced with a copy, thus the heist goes unnoticed. The forger portrayed in the film is an art-talented thief that has knowledge not only about art history and techniques, but also about the scientific methods of painting investigation: he is aware of the period substrate investigation, and so he buys a canvas of a lesser-known artist painted in the same year as the original "Woman with Parasol". He then orders historically accurate pigments that Monet was known to have used and assumes that the scientists will check the anachronism of the materials. Thus, the forger showcases himself as an informed and knowledgeable concealer who anticipates the scientific investigation of his fraud. In parallel, "The Best Offer" spotlights a famous art expert who works as art auctioneer and abuses his incontestable authority in the field to misattribute originals and belittle their value so that they can be sold for an affordable price to a friend auctioneer, after which he himself can buy them for his personal collection. Such an original painting that gets miscatalogued for a less valuable painting is called "a sleeper" (BBC 2019) and exists as a reality in the art market. Moreover, the plot of "The Best Offer" movie reveals how, in the end, even an impassible art expert can be deceived if he lets his judgement be fogged by emotional interferences.

All the above-mentioned examples introduce several of the key arguments in this essay, as follows.

The dissemination of knowledge on authentication methods to the general public runs the risk of this knowledge being imparted to forgers, who can then use it to perfect their concealing techniques. Moreover, while keeping the authentication judgements on the objective side, scientific investigation is not a stand-alone entity in authentication studies. It has to be supported by provenance proofs, an "unbroken chain of custody" and by the confirmations of art historian regarding the stylistic and semantic integrity that ascertains the artist's expression. In addition, all this evidence needs to be supported by cooperative ethical and legal measurements in order to avoid the contamination of the art market with forgeries. These aspects will be discussed in the first part of the essay (section 2).

Moreover, the digital era is bringing new challenges for cultural heritage and adds new layers of complexity to modern authentication studies. More than a medium, digital has become a form of creative expression and a legacy in its own right, whether it concerns a digitally created object

or a digitized rendering of an already existing cultural heritage item. This is an aspect that has not escaped the attention of policy-makers. As a matter of fact, the European Framework for Action on Cultural Heritage (European Commission 2019) puts forward a definition of its own to the digital cultural heritage: "cultural heritage consists of the resources inherited from the past in all forms and aspects - tangible, intangible and digital (born digital and digitized), including monuments, sites, landscapes, skills, practices, knowledge and expressions of human creativity, as well as collections conserved and managed by public and private bodies such as museum, libraries and archives".

The second part of this essay (section 3) will tackle the implications of digitization in matters of authentication. In particular, it will showcase how repositories of digitized cultural heritage can be altered with software tools in order to support attribution instances. At the same time, it will argue to what extent forensic software can be used to recover the digital fingerprint of digital scientific data. Furthermore, this essay introduces the term of "reverse-engineering digitization" for referring to cases where digitized and born-digital heritage can be used as sources of inspiration for real, tangible replicas, where copyright regulations are rather fuzzy. Since new artificial intelligence algorithms have been trained to generate realistic-looking paintings, this "reverse-engineering digitization" might represent a potential new tool for forgers. Nonetheless, software tools can serve both forgers and detectives alike in art authentication studies.

Fig. 1 depicts a graphical representation of the concepts analyzed in this article. Sensors and forgers are placed in an adversarial learning loop whereby, competing with each other, they push for each other's progress. This progress is influenced by media used for producing and disseminating knowledge. Digital technologies are nowadays essential in this process.

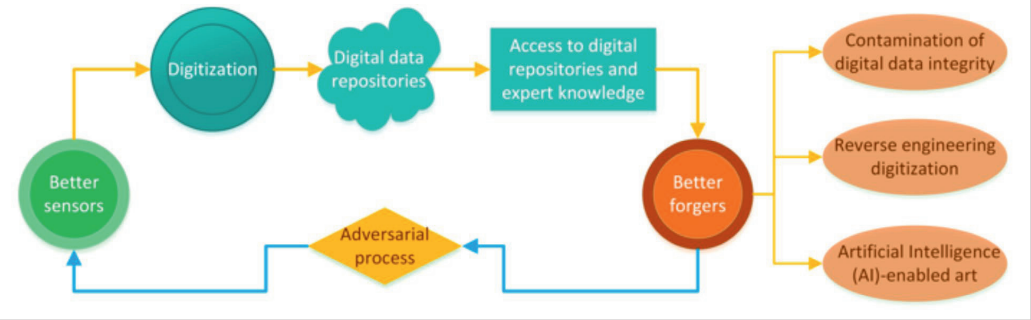

Fig. 1. This essay discusses the adversarial process between sensors and forgers, that mutually improve each other in the context of art authentication studies. Particular attention is given to the implications of digital technologies for producing and presenting knowledge, which act as an intermediary between the two ends of the adversarial framework.

II. BETTER SENSORS, BETTER FORGERS

This section is a brief overview of the reciprocal progress of sensors and forgers, highlighting key case studies.

2.1 Better Sensors

In the monograph entitled "Scientific Investigation of Copies, Fakes and Forgeries" (Craddock 2009), Craddock, a conservation scientist at British Museum, recommends three steps towards the study of authenticity: the observation and visual examination, material analysis, and physical age determination. Similarly, Brainerd (Brainerd *et alii* 2007) reiterates these methods as: provenance, dating and connoisseurship (Overgaard and Loiselle 2017).

The visual inspection can be magnified by microscopes and enhanced by using light sources with different spectral power distributions (infrared, ultraviolet) or placed at different illumination angles (raking or grazing angles) (Craddock 2009). The various modulations in light frequency or angularity can unveil peculiar elements in a work of art (Ciortan *et alii* 2018), such as repairs super-positions of materials or patches of foreign materials, or they can enhance the visibility and legibility of inscriptions or signatures in an otherwise poor display condition (Johnson *et alii* 2014). Because certain pigments, binders and varnishes fluoresce under ultraviolet (UV) light, restorations and inconsistencies can be detected by having different intensities in the UV fluorescent (UVF) image (Douma 2008). Similarly, infrared reflectography (IRR), thanks to the penetration of the infrared (IR) light beyond the pictorial layer, reveals under-drawings, as well as changes of mind (*pentimenti*) in the artist's intention when sketching the painting. The *pentimenti* are proof of spontaneity and genuineness that might not exist in forged paintings, which might be mechanically copied and devoid of out-of-the-line creative movements of brushstrokes (Djuric *et alii* 2018).

For structural analysis of the substrates of works of art, radiographies are a suitable technique to visualize the skeletons of ceramics and painting's canvases, due to the X-Ray absorption that varies according to the thickness and atomic density of a material (Newman, 1998, Riederer 2012). X-Ray images can reveal metallic structures used for reassembling torn ceramics (Berg 2018), stitches and sewing in canvas or panel substrates, and it can detect underdrawings as well as a hidden painting underneath the visible one (Tum and Middleton 2006). This last application is especially relevant for investigating forgeries, since historic substrates might be reused in order to trick the dating of the materials. As far as the substrate analysis go, X-ray determines the way a canvas is weaved and is an alternative to the manual "thread count" device (BBC 2019) used to detect the same source/provider of the canvas (Johnson *et alii* 2010). As an example, Erdmann *et alii* (2013) compared through computational analyses the weave patterns in all the three canvases from Poussin's Bacchanal series commissioned by Cardinal Richelieu in the 17th century. Out of the three paintings, only one, the Triumph of Pan, was formerly appreciated as authentic by art experts, while the others were, though not unanimously, perceived as copies based on stylistic inconsistencies and doubtful provenance (Erdmann *et alii* 2013). The computational analysis of the radiographs executed by Erdmann *et alii* (2013) showed

that all the three paintings belonged to the same bolt of canvas, indicating the authenticity of the full series. In the case of the Triumph of Silenus, this discovery was further supported by subsequent cleaning and technical examination of the painting (Whitlum-Copper 2021).

An extension of the radiographic technique is the Computed Tomography (CT), which instead of framing only a 2D image, captures the X-ray absorption of volumes and can then generate cross-sectional X-Ray images from that volumetric data (Bettuzzi *et alii* 2015). For art forgery detection applications, CT is especially informative for non-flat objects such as ceramics, sculptures, etc.

Continuing the line of "seeing the unseen", non-invasive imaging techniques are predominant in detecting primary inconsistencies (Simon and Röhrs 2018) and reveal information that is not visible to the naked eye with respect to the materials employed in a work of art. For example, multispectral digital cameras output a reflectance image for a limited number of bands (typically around 30 spectral bands) in the visible and invisible electromagnetic spectrum, can isolate restored or overpainted areas, and discriminate between paints with different spectral formulations but similar color appearance (Simon and Röhrs 2018; Hameeuw *et alii* 2017). Taking possibilities further, hyperspectral sensors (that can acquire hundreds of channels) allow the recovery of a spectral reflectance distribution of the studied material, which can become the signature of the painting materials, enabling the detection of anachronic pigments that determine a *"terminus post quem"* for the creation of the artwork. As a matter of fact, hyperspectral imaging in combination with classification approaches has proven effective for ink segmentation in old documents (Khan *et alii* 2018; Ciortan *et alii* 2015), craquelure pattern identification (Deborah *et alii* 2015), pigment mapping, as well as layer separation in Old Masters sketches (Polak *et alii* 2017). The benefits of image spectroscopy techniques as opposed to single-point spectroscopic instruments such as spectrophotometers is that instead of providing point-based reflectance measurement, hyperspectral techniques offer a spatial distribution of the reflectance curve under visible as well as invisible light (UV, near IR). In this way they present a map, a holistic image, that might prove very helpful for untying the knots in an art forgery case.

Whilst image spectroscopy can offer valuable clues and general overview, its interpretation is prone to the use of heuristics and thus contains a certain relativity in ascertaining the authenticity of some materials. Therefore, forensic art investigators must resort to more established, quantitative methods, that are also used in the field of art conservation diagnosis. X-Ray Fluorescence (XRF) and X-ray Fluorescence scanning are elemental techniques that output the chemical elements in a material with a high degree of confidence. The former is a single point of capture technique, while the latter provides an elemental map over a given area (Saverwyns *et alii* 2018). XRF is useful for identifying pigments in a work of art based on their chemical composition (Newman 1998). Alternative names for this technique in the literature are Energy-Dispersive X-ray Fluorescence (EDXRF) or Portable-EDXRF (Aydin 2014).

An important proof of authentication is given by dating methods. If a work of art is discovered to be anachronistic, then this is a convincing argument against its authenticity. Craddock (Craddock 2009) analyzes the major techniques for dating: radiocarbon dating (RC), thermoluminescence (TL) and dendrochronology. RC specifies the date when an organic raw material constituent of a CH artifact, not the artifact itself, has ceased to live. The underlying science gleans from

the measurement of one of the isotopes of carbon (carbon-14), which s present in all natural materials. Dendrochronology is the method of dating wood-based materials by assessing the rings in the wood's nucleus and it is often used for calibrating and validating the radiocarbon technique. TL dates the last time a material was heated. For this reason, TL is intensively used in investigating the authenticity of ceramics, by determining the time of manufacture

Recently, there has been a great development in affordable three-dimensional modelling technologies, including off-the-shelf digital sensors for acquiring the 3D shape of works of art (Karaszewski *et alii* 2012), as well as software that can create accurate geometric reconstructions and simulations. Some of the commonplace 3D acquisition methodologies are Structured Light (SL) scanning and Laser Scanning (LS) (Douma 2008). The development of 3D capture sensors is connected to the progress of 3D printing technologies, partly because the capture technology creates input models for the printing technology. While the benefits of 3D printing have been proven for the printing of medical prostheses (Li *et alii* 2017), it has also had a positive impact on cultural heritage through the creation of replicas that have educational, restorative (Ceccarelli *et alii* 2015) or demonstrative (Tissen 2020) purposes (for example, enabling the blind people to feel the topography of a painting). The flip side of the coin is the mass production of copies of CH artifacts, dangerous for the illicit trade of fake cultural goods: "Trade in faked antiquities is a potential concern given developments in 3D printing technologies." (Ireland and Schofield 2015).

2.2 Better Forgers

In discussing questions of research disclosure by art experts and conservation scientists faced with the professional intent of sharing their knowledge to bring advancement in their field and at the same time grappling with the danger of fraud and deceit, Craddock (Craddock 2009) opens the matter with a quote by Jack Ogden, reported in Beckett: "Do you risk educating forgers or having generations of ignorant museum curators?". Craddock continues by identifying four categories of knowledge that, if disclosed, can help the forgers in their fraudulent intents. The first one entails the correct materials and techniques employed in the creation of the genuine artifact. The second one refers to the scientific and other investigation methods by which forgeries can be uncovered. The third category comprises the knowledge behind natural aging processes and how their can be discriminated from the forced, artificial aging processes. Furthermore, the fourth class of risky information is comprised of the knowledge of how a copy can be adjusted to look like an original. Despite analyzing all these categories and providing many examples where the divulgence of such information has led to an increased number of forgeries on the illicit market, or making forgeries more difficult to unmask, Craddock concludes that information suppression is not worth it in the end and the balance of benefits tilts towards the detection of forgeries against the refinement of forgeries. In a nutshell, "one does not fight fraud with ignorance".

Nevertheless, one cannot deny the improvement of the forgers triggered by the improvement of sensors. The growing amount of knowledge on technology and its diagnostic potential is owed to the advancements of detectors and sensors. For instance, in the book "Art: Authenticity, Restoration, Forgery" (Scott 2017), Scott reports the findings of Stanish (Stanish 2009) concerning the forging of Peruvian pottery. As it seems, the Peruvian local community, who

were producing antique ceramics for commercial profit, had learned "by reading the right report" what carbon-dating does, and so they mixed in with the present-day clay some 2000 years old straws previously found in a nearby archaeological middens. In this way they managed to trick the RC. This trick would have been revealed immediately by a TL analysis, since the firing of the pottery was performed in current times, 2000 years later than the fabrication of the artificially inserted midden straw. Unfortunately, the cost of TL being much higher than RC and much higher altogether than the sell price of the so-called "antique" pot, nobody deemed it financially worthy to carry out the TL analysis. This is partly because "only in professional circles are these scientific tests (n.r.: TL) routinely employed because [...] the cost of ensuring material authenticity becomes prohibitive" (Scott 2017).

Other times, forgers rely on the limitations of the art forensic techniques and the weakness of the authority delegation mechanisms (see Section 2.3). A relevant case study in this sense is that of the forger Brigido Lara reported by Scott (2017). The storyline unfolds like this: Lara and his colleagues were arrested in the 1970s for looting ceramics characteristic of the Mesoamerican civilization Totonac. Archaeologists and art historians were convinced that the unveiled ceramics were originals looted from a Totonac site, even though Lara denied the looting and claimed that he was the craftsman behind the pottery. In planning his defense, when in jail, Lara asked for a chunk of clay, from which he made a Totonac-like ceramics. He asked for these "test" ceramics to be shown to expert archaeologists without them being informed on how, where and by whom it was created. On viewing the test ceramics, the archaeologists were once again deceived into giving the wrong verdict, thinking that the test ceramic created by Lara in the prison cell was a looted Totonac original. However, it was actually a fake, much like the ceramics that were previously considered looted. How could the archaeologists be deceived so easily? One answer is that Lara had been perfecting already at his forging technique. Nonetheless, to this deception also contributed the lack of certainty that could have been provided by TL tests. This lack of certainty derived from the material of the pottery of West Mexican area, that had in its composition volcanic minerals. Such volcanic minerals produce a saturated TL curve that makes it impossible to recover the normal clay firing signal (Scott 2017). In the case of Brigido Lara, both artistic and scientific connoisseurship have failed to detect the forged artifacts.

The Lara case resembles another story, that of the lost-and-found stone heads from some of Modigliani's sculptures. When two stone heads were found in Arno in the 1980s, renowned Italian art historians and sculptors - among them historian and writer Cesare Brandi, art historian Carlo Giulio Argan, sculptors Corrado Guerin and Carlo Signori - expressed their conviction that the two heads were authentic sculptures by Modigliani (Stobart 1984). In reality, it was a practical joke designed by Italian students, who themselves created the sculptures with the intention of mocking the easily deceitful art world (Stobart 1984), and who quickly acclaimed the bluff. Another forger with a sense of humour was Tom Keating (Magnusson 2006) who, when making pastiches of other famous artists such as Samuel Palmer, included clues such as contemporary messages, misspelled signatures and even distorted shapes that on closer inspection would reveal the fake in an almost obvious manner. This was in addition to the fact that he didn't employ historically accurate pigments. For example, in Keating's pastiche, "Sepham Barn" (see **Fig. 2**), misattributed to Samuel Palmer, a flying bat was eventually compared to a Boeing 707

during the 1979 trial R v. Keating (Grant 2015 p. 206), indicating negligent execution overlooked by the art dealer. Originally a restorer, Keating declared his intention was to mock the art market, not to deceive the scholars who would knowledgeably examine the painting (Grant 2015).

When the different expert authorities fail to reach an agreement between themselves, the third-party, in this case the forger, usually wins, at least in an incipient stage. An illustrative case where lack of consensus among expert authorities steered to omission of fakes is that of the forgers' couple formed by John Drewe and John Myatt (Carter 2007). They fabricated numerous forgeries, without even having considered the right materials or proper techniques. Instead, they offered the right provenance proof, since Drewe had access to the archives of main cultural institutions that he could tamper with, thus producing a fake chain of custody for the fake paintings (Sladen 2010).

Fig. 2. "Sepham Barn", as painted by Tom Patrick Keating. This painting was initially attributed to Samuel Palmer. In the trial R v. Keating (1979), the bats flying by the setting moon were infamously compared with a "Boeing 707" as a way to humorously criticize the art dealer who failed to notice the stylistic fake details (Grant 2015 p. 206). Image source: (Bonhams, 2007).

2.3 Authority Delegation

The hermeneutics of forgeries and authentication is very intricate, and this entanglement was visually described by a mind map (Buskes 2011) based on the considerations of Gladwell (2012) on impulsive versus considerate judgement concerning the matter of the fake Kourous that the Getty Museum had purchased. The map suggests a non-exhaustive screening process when studying the authentication of an art object, composed of six branches: checking the reasonableness of the price by comparing it to previous values listed on the art market; comparing style, colours and details to other object of the same category that were validated as being authentic; use carbon-14 dating; analyzing the materials, their origin and composition; have a collaborative judgment formed by a panel of experts and finally screening the sale records and the trustworthiness of the seller/auction house.

Overgaard *et alii* (2017) characterize the art market as subject to biased authority delegation, where "In essence, the art market community has delegated authority over the authentication of works of art to the art expert community. In doing so, the art market accepts the authenticity of whatever artwork is deemed authentic by art experts". They introduce two novel concepts of authority delegation that are supportive to the pluralism of stakeholders in the authentication studies: one-sided and mutual authority delegation. Simply put, the former concept purports that one community accepts the theory of the other while in the latter concept, both communities accept one another's theories on certain topics.

Craddock (2009) emphasizes that the stylistic analysis promoted by the art historians should be complementary and not in conflict with the scientific investigations. Nickell (2005) also encourages a multi-evidential approach in a study of authentication of written documents, where the evidence is fused from various sources, including provenance, macroscopic and microscopic study, spectral imaging and chemical examinations.

Personal beliefs and religious faith transform authentication studies from objective analysis to a subjective, emotionally based judgment that conflicts with authority delegation. For instance, art dealers might be so attached to an artist, that when they are faced with a forgery, their emotions stand in the way of a clear judgement: "It is a well-known phenomenon in the art world that a dealer or curator can become fixated on the idea that they discovered a long-lost work of a master. Once one has convinced oneself it is right, it becomes psychologically impossible to reject that conclusion and accept it is wrong." – Brian Sewell as quoted in (Grant 2015 pp. 210-211). Psychological bias of art dealers was a contributing factor in both Tom Keating's case (Grant 2015) and the Knoedler's Gallery case (Miller 2016), where art dealers were more inclined to listen to their own intuition rather than to scientific evidence. In an analogous way, the authentication of religious relics has been a controversial subject, prone to fierce and passionate debates (Nickell 2007). An illustrative case is the Turin Shroud, where the carbon dating of the textile proved that the shroud belongs to the medieval period as opposed to the hypothesis that stated it should be 2000 years old (Di Minno *et alii* 2016). Another relevant case is that of the "Dead Sea Scroll" fragments from the collection of the Museum of Bible in Washington DC, that after several suspicions raised by scholars and after a series of scientific investigations, have been revealed to be all forgeries (National Geographic 2020). This finding planted doubts about all the Dead Sea Scrolls fragments that have appeared on the antiquity market after 2002 (Davis *et alii* 2017) and as a consequence, multidisciplinary projects such as "The Lying Pen of Scribes" aim to continue researching on the authenticity of unprovenanced Dead Sea manuscripts (Agder 2019-2014.).

2.4 Towards Prevention of Forgery from an Ethical and Legal Perspective

According to the 1970 UNESCO Convention on the Means of Prohibiting and Preventing the Illicit Import, Export and Transfer of Ownership of Cultural Heritage Property (UNESCO 1970), cultural heritage is "one of the basic elements of civilization and national culture" whose authenticity and integrity needs to be protected and legally defended (Lagrange *et alii* 2018). However, UNESCO has a soft power in handling the local management against illicit trade at the

level of each member state that is responsible for the cultural heritage property on their territory according to their state jurisdiction. As a matter of fact, UNESCO compiled a database of the national laws useful to fight the illicit trading of cultural heritage property of the member states of the 1970 Convention in order to keep track of the similarities and differences between the national jurisdictions as well as the heritage under peril (UNESCO 2003) and push for international cooperation. For instance, in Italy, a dedicated body of the military forces was formed to be entirely dedicated to the supervision of cultural heritage trade: The Carabinieri Commando for the Protection of Cultural Heritage (Carabinieri 2017). Since 1980, the Carabinieri implemented a database to help them keep track of illegal records concerning the theft and commercialization of removed or fake cultural heritage goods. The "Database of illegally removed cultural artifacts" (Carabinieri 2017) has been an important aid for the Carabinieri in conducting a careful analysis of criminal phenomenon and enforcing the law concerning the illicit trafficking of cultural property.

Some jurisdictions are radical about the destruction of forged works of art as a measure to stop the contamination of the art and research even if this interferes with the property rights of the owner. Exemplary in this sense is the story of the fake Chagall (Herman 2014), seemingly entitled "Nude 1909-1910". The owner was a British businessman, who purchased the painting after the fall of the Soviet Union and, for this reason, the provenance of the painting in the last years prior to its purchase contained dubious and unclear details. The owner appealed to the help of the BBC's "Fake or Fortune" crew. However, all the local tests and experts were reluctant to vouch for the genuineness of the painting, so the owner decided to resort to the French Chagall Committee, the authoritative body on the painter's opus. The Committee denied the authenticity of the painting, judging that it was a copy of the "Reclining Nude". The consequences didn't stop with the verdict of forgery. The Committee and its members, out of which two are Chagall's heirs, wanted to proceed with the destruction of the painting and they had the support of the French law. More precisely, the moral rights of an artist, also called the inalienable rights are protected under the Intellectual Property Code in the French Jurisdiction. This however is clashing with the property law defended by the British jurisdiction, to which the owner of the painting is entitled. Philip Mould, the art dealer and cohost of the BBC series, argued against this "pro-destruction" verdict claiming that it is "anti-academic". Indeed, forgeries might have an educational, if not artistic, value and they can be secured as negative examples or as a threat to forgers, showing that even a "perfect" forgery was in the end possible to uncloak. For example, two of the Han van Meegeren's forgeries are on display in a side corridor in the Rijksmuseum (Essential Vermeer 3.0 2021), therefore not in a top location along with the genuine masterpieces, but admittedly exhibited as second-hand art as opposed to being hidden in a deposit.

Nonetheless, Craddock (Craddock 2009) reflects not without a note of disbelief upon the rate of success with which the conventions and international agreements such as the 1970 UNESCO convention have achieved to diminish the forgeries. The author is reluctant to concede that such movements have succeeded to "even slow down the growth in the international traffic in looted antiquities, much less stop it. Ultimately, the prices collectors and museums around the world have been prepared to pay are just too tempting.". He considers that forgeries are an evil that scholar need to fight by perfecting their knowledge and methods of investigations and by sharing these advancements with bona fide community, without being stuck in a stage of isolation and

ignorance provoked by the fear of forgery. The fear of forgery is a greater threat than the fear of legal action to the traders or illegal cultural property, because once the authenticity is questioned, rumours spread fast, the market collapses, and the prices become uninteresting or unworthy.

A simple conclusion of this essay might be that better sensors evolve along with better forgers. Primarily they push for better-quality, objective research and smarter detection of past and present forged CH objects, leaving less room for subjective and cultural or emotional-driven deceptions.

III. ART AUTHENTICATION IN THE DIGITAL ERA

The role of computational techniques and digital image analysis in forgery detection has grown so important that recently the term "computational connoisseurship" (Ellis and Johnson 2019) has been coined. Ellis and Johnson (2019) showcase in a non-exhaustive way four projects where digital tools showed a major contribution to art history and art attribution: canvas thread count automation project, historic photographic paper classification, chain line pattern marking and in paper drawings, and watermark identification in Rembrandt's etchings. For this reason, the number of research projects dealing with digitization of cultural heritage collections has incremented in the past years. For instance, in (Lopatin 2006), the authors agree that digitization enhances the visualization of libraries' collections, supporting the notion that "collections can be made accessible, via digital surrogates in an enhanced format that allows searching and browsing, to both traditional and new audiences via the Internet". Such digital surrogates can represent a back-up solution for CH at risk. Recent armed conflicts in Syria and Iraq brought the CH to the battlefield, provoking direct or collateral damage to world heritage sites (Soderland and Lilley 2015). Furthermore, following natural disasters that are less controllable and preventable by human intervention, such as the 2019 fire at the Notre-Dame Cathedral in Paris (Metro Game Central 2019), digitization provides a memory of the heritage, offering the possibility to restore it as it was, if desired. This has been done in the past for the cities of Warsaw and Munich (Sorbo 2019; Bevan 2007). While a major purpose of digital surrogates is to document, monitor and improve the state of conservation, there are several less noble collateral effects, such as commodification of CH objects, and the generation of fakes and replicas. In this context, one possible prevention method lies in the separability of access to the CH repositories and expert knowledge.

Beyond documentation, many CH digitization campaigns are research-driven, where the main purpose is not solely the preservation of the object, instead it is the potential of novel sensing technologies to answer questions about the history, material, meaning, creative process and verisimilitude associated with a work of art (Books 2012; NTNU 2018). An important aspect of the research-driven digitization is the integrity is the integrity of the digital data, which may be subject to alteration as it can be altered either during the data capture process or in the post-processing stage via software tools.

This section starts with a polemic on the nature of the digitization process (subsection 3.1). The extent of standardization or creative input during the digitization procedure is a first

variable influencing the digital data integrity. Subsection 3.2 delves into post-acquisition aspects concerning digital data integrity and is followed by a discussion on data access (subsection 3.3). Ultimately, in 3.4, the concept of "reverse-engineered digitization" is explained and linked to the take-off of computational creative systems.

3.1 CH Digitization: A Mere Protocol or a Creative Process?

There are two main concerns when it comes to a digitization process: ensuring the safety and integrity of the CH original objects and at the same time, maximize the quality of the collected data. Hence, a big amount of work is tunneled to define quality standards by art curators, scientific experts, museum photographers and governance stakeholders in order to issue good practice guidelines for CH digitization (Still Image Working Group 2016; Digital Transitions 2019; Van Dormolen 2008). For instance, the National Library of Netherlands teamed up with the National Archives, under the coverage of the Dutch Ministry of Education, Culture and Sports and developed the Metamorfoze quality guidelines (Van Dormolen 2008), defined for the photographic digital reproductions of two-dimensional, paper-based artworks and split along three axes of quality depending on the rank of importance and complexity of the objects studied. The quality parameters are based on universal test targets, scanner reference charts and other test charts and gather criteria and tolerance thresholds for evaluation indicators specifying among others color accuracy, illumination, white balance, spatial resolution, and dynamic range. With the Metamorfoze imaging guidelines, the goal of the institutional triangle was to create a "Preservation Master ", which is the first file generated during digitization with a resemblance to the original as loyal as possible and used as reference for all other digital derivatives. Similar to Metamorfoze, the Federal Agencies Digital Guidelines Initiative (FADGI) Still Image Working Group from United States is another example of a collaborative approach channeled towards establishing instructions for ensuring the quality of images acquired in CH digitization campaigns (Still Image Working Group 2016). They adopt a four-tiered quality classification, building on top of the three-layered podium proposed by Metamorfoze. As a wrap-up of the combined efforts in this sense, the International Standards Office (ISO) proclaimed a new working group, JWG26 under the Technical Committee 42 with the scope to "unify metrics, related methods, and tools used to specify and measure image quality capability of systems for the recording and evaluation of CH materials for archival purposes".

However, it is not always the case that a collaboration between stakeholders exists so as to propose long-term, systematic decisions over fragmentary shortcuts in digitization projects and digital resource planning. A survey (Abd Manaf and Ismail 2010) based on structured interviews answered by three Malaysian governmental cultural organizations pointed out an insufficiency of cross-institutional collaboration which poses a risk for the national heritage because that "the implementation of digitization projects is piecemeal basis and their management may not facilitate structured implementation of the project [...] Collaborative effort and holistic approach across the three studied organizations are not present and they are not merging their efforts towards one common goal of preserving the national cultural heritage".

Another challenge of digitization projects stands in the know-how of handling the software and hardware behind sensing systems. As supported by Abd Manaf and Ismail (2010), a poor

knowledge of dealing with these systems leads to poor-quality data: "The quality of digital objects greatly depends on the staff expertise on utilizing the available technology". Training is deemed to receive specific importance in the generation of research data and the research institutions are the ones responsible for filling in the knowledge gaps of operators working with on-site and off-site CH sensing activities mitigating this digital literacy risk in ensuring the quality and integrity of the scientific data produced (Kleppner 2009).

Beyond digitization protocols, the handling of hardware and software in art scanning operates partly in a space of subjective choices. How much creativity and subjectivity are undertaken, for example, by a museum photographer when digitizing paintings? To answer this question, a relevant case is the Bridgeman Art Library, Ltd. v. Corel Corp. court case (Justia US Law 1998), handled by the District Court of US. It is perceived as the pioneer case to have first created opposing parties among the experts, arguing whether digitization of the two-dimensional public domain artworks are mere "slavish reproductions" that lack sufficient creativity and originality to be entitled to a copyright of their own or they comprise minimal creativity so as to become copyrightable (Petri 2014; Kogan 2012). In the late 90s, the UK Bridgeman Art Library filed a lawsuit against the Canadian DVD company, after coming to knowledge that the defendant commercially distributed DVDs with two-dimensional images of artworks found in Bridgeman's collection. Even though the paintings in the collection were appropriated to the public domain, the plaintiff claimed that their institution was the only one to have had access to perform full-fidelity reproductions of the artworks. Moreover, some of the paintings belonged to the Bridgeman's private collection, to which third-party access was claimed to have not been granted at all, not even for the exhibition. Regardless of the lack of factual evidence that the photographs sold by Corel were the same as those produced by Bridgeman the library lost the case at any rate on the account that the photographs "lacked sufficient originality to be copyrightable under United Kingdom law**".** In other words, they were considered mere faithful reproductions of the works of art, without adding novel elements of creativity so as to be deemed *de jure* originals, notwithstanding the position of those who opposed this decision, who are supporters of "the sweat of the brow" concept where technical skills and intensive labour behind faithful reproductions are worth of a *de facto* original work.

The decision in the Bridgeman case and the belittling of the digital reproductions of two-dimensional works of art by referring to them as "slavish reproductions" has generated a buzz in the literature of CH field. One of the reasons for this is the unclear bounds of the threshold of originality in the copyright law and the determination of the slavish copy, since they were first coined in the mid-19th century (Kogan 2012). According to the 1991 US Supreme Court Case Feist Publications, Inc., v. Rural Telephone Service Co. (Kleppner 2009), there are two criteria of originality: independent contribution to the work and minimal creativity "[T]he work [must have been] independently created by the author (as opposed to copied from other works), and... it [must] possess [] at least some minimal degree of creativity". However, "minimal" does not eradicate the subjectivity to the notion and content of creativity. Perhaps it is this relativity that opened the controversies. To begin with, the law changes its judgement when pictures are taken of three-dimensional art items, as they are considered copyrightable, because the choice of angle and shoot perspective necessary for capturing a sculpture for example entails a minimal creative choice. At this point one might argue that the technical skill behind photography

is very similar regardless of the object having a more or less pronounced three-dimensional geometry and relief, and the reason why 2D-like objects seems more simple and less creative is simply the history and long practice of 2D photography as opposed to 3D photography. If the counter-argument is the fact that one photograph of a 3D object doesn't reveal a high-fidelity reproduction of the object, then does it mean that using a laser scanner that generates a 3D model and reconstruction of the object is the equivalent of 2D digitization of 2D-like paintings? These are all questions that, to the best of my knowledge, are not yet to be answered in the law textbooks and might point out some inconsistencies to the copyright looseness in the digitization of public domain artworks.

Kogan (Kogan 2012) revolts against this blurry threshold of originality that names a reproduction of a painting "slavish copy" and at the same time an amateur selfie with a painting, taken with a point-and-shoot camera, is deemed original and protected by copyright. The author believes that museum photographers should be given more credit and that museum's work in digitization of public domain artworks should not be perceived as a "copyfraud", instead it should be protected as an original work. One of Kogan's most powerful dialectics is the comparison of a 2D painting's digitization with a map instead of comparing it to a transparent window whose only purpose is to help the viewer peek into the initial creation of the artist - the way "ordinary viewers" such as the judges choose to see it. The author elaborates the map comparison putting it in balance with an aerial photo of a city: the same way the aerial photograph correlates each physical location and feature of the city into the image coordinate systems stored in photodetector's on the instrument's sensor, the same way a picture of a painting maps each visual attribute of the work of art into another coordinate system and most often this is not a one-to-one mapping. Kogan considers that both the aerial capture (actually, areal could be extended to the remote sensing field from which photographic techniques are often transferred and applied to CH digitization) and the reproduction of the painting are original work, not mere slavish copies. In his article, he brings arguments based on the philosophy of the photography and the cultural tendencies and habits of viewing photography as a mechanical reproduction, misconceived to be purely factual and truth to reality images, ignoring the creative choices that go beyond pure technical skills in acquiring photographs and that can play with light and shadow or color filters to impinge an artistic reinterpretation of the reality.

Kogan continues with debates from the visual arts, asserting that "many photographic attributes of a photographic reproduction—size, surface texture, interplay with light, etc.—are fundamentally different from the pictorial and painterly attributes of the depicted painting" and delineating the difference between photographic document and duplicate. While a photographic reproduction is a document of the painting, recording the existence of the painting, with high-quality equipment and trying to secure as truthful as possible the visual attributes of the painting, it cannot capture the exact appearance aspect and it is thus not an exact imitation or duplicate. He concludes that in evaluating the independent artistic contribution of Bridgeman's photographers, the judges fell in the trap of ordinary cultural habits, looking to the digitization as to see-through photographs and mistaking them for duplicates instead of "documents of the world" by overlooking the myriad differences between the painting and its digitization. In response to the critiques claiming that the digitization process is protocol-based and formulaic, where the same output can be repeated once the recipe and the ingredients are well-written, regardless of

the photographer's creative input, Kogan quotes from the working diary of a former photograph of the Metropolitan Museum of Art, Sheldan Collins - who, acknowledging the great complexity of CH digitization, agrees that a set of guidelines is necessary, however not comprehensive since a great deal of creativity, artistic style and self-expression is required for achieving excellence in the documentation: "Photographic technique easily blurs the distinction between the beauty of the subject and the beauty of its image. […] Insofar as the photo-documentation of works of art necessarily involves distorting and abstracting—lying and beautifying—it partakes of the nature of those higher art forms that comment on reality. Here we have a neat paradox: one potential art form—photography—remarking on another. It is like holding two mirrors face-to-face. But unlike a static mirror reflection, the photographic process has a dynamic mind controlling it, editing and selecting which "truths" about a work of art will be formed in the camera's ground-glass".

Nevertheless, by striving to prove the creativity of photographic documentations of CH and defend the ethics of the cultural institutions and the museum photographers, another aspect of ethics might be violated, which is the truthfulness of the images produced. As highlighted in Ireland and Schofield (2015), non-photorealistic renderings, interpretations, and visualizations in the process of digitization are looked upon as an unethical professional behaviour: "Trust, truthfulness and transparency are professional and ethical values. An opinion survey showed that local people trusted North American museums to be accurate and authentic. Ethical codes for archaeology, museums and archival practice stress professional obligations to retain and value authenticity and uphold intellectual integrity by separating factual evidence from interpretation and unfounded opinion.". Therefore, admitting that the digital images are too faithful to the original work of art trades their copyright protection, while pretending a high share of interpretative and subjective contributions in the imaging process might trade their ethical value.

3.2 Integrity of Digital Repositories

As defined in Pelagotti *et alii* (2020), integrity of digitized artworks implies that no creative choices taken in the acquisition process or in the post-processing stage significantly alter the data so that they result in a deceiving representation of the real object.

As introduced in the previous section, the separation between facts and interpretative choices during the acquisition process ought to be detailed in the metadata files that should accompany the images and other file formats generated during digitization. Metadata is "data about data" and it is crucial for the preservation of digitized CH, the verification of the data integrity and data stewardship, since metadata also includes the selection of the data types, file formats and the key to read and decipher these formats. In an overview about digital data aspects, Kleppner (2009) follow the definition of metadata provided by the sources of National Science Foundation Report on Cyber infrastructure Vision for the 21st Century: metadata "summarize data content, context, structure, interrelationships, and provenance (information on history and origins). They add relevance, purpose to data, and enable the identification of similar data in different data collections."

Metadata enables data users to navigate machine-readable data and in the case of CH databases, they can retrieve similarities in the CH collections, filter and display them by user-

selected criteria and draw research conclusions faster than in traditional source browsing. Metadata can be useful when format migration needs to happen or when parties other than the digital data patron and creator need to work and parse the meaning of the images, a situation quite common in interdisciplinary and multi-partner CH projects. Some digitization experts prefer to make a distinction between metadata - description of the raw data - and paradata - annotation of the processed data (Bentkowska-Kafel *et alii* 2012), as the main byproduct of digitization consists in the analysis and visualization of different layers of data and extracted information. In this sense, proposals have been made towards an exhaustive metadata model where the intermediate computational data and the software used for the simulations should be stored together with the data and their descriptive files (Kleppner 2009). This is in line with the FAIR principles (Hagstrom 2014) drafted by the European Commission (2019) and suggesting that the CH databases should meet the following adjectives: Findable, Accessible, Interoperable and Re-usable. Special attention needs to be given to the metadata of the physical object that is being digitized as this metadata is usually associated with the valuable clues related to the provenance of the work of art and the provenance is often considered as legal evidence in art forgeries determination (Carter 2007). Metadata is for the digitized archives what the physical archives of provenance are to real artworks. And like the faked physical archives in John Drewe's case (Sladen 2010) previously mentioned in subsection 2.2, the digital metadata files run the same or even greater risk of being altered as the physical records.

Art diagnostic evidence in the form of images is prone to malicious post-processing techniques that can alter the original digitization to support or dismiss attributions, as shown in Pelagotti *et alii* (2020). In fact, the manipulation of digital images is of interest to and highly debated by the general scientific research community. In the majority of cases, researchers might alter their data only to "beautify" its presentation in scientific publications, without openly mentioning it and therefore, deceiving the reader. In the minority of cases, images suffer severe manipulations regarding their content in order to falsify results in favour of the research performance. For these reasons, a set of 12 ethical guidelines has been proposed in 2010 by Cromey (2010), which draws the line between what is appropriate and not in the manipulation of scientific digital images. In order to ensure truthful and credible pixels, this ethical code recommends among others: the storage of the untouched original file, the use of lossless compression file formats and the avoidance to use operations such as cloning to obscure local imperfections of the image. What happens though when this code of ethics is broken, when the traces to the original image are lost, and so there is an interrupted *chain of digital custody*? Pelagotti *et alii* (2020) proposes the application of multimedia forensic tools on X-ray and Infrared art diagnostic images to retrace any retouching performed in post-processing. This approach assumes that forensic algorithms can decode any manipulation and provide a timeline of changes with respect to the original image through the computation of several computer vision descriptors that quantify entropy at various levels. To test this method, the authors artificially simulate *pentimenti* digital images of two paintings by El Greco and Pietro Novelli, using cloning tools like in image editing software where regions in the image can be copied and pasted at another location in the image. Notwithstanding a preliminary study, Pelagotti *et alii* (2020) managed to detect the tampering with some of the tested forensic tools.

3.3 Levels of Access for Digital Repositories

As regards the access to the repositories of digitized images of CH research projects, one of the main challenges is how a middle way can be reached between the two extremes: the first one is the choice of full data retention, completely hiding the digital data, without enabling the scholarship to examine it and thus hindering what could potentially be an advance in research and the second one is unrestricted open access to high-quality data without any thought of the background and intentions of the party who might access it, nor if such an access can open a path to further derivative works done in perhaps bad-faith by ill-disposed entities.

The drawback of the first approach is obscuring the transparency of the research projects, that could lead to unchecked and unverified data and other errors that might arise due to the blindness of single-minded or single-grouped research. This is an obstacle for ensuring data integrity. A good research practice would be to have continuous and if possible external other than internal peer-reviewed feedback on the research data, its processing, analysis and the computing of the results. One could argue that external peer-review is achieved by means of scientific publications, yet few publishers have developed a protocol for the upload of supplementary material and a method to check its verisimilitude or correctness. Developing such protocols would avoid situations where researchers "willing to share their older information online will not release more recent or current information due to business competition. Others may not wish to draw public attention to substandard work produced under commercial pressure of development-driven archaeology. Fear of 'airing dirty linen in public' inhibits information sharing in archaeology elsewhere and in other disciplines. Most of us want to showcase our better work." (Ireland and Schofield 2015). Participatory design principles and agile design methodologies, where "technical and project managers work closely with clients, users and other stakeholder in an iterative manner so that consultation, testing and feedback are automatically incorporated into the design and development process" are encouraged in CH project and considered as ethical professional behaviour (Ireland and Schofield 2015).

On the other hand, the second extreme approach is risky if knowledge gets on wrong hands and an example in the case of CH, would be the use of knowledge to create forgers and trick the detection systems. The same way some researchers are embarrassed to make low-quality data publicly available other researchers might want to boast their high-quality experiments and results as measure of the quality of their research and hence, as recognition of their success: "Evidently, successful digital projects are the result of not only consistent high-level image quality, but also convenient access to these digital images through the facilitation of appropriate procedures and accepted standards." (Abd Manaf and Ismail 2010).

However, one shouldn't fall into the illusion of pride of high-quality image, nor in the caves of deception provoked by bad results and publish their research results on different levels of representation corresponding to distinct levels of expertise of the intended audience that has or can deal with the data and applying protection measures accordingly. For instance, in case of online repositories, such protection measures can vary from the specification of licenses where rules on how to use the data are negotiated into a legal-binding contract, to password-protected data or to the requirement of user registration as a way to inspect and validate the affiliation of the user and discover whether the intentions with respect to the data are under fair use principles to

developing smarter technologies that impede harvesting and data mining (Ireland and Schofield 2015) unless for a good research-oriented cause.

Drawing from the ethics of heritage conservation, public ownership and open-access are promoted and the righteousness of the public is "tempered only by consideration of privacy, confidentiality of commercial information and cultural rights of traditional owners and descendants" (Ireland and Schofield 2015). From an ethical point of view, access to CH research data should be restricted when it includes sensitive information about a specific group of people and their culture (Nicholas and Egan 2012). This is especially relevant for indigenous, community-based cultural heritage: "Ethical technologies could be, for example, web pages that allow users to view but not download, copy, alter or redistribute digital assets or which restrict access to online information deemed culturally sensitive." (Ireland and Schofield 2015). As an example of an ethical webpage, the National Centre for Research and Restoration in French Museums showcases several works of art on a webpage (C2RMF 2021), where the viewer can see a painting in high-resolution and can browse through its multispectral channels (Aitken *et alii* 2007), but without being able to download the images. Likewise, the BOSCH project allows zoomed in visualization of details in the paintings of Hyeronymus Bosch scanned at high resolution, disabling the possibility of downloading the pictures from the website (Erdmann *et alii* 2010).

3.4 Reverse-engineering Digitization

Access to digitized works of art raises the risk of them being replicated and manufactured into real objects. This can be seen as a reverse-engineering digitization process. A relevant case of reverse-engineering digitization that has got legal attention is Roger v. Koons court case (Artist Rights 1992; Copyright in the Visual Arts 1992). The artist Jeff Koons drew his inspiration from a black-and-white postcard copyrighted by the photographer Rogers and enacted the subjects of the postcard - a couple holding many, seemingly lookalike puppies - by ordering his craftsmen to transform the photograph into a sculpture (see **Fig. 3**). He designed the sculpture without crediting the photographer, who, in his turn, filed a copyright lawsuit against Koons. The plaintiff won on the ground that the sculpture was an exact imitation of the photograph, especially because of being a copy of the artistic expression. Koons claimed in his defense that he brought his own artistic contribution and stylistic changes in designing the sculpture (color, decorations) and that also his purpose was an intellectual concept devised by himself, that of making a parody of the commodification of society. In spite of the defendant's arguments, the court deemed that Koons acted in "bad faith" in pursuing an enactment of the photograph.

Fig. 3. A reverse-engineering digitization case. Left: Photograph captured by Rogers. Right: Rogers photograph enacted into a sculpture by artist Jeff Koons. Image source: (Copyright in the Visual Arts 1992).

The reverse-engineering digitizations have the potential of becoming more widespread now that the technologies that facilitate the creation of digital art are getting more diversified and advanced.

The project "Next Rembrandt" (Microsoft, ING 2016) had the goal of resuscitating Rembrandt's style, by creating *ex-novo* a computer-generated painting in his style. By implementing various artificial intelligence (AI) based algorithms, scientists were able to determine the most common subject in Rembrandt's painting (masculine portrait), and to extract common geometric proportions as well as color palette. Based on these features, a new, unseen portrait in Rembrandt's style was generated, 3D printed and exhibited in physical format (Microsoft, ING 2016). More recently, Yaniv *et alii* (2019a) created a dataset of artistic faces, by detecting and studying the landmarks of faces from existing artist portraits. Starting from the original faces, they augment the dataset by inserting variations in artist-specific facial proportions that modulate the level of abstractness of the portrait from very realistic to very artistic. One of the results of their method is the generation of average portraits (see **Fig. 4**) given a certain artist (Yaniv *et alii* 2019b).

In the above-mentioned cases, handcrafted machine learning techniques were used to computer-generate artworks where the important features to be extracted were user-defined. In contrast to traditional machine learning, deep learning methods identify the features in an automatic way that mimics the neural brain activity. The case of Edmond de "Belamy" artwork (see **Fig. 5**) has created a precedent of a digital-born artwork that was generated with a deep learning algorithm and was printed on canvas by a collective French artist group, called Oblivious.

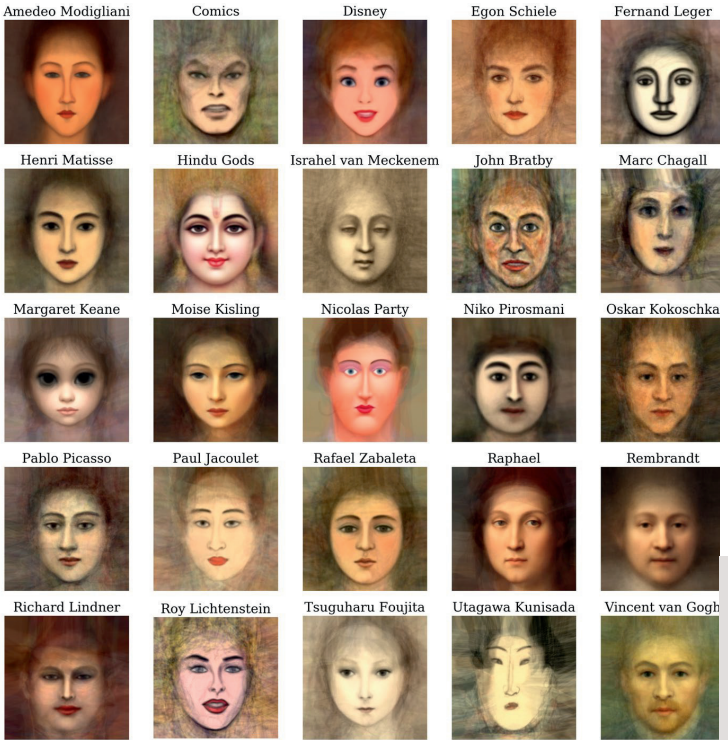

Fig. 4. Average portraits created by computing the average facial shape and color for various artists included in the work of (Yavin *et alii* 2019a). Image source: (Yavin *et alii* 2019b).

This artwork has unfolded many controversies. To begin with, it was sold at Christie's Art Auction in 2018 at an exhilarating price of $432,500. Then, its authorship is very ambiguous, as debated in (Epstein *et alii* 2020). The backbone of the artificial intelligence algorithm that was used for generating the digital portrait is called Generative Adversarial Networks (GAN) and was proposed by Goodfellow *et alii* in 2014 (Goodfellow *et alii* 2014) with the purpose of creating *ex novo* realistic-looking images. When these synthetic images represent human appearance, they carry the name of "deep fakes".

GAN is a deep learning method, that consists of two convolutional neural network submodules: a generator and a discriminator. Given an input dataset, the generator's objective is to concoct new, unseen data that has the same statistics as the input. In the case of visual data, the discriminator's role is to detect that the images fabricated by the generator are fake and are not part of the original input dataset. The two submodels are trained in parallel and learn from each other in an adversarial way, perfecting their game until the generator creates images that the discriminator fails to detect as fake.

Interestingly, the logic that stands at the core of GAN's development (and other related methods) matches the underlying thesis of "better sensors, better forgers" of the current essay. As described in the original GAN paper (Goodfellow *et alii* 2014): "The generative model can be thought of as analogous to a team of counterfeiters, trying to produce fake currency and use it without detection, while the discriminative model is analogous to the police, trying to detect the counterfeit currency. Competition in this game drives both teams to improve their methods until the counterfeits are indistinguishable from the genuine articles".

Building on GAN, Radford *et alii* (2015) implemented a network with a certain architecture, called Deep Convolutional GAN (DCGAN). AI-artist Barrat (2017) trained the DCGAN model on images of Renascent paintings, which resulted in the portrait that is mainly the base of the "Edmond Belamy" print. Arguably, the contribution of the Oblivious collective artist (the ones who go the full credit and financial remuneration) consists in selecting that specific artwork from a pool of other options, preparing it for fabrication, actually manufacturing it and marketing it. Furthermore, the authors of Epstein *et alii* (2020) claim that the success of "Edmond de Belamy" is highly linked with the anthropomorphization of the AI which inoculated the idea that the AI system acted on its own, while discarding the intellectual work behind the design of the algorithm or the creative choice of configuration and dataset to tailor the system to art-creation. By carrying out several vignette experiments, Epstein *et alii* (2020) found that participants were inclined to a distributed authorship, giving credit to all the intermediate parts involved in the process that led to "Edmond de Belamy" as final product.

One might expect that "Edmond de Belamy" is only the first artworks of the many to come, that will write the history of AI-generated art. As a matter of fact, building on GAN, Elgammal *et alii* (2017) invented a new computational creative system to generate art, called Creative Adversarial Network (CAN) (Elgammal 2020). This method models two factors that make novel art attractive as explained by Martindale's psychology theory: a new art-piece needs to be original and surprising enough so as to contrast with the old, but at the same time this increment in contrast with the old needs to have a maximum bound so as not to generate discomfort. CAN has created art that was deemed indiscernible from that of contemporary artists, as

appreciated by human subjects in a visual Turing test. Mazzone and Elgammal (2019) discuss the potential of the new wave of AI-enabled art and share success of exhibitions of artworks designed by CAN system. Indeed, in 2021, several AI-art exhibitions were organized that featured: GAN generated paintings of horses (Fire Station 2021), which are a metaphor of the universal need for persistence and resilience during the covid-19 pandemic (James, Sheng 2020); AI-art that transcends visual arts and incorporates music as well (NVIDIA 2021); cross-media artworks that use various computer vision techniques (CVPR 2021). An innovative exhibit at GPU Technology Conference 2020 (NVIDIA 2021) was that of the artist collective Oxia Palus (2021) who proposed a digital reconstruction of Leonardo Da Vinci's "Virgin of the Rocks" (see **Fig. 6**) by translating X-ray images to paintings, thus exploiting multispectral images that are otherwise used for forgery detection towards an artistic restorative endeavour. Oxia Palus (2021) reinterpreted other two lost masterpieces with their multidisciplinary approach: Picasso's "La Femme Perdue" and Rusiñol's "Parc del Laberint d'Horta". The latter is on display for purchase at Morph Gallery (2021) for approximately $11, 000. On the Morph Gallery's (2021) website, the *modus operandi* of Oxia Palus, that is "to combine spectroscopic imaging, artificial intelligence, and 3D printing to actualize the *pentimento*" with the purpose "to recreate exacting homages to a new breed of fine art" is described as the "NeoMaster Style".

Fig. 5. "Edmond de Belamy" (print on canvas). The first deep learning generated artwork, sold in 2018 at Christie's Art Auction for $432,500. The print generated many controversies regarding its righteous authorship. It is a born-digital artwork reverse-engineered to a tangible object. Image source: Wikimedia Commons. The image belongs to the public domain "because, as the work of a computer algorithm or artificial intelligence, it has no human author in whom copyright is vested".

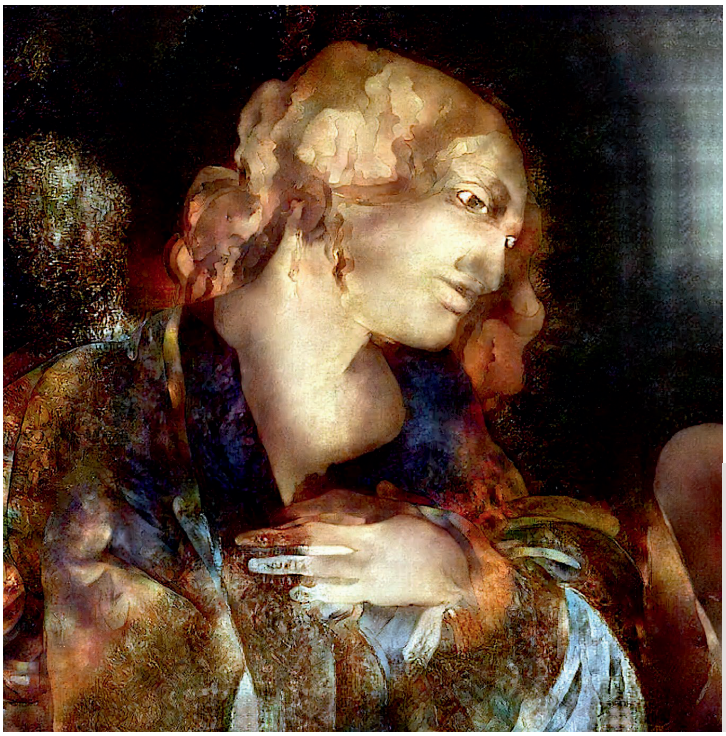

Fig. 6. The digital resurrection of Leonardo da Vinci's "Madonna" as portrayed by the artist collective Oxia Palus. The painting was created using deep learning algorithms, X-ray images, edge and color maps, style transfer, and manual editing. It was exhibited online at GPU Technology Conference 2020 Image source: (NVIDIA, 2021).

Floridi (2018) highlights the dangerous potential of digital technologies in trespassing authenticity and in producing fake works of art. In addition, he debates the importance of nomenclature of AI-generated artworks and proposes the name *ectype* to define the "Next Rembrandt" (Microsoft, ING 2016). The etymology of the word is Greek and refers to a copy that remains connected to the original because they both share the same archetypal source. Floridi (2018) implies that there are two faces to an *ectype*, original source and production, and that they can be in turn authentic or fake. Following this rationale, he states that the "Next Rembrandt" is an ectype with inauthentic source, but with genuine production. What about the *neomastic* process of Oxia Palus (Morph Gallery 2021) – are the resurrections of lost masterpieces with (partially) authentic source and authentic productions *ectypes* as well? How much of the original source is preserved and how much creative content is added to these lost art reconstructions? Probably, future research and debate will make way for answering these questions. Nonetheless, while envisioning the future in the light of the digital era, Floridi concludes that even though "digital technologies seem to undermine our confidence in the original, genuine, authentic nature of what we see and hear", at the same time "what the digital breaks it can also repair, not unlike the endless struggle between software virus and antivirus".

IV. DISCUSSION AND CONCLUSION

This essay has explained the adversarial relationship between forgers and sensors. In a broad sense, the word "sensors" refers to the full set of technological tools employed by art authentication experts to help them gather evidence for a verdict. The digital backdrop and the wave of AI-enabled art raise many anthropological, political, ethical, legal considerations but at national and international levels. The plethora of advantages that technology can bring to the conservation and preservation of CH is undeniable, but it doesn't come free of side-effects that need to be regulated by clauses, conditions and efforts. Researchers and all the CH stakeholders, including the community spaces, need to commit to upholding digital data integrity, by respecting ethical and legal norms with respect to data collection, archiving, access and stewardship. In their work, pursuers of digital CH projects need to discern between *bona fide* and ill-disposed practitioners and share their research outcomes according to established hierarchies of privacy and expertise of involved third parties. The fabrication of art using computational creative systems, in particular the systems based on Generative Adversarial Network algorithms open unexplored considerations for art authentication and attribution. GAN algorithms are actually inspired by the principle of "better sensors, better forgers" and their potential in producing artworks that are considered by human viewers as painted by artists has already been proved. These methods have prospects as well in the CH reconstruction. The subject of AI-enabled art restoration and triggered ethical issues would be a major topic in itself, that would definitely be worth looking into in the future. In conclusion, this essay brings the following contributions to state-of-the-art: 1) presumably, it is the first attempt to make the analogy between an adversarial process from the machine learning field and the relationship of sensors and forgers from authentication studies; 2) it presents an overview of acquisition, integrity and access of CH digital repositories; 3) it introduces the concept of "reverse-engineering digitization" and anticipates the importance of AI-enabled art for matters of art forgeries and attributions.

References

Abd Manaf Z., Ismail A. 2010, *Malaysian Cultural Heritage at Risk?: A Case Study of Digitisation Projects*, "Library Review", 59 (2), pp. 107–16. https://doi.org/10.1108/00242531011023862.

Agder, University of 2019-2024, *The Lying Pen of Scribes-Manuscript Forgeries, Digital Imaging, and Critical Provenance Research (RCN Fripro Toppforsk 2019–2024)*. Available at: https://lyingpen.uia.no/about/ (Accessed: 2 February 2021).

Aitken G. *et alii* 2007, *Archive Visualisation and Exploitation at the C2RMF*, Toronto.

Artist Rights 1992, *Roger v. Koons Court Case Description*. Available at: http://www.artistrights.info/rogers-v-koons (Accessed: 15 February 2021).

Aydin M. 2014, *Using Technology Against Theft and Forgery of Cultural Heritage Goods*, "Mediterranean Journal of Social Sciences", 5 (22), pp. 32–42. https://doi.org/10.5901/mjss.2014.v5n22p32

Barrat R. 2017, *Art-DCGAN*. Available at: https://github.com/robbiebarrat/art-DCGAN (Accessed: 15 February 2021).

Bastidas D. M. and Cano E. 2018, *Advanced Characterization Techniques, Diagnostic Tools and Evaluation Methods in Heritage Science*, Springer.

BBC British Broadcasting Corporation 2019, *BBC Art Investigation Series: Fake or Fortune?*. Available at: https://www.bbc.co.uk/programmes/b01mxxz6 (Accessed: 15 February 2021).

Bentkowska-Kafel A., Denard H. and Baker D. 2012, *Paradata and Transparency in Virtual Heritage*, London.

Bergl I. 2018, *X-Radiography and Ceramics*, in The Encyclopedia of Archaeological Sciences, pp. 1-3.

Bevan R. 2007, *The Destruction of Memory: Architecture at War*, Islington.

Bettuzzi M. *et alii* 2015, *Computed Tomography of a Medium Size Roman Bronze Statue of Cupid*, "Applied Physics", 118 (4), pp. 1161–69.

Boochs F. 2012, *COSCH – Colour and Space in Cultural Heritage, A New COST Action Starts*, in Marinos I. *et alii* (eds.), Progress in Cultural Heritage Preservation, Berlin, pp. 865–73. https://doi.org/10.1007/978-3-642-34234-9_93.

Bonhams 2007, *Bonhams: Tom Keating (British, 1918-1984) Sepham Barn - 1831' after Samuel Palmer 26 x 33cm (10 1/4 x 13in)*. Available at: https://www.bonhams.com/auctions/15019/lot/309/ (Accessed: 15 August 2021).

Brainerd A. W., Boime A. and Kosolapov A. I. 2007, *On Connoisseurship and Reason in the Authentication of Art*, Chicago.

Buskes H. 2011, *The Mind Map of the Thinking Process Behind Buying a Kouros*. Available at: https://mastermindmaps.wordpress.com/2011/05/24/fast-decisions-or-slow-decisions/ (Accessed: 10 February 2021).

C2RMF 2021, *Multispectral visualization of Lady Praying*. Available at: https://merovingio.c2rmf.cnrs.fr/iipimage/iipmooviewer-git/multispectral.html (Accessed: 15 February 2021).

Carabinieri 2017, *The Carabinieri Commando for the Protection of Cultural Heritage*. Available at: http://www.carabinieri.it/multilingua/en/the-carabinieri-tpc (Accessed: 15 February 2021).

Carter R. G. S. 2007, *Tainted Archives: Art, Archives, and Authenticity*, "Archivaria", 63, pp. 75–86.

Ceccarelli M. *et alii* 2015, *A Robotic Solution for the Restoration of Fresco Paintings*, "International Journal of Advanced Robotic Systems", 12 (11), p. 160. https://doi.org/10.5772/61757.

Ciortan I. *et alii* 2015, *Color and Hyperspectral Image Segmentation for Historical Documents*, "Digital Heritage", 1, pp. 199–206.

Ciortan I. M. *et alii* 2018, *Artworks in the Spotlight: Characterization with a Multispectral LED Dome*, "IOP Conference Series: Materials Science and Engineering". 10.1088/1757-899X/364/1/012025

Copyright in the Visual Arts, 1992, *Roger V. Koons Copyright Infringement*. Available at: https://cpyrightvisualarts.wordpress.com/2011/12/20/art-rogers-vs-jeff-koons/ (Accessed: 10 January 2021)

Craddock P. T. 2009, *Scientific Investigation of Copies, Fakes and Forgeries*, Oxford.

CVPR, Computer Vision and Pattern Recognition Conference 2021, *Computer Vision Art Gallery: CVPR 2021*. Available at: https://computervisionart.com/ (Accessed: 10 September 2021).

Cromey D. W. 2010, *Avoiding Twisted Pixels: Ethical Guidelines for the Appropriate Use and Manipulation of Scientific Digital Images*, "Science and Engineering Ethics", 16 (4), pp. 639–667.

Davis K. *et alii* 2017, *Nine Dubious 'Dead Sea Scrolls' Fragments from the Twenty-First Century*, "Dead Sea Discoveries", 24 (2), pp. 189–228.

Deborah H., Richard N. and Hardeberg J. Y. 2015, *Hyperspectral Crack Detection in Paintings*, "2015 Colour and Visual Computing Symposium (CVCS)", pp. 1–6. https://doi.org/10.1109/CVCS.2015.7274902.

Digital Transitions 2019, *Planning a Digitization Program (PDF Download) DT Cultural Heritage*. Available at: https://

dtculturalheritage.com/store/planning-a-digitization-program-pdf-download/ (Accessed: 20 May 2020).

Di Minno G. *et alii* 2016, *Blood Stains of the Turin Shroud 2015: Beyond Personal Hopes and Limitations of Techniques*, "Internal and Emergency Medicine", 11 (4), pp. 507–16. https://doi.org/10.1007/s11739-016-1433-7.

Djuric M. *et alii* 2018, *Comparative Analysis of Two Self-Portraits by Igor Vasiljev Using Non-Invasive Methods*, "IOP Conference Series: Materials Science and Engineering". 10.1088/1757-899X/364/1/012065

Douma M. 2008, *Pigments Through the Ages*. Available at: http://www.webexhibits.org/pigments (Accessed: 15 February 2021).

Elgammal A. 2020, *Creative GAN Generating Art Deviating from Style Norms*, United States Patent 10853986.

Elgammal A. *et alii* 2017, *CAN: Creative Adversarial Networks, Generating Art by Learning About Styles and Deviating from Style Norms*. *arXiv Preprint arXiv:1706.07068*

Ellis M. H., Johnson C. R. 2019, *Computational Connoisseurship: Enhanced Examination Using Automated Image Analysis*, "Visual Resources", 35 (1–2), pp. 125–40. https://doi.org/10.1080/01973762.2019.1556886.

Epstein Z. *et alii* 2020, *Who Gets Credit for Ai-Generated Art?*, "iIScience", 23 (9). https://doi.org/10.1016/j.isci.2020.101515

Erdmann R. *et alii* 2013, Reuniting Poussin's Bacchanals Painted for Cardinal Richelieu through Quantitative Canvas Weave Analysis, "Journal of the American Institute for Conservation", pp. 1-21.

Erdmann R. G. *et alii* 2010, *BOSCHPROJECT*. Available at: http://boschproject.org/#/. (Accessed: September 3, 2021).

Essential Vermeer 3.0. 2021, *Han van Meegeren's Fake Vermeers*. Available at: http://www.essentialvermeer.com/misc/van_meegeren.html (Accessed: 20 January 2021).

European Commission 2019, *European Framework for Action in Cultural Heritage, Commission Staff Working Document*. Available at: https://ec.europa.eu/culture/library/commission-swd-european-framework-action-cultural-heritage_en (Accessed: 10 February 2021).

Firestation 2021, *EXHIBITION |Keep Running: AI, Art and Qatari Heritage*. Available at: https://www.firestation.org.qa/en/content/exhibition-keep-running-ai-art-and-qatari-heritage (Accessed: 15 March 2021).

Floridi L. 2018, *Artificial Intelligence, Deepfakes and a Future of Ectypes*, "Philosophy & Technology", 31 (3), pp. 317–21. https://doi.org/10.1007/s13347-018-0325-3.

Gladwell M. 2012, *Blink: The Power of Thinking Without [Thinking]*, Boston.

Goodfellow I. J. *et alii* 2014, *Generative Adversarial Networks*. *arXiv Preprint arXiv:1406.2661*.

Grant T. 2015, *Jeremy Hutchinson's Case Histories: From Lady Chatterley's Lover to Howard Marks*, Boston.

Hagstrom S. 2014, *The FAIR Data Principles*, "FORCE11". Available at: https://www.force11.org/group/fairgroup/fairprinciples (Accessed: 20 January 2021).

Hameeuw H., Van der Perre A., Vandermeulen B., Proesmans M., Delvaux L., Boschloos V., Ossieur F., Braekmans D. 2017, *Conservation, Ir, Uv and 3D-Imaging: The Egyptian Execration Statuettes Project (Ees). Final Report*, Brussels, 2017-03.

Herman A. 2014, *The Fake Chagall, the Asphalt Jungle and Moral Rights in France*, "Art Antiquity and Law" 19 (2).

Ireland T., Schofield J. 2015, *The Ethics of Cultural Heritage,* in *Ethical Archaeologies: The Politics of Social Justice*, 4, New York, pp.13–32.

Johnson D. H., Sun L., Johnson C. R., Hendriks E. 2010, *Matching Canvas Weave Patterns from Processing X-Ray Images of Master Paintings*, in *IEEE International Conference on Acoustics, Speech and Signal Processing*, pp. 958–61. Available at: https://doi.org/10.1109/ICASSP.2010.5495297.

Johnson C. R., Messier P., Sethares W. A., Klein A. G., Brown C., Do A. H., Klausmeyer P., Abry P., Jaffard S., Wendt H. 2014, *Pursuing Automated Classification of Historic Photographic Papers from Raking Light Images,* in "Journal of the American Institute for Conservation" 53 (3), pp. 159–70.

Justia US Law. 1998. "Bridgeman Art Library, Ltd. v. Corel Corp., 25 F. Supp. 2d 421 (S.D.N.Y. 1998)." Available at: https://law.justia.com/cases/federal/district-courts/FSupp2/25/421/2325910/ (Accessed: 20 August 2021).

Karaszewski M., Sitnik R., Bunsch E. 2012, *On-Line, Collision-Free Positioning of a Scanner During Fully Automated Three-Dimensional Measurement of Cultural Heritage Objects*, "Robotics and Autonomous Systems", 60 (9), pp. 1205-1219. https://doi.org/10.1016/j.robot.2012.05.005.

Khan M. J., Yousaf A., Khurshid K., Abbas A., Shafait F.. 2018, *Automated Forgery Detection in Multispectral Document Images Using Fuzzy Clustering*, in 2018 13th IAPR International Workshop on Document Analysis Systems (DAS), pp. 393–398. https://doi.org/10.1109/DAS.2018.26.

Kleppner D. 2009, *Ensuring the Integrity, Accessibility, and Stewardship of Research Data in the Digital Age*. Washington, D.C. https://doi.org/10.17226/12615.

Kogan T. S. 2012, *Photographic Reproductions, Copyright and the Slavish Copy*, in "Journal of Law and the Arts", 3, pp. 445-502.

Lagrange E., Oeter S., Uerpmann R. 2018, *Cultural Heritage and International Law: Objects, Means and Ends of International Protection*. Cham.

Lopatin L. 2006, *Library Digitization Projects, Issues and Guidelines: A Survey of the Literature*, "Library Hi Tech", 24 (2), pp. 273–89.

Li L. *et alii* 2017, *In Situ Repair of Bone and Cartilage Defects Using 3D Scanning and 3D Printing,* Scientific Reports 7, 1, pp. 1–12.

Magnusson M. 2006, *Fakers, Forgers & Phoneys: Famous Scams and Scamps*, Edinburgh.

Mazzone M., Elgammal A. 2019, *Art, Creativity, and the Potential of Artificial Intelligence*, "Arts", 8 (26.1). Available at: https://doi.org/10.3390/arts8010026

Metro Game Central 2019, *Ubisoft Donates the Almost 1:1 Scaled 3D Model Developed for Assassin's Creed Game Towards the Reconstruction of the Cathedral After Damage*. Available at: https://metro.co.uk/2019/04/17/ubisoft-donates-e500000-to-notre-dame-restoration-gives-away-assassins-creed-unity-for-free-9237251/ (Accessed: 15 February 2021).

Microsoft, and ING. 2016, *The Next Rembrandt*. Available at: https://www.nextrembrandt.com (Accessed 15 February 2021).

Miller M. H. 2016, *The Big Fake: Behind the Scenes of Knoedler Gallery's Downfall,* in ARTnews.Com (blog), April 25, 2016. Available at: https://www.artnews.com/art-news/artists/the-big-fake-behind-the-scenes-of-knoedler-gallerys-downfall-6179/ (Accessed: 15 February 2021).

Morph Gallery 2021, *Parc Del Laberint D'horta*, in MORF. GALLERY (blog). Available at: https://morf.gallery/artwork/oxia-palus/parc-del-laberint-dhorta/ (Accessed: 10 September 2021).

National Geographic 2020 Greshko M. 2020, *Dead Sea Scrolls' at the Museum of the Bible are all Forgeries*, "National Geographi, History & Culture news", Available at: https://www.nationalgeographic.com/history/2020/03/museum-of-the-bible-dead-sea-scrolls-forgeries/ (Accessed: 15 February 2021).

Newman R. 1998, *Applications of x Rays in Art Authentication: Radiography, x-Ray Diffraction, and x-Ray Fluorescence*, "Scientific Detection of Fakery in Art", 3315, pp. 31–41.

Nicholas G., Egan B. 2012, *IPinCH. Intellectual Property Issues in Cultural Heritage: Theory, Practice, Policy, Ethics*, Simon Fraser University–Social Sciences, Humanities Research Council. Available at: http://www.sfu.ca/ipinch/ (Accessed: 15 February 2021).

Nickell J. 2005, *Detecting Forgery: Forensic Investigation of Documents*. Lexington.

Nickell J. 2007, *Relics of the Christ*, Lexington.

NTNU 2018/2019, CHANGE – Cultural Heritage Analysis for New Generations, Norwegian University of Science & Technology. Available at: https://change-itn.eu/about/ (Accessed: 15 February 2021).

NVIDIA. 2021, The *AI Art Gallery – Art and Music in Light of AI* (part of the online GPU Technology Conference 2020). Available at: https://www.nvidia.com/en-us/deep-learning-ai/ai-art-gallery/ (Accessed: 1 May 2021).

Overgaard N., Loiselle M. 2017, *Authority Delegation,* in "Scientonomy: Journal for the Science of Science", 1, pp. 11–18. Available at:

https://doi.org/10.33137/js.v1i0.27065.

Oxia Palus 2021 – Our Gallery - Resurrecting Lost Art with AI, in "Oxia Palus. 2021". Available at: https://www.oxia-palus.com/gallery (Accessed: 10 September 2021).

Pelagotti A., Piva A., Uccheddu F., Shullani D., Alberghina M.F., Schiavone S., Massa E., Menchetti C.M. 2020, *Forensic Imaging for Art Diagnostics. What Evidence Should We Trust?,* in *IOP Conference Series: Materials Science and Engineering*, Proceedings of the 2nd International Conference Florence Heri-Tech: The Future of Heritage Science and Technologies, HERITECH 2020 (14 -16 October 2020), IOP Conference Series: Materials Science and Engineering. Available at: http://dx.doi.org/10.1088/1757-899X/949/1/012076

Petri G. 2014, *The Public Domain Vs. The Museum: The Limits of Copyright and Reproductions of Two-Dimensional Works of Art*, "Journal of Conservation and Museum Studies", 12 (1), Available at: https://doi.org/10.5334/jcms.1021217.

Polak A., Kelman T., Murray P., Marshall S., Stothard D.J.M., Eastaugh N., Eastaugh F. 2017, *Hyperspectral Imaging Combined with Data Classification Techniques as an Aid for Artwork Authentication*, "Journal of Cultural Heritage", 26, pp. 1–11.

Radford A., Metz L., Chintala S. 2015, *Unsupervised Representation Learning with Deep Convolutional Generative Adversarial Networks*, arXiv Preprint arXiv:1511.06434.

Riederer J. 2012, *The Detection of Art Forgeries with Scientific Methods*, "Forensic Science Progress", 1, p. 153.

Saverwyns S., Currie C., Lamas-Delgado E. 2018, *Macro X-Ray Fluorescence Scanning (MA-XRF) as Tool in the Authentication of Paintings,* "Microchemical Journal", 137, pp. 139–47.

Scott D. A. 2017, *Art Restoration and Its Contextualization*, "Journal of Aesthetic Education", 51 (2), pp. 82–104.

She J., Ng C., Sheng W. 2020, *Keep Running - AI Paintings of Horse Figure and Portrait*, in *Proceedings of the 28th ACM International Conference on Multimedia*, pp. 4403–4404. Available at:

https://doi.org/10.1145/3394171.3416342.

Simon S., Röhrs S. 2018, *Between Fakes, Forgeries, and Illicit Artifacts – Authenticity Studies in a Heritage Science Laboratory*, "Arts", 7 (2), p. 20. https://doi.org/10.3390/arts7020020.

Sladen O. 2010, *Faking History: How Provenance Forgery Is Conning the Art World*, "J. Art Crime", 3, p. 47.

Soderland H. A., Lilley I. A. 2015, *The Fusion of Law and Ethics in Cultural Heritage Management: The 21st Century Confronts Archaeology*, "Journal of Field Archaeology", September. Available at: https://doi.org/10.1179/2042458215Y.0000000024.

Sorbo E. 2019, *Restoration, Strengthening and Planning in Italian and German Reconstruction After World War II: Essay in Three Steps*, "Journal of Civil Engineering and Architecture", 13, pp. 115–24.

Stanish C. 2009, *Forging Ahead*, in "Archaeology", 62 (3), pp. 18–66.

FADGI, *Technical Guidelines for Digitizing Cultural Heritage Materials: Creation of Raster Image Files*, in *Still Image Working Group, Federal Agencies Digital Guidelines Initiative*. *2016*. Available at: http://www.digitizationguidelines.gov/guidelines/digitize-technical.html (Accessed: 20 May 2020).

Stobart J. 1984, *Modigliani Missing Heads Hoax,* "The Christian Science Monitor". Available at: https://www.csmonitor.com/1984/0907/090749.html (Accessed: 15 February 2021).

Tissen, L. N. M. 2020, *A Rebirth of Reproductions; 3D Printing as a Conservation Strategy for Paintings*, *The Fragment in the Digital Age, Opportunities and Limitations of New Conservation-Restoration Techniques* (Hildesheim, 6-8 May 2021). Available at: https://hornemann-institut.de/de/epubl_txt/2020PosterTissen.pdf.

Tum J., Middleton A. 2006, *Radiography of Cultural Material*. Oxford.

UNESCO. 1970, in "UNESCO 1970 Convention on Illicit Trafficking of Cultural Heritage Property". Available at: http://www.unesco.org/new/en/culture/themes/illicit-trafficking-of-cultural-property/unesco-database-of-national-cultural-heritage-laws/ (Accessed: 15 May 2021).

UNESCO 2003, in "UNESCO Database of National Cultural Heritage Laws Against Illicit Trafficking of Cultural Heritage Property." Available at: http://portal.unesco.org/en/ev.php-URL_ID=13039&URL_DO=DO_TOPIC&URL_SECTION=201.html (Accessed: 15 May 2021).

Van Dormolen H. 2008, *Metamorfoze Preservation Imaging Guidelines*, "Proc. Archiving Conf.", IS&T, pp. 162-165.

Whitlum-Cooper F. 2021, *Poussin's 'Triumph of Silenus' Rediscovered,* "The Burlington Magazine", 163, pp. 408-415.

Yaniv J., Newman Y., Shamir A. 2019a, *The Face of Art: Landmark Detection and Geometric Style in Portraits*, "ACM Transactions on Graphics" 38 (4), pp. 1–15.

Yaniv J., Newman Y., Shamir A. 2019b, *The Face of Art*. Available at: https://faculty.idc.ac.il/arik/site/foa/face-of-art.asp (Accessed: 15 May 2021).

Università
degli Studi
di Padova

Progetto
MemO

Progetto grafico e stampa
Publicad - Udine
www.publicad.it - www.pcrea.it

Edizione / 1.0
Anno 2022

ISBN 978-82-326-7160-1 (printed ver.)
ISBN 978-82-326-7159-5 (electronic ver.)
ISSN 1503-8181 (printed ver.)
ISSN 2703-8084 (online ver.)

NTNU
Norwegian University of
Science and Technology